

**FIRST PRINCIPLES STUDIES OF ELECTRONIC  
AND MAGNETIC PROPERTIES OF ATOMIC  
CLUSTERS AND POLAR OXIDES**

*By*  
**ARPITA SEN**  
**PHYS08201404001**

**Harish-Chandra Research Institute, Allahabad**

*A thesis submitted to the*  
*Board of Studies in Physical Sciences*  
*In partial fulfillment of requirements*  
*for the Degree of*  
**DOCTOR OF PHILOSOPHY**  
*of*  
**HOMI BHABHA NATIONAL INSTITUTE**



**December, 2020**

# Homi Bhabha National Institute<sup>1</sup>

## Recommendations of the Viva Voce Committee

As members of the Viva Voce Committee, we certify that we have read the dissertation prepared by Arpita Sen entitled "First principles studies of electronic and magnetic properties of atomic clusters and polar oxides" and recommend that it may be accepted as fulfilling the thesis requirement for the award of Degree of Doctor of Philosophy.

---

Chairman – Prof. Sumathi Rao



Date: 05-04-2021

---

Guide / Convener – Prof. Prasenjit Sen



Date: 05-04-2021

---

Examiner - Prof. Tanusri Saha Dasgupta



Date: 05-04-2021

---

Member 1- Prof. Pinaki Majumdar



Date: 05-04-2021

---

Member 2- Prof. Santosh Kumar Rai



Date: 05-04-2021

---

Member 3- Prof. Anshuman Maharana



Date: 05-04-2021

---

Final approval and acceptance of this thesis is contingent upon the candidate's submission of the final copies of the thesis to HBNI.

I/We hereby certify that I/we have read this thesis prepared under my/our direction and recommend that it may be accepted as fulfilling the thesis requirement.

Date: 05.04.2021

Place: Prayagraj



Prof. Prasenjit Sen  
Guide

---

<sup>1</sup> This page is to be included only for final submission after successful completion of viva voce.

# STATEMENT BY AUTHOR

This dissertation has been submitted in partial fulfillment of requirements for an advanced degree at Homi Bhabha National Institute (HBNI) and is deposited in the Library to be made available to borrowers under rules of the HBNI.

Brief quotations from this dissertation are allowable without special permission, provided that accurate acknowledgement of source is made. Requests for permission for extended quotation from or reproduction of this manuscript in whole or in part may be granted by the Competent Authority of HBNI when in his or her judgment the proposed use of the material is in the interests of scholarship. In all other instances, however, permission must be obtained from the author.

A handwritten signature in black ink that reads "Arpita Sen". The signature is written in a cursive, flowing style.

Arpita Sen



# DECLARATION

I, hereby declare that the investigation presented in the thesis has been carried out by me. The work is original and has not been submitted earlier as a whole or in part for a degree/diploma at this or any other Institution/University.

A handwritten signature in black ink that reads "Arpita Sen". The signature is written in a cursive, slightly slanted style.

Arpita Sen



## List of Publications arising from the thesis

### Journal

1. “Properties of Highly Oriented Pyrolytic Graphite Supported TaSi<sub>16</sub> Clusters: A Density Functional Investigation”, Arpita Sen and Prasenjit Sen, *J. Phys. Chem. C*, **2017**, *121*, 28490-28497.
2. “Designing rare earth free permanent magnets: Insights from small Co clusters”, Arpita Sen and Prasenjit Sen, *Phys. Chem. Chem. Phys.*, **2019**, *21*, 22577-22583.

### In preparation

1. “Competing Structural and Electronic Instabilities at the Surfaces of Polar Insulating BeO: Emergence of Two Dimensional Electron Gas”, Arpita Sen, Prasenjit Sen and Umesh V Waghmare.
2. “Electronic structure and stability of Polar oxide surface”, Arpita Sen, Prasenjit Sen and Umesh V Waghmare.

### Other publications (Not included in the thesis)

1. “Localized spin waves at low temperatures in a cobalt carbide nanocomposite”, Nirmal Roy, Arpita Sen, Prasenjit Sen and S.S Banerjee, *Journal of Applied Physics*, **2020**, *127* 124301-1 - 124301-6
2. “The Exchange Bias effect in pure Co<sub>2</sub>C nanoparticles”, Nirmal Roy, Md. Arif Ali<sup>1</sup>, Arpita Sen, Prasenjit Sen, S.S. Banerjee, (*arXiv:2005.04904*)s.

## Conference

1. Attended and presented a poster in **International Conference on Magnetic Materials and Applications** at NISER, Bhubaneswar, India, 2018 on “Enhancement of Magnetic Anisotropy of Cobalt Cluster by Doping”.
2. Attended and presented a poster in **19th International Workshop on Computational Physics and Material Science: Total Energy and Force Methods** at ICTP, Trieste, Italy, 2019 on “Enhancement of Magnetic Anisotropy of Cobalt Cluster by Doping”.
3. Attended and presented a poster in **Workshop on Crystal Structure Prediction: Exploring the Mendeleev Table as a Palette to Design New Materials** at ICTP, Trieste, Italy, 2019 on “TaSi<sub>16</sub> clusters on HOPG: Structures and electronic properties.
4. Attended and presented a poster in **International Workshop on Advanced Materials** at Ras Al Khaimah, 2019 ”Emergence of 2DEG at the surface of polar oxides”.



Arpita Sen

To my Rudro Da...(Dr. Rudranil Basu, BITS Pilani Goa)



## ACKNOWLEDGEMENTS

I am thankful to Prof. Prasenjit sen for giving me the opportunity to work under his supervision. I am grateful to HRI cluster facility without which it was just not possible to complete this thesis work. I would like to convey my sincere gratitude to Mr. Amit Khulve, the ex-cluster admin of HRI from whom I have learnt various important technical stuffs in computational works from very early days of work. I am grateful to Mr. Rajiv Kumar, present cluster admin for his cooperation. I am very much grateful to Masud Da (Dr. Mehedi Masud), for introducing me shell scripting in linux environment initially. His careful guidance regarding script writing and others linux stuffs has given me confidence to work in computational field. I would like to convey my deepest sense of gratitude to Prof. Umesh V. Waghmare for giving me the opportunity to work with him in some crucial projects. His sense of appreciation for every details in a scientific problem, gives exciting dimension in my thoughts. His critical comments in every small wrong step used to make me more careful in my research. On the other hand his joyful expressions in every slight new finding gives a lots of encouragement at every step. I am thankful to Akasha Didi (Dr. Akansha Singh) for her suggestions. I am thankful to Mr. Sanjai Verma, Mrs. Anju Verma, Mr. Yashpal Singh, Ms Archana Tandon for their cooperation during my stay at HRI. I am specially thankful to Prof. Ujjwal Sen, Prof. Sumathi Rao and Prof. Anirban Basu for their continuous encouragement of finishing the thesis work. I am very much grateful to Prof. Ujjwal Sen and Prof R. Thangadurai for helping in various non academic issues during my stay at HRI. I am thankful to Samarat Bhaiya and Joshi Bhaiya for their support in some technical difficulties I faced in programming and plotting. I would like to convey thanks to my friend Suchitra and Ruchi for

giving constant motivation in my works. Last but not the least I would like to convey my sincere gratitude to the people, without whom it was not possible for me to come to HRI and take research in physics as a career option. My Rudro Da is the first person, who gave me the direction of taking physics as a career from my school going day. His constant motivation pushed me here today to submit the thesis. I am grateful to Prof. Krishnendu Mukherjee for his encouragement in research during my MSc. days. I am thankful to him for teaching me 'Latex' during my MSc. projects.

# Contents

<b>Summary</b>	<b>1</b>
<b>List of Figures</b>	<b>5</b>
<b>List of Tables</b>	<b>15</b>
<b>1 Introduction</b>	<b>17</b>
1.1 Atomic clusters . . . . .	17
1.1.1 Surface supported clusters . . . . .	19
1.1.2 Production of substrate supported clusters by atomic vapor deposition . . . . .	23
1.1.3 Deposition of preformed cluster . . . . .	25
1.1.4 Softlanding . . . . .	28
1.1.5 Cluster assembled films . . . . .	30
1.2 TM doped Si clusters . . . . .	31
1.2.1 Studies on structure of TM-Si clusters . . . . .	33
1.2.2 Relative Stability of $\text{TMSi}_n$ Clusters . . . . .	45
1.3 Permanent magnet . . . . .	63
1.3.1 Properties of PM . . . . .	64

1.4	Polar oxide . . . . .	76
1.4.1	ZnO and BeO . . . . .	79
1.5	Structure of the thesis . . . . .	82
<b>2</b>	<b>Theoretical Methods</b>	<b>85</b>
2.1	Introduction . . . . .	85
2.2	The many body problem and Born-Oppenheimer Approximation .	86
2.3	The Density functional theory . . . . .	89
2.3.1	The Hohenberg-Kohn (HK) theorems . . . . .	89
2.3.2	The Kohn-Sham (KS) equations . . . . .	91
2.3.3	The exchange-correlation functional . . . . .	95
2.4	The Plane wave basis set . . . . .	97
2.5	The pseudopotential theory . . . . .	100
2.5.1	Projector Augmented Wave method (PAW) . . . . .	103
2.5.2	van der Waals corrections . . . . .	106
2.6	Calculation of properties beyond electronic energies . . . . .	109
2.6.1	Geometry optimization . . . . .	109
2.6.2	Finding the minimum energy structure of clusters . . . . .	111
2.6.3	Molecular dynamics simulations . . . . .	114
2.6.4	Nudged elastic band method . . . . .	118
2.6.5	Bader charges . . . . .	121
2.6.6	Calculation of phonons . . . . .	124
2.6.7	Magneto crystalline anisotropy (MCA) . . . . .	128
<b>3</b>	<b>Adsorption of TaSi<sub>16</sub> cluster on HOPG</b>	<b>135</b>
3.1	Motivation . . . . .	135
3.2	Computational methods . . . . .	138

3.3	Results and discussions . . . . .	140
3.3.1	Bulk graphite . . . . .	140
3.4	Structure of Isolated TaSi <sub>16</sub> Clusters . . . . .	142
3.4.1	Magnetic moment and charge transfer of ground state TaSi <sub>16</sub>	144
3.5	Adsorption of TaSi <sub>16</sub> on HOPG . . . . .	146
3.5.1	Structure of deposited TaSi <sub>16</sub> clusters . . . . .	146
3.5.2	Comparative study of TaSi <sub>16</sub> cluster at different site on HOPG . . . . .	148
3.5.3	Properties of adsorbed TaSi <sub>16</sub> cluster on HOPG with high- est $E_a$ . . . . .	151
3.5.4	Structural and chemical stability:Reaction with oxygen . .	154
3.5.5	Finite temperature behavior:Molecular dynamics simulation	156
3.6	Conclusions . . . . .	160
<b>4</b>	<b>Designing of rare earth free permanent magnet:Insights from small Co cluster</b>	<b>163</b>
4.1	Motivation . . . . .	163
4.2	Computational methods . . . . .	166
4.3	Results and discussions . . . . .	168
4.3.1	Pure Co <sub>4</sub> and Co <sub>6</sub> clusters . . . . .	168
4.4	Doped Co clusters . . . . .	169
4.4.1	Co <sub>4</sub> doped with group 14 elements . . . . .	170
4.4.2	Doped with group 15 elements . . . . .	171
4.4.3	Discussions on MAE:search for trends . . . . .	174
4.4.4	Central question:Which is(are) responsible factor(s) for con- trolling the MAE value? . . . . .	176

4.5	Conclusions . . . . .	184
<b>5</b>	<b>Electronic and magnetic properties of polar oxide surface:Emergence of 2DEG</b>	<b>187</b>
5.1	Motivation . . . . .	187
5.2	Computational methods . . . . .	189
5.3	Results and discussions . . . . .	189
5.3.1	Bulk BeO and ZnO . . . . .	189
5.3.2	Electronic structure of glide surface of BeO and ZnO . . .	191
5.3.3	Bulk insulator to surface metal transition:cleaving of crystal	193
5.4	Conclusions . . . . .	202
<b>6</b>	<b>Studies on dynamical stability of glide BeO and ZnO surfaces</b>	<b>215</b>
6.1	Motivation . . . . .	215
6.2	Dynamical stability BeO glide surface . . . . .	215
6.2.1	Phonon dispersion of BeO glide surface . . . . .	216
6.3	Dynamical stability of ZnO glide surface . . . . .	219
6.4	Conclusion . . . . .	222
<b>7</b>	<b>Summary and future outlook</b>	<b>223</b>
7.1	TaSi <sub>16</sub> on HOPG: A DFT study . . . . .	223
7.2	Designing of RE free PM: Insights from small Co clusters . . . .	224
7.3	Emergence of 2DEG in polar oxide surfaces . . . . .	225
	<b>APPENDIX</b>	<b>227</b>
<b>A</b>	<b>Adsorption of TaSi<sub>16</sub> cluster on HOPG</b>	<b>227</b>
	<b>Bibliography</b>	<b>233</b>

# List of Figures

1.1	Molecular-dynamics simulations of the morphology of films obtained by Mo <sub>1043</sub> cluster deposition onto a Mo(001) substrate with different incident kinetic energies per atom. . . . .	27
1.2	Possible elementary growth processes for two clusters meeting on a surface (a) aggregation (b) coalescence. . . . .	28
1.3	Variation of RAR as a function of number of Si atom in Sc-Si, Ti-Si and V-Si clusters. This AR is for the reaction with H <sub>2</sub> O. The threshold size for Si, at which the clusters become completely indifferent towards H <sub>2</sub> O, is shown by arrow in each panel. The figure is adapted from ref [66] . . . . .	35
1.4	RAR towards H <sub>2</sub> O as a function of number of Si atoms in different TM-Si clusters ( $n$ ), when the TMs are 3d, 4d and 5d. The open and filled symbols present clusters containing single and double TM atoms respectively. Figure is adapted from ref [66] . . . . .	37

1.5	Variation of fraction of argon complexes produced with various TMSi <sub>n</sub> clusters, with number of Si atoms in a cluster <i>n</i> . Clusters containing one or two TM atoms are involved here. This figure is adapted from ref [68] . . . . .	39
1.6	Experimentally measured IR-UV2CI and theoretically calculated IR spectra for a few low-energy isomers of CoSi <sub>n</sub> clusters, with <i>n</i> = 10 – 12: A comparative demonstration. Figure is adapted from Ref [73] . . . . .	41
1.7	Variation of relative abundance of TMSi <sub>n</sub> <sup>+</sup> among TMSi <sub>n</sub> H <sub>x</sub> <sup>+</sup> clusters as a function of <i>n</i> . Figure is adapted from Ref. [61] . . . . .	47
1.8	Mass spectra of (a) ScSi <sub>n</sub> , (b) TiSi <sub>n</sub> and (c) VSi <sub>n</sub> <sup>+</sup> clusters. Figure adapted from Ref. [63] . . . . .	49
1.9	PES of (a) and (b) ScSi <sub>16</sub> <sup>-</sup> , (c) and (d) TiSi <sub>16</sub> <sup>-</sup> , (f) and (g) Vsi <sub>16</sub> and (e) TiSi <sub>16</sub> F <sup>-</sup> clusters. Figure adapted from Ref. [63]. . . . .	51
1.10	Representation of (a) EE and (b) EE <sup>WW</sup> for 3d TM encapsulated caged Si <sub>12</sub> clusters. Figure is adapted from Ref. [79] . . . . .	60
1.11	The maximum energy density product $(BH)_{max}$ is shown by the area of the largest rectangle that can occupy below the second quadrant of the $B(H)$ curve. For an ideal PM Left: M(H) loop, right: B(H) loop respectively. . . . .	66
1.12	$K_U$ is the uniaxial anisotropy. $K_U$ for ternary (Fe <sub>0.4</sub> Co <sub>0.6</sub> ) <sub>0.98</sub> C <sub>0.02</sub> (full squares) and binary Fe <sub>0.45</sub> Co <sub>0.55</sub> films (open triangles) grown on Au <sub>0.5</sub> Cu <sub>0.5</sub> buffers varies with film thickness. Figure is adapted from ref [113]. . . . .	69

1.13	During magnetization reversal, a finite-element model of two interacting D30H100 Co nanorods. (b) How coercivity depends on the distance between two D10H100 (blue diamonds), D20H100 (green triangles) and D30H300 (red squares) nanorods. The coercivity of a single nanorod acts as an upper limit for structures containing several nanorods. Figure is adapted from [113]. . . . .	72
1.14	Magnetic properties of the experimentally produced $\text{Co}_3\text{C}$ . (a) The profile of magnetic hysteresis loops at different temperatures. (b) The dependence of coercivity on temperature to find out blocking temperature ( $T_B$ ). Figure is adapted from [5]. . . . .	74
1.15	Variation of MAE with spherical angles $\theta$ and constant $\phi$ . Figure is adapted from [5]. . . . .	75
1.16	Relaxed clusters (a) $\text{Co}_4\text{C}_2$ and (b) $\text{Co}_{12}\text{C}_4$ with the z-axis perpendicular to the plane. The number near each atom represents the local moment of that atom in $\mu_B$ . (c) and (d) are the anisotropy landscapes of $\text{Co}_4\text{C}_2$ and $\text{Co}_{12}\text{C}_4$ clusters respectively, with $\theta$ and $\phi$ as the polar and azimuthal angles respectively. Figure is adapted from [6]. . . . .	77
2.1	(a) Schematic diagram of all-electron (solid lines) and pseudoelectron (dashed lines) potentials and their corresponding wave functions. The radius at which pseudoelectron and all-electron values match is indicated $r_c$ (b) Oxygen $2p$ radial wave function (solid line) and corresponding norm-conserving [206] (dotted line) and ultrasoft [207] (dashed line) pseudo wave functions. The figure is reproduced from Ref. [207] . . . . .	101

2.2	Schematic representation of the PAW transformation. The auxiliary wave function is constructed from the full wave function by subtracting the oscillatory part close to an atom and replacing it by a smooth function. Figure is adopted from reference [210] . . .	103
2.3	Schematic 1D energy profile showing minimum energy path (MEP) which connect two local minima A and B separated by a transition state $X^\ddagger$ [244]. . . . .	118
2.4	DFT calculations of the MEP for $\text{CH}_4$ dissociative adsorption on the Ir(111) surface. A comparison between a regular NEB calculation and a CI-NEB calculation, both involving 8 movable images. The regular NEB results in a low resolution of images near the SP, and underestimates the activation energy. The CI-NEB put one of the images at saddle point giving accurate energy barriers [246].	120
2.5	Phase portraits. A pair of gradient paths terminates or originates respectively, at the CP for a 1D maximum or minimum. In 2D, all of the gradient paths in a plane terminates or originates, at the maximum or minimum (CP) respectively. At (2,0) CP, a pair of paths originates at the CP, (positive curvature), and another pair terminates at the CP (negative curvature). All other gradient paths avoid the CP. A 3D display of a (3, 1) CP shows the set of trajectories that terminate at the CP and define a surface and the unique pair that originates there and defines a line [104]. . . . .	133
3.1	Ground state optimized structures for $\text{TaSi}_{16}$ from same initial structure with different exchange correlation . . . . .	142

3.2	Structures of isolated globally optimized TaSi <sub>16</sub> cluster with energy level upto 1 eV higher from ground state, calculated including vDW-DF2. . . . .	145
3.3	Relaxed structure of deposited TaSi <sub>16</sub> cluster on HOPG . . . . .	146
3.4	Special symmetry points on HOPG . . . . .	148
3.5	Adsorbed TaSi <sub>16</sub> on HOPG at $\beta$ site with highest $E_a$ . . . . .	150
3.6	Spin density isosurface in TaSi <sub>16</sub> cluster deposited on HOPG. . . . .	151
3.7	Isosurface plots for (a) $\Delta\rho$ and (b) total charge density with iso-value 0.06 $e/bohr^3$ . . . . .	153
3.8	Initial structure for reaction with Oxygen . . . . .	155
3.9	Relaxed structure after oxygen atoms get attached with the cluster	155
3.10	Relaxed structure of deposited cluster on HOPG including reaction with Oxygen . . . . .	156
3.11	Energy barrier from CI-NEB calculation . . . . .	159
3.12	Variation of HOMO energy of deposited TaSi 16 cluster at (a) 400 K and (b) 700 K. . . . .	160
4.1	Two lowest energy Co <sub>4</sub> and Co <sub>6</sub> clusters obtained from global search.	169
4.2	Globally optimized Co <sub>4</sub> C <sub>2</sub> clusters:upto $\sim 0.5$ eV . . . . .	170
4.3	Globally optimized Co <sub>4</sub> Si <sub>2</sub> clusters:upto $\sim 0.5$ eV . . . . .	171
4.4	Globally optimized Co <sub>4</sub> Ge <sub>2</sub> clusters:upto $\sim 0.5$ eV . . . . .	171
4.5	Globally optimized Co <sub>4</sub> N <sub>2</sub> clusters:upto $\sim 0.5$ eV . . . . .	172
4.6	Globally optimized Co <sub>4</sub> P <sub>2</sub> clusters:upto $\sim 0.5$ eV . . . . .	173
4.7	Globally optimized Co <sub>4</sub> As <sub>2</sub> clusters:upto $\sim 0.5$ eV . . . . .	173
4.8	MAE in HOMO-LUMO gap - $\Delta L$ plane . . . . .	178
4.9	MAE in $\sum_i  m_i $ - HOMO-LUMO gap plane . . . . .	179

4.10	MAE in HOMO-LUMO gap - $M_{dp}$ plane . . . . .	180
4.11	MAE in $\sum_i  m_i $ - $\Delta L$ plane . . . . .	181
4.12	MAE in $\sum_i  m_i $ - $M_{dp}$ plane . . . . .	182
4.13	MAE in $\Delta L$ - $M_{dp}$ plane . . . . .	183
5.1	(a)Atomic and (b) electronic structure of wurtzite BeO. Green sphere represents Be atom and red sphere represents O atom. . .	190
5.2	(a)Atomic and (b) electronic structure of wurtzite ZnO. Purple sphere represents Be atom and red sphere represents O atom. . .	191
5.3	Bulk like Atomic structure of (a) glide and (b) shuffle surface of $1\times 1\times 3$ wurtzite BeO. . . . .	192
5.4	(a) Bulk like structure, (b) relaxed structure of (0001) glide surface of BeO. . . . .	193
5.5	Electronic structure of BeO glide surface obtained using (a) spin unpolarized and (b) spin polarized calculation respectively. The same colour has been used for a band of states spin up (solid lines) and spin down (dashed lines) channels for (b). Green solid line parallel to X axis represents Fermi level. . . . .	194
5.6	(a) Bulk like structure, (b) relaxed structure of (0001) glide surface of ZnO. . . . .	195
5.7	Electronic structure of ZnO glide surface obtained using (a) spin unpolarized and (b) spin polarized calculation respectively. The same colour has been used for a band of states spin up (solid lines) and spin down (dashed lines) channels for (b). Green solid line parallel to X axis represents Fermi level. . . . .	196
5.8	Labeling of atoms and $d_{vac}$ for BeO $1\times 1\times 3$ glide BeO surface . .	196

5.9	Cleaving across (0001) plane achieved with gradual increment in distance between the slab and its periodic image(vacuum thickness) maintaining the bulk structure. . . . .	197
5.10	Evolution of electronic structure during cleavage of BeO at basal glide plane: Origin of 2DEG . . . . .	198
5.11	Emergence of metallicity and magnetization upon cleavage as seen in (a) band gap ( $E_g$ ) and (b) magnetization (M) with interplanar separation at cleavage $d_{vac}$ as defined in figure 5.8 (a) . . . . .	199
5.12	Contour plots of charge density of the lowest energy conduction band with $d_{vac}=0.6\text{\AA}$ , in (a) plane containing $O_6$ .(b) intermediate plane between $O_6$ and periodic image of $Be_1$ (c) plane containing periodic image of $Be_1$ . . . . .	203
5.13	Projected density of states of the relaxed structure of (0001) glide surface of BeO showing contribution of O atoms (a) spin polarized with down spin channel (b) spin unpolarized. The vertical dashed line indicates the Fermi level. . . . .	204
5.14	Projected density of states.Upper panels (a) and (b) are for up spin channel with contributions from all Be and all O atoms respectively.Lower panel (c) for down spin channel with Be contributions. The dashed blue line indicates the Fermi level. . . . .	205
5.15	Isosurface of spin density of BeO slab terminated with glide surfaces.	206
5.16	Density of states projected on the orbitals of Be atoms. . . . .	206

5.17	Planar (red solid line) and macroscopic (green dashed line) average of the electrostatic potential along z axis (direction perpendicular to the glide surface of BeO), obtained employing dipole correction, demonstrating its spontaneous dipole and an internal electric field causing polar catastrophe. . . . .	207
5.18	Magnetoelectric effect evident in linear variation in magnetization at (0001) glide surface of BeO in response to electric field perpendicular to the surface. . . . .	208
5.19	Evolution of electronic structure during cleavage of ZnO at basal glide plane: Origin of 2DEG . . . . .	209
5.20	Emergence of metallicity and magnetization upon cleavage as seen in (a) band gap ( $E_g$ ) and (b) magnetization (M) with interplanar separation at cleavage $d_{vac}$ . . . . .	210
5.21	Contour plots of charge density of the lowest energy conduction band with $d_{vac}=0.6\text{\AA}$ , in (a) plane containing $O_6$ , (b) intermediate plane between $O_6$ and periodic image of $Zn_1$ (c) plane containing periodic image of $Zn_1$ . . . . .	211
5.22	Projected density of states of the relaxed structure of (0001) glide surface of ZnO showing contribution of O atoms (a) spin polarized with down spin channel (b) spin unpolarized. The vertical dashed line indicates the Fermi level. (c) Spin density iso surface for ZnO glide surface. . . . .	212
5.23	Planar averaged potential of ZnO along c axis with dipole correction	213
5.24	Magnetoelectric behaviour ZnO glide plane. . . . .	213

6.1	(a) Phonon dispersion of (0001) glide surface of BeO shown in Figure 5.4(a). (b) visualization of highest imaginary modes at M point, showing lattice instabilities at M point that would cause its reconstruction. . . . .	216
6.2	Reconstructed structure of $2 \times 1 \times 1$ supercell of BeO (0001) glide surface of figure 5.4 (a) with eigen displacements for unstable mode at M point, initial (a) and relaxed (b). . . . .	217
6.3	Electronic structure of reconstructed $2 \times 1 \times 1$ supercell BeO glide surface (as shown in figure 6.2 (b)) . . . . .	218
6.4	Phonon dispersion of reconstructed $2 \times 1 \times 1$ supercell BeO glide surface (as shown in figure 6.2(b)) . . . . .	218
6.5	Reconstructed structure of $2 \times 2 \times 1$ supercell BeO glide surface (as shown in figure 6.2 (b) with eigen displacements for imaginary mode at S point). Panel (a) and (b) for initial and relaxed structure respectively. . . . .	219
6.6	Electronic structure of $2 \times 2 \times 1$ reconstructed glide surface of BeO (shown in figure 6.5(b)), calculated with (a) spin-independent and (b) spin-dependent DFT respectively. . . . .	220
6.7	Phonon dispersion of ZnO $1 \times 1 \times 3$ glide surface(as shown in figure 5.6(b)) . . . . .	220
6.8	$2 \times 1 \times 1$ reconstruction of (0001) glide surface of ZnO (shown in figure 5.6(b)), structure before (a) and after (b) relaxation. . . .	221
6.9	Electronic structure of ZnO $2 \times 1 \times 1$ reconstructed glide surface (shown in figure 6.8(b)). . . . .	221

A.1 Structures of isolated globally optimized Tasi<sub>16</sub> cluster with energy larger than 1 eV from ground state, calculated including vDW-DF2. [228](#)

# List of Tables

1.1	The metallic bond radii and threshold size for loss of AR in three different charge states corresponding at which the $\text{TMSi}_n$ clusters fail to react with $\text{H}_2\text{O}$ . . . . .	38
3.1	Properties of bulk graphite for different exchange correlation functionals . . . . .	141
3.2	Adsorption energies of a $\text{TaSi}_{16}$ cluster on HOPG in different structures. . . . .	150
5.1	Optimized lattice parameters of wurtzite BeO estimated using different exchange correlation energy functionals . . . . .	190

## Summary and future outlook

This thesis composed of three projects. The first two are on atomic cluster systems and the third one involves studies on polar oxide surfaces. All of them are studied incorporating first principles density functional theory (DFT) calculation.

### 7.1 TaSi<sub>16</sub> on HOPG: A DFT study

In this project extensive studies of electronic structure of HOPG supported TaSi<sub>16</sub> cluster has been performed. For computational cost a single structure has been deposited. After checking the chemical stability and molecular dynamics simulation, it was found that it is physisorbed and the cage structure distorted but it never broke. It can be predicted that these properties will remain same when more number of clusters will be deposited. So this can be taken as ideal system for self assembly of deposited cluster system which is used in cluster assembled material. Here due to weak interaction of cluster and substrate the properties of isolated clusters remains almost same after adsorbed on HOPG. Hence the next work can be performed by changing the central Ta atom with V with DFT calculatuon, as they are in same group in periodic table. For deposited TaSi<sub>16</sub>,

the experimental studies are already there. If the DFT results from V doped systems are similar as Ta doped systems, without experimental evidence of deposited V doped Si cluster, it can be predicted that if the central atom is from same group the supported cluster will behave in similar manner. If the V doped system behaves differently, then it will also very interesting to study further.

## **7.2 Designing of RE free PM: Insights from small Co clusters**

In this section of the thesis, the importance of various quantities like HOMO-LUMO gap, mixing, magnetic moment etc. has been demonstrated predicting them as possible responsible parameters for determining the MAE in doped Co cluster systems. We have studied with total 60 doped Co clusters by taking 10 of each doping elements. Incidentally mixing was not found as an important parameter for controlling the MAE of doped Co cluster systems. We checked with non magnetic doping elements from group 14 and group 15 and “which element is doped with the Co cluster”, this fact did not play any role in controlling the MAE values. The amount of mixing was found also insignificant in determination of MAE. The next work can be a checking whether mixing plays any important role while doping with non magnetic elements from other group. From these results a machine learning study can be done taking the parameters as descriptors and study further for other cluster systems with different sizes and changing the Co atom to another magnetic elements.

### 7.3 Emergence of 2DEG in polar oxide surfaces

Glide surfaces of wurtzite BeO and ZnO have been studied extensively. Insulator to metal transition has been found with emergence of 2DEG in both cases. Strong magneto electric coupling found interestingly. These systems can be used further in spintronics. Most importantly the metallicity in the glide surfaces is found with surface reconstruction. The reconstructed surfaces are dynamically stable than the un reconstructed one, but metallic.

BeO is a rather large band gap insulator. It will be interesting to consider its solid solution with ZnO and its surface, substitution at the surface to control and achieve these unusual properties of 2DEG and magneto electric effect in a robust way so that they could be useful in a number of applications from catalysis to sensors.

## Summary

Over the last two-three of decades, extensive studies including theories and experiments have been performed in the field of transition metal (TM) doped silicon clusters. Proper understanding of metal-semiconductor interfaces along with coupling of magnetism in the TM atoms with the semiconducting characteristics of Si, was the initial motivation. Unlike C, Si only prefers *sp* hybridization[1, 2] which is not favorable for stable cage structures. From first-principles electronic structure calculations, Jackson and Nellerhoe[3] demonstrated that stabilization of a Si<sub>20</sub> cage could be possible by keeping a Zr atom inside it. After This finding, several experiments have produced a variety of clusters in this series. Depending on the encapsulated TM atom, clusters at specific sizes were found to be more stable than others. Several attempts were taken to justify the observed stability of TM-Si clusters for a given size, in terms of several well known electron counting rules. These kind of attempts generate some interesting debate in literature. While isolated clusters are interesting systems in their own way, any application requires them to be deposited on some substrate. In this direction, Shibuta et al.[4] performed the first experiment with Ta encapsulated caged Si clusters on highly oriented pyrolytic graphite (HOPG) using X-ray photoelectron spectroscopy (XPS). In order to understand the properties of TaSi<sub>16</sub> on HOPG from microscopic origin, we have explored adsorption of TaSi<sub>16</sub> on HOPG using density functional theory (DFT).

Permanent magnets (PM) form essential parts in various devices in a wide range of applications, such as, in hybrid and electric cars, wind turbines, motors in many household appliances, satellite communications systems and magnetic data storage systems. There is an urgent drive to design PM without rare earth (RE) elements due to supply side constraints of RE elements like Dy, Tb, Nd

etc. Generally, they are required to have large Curie temperature ( $T_c$ ), large saturation magnetization ( $M_S$ ), and large coercivity ( $H_c$ ). Large coercivity is a result of large magnetic anisotropy energy (MAE). The most widely used permanent magnets in present day applications are  $\text{Nd}_2\text{Fe}_{14}\text{B}$  and  $\text{SmCo}$  type alloys. El-Gendy et al. [5] explored cobalt-carbide nano-particles as RE-free magnets at the nano-scale. They reported MAE values close to  $100 \text{ meV/Co}$  ( $0.75 \text{ MJ m}^{-3}$ ), significantly larger than that of bulk hcp Co. For understanding of the factors that control MAE, to design new RE free PM, Islam and Khanna[6] worked on  $\text{Co}_4\text{A}_2$  ( $A = \text{C, Si}$ ) clusters theoretically and found large enhancement of MAE the clusters and their assemblies. Given the state of affairs, we tried to figure out the the main factors controlling MAE and whether any trend could be found with these factors responsible for enhancement of MAE in small doped Co clusters.

Polar oxide surfaces have been studied extensively theoretically and experimentally for fundamental issues regarding their stability. Among the polar oxides the  $\text{ZnO}(0001)$  surfaces has been studied widely as a prototypical example of a polar oxide surface. The wide band gapped semiconductor  $\text{ZnO}$  with wurtzite structure itself is of interest for a wide range of applications ranging from catalysis, gas sensing, to opto and micro electronics [7–13]. Wurtzite  $\text{BeO}$  has the same crystal structure as  $\text{ZnO}$  and it is also widely used as large band gap insulator with pizeoelectric properties. Various studies with shuffle  $\text{BeO}$  and  $\text{ZnO}$  interfaced with some other materials showing presence of 2 dimensional electron gas (2DEG) at the interface as a result of discontinuity of polarization. We checked if 2DEG can be found naturally at the surface of  $\text{BeO}$  and  $\text{ZnO}$  without making any interface. We found that glide surfaces of  $\text{BeO}$  and  $\text{ZnO}$  are metallic and have emergent 2DEG in. Moreover the glide surface is magnetic with appreciable magneto electric effect.

In summary, this thesis is comprised of two themes: study of (1) electronic and magnetic properties of atomic clusters both isolated and surface supported, and (2) stability and electronic structures of polar oxide surfaces.

# Introduction

## 1.1 Atomic clusters

What is atomic cluster? Atomic cluster is basically defined as a collection of finite number of atoms that are mainly (or at least to a significant extent) connected by direct chemical interactions between the constituent atoms. The formation of clusters and their aggregates, ie whether these will be formed in gas phase, liquid phase or will be suitable for deposition on solid substrate, depends on the experimental techniques and methodology.

Atomic clusters are composed of a few to a few hundred atoms. Due to the wide range of their possible sizes, compositions and charge states, the properties exhibited by them are distinct from those an atom. The number of atoms on the surface of a cluster is a substantial fraction of the total number of atoms and the arrangement of atoms in a cluster is very different from that in the corresponding bulk. Due to this, the properties of clusters are also different from molecules. Molecules are usually formed by either covalent or ionic bonds between the atoms, while bonding within clusters could be metallic, covalent, van

der Waals or ionic also. Molecules are very stable against coalescing, but clusters are metastable objects. Atomic clusters show extreme size-dependent electronic, magnetic, chemical and optical properties. Addition or removal of even one atom or one electron can induce dramatic changes in these properties[14]. This exciting feature gives us the opportunity to tune properties of cluster according to our requirements. For this reason clusters are considered as the ideal candidates to serve as building blocks for novel materials. To analysis the properties of atomic clusters, they are classified in various ways. Depending upon the types of the constituent atoms and the nature of bonding between them, atomic clusters can be classified into following categories. (i) semiconductor clusters such as  $\text{Ge}_N$ ,  $\text{Si}_N$ , (ii) ionic clusters, such as  $(\text{NaCl})_N$  (iii) rare gas clusters, such as  $\text{Ar}_N$ , (iv) metal clusters with metallic bonding such as  $\text{Na}_N$ . In cluster science, clusters formed out of atoms that are metallic in the bulk are termed metal clusters. Bulk metallic systems have finite density of states at the Fermi level and hence have gapless spectra. But metal clusters can't be defined in the same way as they always show discrete electronic spectra because of their finite size. Metal clusters can be of simple metals, noble metals, transition metals (TM). Clusters can also be formed of more than one species, called mixed clusters. In case of mixed clusters, the constituent atoms may be metals, or one metals with another semiconductor or insulator etc. In the later sections we will discuss elaborately about TM doped Si clusters, and Co clusters doped with some nonmagnetic elements. Both of them can be considered as mixed clusters.

### **Cluster assembled materials**

As clusters show fascinating size and shape dependent properties, they are considered as building blocks for designer new materials [14–17]. By assembling

clusters, materials with novel functional and structural properties can be produced. These are called cluster assembled materials (CAM). Properties of CAMs can be tuned by choosing appropriate building blocks.

Fullerene based materials are one of the popular examples of CAM [18].  $(C_{60})$  carbon fullerene can be combined to form a face-centered cubic solid. Such crystals are known as fulleride. In fulleride, structural identities of  $C_{60}$  cluster are retained and they have very different properties than diamond or graphite. Alkali-doped fullerides  $A_3C_{60}$  ( $A = K, Rb, Cs$ ) are also capable of forming high crystalline solids with interesting properties [19]. These doped fullerides exhibit superconductivity which can be tuned by changing the interfullerene spacing. Liu et al. studied another class of CAM, which are made from Al clusters [20]. They reported  $Al_{13}K$  cluster, which is an ionically bonded complex, have properties similar to KCl molecule. These facts lead to the idea that such motifs can be used for CAM. There are some theoretical and experimental studies exploring properties of clusters which can be used as building blocks for CAM's [21–24].

### 1.1.1 Surface supported clusters

To use clusters in various devices, it is necessary to deposit on a suitable substrate. Surface supported clusters is one of the most active fields of research in material science due to the industrial demand for miniaturization of electronic devices [25]. Surface supported clusters provide a way for bottom-up approach using which materials can be synthesized through self-assembly. The self-assembly is known as a phenomenon where clusters are spontaneously assembled themselves and larger units or films are formed. There are two different methods can be employed in fabrication of supported clusters [26]: (i) deposition of atomic vapor, (ii) deposition of preformed clusters from a cluster source, either size-selected or

otherwise. The deposition of clusters over surfaces often changes its properties compared to that of the isolated clusters by the cluster-substrate interaction (due to hybridization, changes in the structure, diffusion, alloy formation etc.,) and cluster-cluster interaction (in case of high coverage).

Adsorption of clusters over substrates can be broadly classified into two categories depending upon the nature of bonding between the cluster and substrate. (i) Physisorption: Here cluster-substrate interactions are weak van der Waals type, and most of the properties of the gas phase clusters remain same after deposition. Deposition of xenon clusters on graphite [27], adsorption of noble metal clusters on MgO substrate [28] etc. are examples of physisorption scenario. (ii) Chemisorption: Here interactions between the cluster and the substrate are strong and as a result structure and properties of the isolated gas phase clusters are significantly modified after deposition. New chemical bonds form between the clusters and the substrate. Au clusters on CeO<sub>2</sub> substrate [29], Au and Pt clusters on TiO<sub>2</sub> substrate [30] etc are examples of chemisorption.

### **Characterization of the surface supported clusters**

Several experimental techniques have been used to measure and understand properties of surface supported clusters [31]. Among them X-ray photo electron spectroscopy (XPS), scanning tunneling microscopy (STM), scanning electron microscopy (SEM), atomic force microscopy (AFM), transmission electron microscopy (TEM/HRTEM), Raman spectroscopy etc are very well-known. Brief discussions of some of these techniques are given below.

#### **X-ray photoelectron spectroscopy (XPS)**

XPS is used to understand changes in the electronic structure of a cluster due to the presence of a substrate. Electronic properties of gas phase clusters are very

much sensitive to the number of atoms. The electronic properties of the cluster may be significantly influenced by the presence of surface. When cluster and the substrate brought in contact, due to cluster-surface interaction, the highest occupied level in cluster will adjust to the Fermi level of the substrate. A charge accumulation at the cluster-surface interface can also be induced for this [32].

The other energy levels (valence as well as core) of the supported cluster may also change compared to those in the gas phase. The shift in core-level binding energy in comparison to the bulk value is known as core-level shift. As core-level shift depends on the bonding environment, so information about the nature of the cluster-surface interaction can be obtained.

In XPS, a material is irradiated with X-ray beam. Here a photon is absorbed by an atom in the material, which leads to the emission of a core electron. The kinetic energy distribution of emitted photo electrons is measured. The binding energy (BE) of the emitted electron can be calculated as

$$E_b = h\nu - E_{kinetic} - \phi \quad (1.1)$$

$h\nu$  is the energy of an incident X-ray photon, which is known,  $E_b$  is the binding energy (BE) of the emitted electron,  $E_{kinetic}$  is the kinetic energy of the emitted electron and  $\phi$  is the work function which has to be overcome by the electron reaching the vacuum. The binding energy of an electron is defined as the energy difference between the initial (with  $n$  electrons) and final states (with  $(n - 1)$  electrons) of the atom.

$$E_b = E^f(n - 1) - E^i(n) \quad (1.2)$$

$E^f(n-1)$  and  $E^i(n)$  are the energy of the final and initial states respectively. In

final state  $(n - 1)$  electrons have been relaxed after the emission of the core electron. In absence of relaxation of these electrons, the binding energy would be exactly equal to the negative of the orbital energy ( $\epsilon_k$ ) from which the photoelectron is emitted. This approximation is known as Koopmans theorem.

$$E_b = -\epsilon_k. \quad (1.3)$$

the atom is not in its ground state, when the relaxation of  $(n - 1)$  electronic states is absent. The removal of a photoelectron creates a hole in the atom. The remaining electrons can relax to screen the hole, and thus the final state becomes lower in energy. Therefore  $E_b$  of an electron depends on both the initial and final state effects. The core-level energy shifts are closely related to the charge transfer in the outermost electronic orbitals of the atoms. Shifts in the binding energies of the core-electrons are induced by the charge redistribution of the valence electrons. Thus the information about the valence state (oxidation state) of the atoms can be obtained from the core-level shifts. Binding energies of the core electrons are increased due to the loss of electrons in the valence orbitals and as a result a positive shift in the core-levels is found. On the other hand, an excess of electronic charge in the valence orbitals is responsible for decrease in the binding energies of core electrons and a negative core level shifts is happened.

### **Scanning tunneling microscopy (STM)**

Surface images with atomic scale resolution is produced using Scanning tunneling microscopy technique . The principle of STM is based on the phenomenon of quantum tunneling. Here a fine probe tip scans the surface with clusters, measuring the tunneling current at constant voltage (constant voltage imaging mode) as a function of its position. When a conducting tip is brought very closed to

a metallic or semi-conducting surface, a voltage bias between the two can allow electrons to tunnel through the vacuum region between them. The convolution of the density of the occupied surface and unoccupied tip states is represented by the STM image. The STM images are correlated with the position of the atoms, as the density of states is correlated with the positions of the nuclei. More technical details about STM can be found in Ref.[31].

### **Scanning electron microscopy (SEM)**

In the scanning electron microscope technique the sample surface supporting clusters are imaged by scanning it with a focused beam of electrons. In this method, electrons produce various signals in the form of secondary electrons, back scattered electrons and characteristic X-rays when they interact with atoms of the sample. These signals contain information about the topography of the sample's surface, composition, etc. The details about this method can be found in Ref. [31].

### **1.1.2 Production of substrate supported clusters by atomic vapor deposition**

In this method, thermal evaporation is used to vaporize the material, whose clusters are to be produced, Then atomic vapor is deposited onto the substrate with thermal energy ( $\sim 0.1$  eV) and flux under Ultra High Vacuum (UHV) condition. The flux is expressed in units of monolayer (ML) per second, where 1 ML is defined as a single continuous layer or film which is one unit cell in thickness. The deposited flux of atoms undergoes elementary growth processes and then condensed into the stable clusters. These elementary growth processes includes nucleation, diffusion, aggregates, and evaporation of the atoms.

The terrace of a substrate has periodic lattice sites or adsorption wells, which are separated by energy barriers. Along with it can also have some defects such as vacancy, dislocation etc. The adatoms can come on the terrace at different random positions. Some adatoms can bind to the surface defect sites, some of them can evaporate from the surface, and rest can diffuse on the terrace.

Among all the elementary growth processes, the most fundamental process is diffusion of adatoms. The diffusion processes are thermally activated jumps mostly in form of straight adatom movements between adjacent lattice sites. In diffusion sometimes concerted movements of several atoms may also be involved. Transition state theory (TST), assumes that the adatom stay in their adsorption wells are large enough for thermal equilibration. When the adatoms have sufficient thermal energy to cross the energy barriers between the neighboring lattice sites, they perform the thermally activated jumps.

Adatoms may also undergo aggregation and form bonds to form as clusters during collisions. In aggregation process diffusing adatoms assemble together to form clusters. In this process produced clusters can remain stable or decay again as adatoms, depending on the bond energy and the number of neighbors. If the produced clusters are large enough to grow more rapidly than it decays on the time-scale of deposition, the process is known as nucleation. Nucleation is the series of atomic processes where the adatoms condense as stable clusters. It is the first irreversible step towards the formation of new phase (cluster) on the terrace. A stable cluster is known as the nucleus for the growth processes. The attachment of a single adatom to the critical size above which cluster remains stable, results into a stable nucleus. The critical cluster size can be defined as  $(i_{c1})$ , where  $i_c$  is the number of atoms in the smallest stable cluster. The details about the methods and different elementary processes can be found in the Ref

[32].

### 1.1.3 Deposition of preformed cluster

The major limitation with atomic deposition is that, the size and shape of the clusters can't be controlled. Deposition of preformed clusters on a substrate is a more controlled way to fabricate substrate supported clusters. By selecting the size of the incident clusters, the growth mechanisms and characteristics of the materials can be changed [33, 34]. For example, it has been shown that the properties of carbon film can be changed from graphitic to diamondlike by changing the mean size of incident carbon clusters [35]. Two types of nanostructures can be built by depositing preformed clusters on a substrate : (i) separated clusters or islands in submonolayer range. (ii) Thin films or cluster-assembled materials (CAM) (up to few monolayers). Organized arrays of low coordinated clusters with specific electronic properties can be grown as they can have potential use in many applications. The nanostructured materials as thin or thick films, exhibit mechanical, catalytic, and magnetic properties different from their crystalline counterparts [36–38].

Various factors like the cluster and substrate materials, size of the cluster, temperature, cohesive energies, and kinetic energies of the cluster strongly influence the outcome of the complex cluster-substrate collision process [32, 39] . Based on the impact energy of the incident clusters, collision process can be classified in to three regime .

(i)Low energy depositions: When the kinetic energy per atom ( $E_{at}$ ) of the incoming cluster is smaller than the binding energy per atom ( $E_{coh}$ ), the interaction is considered to be low energy . Typical limits for this deposition are around  $E_{at} = 0.1$  eV. In this case, deposited clusters exhibit the properties the gas-phase

clusters and elastic collisions induce cluster deformations..

Medium energy depositions: If  $E_{at}$  is comparable to  $E_{coh}$ , clusters may undergo plastic deformations. In this regime  $E_{at}$  can have the values between 1-10 eV. Defects can be induced for deposition of clusters on the surface.

High energy depositions: The impact is considered to be high energy if  $E_{at}$  is higher than  $E_{coh}$ . Typically, a lower bound of 10 eV for  $E_{at}$  is considered in this regime. The incoming cluster decomposes upon impact at this high energies. Part of the cluster is implanted in the surface resulting in an intermixing of the cluster and the surface.

The films made by clusters in different energy regimes are distinct and can be easily identified. Amorphous and easily removable films are produced in low-energy deposition. In case of medium energies, the film adheres more strongly to the substrate. High energy deposition gives a hard shiny metallic coating. Haberland et al. studied these processes theoretically using molecular dynamics (MD) simulations [40]. Deposition of  $Mo_{1043}$  on the  $Mo(001)$  surface were studied at different impact energies. The resulting film morphologies are in figure 1.1. Clusters retain their gas phase properties with little structural distortion, at low impact energies, There is no damage to the surface. Clusters tend to pile up on the substrate leaving large cavities in the film. At medium energies, deposition will induce some defects on the terrace. In this case individual clusters can be identified, but they are deformed from their gas-phased structures. At high impact energies, clusters are totally fragmented and lose their identity. The flattening of the cluster makes the film smooth. A fraction of the cluster intermix with surface layers and this implantation runs several layers deep. After deposition over the surface, clusters also undergo various elementary growth processes. Like the atomic deposition, they may nucleate, diffuse, aggregate and evaporate

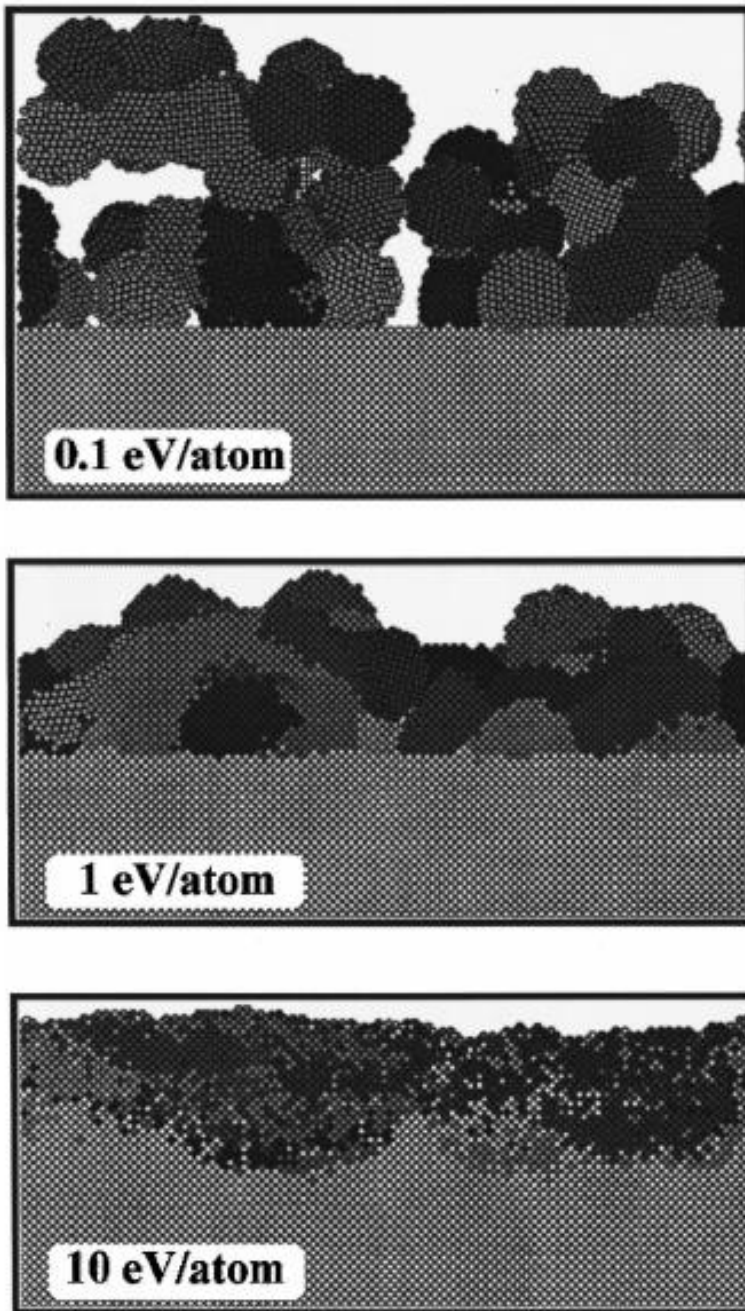


Figure 1.1: Molecular-dynamics simulations of the morphology of films obtained by Mo<sub>1043</sub> cluster deposition onto a Mo(001) substrate with different incident kinetic energies per atom.

on the terrace of the substrate. Clusters can merge to form another larger cluster during the diffusion. This process is known as coalescence of the clusters. Coalescence is not possible in case atomic deposition. When two clusters meet at the surface by diffusion, they may either aggregate or coalesce. A schematic diagram of aggregation and coalescence is shown in figure 1.2 The choice between two

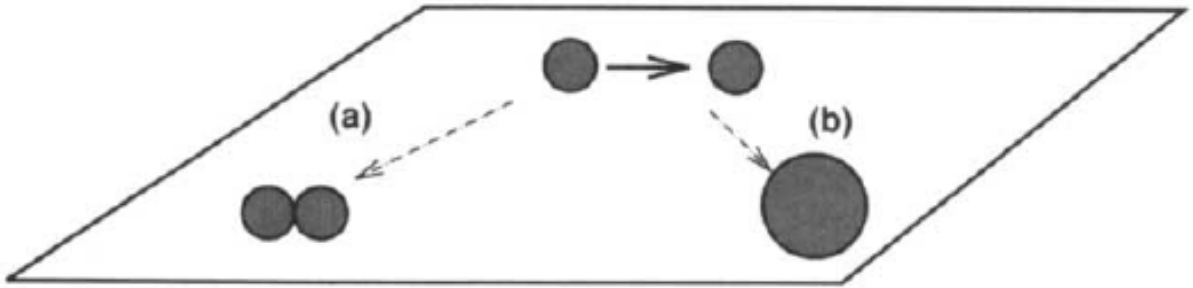


Figure 1.2: Possible elementary growth processes for two clusters meeting on a surface (a) aggregation (b) coalescence.

type of interaction depends on several factors such as cluster size, temperature, cluster and substrate materials etc. For a critical size  $N_c$ , if two clusters of size  $N > N_c$  collide with each other, they will not merge to form a larger clusters and aggregate with each other. On the other hand if size of one of the cluster is smaller than  $N_c$ , they will coalesce into a single cluster.  $N_c$  depends on the bonding strength of the cluster atoms. More details are given in ref [39, 41]

#### 1.1.4 Softlanding

Softlanding is driven by the idea to preserve the unique properties of preformed size-selected clusters and stabilize them on the surface. The adsorption of cluster on the surface without any collision-induced deformations and implantation is the criterion for softlanding. This process strongly depends on cluster size and material, as well as the substrate properties like surface energy, hardness,

polarizability, corrugation and temperature [41]. When a cluster reaches at the surface, it accelerates due to the attractive cluster-substrate interaction. The translational energy is converted into internal energy and both the surface and the cluster get heated. For small clusters, this internal energy leads to atomic rearrangement and implantation. Softlanding does not necessarily preserve the properties of the small gas phase clusters on those surfaces with large cluster-substrate interactions. For example, MD simulations of  $\text{Ag}_7$  and  $\text{Ag}_{19}$  clusters, deposited on Pd(100) and Pd(111) surface with almost zero impact energy exhibit partial implantation and atom exchange [42]. In case of larger clusters with several hundreds of atoms, the structural deformation and implantation are less important. For large clusters at low energy depositions the energy available to each atom is small. So atom exchanges required for the implantation is not possible. In case of  $\text{Cu}_N$  and  $\text{Au}_N$  up to  $N = 55$  deposited on Pd(100) a pronounced atomic rearrangement has been found but there is no significant atom exchange at negligible kinetic energy [43]. In case of inert surfaces softlanding is more simple. Small clusters do not gain translational energy due to the smaller cluster-surface interaction. Small as well as larger clusters retain their gas phase identity after deposition when deposited at low impact energies. Honea et al.[44] compared the Raman spectra of the mass selected small silicon clusters with size 4, 6 and 7, deposited over solid  $\text{N}_2$  with gas phase case. Raman spectroscopy gives the information about the geometry of the cluster. They found that geometry of the deposited clusters is same as in the gas phase. Busolt et al. [45, 46] measured the spectra of small silver clusters deposited over graphite for the two photon photoelectron processes. They reported a strong dependence of the spectra on cluster size which shows that their gas phase identities are retained and no fragmentation has been found.

### 1.1.5 Cluster assembled films

Cluster assembled films can be obtained by depositing clusters using the softlanding or low energy cluster beam deposition (LECBD) technique. The morphologies of the cluster assembled films depends upon the strength of the cluster-substrate interactions [47]. For large cluster-substrate interactions the diffusion of the clusters will be limited and the growth will be organized as random paving of the individual clusters. In case of weak cluster-substrate interaction the diffusion will be large and cluster will prefer to form large ramified islands on the surface. The diffusion and coalescence of the supported clusters leads to growth of granular thin film depending on the deposition conditions (cluster size, cluster and substrate material, flux, temperature etc.). The grain size for the coalescence of the clusters is limited by a critical size ( $N_c$ ). Using LECBD technique, cluster assembled films by depositing the TM clusters ( $Fe_N$ ,  $Ni_N$ ,  $Co_N$  etc.) can be formed [48–50]. For TM clusters, only the random paving type of growth is possible for a wide range of substrates including graphite, organic materials and various other metals. So we can assume that cluster assembled magnetic films produced by depositing TM clusters always grow from random paving of individual clusters. At finite thickness of the film, TM clusters will undergo various growth process like diffusion, coalescence, etc. and usually organized as highly porous and granular thin film. The competition between the grain anisotropy and the exchange interactions between grains determines the characteristics magnetic behavior of these films. When cluster of average size  $Fe_{150}$ ,  $Co_{300}$ ,  $Ni_{300}$  are deposited at 300K, the mean size of the supported grains are found to be 5 nm, 3 nm, and 4 nm respectively [48–50]. It has been reported that for Fe clusters, the grains crystallizes in a BCC structure and for Co and Ni, grains crystallizes in the FCC structures. Such magnetic films have huge applications in the high density memory devices

and spintornics.

## 1.2 TM doped Si clusters

Over the last 20-30 years, TM doped silicon and germanium clusters have been studied extensively. In this section we will discuss TM doped Si clusters.

The studies of doped metal-silicon clusters was started in the late 1980 initially. Regarding this one can consider Beck's two seminal papers [51, 52] as the initial motivation. Beck's actual motivation for exploring these cluster systems was significantly different from the motivation of post-1990 work. During 1980, people knew that, the electrical properties at the metal-semiconductor interfaces is directly effected by the chemistry of this metal-Si interface. Due to this reason, the study of metal-Si interface was relevant for better insight for these systems. That time, the chemical processes or the reaction products at these interfaces were not known [53, 54]. Tu [55] and Hiraki [56] proposed two completely different mechanisms to explain the reaction of a metal film with a Si substrate in formation an alloy, or silicide. None of these proposals had any direct experimental or theoretical proof as there were some technical difficulties in exploration of these above mentioned proposals. One of the crucial problem was, at the interface, there was involvement of the large number of atoms. The symmetry of the bulk structure was not paid attention. The properties those are produced by the surface sensitive experimental techniques, were statistical averages over many possible local geometries, but there was no information found regarding the local chemistry of metal-Si bonding. Small binary clusters containing a single TM atom were explored by Beck. He produced and studied binary clusters made with three different TM atoms W, Mo and Cr with Si for better understanding

of bonding and chemistry of TM-Si systems. From Beck's experiments, it was noted that stabilization of a Si cluster can be possible with keeping a TM atom in the cluster. It was shown experimentally that for a specific size range, where unstable bare Si clusters were found, after a single TM atom was incorporated, the Si cluster became stable.

In electronics industry, Silicon is one of the most popular and widely used materials from very early days to today. After the discovery of C fullerenes, questions were asked if cages of Si would also be stable and could be used as building blocks to synthesize novel materials. In the year 1990s, the searching for small Si clusters was begun with a motivation of using them as building blocks of some novel materials. But the realization for the difficulties was happened soon. Firstly, elemental Si clusters are highly reactive as they have dangling bonds [57], and so they are not suitable to be used as building blocks for CAM. Secondly, Si prefers  $sp$  hybridization [1, 2] only, where in case of C  $sp$ ,  $sp^2$  or  $sp^3$ , these three kinds of stable hybridization are found depending upon the structure and composition of C based compounds. So formation of stable cage structures by Si is not possible, due to its  $sp$  hybridization. Non-planar prolate structures were formed by Si clusters, instead of cage structure [58, 59] as observed from ion mobility experiments. These prolate structures were different from bulk fragments [60]. The stabilization of  $Si_{20}$  cage was found when a Zr atom was encapsulated in it. This was reported by Jackson and Nellesmoe from their first principles calculation[3]. After this finding, encapsulation of a metal atom inside the Si cage, was considered as a probable way to form stable Si cage clusters.

In the pioneering experiment by Hiura et al.  $TMSi_nH_x^+$  cluster ions were produced for 5 TM atoms including Ir, Re, W, Ta and Hf [61]. Completely dehydrogenated clusters were formed there at certain sizes depending upon the

TM atom. This indicates that those TM-Si clusters were stable. Particularly, stability was found in  $\text{WSi}_{12}$  cluster. Their proposal was  $\text{WSi}_{12}$  cluster with hexagonal prism (HP) structure is the ground state structure. From first principle calculations they proposed it. This work gave new dimension in the field of metal-Si clusters, particularly in TM-Si clusters. Several theoretical and experimental studies were performed with TM-Si clusters for their structural, electronic and magnetic properties. In order to justify the stability found in TM-Si clusters, some attempts were made using the electron counting rules commonly known in chemistry and in the metal cluster field also. In the literature an interesting debate was found with these ideas of explanation of stabilities in TM-Si clusters from the point of view of electron counting rule.

### 1.2.1 Studies on structure of TM-Si clusters

Knowledge of the structure of TM-Si clusters is very important to understand their properties like any other atomic clusters. Several theoretical and experimental studies have attempted finding the structures of these clusters. In order to study the structures of small atomic cluster, no direct experimental probes are found and this fact is well known. For a given cluster, “what is the ground state structure”, this is the most important and difficult question in theory. In case of experiments, the most important question is, among the produced clusters, which isomers are showing largest abundance.

Regarding the structural stability of  $\text{TMSi}_N$  cluster, the question what is the smallest  $n$  value of  $\text{Si}_n$  cage, for which encapsulation of a TM atom is possible in the cage? This question was addressed both experimentally and theoretically, and the answer is different for different TM atom encapsulated in the cage, as expected. Let us first review the experimental works and then the theoretical

calculations will be discussed regarding the studies on structures of TM-Si clusters.

## Experimental findings

In order to determine the position of the metal atom in TM-Si clusters, adsorption reactivity (AR) of these clusters toward H<sub>2</sub>O was studied by the group of Kaya and Nakajima [62–64]. From these experiments the measurement of the relative adsorption reactivity (RAR) could be possible. Ohara et al. [65] has shown in their experiments that, the reactivity of bare Si clusters towards H<sub>2</sub>O is low enough compared to the metal atoms. This was established from the fact that the abundance of bare Si clusters remained same after exposure to H<sub>2</sub>O, on the other hand there was found a significant change in the abundance of Tb-Si clusters after the exposure of H<sub>2</sub>O. Therefore a TMSi<sub>n</sub> cluster is with an AR which has a sensitive dependence on the location of metal atom. In case of TMSi<sub>n</sub> cluster with small *n* highly reactivity is found, when the TM atom is attached exohedrally with this cluster. As the number of Si atoms are increased, these clusters become less reactive. During the increase in number of Si atoms (*n*), a threshold size has been found such that if *n* is just larger than this value, the cluster does not participate in reactions. At a particular cluster size, RAR is defined as  $\ln(I_f/I_0)$ , where *I*<sub>0</sub> and *I*<sub>f</sub> represent the intensities of the cluster before and after the reaction respectively in the mass spectrum. In order to explore the structures of several TM-Si clusters including various 3d, 4d and 5d TM, Nakajima and co-workers used this chemical probe method. Their studies included Ta, Hf, Lu, Nb, Zr, Y, V, Ti, Sc encapsulated Si clusters in neutral and in singly charged anionic and cationic states [64]. The variation of RAR of Sc, Ti and V encapsulated clusters with changing *n* are depicted in figure 1.3.

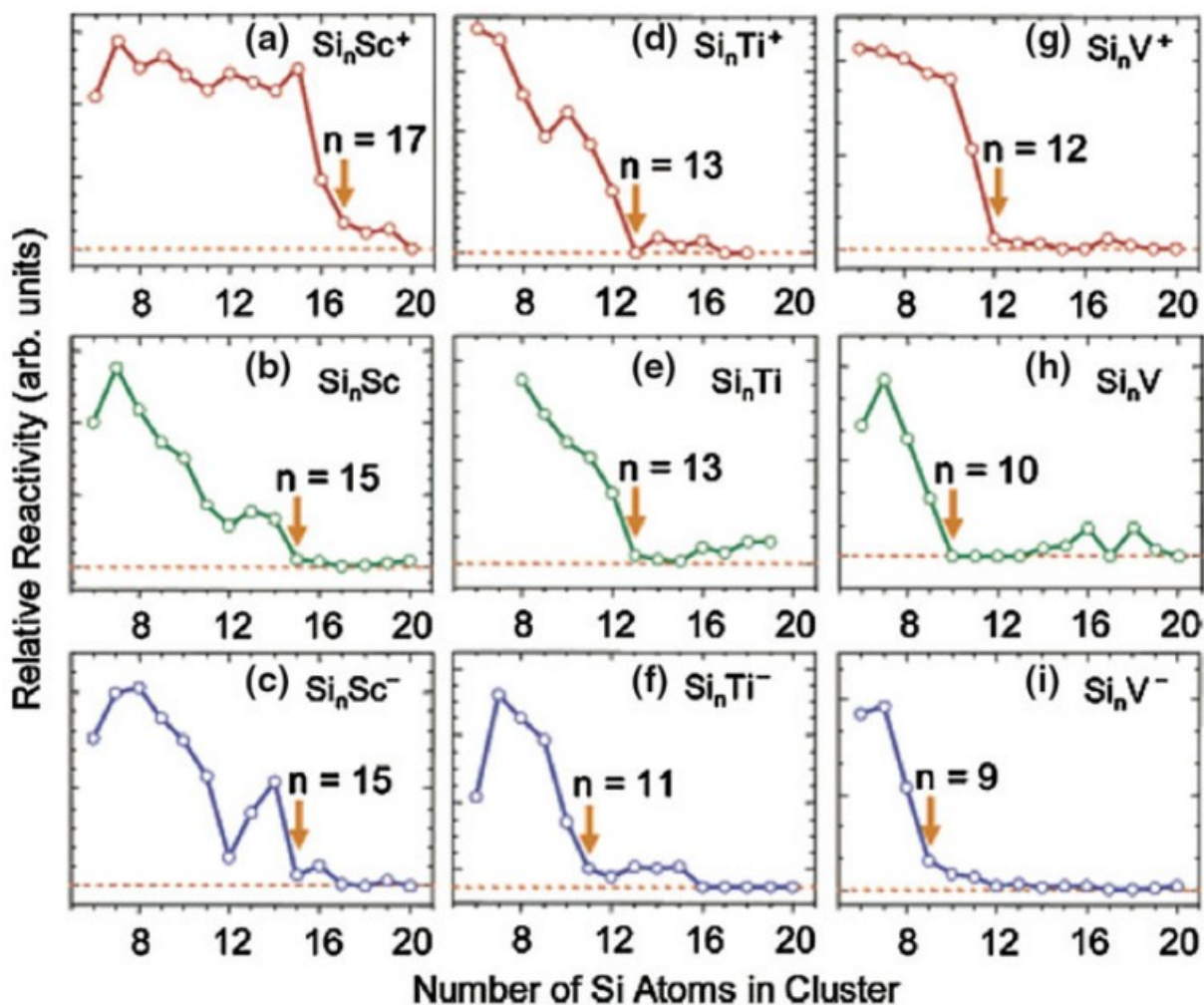


Figure 1.3: Variation of RAR as a function of number of Si atom in Sc-Si, Ti-Si and V-Si clusters. This AR is for the reaction with  $\text{H}_2\text{O}$ . The threshold size for Si, at which the clusters become completely indifferent towards  $\text{H}_2\text{O}$ , is shown by arrow in each panel. The figure is adapted from ref [66]

From these plots, two things regarding the threshold sizes are clearly found.

(1) The charge state of the cluster plays an important role in determination of the threshold size in case of a specific TM metal. The threshold size in a particular TM encapsulated Si cluster, decreases from cation to neutral cluster and further from neutral to the anionic charge state. It is depicted in Figure 1.3 with several

panels clearly in sequential manner. In case of Lu and Ta this rule was not followed and those can be considered as exception.

(2) The dependence of threshold size is also found on the element in same period. There is a reduction of threshold size, as atomic number increases of the TM atom within the same period and having same charge state. This is clearly understood from the pattern in the panels (a)-(d)-(g) etc in figure 1.3. A slight increase in the threshold size with the atomic number for the same group and same charge state has been happened in general. Hence in case of neutral clusters, there is an increment of threshold size from Ti to Zr and Hf. and in case of cations, from V to Nb and Ta has been shown in in figure 1.4 in the panels d)-(e)-(f) etc, sequentially.

In case of anion clusters, from Sc to Y an increment in threshold size has been seen and after that a slight reduction of threshold size has been found in Lu. These observations are consistent with the fact that across a period, during the increment of atomic number, there is reduction of the metallic radii of the TM atoms. In a group, there is an increment found in metallic radii, from 3d elements to 4d elements and then a slight reduction of the metallic radii is found in few 5d elements. There is another finding which justify the indifference of clusters towards the reaction, in terms of entire encapsulation of the TM in Si cage. As the cage size increases, the reactivity can be found again for the situation when a second metal atom comes into play. For a threshold size of Si cage or just bigger which just entirely cover a single TM atom, the presence of second TM atom makes the cluster reactive. This is due to the fact that the second TM atom has to be on the surface of the cluster and hence the enhancement of reactivity is found. The threshold sizes for the above TM-Si clusters, at different charge states and metallic bond radii of the TM atoms are shown in Table 1.1 as reported in

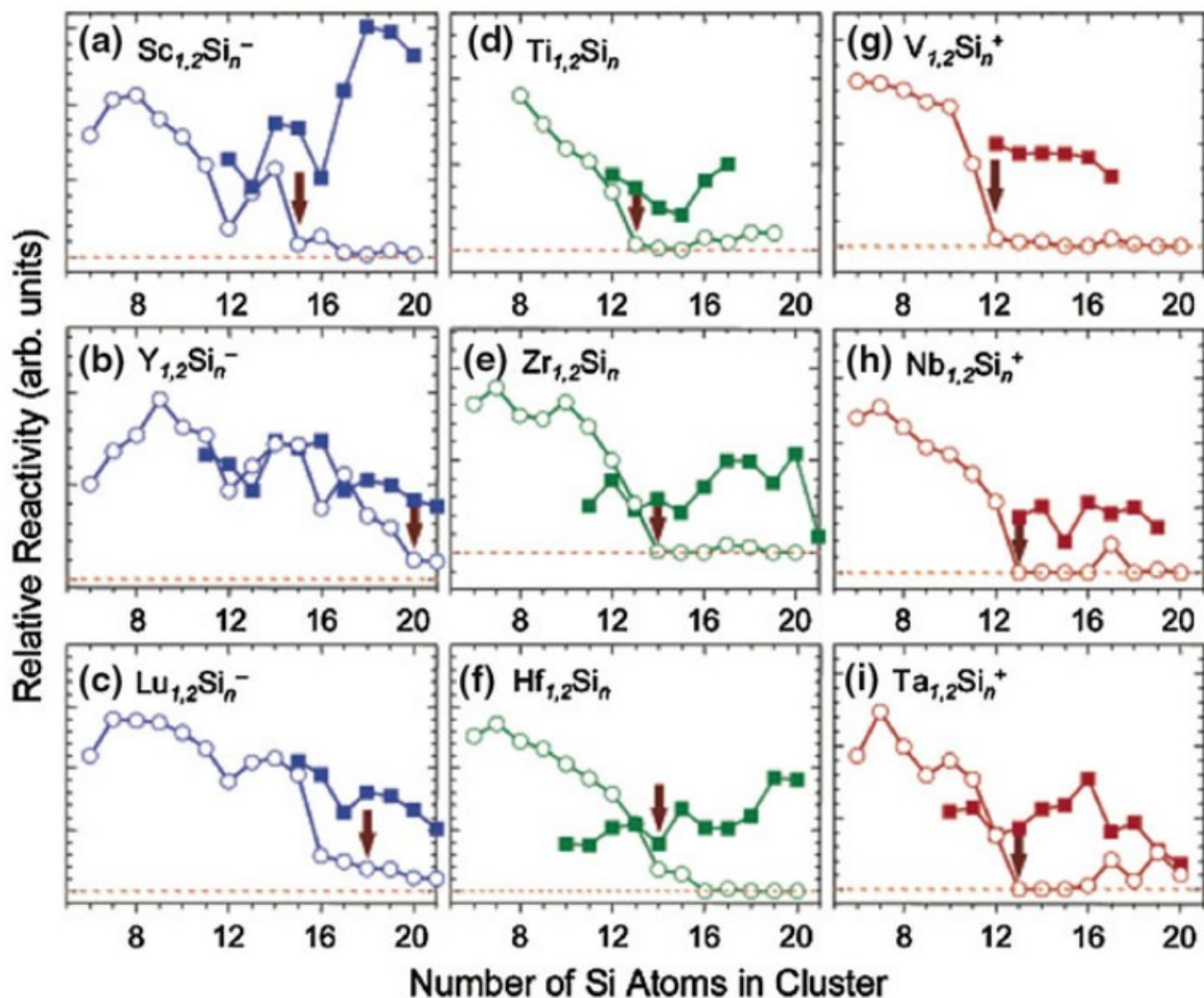


Figure 1.4: RAR towards  $\text{H}_2\text{O}$  as a function of number of Si atoms in different TM-Si clusters ( $n$ ), when the TMs are 3d, 4d and 5d. The open and filled symbols present clusters containing single and double TM atoms respectively. Figure is adapted from ref [66]

Ref. [64]

Jaeger et al. [67] performed photo dissociation experiments. They observed a primary loss of Cr atom in  $\text{CrSi}_7^+$  clusters. But they reported loss of Si atoms

Table 1.1: The metallic bond radii and threshold size for loss of AR in three different charge states corresponding at which the  $\text{TMSi}_n$  clusters fail to react with  $\text{H}_2\text{O}$

TM atom	Metallic radius Å	Cation	Neutral	Anion
Sc	1.63	17	15	15
Ti	1.45	13	13	11
V	1.31	12	10	9
Y	1.78	21	20	20
Zr	1.59	15	14	12
Nb	1.43	13	12	11
Lu	1.72	21	16	18
Hf	1.56	14	14	12
Ta	1.43	13	10	11

in case of  $\text{CrSi}_{15}^+$  and  $\text{CrSi}_{16}^+$  in their experiments. These observations can be justified, if encapsulation the Cr atom can be possible in a larger Si cage. Since only three sizes were produced in enough abundance in their experiments, they were not able to find out the threshold size for which the entire encapsulation could be possible.

Noble gas (NG) physisorption was probed by Lievens and co-workers [68] for endohedrally doped Si clusters. Using this probe production of the bare Si, and TM-Si clusters were possible. As a carrier gas, Helium was used. There was a dual-target dual-laser vaporization source. On adding about 1% of Ar to the He gas, complexes were produced containing one or two Ar atoms by cation clusters.  $\text{Si}_n^+$ ,  $\text{TMSi}_n^+$ ,  $(\text{TM})_2\text{Si}_n$  clusters and  $(\text{TM})_{1,2}\text{Si}_n^+.\text{Ar}_{1,2}$  complexes were found in the mass spectrum.  $\text{Si}_n^+.\text{Ar}_{1,2}$  complexes were absent there. Hence one can get the picture of physisorption scenario of the Ar atoms with the metal atoms only without anything between Si and Ar atoms.

The fraction of  $(\text{TM})_{1,2}\text{Si}_n^+.\text{Ar}_{1,2}$  complexes at different sizes were measured in this work [68]. In case of a particular cluster, this fraction was found with sharp fall at a particular size which depends on the TM atom in this particular

cluster. This size at which sharp fall as mentioned above was found, considered as the threshold. This threshold was considered to point out the size at which, entire encapsulation of the metal atom in the Si cage was happened. Figure 1.5 is showing experimental results.

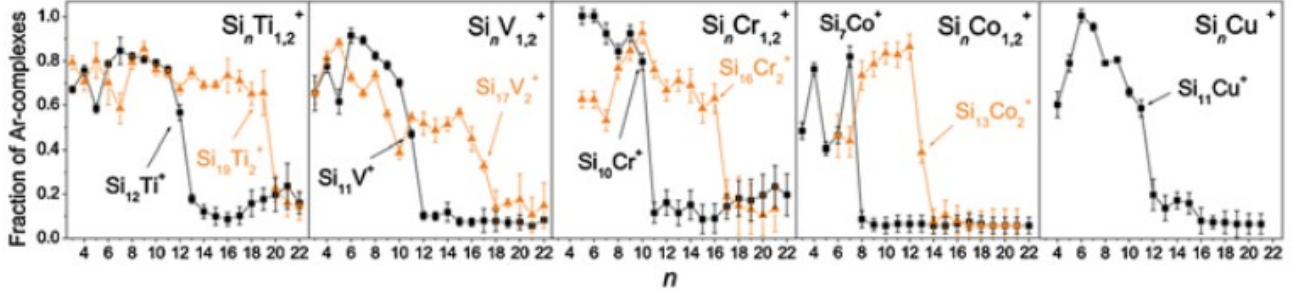


Figure 1.5: Variation of fraction of argon complexes produced with various  $\text{TMSi}_n$  clusters, with number of Si atoms in a cluster  $n$ . Clusters containing one or two TM atoms are involved here. This figure is adapted from ref [68]

The threshold size for TM-Si cluster was found larger for the system which contain two metal atoms. This justifies their entire encapsulation inside the Si cage. The threshold size for V, Ti, Co and Cr were found as 12, 13, 8 and 9 respectively, from these experiments. It is consistent with the results of Koyasu et al. [64].

Lievenss group performed experiments using NG physisorption technique to the IR-MPD of clusters [69–72]. The information regarding the structure of the experimentally originated cluster, could be found along with density functional theory (DFT) calculations. Gruene et al. found that the V atom attached exohedrally in  $\text{VSi}_n^+$  clusters for  $n = 6 - 8$  [69]. Claes et al. reported encapsulation of a V atom inside a  $\text{Si}_n$  cage for ( $n = 12 - 16$ ) in their subsequent work [70]. These observations agreed with the chemical probe experiments. The lowest energy isomers were identified in most cases. Ngan et al. [71] showed that Mn atom is endohedrally attached for  $n = 6 - 10$  in case of  $\text{MnSi}_n^+$  clusters. They

reported encapsulation of the Mn atom inside a Si cage, for  $n = 12 - 14, 16$  Isomer for  $\text{MnSi}_{11}^+$  could not be identified by them and due to mass coincidence with  $\text{Mn}_2\text{Si}_{13}^+$ , they could not measure the spectrum for  $\text{MnSi}_{15}^+$ . Nevertheless, from their study it is confirmed that the Mn atom is encapsulated for  $\text{MnSi}_{12}^+$  onward. In a similar study Claes et al. reported about exohedral attachment of Mn and V atoms in  $\text{MnSi}_n^+$  and in  $\text{VSi}_n^+$  clusters for  $n = 6 - 9$  [72].

The structures to neutral  $\text{CoSi}_n$  clusters were explored by Lievens et al. [73] using Infrared-ultra violet two color ionization (IR-UV2CI) process. A comparative study was done with the experimentally measured vibrational spectra and the spectra obtained from DFT calculation. The conclusion was, the Co atom encapsulated in a Si cage in  $\text{CoSi}_n$  clusters for  $n = 10 - 12$ . In figure 1.6 the IR spectra of few low energy structures of  $\text{CoSi}_n$  clusters obtained from DFT calculations, are presented.

### Theoretical studies

There are several theoretical works on  $\text{TMSi}_n$  clusters. But most of them focused either particularly small size range, or with few specific TM atoms. In this field very few studies can be found which explored low energy isomers of TM-Si clusters incorporating various different TM atoms and with involving a wide range of size. Ma et al. [74] used global search techniques to find out low energy isomer in case of Co-Si clusters.

There are various studies to find out the smallest TM encapsulated Si cage. The question regarding the smallest metal encapsulated cage structure was explored by Guo et al. [75] in case of 3d TM atoms.  $\text{Si}_{14}$  was found as the smallest Si cage encapsulating a Sc atom. Their observation for Sc did not agree with the experiments by Koyasu et al. [64] incorporating the chemical probe method.

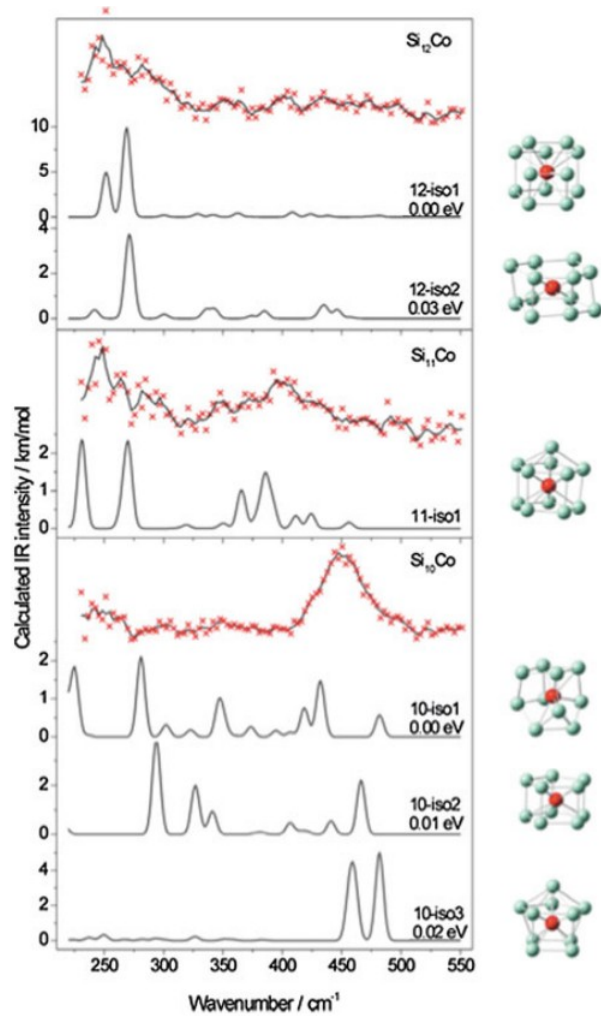


Figure 1.6: Experimentally measured IR-UV2CI and theoretically calculated IR spectra for a few low-energy isomers of  $\text{CoSi}_n$  clusters, with  $n = 10 - 12$ : A comparative demonstration. Figure is adapted from Ref [73]

They reported the encapsulation of Cr, V and Ti atoms in  $\text{Si}_n$  cage with  $n = 12$ . According to them,  $\text{Si}_{11}$  cage can encapsulate one Mn atom and Fe, Ni, Co were encapsulated by smallest  $\text{Si}_{10}$  cage. According to Gueorguiev et al. for TM = Ti, V, Fe, Co, Ni the number of atoms in Si cage was 10 [76]. According to them, the rest other 3d TM atoms attach endohedrally in the Si cage for size starting at  $n = 12$ . In case of  $\text{FeSi}_{10}$  and  $\text{CoSi}_{10}$ , the TM atoms were kept centrally, inside the cage. This arrangement of Tm-Si cluster can be considered as a structure

with two-layers. It consists with one quadrilateral, and one pentagon. The pentagon is capped by the last Si atom. This two-layered structure is different from the structure which was reported by Guo et al. A two-layer Si cage structure for  $\text{CoSi}_{10}$  was also reported by Guo et al. But here instead of the pentagonal face, the capping was found in quadrilateral face [75]. They reported  $\text{FeSi}_{10}$  structure as perfectly symmetric structure with  $D_{5h}$  point group symmetry, where the Fe atom is encapsulated in the pentagonal prism composed of Si atoms. Gueorguiev et al. [76] claimed their reported  $\text{FeSi}_{10}$  and  $\text{CoSi}_{10}$  are energetically not very favorable. But they did not make any clear statement regarding the fact about, which isomers are found with lowest energy from their calculations. During the increment of the cage size, the encapsulation of all the TM atoms were found in  $\text{Si}_n$  cage with  $n = 12$  [76, 77]. A HP cage structure was reported for  $n = 12$  and in some cases distortions also mentioned. In  $\text{TiSi}_{12}$ ,  $\text{VSi}_{12}$  and  $\text{NiSi}_{12}$ , small Jahn-Teller distortions were found in the perfectly  $D_{6h}$  symmetric HP cage structures.

The  $\text{ScSi}_{12}$  cluster was theoretically explored by Sen and Mitas [78] and Reveles and Khanna [79]. Both reported about a HP caged  $\text{ScSi}_{12}$  cluster. Significant distortion of the HP cage was reported by Reveles et al. They found a lowest energy quartet state while a doublet spin state was reported by Sen et al. as energetically lowest state. It is not clearly found, whether this structure is in the the ground state from this report by Sen et al. Reveles et al. considered other structures suggested previously in the literature but Sen et al. did not consider any other structure. In order to find out the lowest energy ground state structure, no global search was involved in these works mentioned above. In case of Ti-Si clusters, a Ti atom encapsulated  $\text{Si}_{12}$  cage with HP structure was reported by Sen et al. [78] and Reveles et al. [79]. A large distortion of the cage in  $\text{TiSi}_{12}$  was reported by Reveles et al. They found comparatively larger distortion in Ti

encapsulated  $\text{Si}_{12}$  cage than the  $\text{ScSi}_{12}$  clusters. Regarding the spin state, Reveles et al. reported a spin singlet state and Sen et al. reported a triplet lower energy state for the  $\text{TiSi}_{12}$  cluster in their corresponding independent studies. Quantum Monte Carlo (QMC) calculations with some acceptable accuracy produced a notable difference in energies (0.7 eV) between the singlet spin state and the triplet spin state with lowest energy. This was an important fact found that time. In case of  $\text{TiSi}_{12}$ , a basket-like structure was found as the ground state isomer by Kawamura et al. They reported about the Ti-encapsulated  $\text{Si}_n$  structures with  $n$  takes value 13 and higher [80]. They reported for Ti-Si, the basket-like ground state structure at  $n = 12$  was found 0.273 eV lower than the distorted HP cage structure at same size of  $n$ . These significant variations between different first principle calculations, point out the fact that either the calculations are incorporating the approximations which do not allow to identify the lowest energy isomers unambiguously, or global search was not performed to determine the ground state structure in some of these DFT calculations or all of these DFT works. Encapsulation of a V atom, by a slightly distorted  $\text{Si}_{12}$  cage with HP structure was reported by Andriotis et al. [81]. This report agrees well with Guo et al.'s result [75]. Apart from Andriotis et al.,  $\text{VSi}_{12}$  clusters was also studied by Reveles et al. [79] and Sen et al. [78] and reported with slightly distorted HP cage structure like Andriotis et al. [81]. Sen et al. [78], Reveles et al. [79], Khanna et al. [82], and Abreu et al. [83], all of them reported encapsulation of Cr atom in a  $\text{Si}_{12}$  cage with HP structure. Reveles et al. reported a  $\text{CrSi}_{12}$  structure which is perfectly symmetric  $D_{6h}$  [79]. Kawamura et al. studied  $\text{CrSi}_n$  clusters over a size range  $n = 8 - 17$  and reported  $\text{Si}_{12}$  is the smallest cage with HP structure to encapsulate a Cr atom [80]. Mn doped Si clusters were studied by Li et al. [84]. They reported that the  $\text{Si}_n$  cage with  $n = 11$  could encapsulated the Mn atom

in it. This result agrees with Guo et al. [75]. Khanna et al. reported among the  $\text{FeSi}_n$  clusters, the smallest cluster is the  $\text{FeSi}_{10}$ , where the  $\text{Si}_{10}$  cage can encapsulate the Fe atom [85]. This was an independent study apart from Guo et al. and Gueorguiev et al. They also reported Fe atom occupies an interior position in  $\text{FeSi}_9$ , but at this size the entire encapsulation of Fe atom was not found in the Si cage. The reported ground state structure of Khanna et al. was found almost as similar as the reported ground state structure by Gueorguiev et al. [76]. A pentagonal pyramid structure for  $\text{FeSi}_{10}$  cluster was studied by Sen et al [78]. Encapsulation of a Fe atom in between two  $\text{Si}_5$  pentagons were mentioned by them. For the first time, Wang et al. [86] reported about  $\text{CoSi}_{10}$  cluster, in which encapsulation of Co atoms happened in a Si cage and the cluster was formed with a basket like structure. In an earlier work [74], in case of  $\text{CoSi}_9$ , the same authors claimed a cage-like structure. According to Ren et al. [87] and Li et al. [88], for  $\text{NiSi}_n$  systems, the endohedral motifs are found to be most favorable for  $n = 8$  and more. Their claims disagree with Guo et al. and Gueorguiev et al. and also the results of Wang et al.[89]. Wang et al. [89] reported encapsulation of a Ni atom in a Si cage at  $\text{NiSi}_9$ .

Some theoretical studies of 4d and 5d  $\text{TMSi}_n$  clusters are discussed here. Kawamura et al. [80] and Gueorguiev et al. [77] reported that group-IV atoms Hf and Zr take endohedral position in a  $\text{Si}_{12}$  cage. In case of Zr the cage is distorted from a perfect  $D_{6h}$  symmetry as claimed by Gueorguiev et al. [77] and for Hf, the endohedral occupation was found in  $\text{Si}_{10}$  even. But Zr was attached exohedrally at this  $n = 10$ . A distorted HP cage for  $\text{HfSi}_{12}$  was reported by Uchida et al.[90]. Sen et al. [78] also considered a structure where Hf was kept endohedrally in a  $\text{Si}_{12}$  cage having HP geometry. So we can conclude from these results that, definitely encapsulation of group-IV elements are happened in  $\text{Si}_n$

cages, for  $n = 12$ . Among the Group-V element Nb attached endohedrally in  $\text{NbSi}_{10}$ , but the 5d group-V atom Ta, was found attached exohedrally in  $\text{TaSi}_{10}$ . For  $\text{Si}_{12}$  cage, the perfect encapsulation of Ta has been found the  $\text{TaSi}_{12}$  structure was found with HP structure with  $D_{6h}$  point group symmetry. The well-known 18-electron counting rule, are expected to satisfy by the Group-VI atoms Mo and W, during their encapsulation in a  $\text{Si}_{12}$  cage after getting motivations from the work of Hiura et al. [61]. All the works [76, 78, 80, 90–92] agree with the fact that they are encapsulated inside a  $\text{Si}_{12}$  cage. According to Abreu et al. [93] partial encapsulation was found for W atom in  $\text{Si}_{11}$  cage. In case of  $\text{WSi}_{12}$  the entire encapsulation takes place. The rest of 4d TM-Si clusters (TM = Tc-Pd) and the remaining 5d TM-Si clusters (TM = Re-Pt), used to encapsulated in  $\text{Si}_n$  cage with  $n = 12$  as reported in Refs. [76, 77, 90]. Among them Pd takes an endohedral position for  $n = 10$  where, Pt attached exohedrally with  $\text{Si}_{10}$  cage [77]. Below size  $n = 12$ , Ir, Os, Re, Rh, Ru, Tc attached exohedrally with the Si cage, and these are encapsulated by the  $\text{Si}_n$  cage at  $n = 12$  [76].

### 1.2.2 Relative Stability of $\text{TMSi}_n$ Clusters

As a particular series of clusters is studied extensively, one of the important fundamental questions which should be addressed is, variation of their relative stability with change in size and composition. In this case the most important question is, which  $\text{TMSi}_n$  cluster is found with the greatest stability for a particular TM atom? Then for different TM atoms, what is this magic number? By measuring the mass abundance spectra of these clusters, these questions are addressed experimentally. But only identification of the stable clusters is not enough, rather to understand of the origin of their stability is more important. Here the relevant point is, whether geometric close packing is responsible for this

observed stabilities or some electronic shell closing effects are the reason behind it. The experimental works and theoretical studies play equal role here.

### Experimental search

In the first experiment [51] by Beck, it was found that, the  $\text{TMSi}_{15}^+$  and  $\text{TMSi}_{16}^+$  clusters mostly dominated the mass spectra, for the W, Mo, Cr TM atoms. But at these sizes, no pure Si clusters were found. Hence after incorporating TM atoms, stable clusters were obtained. The speculation was like that either (i) metal atoms played the role of 'seed' around which a compact atomic shell is found. This atomic shell corresponds to a particular number of Si atoms (here 15 and 16). This leads to enhancement of stability in these particular TM-Si clusters or (ii) during photoionization process, in the photo-fragmentation of larger clusters the most stable fragments were found for the  $\text{TMSi}_{15}^+$  and  $\text{TMSi}_{16}^+$  clusters. Beck produced  $\text{TMSi}_n$  clusters for TM = Cr, Mo and W in the subsequent work. They used three different variations of the laser vaporization setup. Interestingly and strikingly for all cases, the observed mass spectra were observed similar. The  $\text{TMSi}_{15}^+$  and  $\text{TMSi}_{16}^+$  clusters mostly dominated it during ionization of the neutral clusters with high laser fluence.

From Hiura et al.'s breakthrough experiment where silane ( $\text{SiH}_4$ ) gas was used as reactant of producing  $\text{TMSi}_n\text{H}_x^+$  clusters, a sequential growth was found from  $\text{W}^+$  up to  $\text{WSi}_{12}\text{H}_x^+$  [61]. In case of  $\text{WSi}_n$ , similar cluster for  $n > 12$  was not seen often. For all other TM atoms a similar behavior was found. Depending on the TM atom the reactivity with  $\text{SiH}_4$  almost stopped when  $n$  reached a particular value  $m$ . This value of  $m$  was found to be 12 for W, 14 for Hf, 13 for Ta etc. For several TM atoms, the relative abundance of  $\text{TMSi}_n^+$  clusters with variation of  $n$  is depicted in in figure 1.7 Two important features came out from this experimental

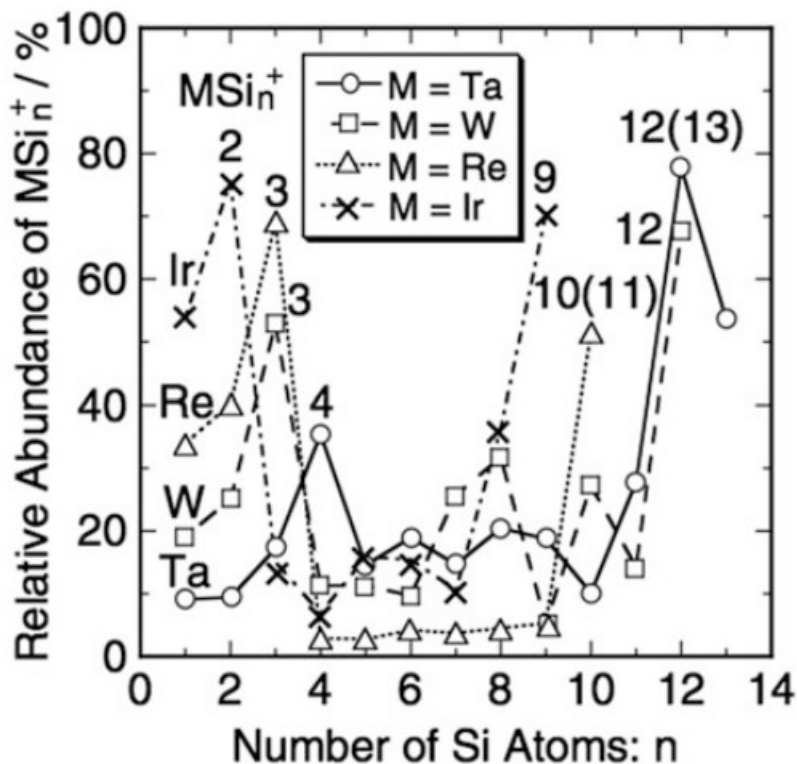


Figure 1.7: Variation of relative abundance of  $\text{TMSi}_n^+$  among  $\text{TMSi}_n\text{H}_x^+$  clusters as a function of  $n$ . Figure is adapted from Ref. [61]

observations. (i) In contrast to Beck's results, no  $\text{TMSi}_{15}^+$  or  $\text{TMSi}_{16}^+$  clusters were observed. (ii) the sum of the atomic number of the TM atom and  $m$  is always 86. This number corresponds to the atomic number of Rn atom, which is a rare gas. According to the speculation of Hiura et al. [61], as the methods of producing TM-Si clusters are different, their observations and those of Beck are different. The second observation gave rise to the idea that well-known 18-electron counting rule of chemistry may explain relative stability of  $\text{TMSi}_m$  clusters for a specific  $m$  value. If we assume the picture in following manner it will be easy to understand. One electron is donated by each Si atoms to the central metal atom. According to this assumed scenario, in  $\text{WSi}_{12}$ , the W atom is with 18 valence electrons. This leads to a closed electronic shell configuration and it is stable. This same

assumption was applied for  $\text{TMSi}_m$  clusters for TM including Ir, Re, Ta, Hf. This electron counting rule strictly applied for the neutral clusters. But when the reaction with  $\text{SiH}_4$  started, the metal atoms becomes positively ionized. Hence, arguments from the authors were arisen as follows. They argued after the entire encapsulation of the TM atom by the Si cage, the metal atoms become almost neutral. Because, the positive charges would be spread over on the whole cluster. Several subsequent studies have explored this simple idea.

Kaya and Nakajima [62–65] performed a numbers of experiments in this TM-Si cluster series. Apart from their works, significant experiments were performed by Lievens et al. [68, 94]. Ohara et al. [62] measured the mass abundance spectra for  $\text{TiSi}_n$ ,  $\text{MoSi}_n$ ,  $\text{HfSi}_n$  and  $\text{WSi}_n$  cluster with anion charge state.  $\text{TMSi}_{15}$  and  $\text{TMSi}_{16}$  clusters mostly dominated all the spectra. This observation does not agree with the Hiura et al.’s experimental findings [61]. In case of  $\text{TMSi}_n$  clusters, Hiura et al. found a local minimum in the the electron affinity (EA) for  $n = 16$  as EA was varying with  $n$ . In general, for a cluster with closed electronic shell, little amount of energy is gained when, an excess electron is added to it. It has a small EA. Their argument was that the electronic effects are not responsible for the stable characteristics of  $\text{TMSi}_{16}$  clusters. They claimed geometry of the clusters as the reason behind the observed stability in this clusters. Koyasu et al. [63] explored the system with V-Si, Ti-Si and Sc-Si clusters. The highest abundance was found for  $\text{TiSi}_{16}$  in the mass spectrum of neutral  $\text{TiSi}_n$  clusters. In case of  $\text{VSi}_n$  and  $\text{ScSi}_n$  clusters the greatest abundance was found at  $n = 16$  but in the cationic and anionic states respectively. The mass spectra of these clusters is shown in figure 1.8.

The further extention of this analysis was performed including with the 4d and 5d TM atoms from the same groups like Sc, Ti, V i.e., Y, Lu, Zr, Hf, Nb, Ta

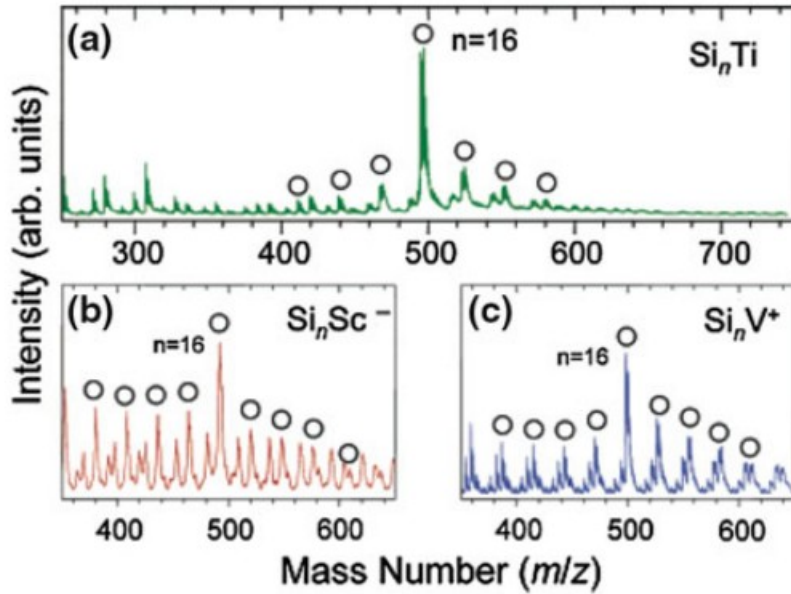


Figure 1.8: Mass spectra of (a)  $\text{ScSi}_n$ , (b)  $\text{TiSi}_n$  and (c)  $\text{VSi}_n^+$  clusters. Figure adapted from Ref. [63]

[64]. Like Ti, tetravalent Zr and Hf produced the highest abundance of neutral  $\text{ZrSi}_{16}$  and  $\text{HfSi}_{16}$  respectively. Like  $\text{VSi}_{16}^+$ , highest abundance was also found in  $\text{TaSi}_{16}^+$  and  $\text{NbSi}_{16}^+$  cation clusters [64]. In comparison with its neighbors,  $\text{LuSi}_{16}^-$  was not found with very significant abundance. In case of Y-Si series, the number of  $\text{YSi}_{16}$  clusters was a bit less than  $\text{YSi}_{15}$  and  $\text{YSi}_{17}$ , its neighbors. The stability of these clusters was explained in terms of combined effect of structural geometry and a filled 20 electron shell.  $\text{ScSi}_{16}$ ,  $\text{TiSi}_{16}$  and  $\text{VSi}_{16}^+$  all are with compact FK polyhedron structures [95, 96]. A closed electronic shell with 20 electrons was formed in case of a tetravalent Ti atom in a  $\text{TiSi}_{16}$ . This model is based on the assumption that the single electron is coming from each of the Si atoms to form this closed shell as mentioned earlier.

This concept of filled electron shell, is taken from metal clusters. There it has been shown that within this approximation of a confined spherical electron gas, valence electrons filled one particle energy states which appear in bunches.

These can be labeled as  $1S^2 1P^6 1D^{10} \dots$  [14, 97]. 2, 8, 18, 20, ... electrons appear as shell filling numbers. Clusters with having these numbers of electrons are found to be more stable. V and Sc both have one valence electron more and less respectively in the viewpoint from shell filling. In comparison to Ti,  $\text{VSi}_{16}$  and  $\text{ScSi}_{16}$  form 20 electrons closed shells in cationic and anionic charge state respectively. High degree of degeneracy of the electronic levels was caused for the highly symmetric FK polyhedron cage. These high degree of degeneracy is necessary for a pronounced closed electronic shell effect. No prominent peak was found in the abundance pattern of  $\text{YSi}_{16}$  and  $\text{LuSi}_{16}$ . This has been explained from the point of view of their structures. These TM atoms do not fit the  $\text{Si}_{16}$  cage very well as they are larger than the Sc atom. Indeed, these two atoms are encapsulated in a larger size cage [64, 98]. The speculation of the electronic shell model which is responsible for enhancement of stability in these clusters was further confirmed by their photo electron spectra (PES). Koyasu et al. [63] reported the experimental PES spectra of anionic  $\text{VSi}_{16}^-$ ,  $\text{TiSi}_{16}^-$  and  $\text{ScSi}_{16}^-$ . These are shown in figure 1.9.

The PES spectra of  $\text{VSi}_{16}^-$  and  $\text{ScSi}_{16}^-$  are completely distinct from the PES of  $\text{TiSi}_{16}^-$ . A low energy peak was found in  $\text{TiSi}_{16}^-$  spectra at both the photon energies (4.66 and 5.82 eV). These were pointed as X in panels (c) and (d) in Figure 1.9. A large energy gap and at higher electron binding energies several discrete transitions were found in these systems. This low energy feature was not found in PES of  $\text{VSi}_{16}^-$  and  $\text{ScSi}_{16}^-$ . The low energy feature X, was assumed by Koyasu et al. as happened for a singly occupied molecular orbital (MO). In case of true assumption, neutral  $\text{TiSi}_{16}$  should be found with a closed electronic shell and with a large HOMO-LUMO gap, according to the suggestions of the spectral feature. The measured value of HOMO-LUMO gap was found as 1.9 eV reported

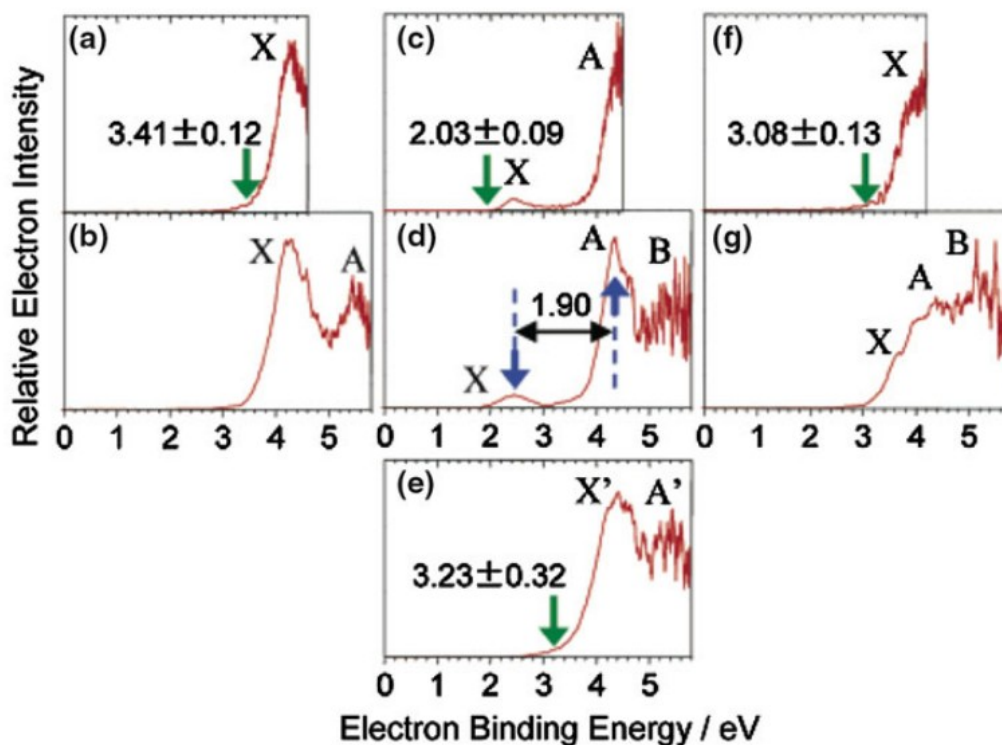


Figure 1.9: PES of (a) and (b)  $\text{ScSi}_{16}^-$ , (c) and (d)  $\text{TiSi}_{16}^-$ , (f) and (g)  $\text{VSi}_{16}$  and (e)  $\text{TiSi}_{16}\text{F}^-$  clusters. Figure adapted from Ref. [63].

by them. The idea that a singly occupied MO is responsible for the feature X, is supported by the fact that  $\text{TiSi}_{16}^-$  clusters reacted with  $\text{F}_2$  to generate  $\text{TiSi}_{16}\text{F}$  molecules. The feature X was absent in the  $\text{TiSi}_{16}\text{F}^-$  spectrum and the other spectral features remain identical. This is appreciated as the F atom, got an electron, from the singly occupied MO and ionic complex was produced. Further support for the feature X because of a singly occupied MO, was found from the measured PES spectra of the group-III, -IV, V TM doped  $\text{Si}_n$  clusters for the complete size range  $n = 6 - 20$  [98]. Neukermans et al. [94] measured mass spectrum of  $\text{CrSi}_n^+$  clusters and reported about the domination of  $\text{CrSi}_{15}^+$  and  $\text{CrSi}_{16}^+$  in it, whereas the abundance at  $n = 18, 17$  and  $14$  was much less in these Cr-Si systems. Mass abundance of  $\text{MnSi}_n^+$  clusters was also found with

same pattern like Cr-Si systems. It is also dominated by  $\text{MnSi}_{15}^+$  and  $\text{MnSi}_{16}^+$ . Neukermans et al. [94] reported  $\text{MnSi}_{17}^+$  and  $\text{MnSi}_{18}^+$  were also produced with large abundance. According to the speculations of these authors, metal encapsulated cage structure was responsible for the observed stability. These authors did not invoke electronic structure of the clusters.

From all the above discussions, it was found that quite different results for relative abundance of various TMSi clusters are obtained from different sets of experiments. But, How much of these experimental observations can be responsible for representing the relative thermodynamic stability and how much of these experimental finding, can be determined from the point of view of formation kinetics still remains an open question.

### **Findings from theoretical studies**

In order to identify the highly stable  $\text{TMSi}_n$  clusters, to get explanations of the experimental mass spectra, and for understanding the source of stability in these clusters, several theoretical studies have been performed. The observed and measured enhanced stability of particular  $\text{TMSi}_n$  clusters, can be explained by invoking three different frameworks. These are (1) metal encapsulated Si cage clusters with a compact geometric structure with a strong bonding between Si and TM; (2) 18-electron counting rule, well-known in chemistry, as suggested by the experimental works performed by Hiura et al.; (3) electron gas shell fillings formed around the metal atom, in the Si cage. To identify stable TM-Si clusters several descriptors have been used theoretically. These are: (i) Binding energy per atom (BE) of the cluster; (ii) Embedding energy (EE) of the TM inside the Si cage. This is defined as the gain in energy for putting the TM atom in the Si cage; (iii) First order energy difference  $\Delta_1(n)$  which is defined as the gain in energy

to produce the  $\text{TMSi}_n$  cluster by adding a Si atom to the  $\text{TMSi}_{n-1}$  cluster; (iv) Second order energy difference  $\Delta_1(n)$ . This is defined as the difference between  $\Delta_1(n)$  and  $\Delta_1(n+1)$ ; (v) The energy difference between the highest occupied and the lowest unoccupied molecular orbitals (HOMO-LUMO gap). Thermodynamic stability of these clusters is measured by the first four quantities in several ways. In chemical reactions, how much the cluster can be stable is mentioned as the kinetic stability. The HOMO-LUMO gap is used to measure this kinetic stability. A cluster is stable or less reactive for large HOMO-LUMO gap and becomes reactive with small HOMO-LUMO gap. These quantities are defined as

$$BE = (E(TM) + nE(Si) - E(TMSi_n))/n + 1 \quad (1.4)$$

$$EE = E(TM) + E(Si_n) - E(TMSi_n) \quad (1.5)$$

$$\Delta_1 = E(Si) + E(TMSi_{n-1}) - E(TMSi_n) \quad (1.6)$$

$$\Delta_2 = E(TMSi_{n+1}) + E(TMSi_{n-1}) - 2E(TMSi_n) \quad (1.7)$$

E's are presented for the total energies of the corresponding systems. Definitions of BE, EE and  $\Delta_1$  has already been stated earlier.  $\Delta_2$  measures the difference between gain in energy from system with size  $n - 1$  to  $n$ , and during going from system with size  $n$  to  $n + 1$ . An enhancement of stability in comparison to the two neighboring sizes, is denoted by a positive value of  $\Delta_2$ . In addition to check their stability, sometimes few other quantities also used. These

are for neutral clusters, vertical ionization potentials (VIP) and adiabatic ionization potentials (AIP). To remove an electron from a neutral cluster keeping it in same structure, the required energy is defined as VIP. The energy difference between the neutral cluster and its cation, both in ground states of is defined as AIP. High VIP/AIP is a signature of stability in neutral clusters. Neutral clusters with closed electronic shells are found with VIP and/or AIP. But in case of a excess single electron after shell filling, it will show low VIP or AIP. Like neutral clusters, these kinds of quantities are defined in charged cluster systems also. In case of anion cluster, the vertical detachment energy (VDE) is defined as difference in energy between the anion and the neutral charge state, keeping the both with anion structure. Adiabatic detachment energy (ADE) is mentioned as the gap in energy between the anion and the neutral cluster at ground state structure. ADE plays the role of adiabatic electron affinity (AEA) of the corresponding neutral cluster. Neutral cluster with a filled electronic shell is found with small AEA. Oppositely neutral cluster with one electron less to complete shell filling, is found with large value of AEA usually. All these concepts are taken from the study of metal cluster field [14, 97].

Let us now discuss some specific studies regarding the stability of TM-Si clusters with or without invoking electron counting rule regarding the explanation of their stabilities.

Inspired by the works of Jackson et al. [3] and Hiura et al. [61], Kumar et al. [95] performed one of the first important theoretical studies exploring the stability of TM-Si clusters. The so-called shell-shrinkage method was used to determine the ground state structures of TM-Si cage clusters. They performed this work including TM = Ti, Zr, Hf, Fe, Ru and Os. In this study, they reported about the cage shrunk of the  $ZrSi_{20}$  cluster during their optimization procedure. They

mentioned that one of the Si atoms stuck out from the cage. After removing this Si atom and after re-optimization, they found a  $\text{ZrSi}_{17}$  cage and here two Si atoms sticking out. A  $\text{ZrSi}_{16}$  cage with one capping Si atom was reported by them on removal of these two atoms and removal of this last Si atom. After re-optimization a symmetric fullerene(f)-like compact cage of  $\text{ZrSi}_{16}$  was formed. For  $\text{TiSi}_{16}$  they reported a FK polyhedron structure was found which was energetically lower by 0.781 eV from the f-like structure. Very large HOMO-LUMO gap with a value of 2.358 eV was reported for this FK isomer. TM atoms with small size like Fe, Ru and Os, stable  $\text{TMSi}_{14}$  cages were found by them. All other details are given in the original paper [95]. They reported all these clusters are found with large HOMO-LUMO gaps more than 1 eV and they also have significant BEs. The large stability of the  $\text{TiSi}_{16}$  cage cluster has been explained interestingly. The f-like  $\text{Si}_{16}$  and the FK both are with four unpaired electrons and spin moments of  $4\mu_B$ . So both of them can share four electrons and can form strong bonds with the central Ti atom, which is tetravalent. and strong bonds with the tetravalent Ti atom could be formed. Depletion of charge on the Si-Si bonds in  $\text{Si}_{16}$  was found in a comparative study of charge densities of the isolated metal atom and empty Si cage with the metal encapsulated Si cage cluster. Similarly, in case of  $\text{Si}_{14}$ , after metal encapsulation, depletion of charge density was occurred at the center of the faces. Additionally charge was accumulated in the TM-Si bonds. Hence, without invoking any electron counting rules, explanation regarding the stability of these clusters could be proceeded by forming strong TM-Si bonds. Kumar et al. [99] performed similar analyses for the group-VI TM elements W, Mo and Cr. As Cr atom is smaller than Ti, it does not fit a  $\text{Si}_{16}$  cage properly. The f-like  $\text{CrSi}_{16}$  structure turns to a  $\text{CrSi}_{15}$  structure with capping by a Si atom, after optimized. When this capping is removed, and it is again re-optimized, a

stable f-CrSi<sub>15</sub> structure was formed. In case of CrSi<sub>15</sub>, the ground state structure was found from the capped cubic structure that was obtained in case of FeSi<sub>14</sub>. In case of W and Mo, this cube derived structure was found as the lowest energy isomer also, as similar as Cr mentioned above. Large HOMO-LUMO gaps, more than 1.5 eV were found in all three clusters. HOMO-LUMO gaps were found for the TMSi<sub>14</sub> clusters, are larger compared to other size. But their BEs are smaller in comparison the corresponding TMSi<sub>15</sub>. The largest . This was mentioned because at size 14, clusters were not found as magic in Beck et al.'s experiments. Unlike Cr, For W and Mo, when the metal atoms were building coordination with all the 16 Si atoms, stable structures were found. But a capped Si<sub>15</sub> f-cage was found to be the lowest energy structure. Based on all these observations it was argued that for the group-VI elements, the most stable structure is a metal encapsulated Si<sub>15</sub> cage structure.

Several other studies [74, 76, 77, 80, 86, 88, 89, 92, 100] have been done addressing the question regarding relative stability of different TM-Si clusters without incorporating electron counting rules necessarily. Kawamura et al. [80, 100] explored the structures and properties of Hf, Zr, Ti, Cr doped Si clusters with using two different exchange correlation functional in their electronic structure calculations. Their study did not incorporate the electron counting rule to explain the relative stabilities of these clusters. Other important theoretical studies was done by Nagase et al. [92]. They explored several TM doped Si clusters over a long size range. In case of Pt, Os, Zr and W doped Si clusters at  $n = 16$ , they reported highest values of both the BE and the EE were found. This is an important information. They mentioned about the local peaks at  $n = 14$  for Zr and Pt,  $n = 12$  for Os and  $n = 8$  and  $12$  for W. Their argument was, as TM-Si clusters were formed when the metal is reacted with Si vapors, after a complete

reaction  $\text{TMSi}_{16}$  would be produced. Locally stable clusters may be the output of incomplete reaction. An incomplete reaction could stop at  $\text{WSi}_{12}$  in case of W. According to this argument the relative abundance of various sizes in a given experiment is determined by the kinetics of formation.

Hiura et al. [61] suggested explanation about the observed non-reactivity of specific  $\text{TMSi}_n$  clusters towards  $\text{SiH}_4$ . The empirical 18-electron counting rule of inorganic and organometallic chemistry can explain this non-reactivity according to them. Getting motivation by their suggestion, there are number of studies performed to check how efficiently electron counting rules can explain the relative stability of TM doped Si clusters. We have already discussed some earlier. Among these theoretical studies, most notable works are by Sen and Mitas [78], Khanna and co-workers [79, 82, 83, 85, 101, 102]. Uchida et al. [90] and Guo et al. [75]. There was attempt to explain the observed stability of  $\text{ScSi}_{16}^-$ ,  $\text{TiSi}_{16}$ ,  $\text{VSi}_{16}^+$ . Using electron counting rule which is applied to a spherical electron gas, Reveles et al. tried to give explanation regarding the observed stability of mentioned clusters [96].

All 3d, and some of 4d and 5d TM doped  $\text{Si}_{12}$  clusters were explored theoretically by Sen et al. They explored the stability of these clusters, in terms of 18-electron rule [78]. They emphasize about the fact that how generally the stability of the  $\text{TMSi}_n$  clusters can be explained by the 18-electron rule. They studied the  $\text{FeSi}_{10}$  and  $\text{ReSi}_{11}$  clusters for further exploring the applicability of the 18-electron count. From a nominal valence electron count,  $\text{FeSi}_{10}$  and  $\text{ReSi}_{11}$  are expected to obey this electron counting rule. Sen et al. [78] calculated the HOMO-LUMO gaps and for all these clusters. It was found that  $\text{WSi}_{12}$  has the largest and a remarkably large EE value of 8.44 eV Among all the TM. But In case of 3d series, the largest EE was found in case of V, not for Cr (4.46 and 2.99 eV respectively). Quite large

HOMO-LUMO gaps have been found for both  $\text{VSi}_{12}$  and  $\text{CrSi}_{12}$ . In contrary to the facts which are expected from the 18-electron counting,  $\text{ReSi}_{12}$  had a larger EE (7.44 eV) than  $\text{ReSi}_{11}$  (6.34 eV). For  $\text{FeSi}_{10}$ , EE was found as 1.07 eV, also small rather. Regarding the applicability of electron counting rule in explanation of stability of these cluster, the argument was like that the 18-electron rule can be considered as just one of the factors, and it can't be applied in general. One of the criticisms of this work by Sen et al. [78] could be that a thorough search of structure was not performed. For  $\text{TMSi}_{12}$  clusters they considered only HP cage structures.

The same question was addressed by Khanna et al. [82, 85] from a slightly different point of view. In case of  $\text{CrSi}_n$  and  $\text{FeSi}_n$  clusters their essential focus was on the quantity  $\Delta_1$ . They reported the largest  $\Delta_1$  at  $n = 12$  among the  $\text{CrSi}_n$  clusters for  $n = 11 - 14$ . They also reported that the only pure Si cluster was found as  $\text{Si}_{12}$ . In case of  $\text{Si}_{12}$ , more energy was gained when bonds between Cr and Si are formed, but during the Si-Si bond formation, energy gain was lower. These things indicate about special stability of  $\text{CrSi}_{12}$ . This stability was explained in terms of the 18-electron rule. Inside the Si cage a uniform charge density around the Cr atom was found. A charge transfer was found from the Si cage to Cr atom with an amount of  $2.6e$ . This was considered as another evidence that around the metal atom, formation of a filled shell of electrons took place. Another fact should be mentioned that, among the studied clusters,  $\text{CrSi}_{12}$  was found neither with the largest BE, nor with largest HOMO-LUMO gap.

Khanna et al. claimed that due to the largest  $\Delta_1$  value  $\text{FeSi}_{10}$  is more stable than  $\text{FeSi}_9$  and  $\text{FeSi}_{11}$  clusters in their early work [85]. Largest BE, also as the largest HOMO-LUMO gap was found in  $\text{FeSi}_{10}$ . It has the largest VIP also, but it does not have the largest EE. magic nature of  $\text{Si}_{10}$  among the pure Si cluster was

claimed to be responsible for this. For  $\text{Si}_{10}^+$  significantly larger peak was found in compared to its neighbour, in the experimental mass spectrum of pure Si clusters [103]. For large value of HOMO-LUMO gap (2.08 eV), it becomes stable as well as non-reactive. Hence, the production of  $\text{FeSi}_{10}$  is likely to proceed by addition of a single Si atom to  $\text{FeSi}_9$ . It is not like the process of incorporating the Fe in a  $\text{Si}_{10}$  cage. The largest stability of  $\text{FeSi}_{10}$  was according to the 18-electron counting rule in any case. But a later work shows that this conclusion can't be drawn here as this picture is not the complete one.

Reveles and Khanna focused on the quantity EE as among the 3d TM atoms, Sen et al. reported the largest value of EE for  $\text{VSi}_{12}$ . Reveles et al. calculated this quantity by incorporating the Wigner-Witmer (WW) spin conservation rule. The main idea of this rule is that during the encapsulation of a TM atom in a Si cage the total spin has to be conserved. Therefore EE, with enforcing the WW rule is defined in equation 1.8.

$$EE^{WW} = E(\text{Si}_{12}) + E^M(\text{TM}) - E^M(\text{TMSi}_{12}) \quad (1.8)$$

M denotes the spin multiplicity of the  $\text{TMSi}_n$  cluster. To maintain same total spin of the reactants and the products, the spin multiplicity of TM atom was taken same as that of  $\text{TMSi}_n$  cluster, instead of its ground state. EE and  $EE^{WW}$  were calculated by Reveles and Khanna for the anion clusters along with the neutral clusters [79]. They reported about the distorted HP cage structures. The amount of distortions was found small in middle of the 3d series, and larger along the both ends of the same series. A perfectly symmetric  $D_{6h}$  structure for  $\text{CrSi}_{12}$  was reported by them. Instead of Cr, the largest values for EE was found for V and Fe in case of neutral clusters. V was found with largest EE for anion also. On the

other hand Cr was found with largest value of  $EE^{WW}$ . The  $EE$  and  $EE^{WW}$  calculated by these authors are shown in figure 1.10 It was claimed that for proper

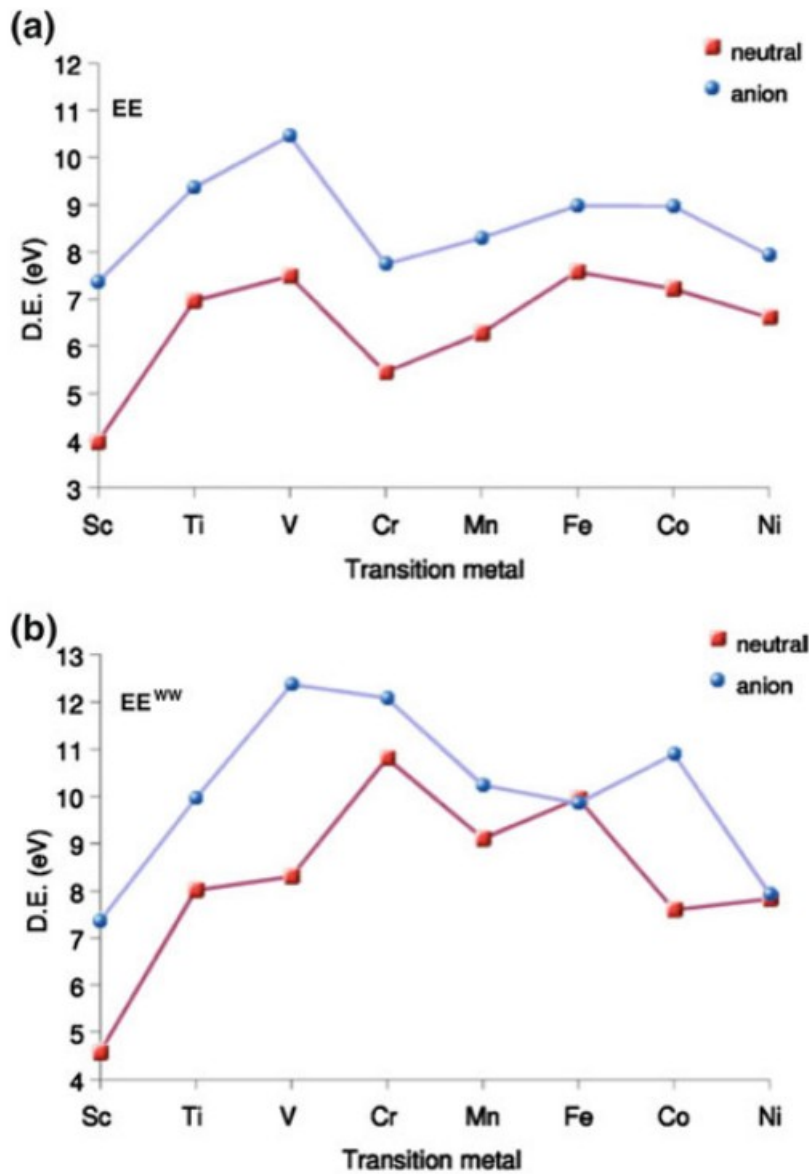


Figure 1.10: Representation of (a)  $EE$  and (b)  $EE^{WW}$  for 3d TM encapsulated caged  $Si_{12}$  clusters. Figure is adapted from Ref. [79]

understanding about relative stability, with variety of sizes, spin conservation must be enforced for calculating  $EE$ . With spin conservation,  $CrSi_{12}$  turns out to be the most stable structure following the 18-electron counting rule. Khanna and

co-workers in another work reported that  $\text{CrSi}_{14}$  follows the 18-electron rule [83]. In this context, it should be mentioned that in the PES spectra of the group-V TM-Si cluster anions, Koyasu et al. did not report about any proof regarding the electronic shell (18 electron) filling picture [98]. They reported that around size 12, smoothness was found in the threshold of the PES. No maxima was found in the threshold for  $\text{NbSi}_{12}^-$ ,  $\text{TaSi}_{12}^-$  and  $\text{VSi}_{12}^-$ . Khanna et al. in their another work, reported a second peak in  $\text{EE}^{WW}$  in case of Fe, that is expected to obey the 20 electron shell filling [98]. This was considered as a evidence of a closed shell electronic structure of this cluster. The experimentally observed mass spectra of the  $\text{TiSi}_n$ ,  $\text{ScSi}_n^-$ , and  $\text{VSi}_n^+$  clusters, measured by Koyasu et al. [63] were explored theoretically for better understanding by Reveles and Khanna [96] in their another interesting work. From the experiments it was found, at  $n = 16$  all these three clusters are with greatest abundance. Reveles and Khanna calculated  $\text{BE}^{WW}$  and  $\text{EE}^{WW}$  of the neutral and charged Sc, Ti and V doped  $\text{Si}_n$  clusters for  $n = 15-17$  incorporating the WW spin conservation rule. These authors performed the bond critical point (BCP) analysis [104] of these clusters.  $\text{TiSi}_{16}$ ,  $\text{VSi}_{16}^+$  and  $\text{ScSi}_{16}^-$  which are expected to be obey the 20 electron counting rule, are found with symmetric FK polyhedron structures. Other clusters which deviate from the 20 electron count, in this series, have distorted structure from a perfect FK polyhedron.

Apart from Khanna and co-workers and Sen et al. some important works regarding the properties of different 3d TM encapsulated Si cage clusters have been performed by Guo et al. [75]. They reported among the  $\text{TMSi}_{12}$  clusters,  $\text{VSi}_{12}$  has the largest BE and EE, which agrees with Sen et al. Truly, among all the cage clusters, these were the largest BE and EE values. Among all the clusters,  $\text{NiSi}_{10}$  was found with largest HOMO-LUMO gap and with the largest VIP. Sur-

prisingly, among the  $\text{TMSi}_{12}$  clusters the largest HOMO-LUMO gap and VIP were found in  $\text{TiSi}_{12}$ . The same conclusion is also made by Guo et al. that, electron counting rule (18 or 20 electrons) is just one of the aspects to determine stability of these clusters.

As discussed, several studies, both theoretical and experimental, have addressed fundamental properties of  $\text{TMSi}_n$  clusters in the gas phase. There were no studies trying to use them in applications, or studying their properties after deposition on a substrate, often a precondition for application. The first such attempt has come from experiments done by Nakajima's group [4]. They have deposited stable  $\text{TaSi}_{16}^+$  clusters on a highly oriented pyrolytic graphite (HOPG) substrate.

In this set of experiments, they explored formation of assemblies of  $\text{TaSi}_{16}$  on the HOPG substrate. Structure and electronic properties of the deposited clusters were studied using scanning tunneling microscopy (STM), X-ray photo emission spectroscopy (XPS), and ultraviolet photo emission spectroscopy (UPS) probes. STM and XPS measurements were performed both on the deposited samples and after heating them at 400 and 720 K. To check the so-called superatomic character of  $\text{TaSi}_{16}$ , they also studied reaction of the deposited clusters with oxygen.

These experiments provided a lot of information on the behavior of deposited  $\text{TaSi}_{16}$  clusters on HOPG, but none of these provides microscopic insights. In order to have a microscopic picture of the system atomistic calculations are required. so, in order to better understand this important cluster-substrate system, we have performed first-principles calculations on free and HOPG-deposited  $\text{TaSi}_{16}$  clusters using density functional theory (DFT). The details are discussed in chapter 3.

### 1.3 Permanent magnet

Permanent magnets (PM) are the basis of an ever increasing number of devices of modern life. PM has a wide range of applications such as hard-disk drives, spintronics, hybrid vehicles, wind turbines, home appliances, and biomedical devices. PM are characterized by a large volume magnetization and a high coercivity. The coercivity measures the resistance to demagnetization by external fields. Proper intrinsic properties of the magnetic material are the prerequisite for these two characteristics. These are (1) a high spontaneous magnetization and (2) high magneto-crystalline anisotropy or magnetic anisotropy energy (MAE). The PM usually have high Curie temperatures ( $T_c$ ) The intermetallic phase  $\text{Nd}_2\text{Fe}_{14}\text{B}$  [105, 106] is very popular rare earth (RE) permanent magnet. It is mainly used in modern acoustic transducers, speakers which are used in consumer electronic devices, cell phones, cars. NdFeB magnets play essential role in eco-friendly transport and sustainable energy production. High performance magnets with 400 kg  $\text{MW}^{-1}$  power is required in a generator of a direct drive wind mill. On average, there is a requirement of 1.25 kg of high end permanent magnets by a hybrid and electric vehicle [107]. Bonded  $\text{Nd}_2\text{Fe}_{14}\text{B}$  magnets are used in hard disk drives. In hard disk it is used in motor that spins the disk. The sintered magnets are used for the voice coil motor for moving the arm. In many applications these are used at higher temperatures. For example, in the motor/generator block of hybrid vehicles it operates at around 450 K. Another popular RE based PM are Sm-Co intermetallics.  $\text{SmCo}_5$  and  $\text{SmCo}_{17}$  have high  $T_c$  with value 1020 K and 1190 K respectively [108], which are much higher than the  $\text{Nd}_2\text{Fe}_{14}\text{B}$  intermetallics ( $T_c = 558$  K). So Sm-Co type intermetallics are preferable to use at high temperature. Sometimes Dy and other RE metals based PM are used in various devices. But

due to high demand of RE metals And supply side constraint there is an urgent drive to design PM without RE elements.

### 1.3.1 Properties of PM

The primary objective of a PM is to generate a magnetic field in the air gap of a magnetic circuit [109]. Magnetic circuit is made up of one or closed loop paths, which contain a magnetic flux usually generated by a PM or electromagnet. The energy which is stored in the field outside the PM can be related to its shape and magnetization. The magnetic induction  $\mathbf{B}$  is divergence free ( $\nabla \cdot \mathbf{B} = 0$ ) and magnetic field  $\mathbf{H}$  is curl free in the absence of any current according to Maxwell's equations. The volume integral of the product of a solenoidal and irrotational vector field over all space becomes zero [110], with the condition that at infinity the corresponding vector and scalar potentials should be regular. The wellknown relation between magnetic induction and magnetization is

$$\mathbf{B} = \mu_0(\mathbf{M} + \mathbf{H}) \quad (1.9)$$

Here  $\mathbf{B}$  is the magnetic induction vector due to the magnetization vector  $\vec{M}$ .

Here

$$\mu_0 = 4\pi \times 10^{-7} TmA^{-1}$$

represents the vacuum permeability. In a volume  $V_a$  of free space, the magneto-static energy is

$$E_{mag,a} = \left(\frac{\mu_0}{2}\right) \int_{V_a} \mathbf{H}^2 dV. \quad (1.10)$$

Separating the space into the volume inside the magnet,  $V_i$ , and  $V_a$ , we get

$$\int \mathbf{B} \cdot \mathbf{H} dV = \int_{V_a} \mu_0 \mathbf{H}^2 dV + \int_{V_i} \mathbf{B} \cdot \mathbf{H} dV = 0 \quad (1.11)$$

and

$$E_{mag,a} = -\frac{1}{2} \int_{V_i} \mathbf{B} \cdot \mathbf{H} dV \quad (1.12)$$

As the left hand side of equation 1.12 is  $> 0$ , so induction  $\mathbf{B}$  and field  $\mathbf{H}$  are with opposite direction to each other inside the magnet. Inside the magnet the magnetic induction  $\mathbf{B}$  and the magnetic field  $\mathbf{H}$  can be approximated by a uniform vector field, and we can write

$$E_{mag,a} = (1/2) \int_{V_i} (BH) dV \quad (1.13)$$

Here  $B = |\mathbf{B}|$  and  $H = |\mathbf{H}|$ . The increment in stored energy in its external field can be done, either by increasing the magnets volume  $V_i$  or by increasing the energy density product  $(BH)$  [111]. The product of the magnetic induction  $B$  and the corresponding magnetic field  $H$ , which is opposite in direction of  $\mathbf{B}$ , is the definition of the energy density product  $(BH)$  [112]. It is found in units of  $\text{J m}^{-3}$ . In absence of any field generating current, the magnetic field inside the magnet is

$$\mathbf{H} = -N\mathbf{M} \quad (1.14)$$

It depends on the shape of the magnet and can be expressed in terms of the demagnetizing factor  $N$ . Our further assumption is, that the magnet is saturated

and no secondary phases are present there. Hence,  $|M| = M_s$ .  $M_s$  represents the spontaneous magnetization of the material. From equations 1.9 and 1.14 the energy density product can be expressed as

$$(BH) = |\mu_0(M - NM)| - NM| = \mu_0(1 - N)NM_s^2$$

[108] The maximum energy density product of a material is found by maximizing the above expression with respect to  $N$ . It is found as

$$(BH)_{max} = \frac{1}{4}\mu_0M_s^2 \quad (1.15)$$

for  $N = 1/2$ . The energy density product becomes maximum and its value is given by equation 1.15, when the magnetization is not reduced with increasing opposing field until  $H > M_s/2$ . For an ideal permanent magnet, the magnetic

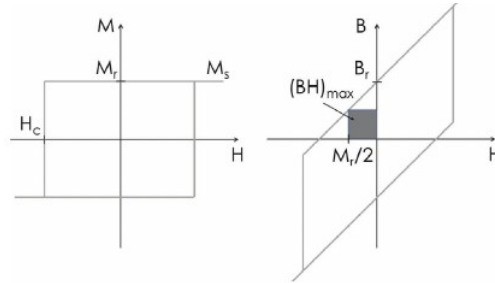


Figure 1.11: The maximum energy density product  $(BH)_{max}$  is shown by the area of the largest rectangle that can occupy below the second quadrant of the  $B(H)$  curve. For an ideal PM Left:  $M(H)$  loop, right:  $B(H)$  loop respectively.

induction  $B$  is a straight line as function of field. The remanent magnetization,  $M_r$  is the spontaneous magnetization,  $M_s$ , in case of an ideal loop as shown in figure 1.11. At fields lower than half the remanence, magnetization reversal may occur in some materials. The energy density product is limited by the coercive

field,  $H_c$ , when  $H_c < M_r/2$ . Similarly, when  $M(H)$  is not found with square shape but decreases gradually with increasing field  $H$ , the maximum value for  $(BH)_{max}$  is not obtained. A higher energy density product is an important figure of merit, as it makes reduction of weight and volume of the PM containing device. Other decisive properties are the remanence, the loop squareness and the coercive field of a PM.

### RE free PM

3d TM can give reasonable saturation magnetization, but they have low MAE in bulk. For example, MAE of bulk HCP Co is  $65 \mu\text{eV}/\text{atom}$  and for Fe and Ni it is even lower than Co. For this reason alloys and compounds of 3d TM are explored for using as RE free PM. FePt, CoPt, HfCo alloys are well-known RE free PM [113]. As Pt and Hf are also very expensive metals, so there is a search for less expensive alternatives. Theoretical modeling is one of the useful paths to find new materials with the properties desired in a PM. The metastable Fe-C martensite phase is an old and as well as popular system. The octahedral interstitial positions of the body-centered cubic (bcc) Fe crystal are taken by C atoms here. This causes a tetragonal distortion [114–116]. By quenching of the high-temperature face-centered cubic (fcc) phase rapidly, the practical achievement of this metastable phase is possible. As the phase diagram of Fe-C and that of Fe-Co-C systems were found similar [117, 118], the reasonable prediction can be used that, same type of structures found in  $\text{Fe}_{1-x}\text{Co}_x\text{C}$  alloy. On producing a tetragonal distortion in the cubic system, the desired PM properties, including a large MAE, can be found in  $\text{Fe}_{1-x}\text{Co}_x$  based systems.

Burkert et al. [119] used theoretical calculations based on density functional theory (DFT). Their prediction was, when a tetragonal distortion was given to the

cubic structure of FeCo, the MAE value can be increased with changing the  $c/a$  ratio. A  $\text{Fe}_{0.40}\text{Co}_{0.60}$  alloy under a tetragonal distortion of  $c/a = 1.2$  was predicted to have MAE of 700-800  $\mu\text{eV}/\text{atom}$  as compared to only 65  $\mu\text{eV}/\text{atom}$  in bulk hcp Co. As a strategy for producing such tetragonal distortions, they suggested depositing FeCo alloy films on suitable substrates. The most preferable approach to strain the lattice was considered as the coherent growth of the films, where FeCo maintains the unit cells volume and adapts to the in plane lattice parameter of a buffer layer and perpendicular strain is applied. But up to a critical thickness  $d_C$ , at which relaxation of lattice is started through misfit dislocations. Induced strain is mostly relieved. Moreover in grown film, ratio of lattice constants  $c/a$  was found as 1. As  $d_C$  is found in the range of 15 monolayers or 2 nm, large MAE are limited to only ultrathin Fe-Co films [120–122].

Delczeg-Czirjak et al.[123] proposed spontaneously strained Fe-Co-C phases to get rid of the problem of thickness limitation. In films, it is given by lattice relaxation with incorporating distortion. Stable energy minima for  $c/a > 1$  for many internally relaxed  $(\text{Fe}_{1-x}\text{Co}_x)_y\text{C}$  systems were presented by them. These mentioned systems are with  $y = 8, 16,$  and  $24$  and C is found in an interstitial positions of the octahedron. This result points out that, there is a possibility to find out the martensite structures with desired properties. They reported comparatively large tetragonal distortion up to  $c/a \approx 1.17$  are found for systems with  $y = 16$ . Hence, significantly large values of the MAE can be found. For systems containing lower amount of C, with  $y = 24$ , the  $c/a$  value is much small and it is almost 1.035. For different values of  $y$  the MAE is calculated They reported MAE value upto  $41.6 \mu\text{eV}/\text{atom} = 0.59 \text{ MJ}/\text{M}^3$ .

We can get an overview from Figure 1.12 about the fact, how spontaneous strain can affect the uniaxial anisotropy constants ( $K_U$ ) of the ternary  $(\text{Fe}_{0.4}\text{Co}_{0.6})_{0.98}\text{C}_{0.02}$

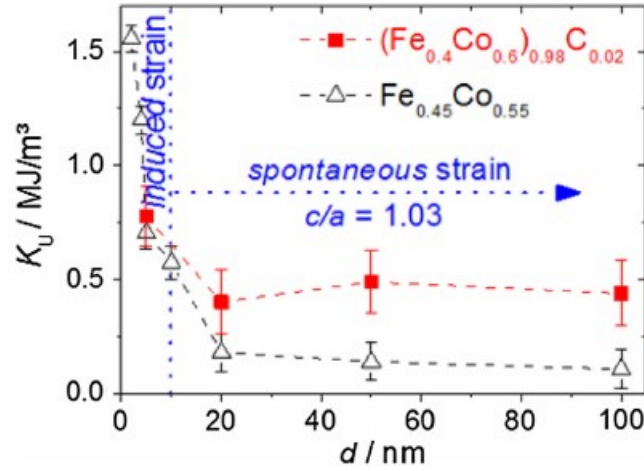


Figure 1.12:  $K_U$  is the uniaxial anisotropy.  $K_U$  for ternary  $(\text{Fe}_{0.4}\text{Co}_{0.6})_{0.98}\text{C}_{0.02}$  (full squares) and binary  $\text{Fe}_{0.45}\text{Co}_{0.55}$  films (open triangles) grown on  $\text{Au}_{0.5}\text{Cu}_{0.5}$  buffers varies with film thickness. Figure is adapted from ref [113].

films. The values for binary  $\text{Fe}_{0.45}\text{Co}_{0.55}$  films without spontaneous strain are added. Because of the induced strain at the interface, the highest  $K_U$  values are present in ultrathin films. There was lattice relaxation within the first 5 nm of a produced film. For higher thicknesses, thus degradation of  $K_U$  happened abruptly [123, 124]. When the induced strain is relaxed completely MAE of the binary films tends to zero. The spontaneous strain in the Fe-Co-C films is responsible for  $K_U$  of  $0.44\text{ MJ/m}^3$  is kept up to a 100 nm thickness. It is confirmed by DFT calculations by Delczeg-Czirjak et al. [123].

Zunger et al. [125] performed supercell calculations utilizing special quasirandom structures of Fe-Co-C systems. They reported slightly larger value of MAE =  $0.75\text{ MJ/m}^3$ . Along with they reported large saturation magnetizations = 2 T for these systems. The strong exchange interactions of Fe and Co atoms, are not affected by nonmagnetic C in small quantity significantly. It is logical to predict a notable Curie temperature. These properties make this system as a highly demanding PM.ss

After these theoretical predictions, the next step should be an experimental confirmation. Reichel et al. used pulsed laser deposition for epitaxial growth of the  $(\text{Fe}_{1-x}\text{Co}_x)_y\text{C}$  system [126]. It was found that during the growth of ternary  $(\text{Fe}_{1-x}\text{Co}_x)_y\text{C}$  system on a CuAu buffer. the saturation of the tetragonal distortion happened towards  $c/a \approx 1.03$  with the film thicknesses of at least 100 nm. This is contradictory to the binary  $\text{Fe}_{1-x}\text{Co}_x$  system. Rapid saturation toward  $c/a = 1$  was found for the binary system. Thus a tetragonal distortion is induced here by C atoms indeed. For  $x = 0.6$ , large magnetocrystalline anisotropy energy with a value  $0.44 \text{ MJ/m}^3$  was measured here. As a small amount of C (approximately 2%) seems to enter the system, a direct comparison with theoretical results [123] was difficult to perform. Therefore, for a  $(\text{Fe}_{0.4} \text{Co}_{0.6})_{32}\text{C}$  system, the experimentally measured lattice constants  $a = 2.81$  and  $c/a = 1.03$ , were taken and calculations were performed in two different methods. The MAE values were found as  $0.22 \text{ MJ/m}^3$  and  $0.51 \text{ MJ/m}^3$  [113]. The experimental value is in between the two theoretical results; therefore, one can consider the theory and experiment agree well with each other.

Another type of material studied as RE free PM, is binary alloys, like FeNi, MnAl, CoNi, MnGa etc. in the  $L1_0$  structure [127]. In spite of the fact that, they are 3d-based magnets, large values of MAEs are found here on the order of  $1 \text{ MJ/m}^3$  or higher. Evaluation of Curie temperatures are done here by applying Monte Carlo simulation. Significant values Curie temperatures are found here. To obtain large  $T_C$  above 600 K, off-stoichiometric Mn-rich compounds are required in case of the Mn based materials.

Involving the usefulness of traditional metallurgical methods for production of novel magnetic materials, is another way of the research toward RE-free PMs. Using arc-melting and melt-spinning probes, several intermetallic compounds were

produced from elemental precursors. MnBi is an important intermetallic compound among them. It has important applications as a PM and for its useful magnetic properties it has drawn much attention. It has a hexagonal structure with a comparatively low temperature of formation along with high magnetocrystalline anisotropy, which gives large coercivity. Similar properties were found with electronic structure calculations [124, 128–130]. Mixing procedure of Mn and Bi is difficult since there is a difference of almost 1000 K in melting temperatures of two metals [131]. For this reason the hexagonal phase with the uniaxial magnetocrystalline anisotropy and the relevant magnetic properties are not easy to be obtained. These materials are synthesized using arc melting, taking into account the loss of Mn during melting process caused by sublimation. This is different from conventional techniques [132]. The lattice parameters were  $a = 0.429$  nm and  $c = 0.612$  nm, as same as those reported in the literature [132, 133]. Large saturation magnetization is not found in it. Magnetic moments up to  $4.0 \mu_B$  per Mn atom were found [134] here. A high coercivity above 1 T is produced here by large magnetic anisotropy with a value of  $2.2 \text{ MJ/m}^3$  at 500 K as reported [128]. Theoretical value of  $BH_{max}$  was reported above  $12.7 \text{ MJ/m}^3$  [135]. The increase of coercivity with temperature was found up to 2.6 T at 523 K. This is an interesting fact in MNBi [128, 133]. For higher temperatures, the structure becomes unstable [132].

Magnetic nanorods have been explored as an interesting class of material of RE free PMs. Cobalt was selected as nanorod material for its uniaxial anisotropy with  $K_1 = 450 \text{ kJ/m}^3$  and saturation polarization  $J_s = 1.76 \text{ T}$  [136]. In experiments, Co nanorods with cylindrical geometry, having different diameter and height have been produced [137, 138]. In order to study the effect of aspect ratio  $H/D$  on coercivity, finite-element micromagnetic simulations have been performed. Here

D and H represent the nanorod diameter and height respectively.

where The finite-element model of Figure 1.13 (a) presents the magnetic nu-

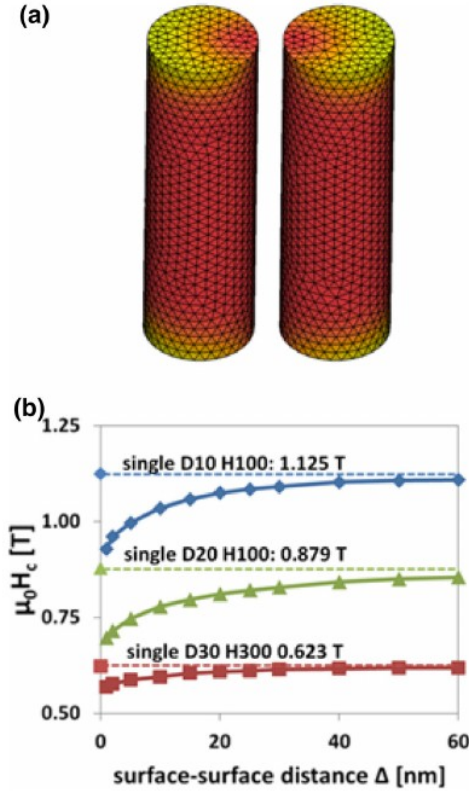


Figure 1.13: During magnetization reversal, a finite-element model of two interacting D30H100 Co nanorods. (b) How coercivity depends on the distance between two D10H100 (blue diamonds), D20H100 (green triangles) and D30H300 (red squares) nanorods. The coercivity of a single nanorod acts as an upper limit for structures containing several nanorods. Figure is adapted from [113].

creation and reversal process of neighboring Co nanorods with  $H = 100$  nm and  $D = 30$  nm starting at the end surfaces of the nanorods. As the diameter decreases, the influence of inhomogeneous reversal processes become less important. This leads to an increase of the coercive field up to  $\mu_0 H_c = 1.125$ T with  $D = 10$  nm as shown in figure 1.13 (b).

## Nanoparticles as RE free PM

Magnetic nanoparticles are widely used in various industrial and medical applications, targeted drug delivery, high-density memory storage, components in nano-electronic circuits [139–144] etc. RE-free permanent magnets at the nano-scale have been notably explored by El-Gendy et al.[5]. They synthesized cobalt-carbide nano-particles by wet chemical means with high MAE values close to 100 eV/Co (0.75 MJ/m<sup>3</sup>), significantly larger than that of bulk hcp Co. These had a blocking temperature of 571 K, and T<sub>c</sub> equal to 650 K, both much higher than room temperature. In order to probe the microscopic source of the experimentally observed large magnetic anisotropy, first principles calculations was performed by them. This phase consists of cobalt layers separated via carbon layers, their magneto crystalline anisotropy was investigated. By finding out the contribution from spin-orbit coupling to the total energy this was calculated. Regarding this spin-orbit coupling contribution, the magnetic moment along various directions was constrained and characterized by the polar and azimuthal angles  $\theta$  and  $\phi$ . One can separate total energy into two parts. One is the direction-independent and the other is the small angular-dependent energy. The so-called anisotropy energy is determined by the angular dependent second part. This can be written as mentioned in reference [5].

$$\Delta E(\theta, \phi) = E(0, 0) + V \sin^2(\theta - \theta_0) \times K + K' \cos[2(\phi - \phi_0)] \quad (1.16)$$

The two magnetic anisotropy constants of the nanoparticle are presented by K and K'. The spherical angles  $\theta_0$  and  $\phi_0$  correspond to the easy axis directed along a minimum of anisotropy energy. They performed calculations of the  $\Delta E(\theta, \phi)$  by fixing spin moment along various directions to determine K and K', until a

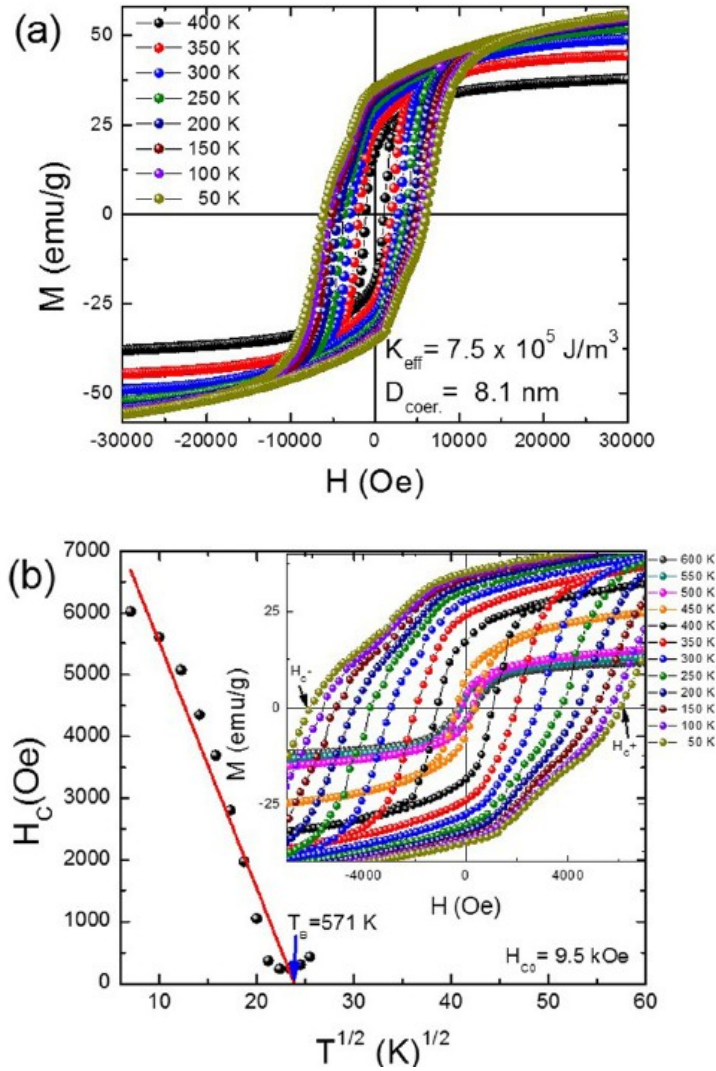


Figure 1.14: Magnetic properties of the experimentally produced  $\text{Co}_3\text{C}$ . (a) The profile of magnetic hysteresis loops at different temperatures. (b) The dependence of coercivity on temperature to find out blocking temperature ( $T_B$ ). Figure is adapted from [5].

local minimum of the total energy can be reached. They found an easy axis along [001] direction with spherical angles  $\theta_0 = \phi_0 = 0$  for  $\text{Co}_3\text{C}$ . This is shown in figure 1.15. The  $\Delta E(\theta, \phi)$  was computed at several  $\theta$  with constant  $\phi = 0^\circ$  and  $90^\circ$ . In order to determine the anisotropy constants, the above equation was numerically fitted to the computed energies. The values of calculated  $K$  and  $K'$  were  $8.4 \times$

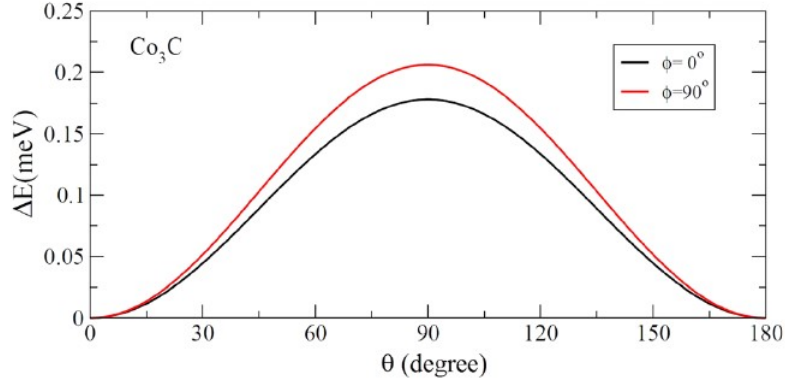


Figure 1.15: Variation of MAE with spherical angles  $\theta$  and constant  $\phi$ . Figure is adapted from [5].

$10^5 \text{ J/m}^3$  and  $-0.61 \times 10^5 \text{ J/m}^3$  respectively. An effective  $K_{eff}$  can be found from numerical fitting of the experimental data. Variation over  $\phi$  is not involved here. From the above equation, and using the calculated values of constants, it was found that, the theoretical  $K_{eff}$  lies between two values, minimum ( $K + K'$ )  $7.8 \times 10^5 \text{ J/m}^3$  at  $\phi = 0^\circ$  and maximum ( $K - K'$ )  $9.0 \times 10^5 \text{ J/m}^3$  at  $\phi = 90^\circ$ . Their calculated values agree well with the experimental measurement of  $7.4 \pm 1.0 \times 10^5 \text{ J/m}^3$  pointing out that the primary contribution to the experimental anisotropy comes from the magneto crystalline energy.

In another work, El-Gendy et al. studied  $\text{CoFe}_2\text{C}$  nano-particles [145]. They synthesized  $\text{CoFe}_2\text{C}$  phase under supercritical ethanolic conditions using cobalt acetate, iron acetate, and fumaric acid as precursors. They reported large MAE value  $4.6 \text{ MJ/m}^3$ , high thermal stability and high blocking temperature with value about 790 K. This MAE value is comparable to the MAE of Nd-based 2-14-1 alloy. Such large increases in MAE in nanoscale systems is interesting, and opens a practical way of designing permanent magnets without RE elements.

## Doped Co clusters as RE free PM

With these startling and encouraging experimental findings, one requires fundamental understanding of the factors that are responsible for controlling the MAE values in these systems for designing new materials. Islam and Khanna addressed this issue in their work on  $\text{Co}_4\text{A}_2$  (A=C and Si) clusters [6]. They reported significant enhancement of MAE in these clusters and their assemblies compared to bulk Co. They further extended their works on bigger system of  $\text{Co}_{12}\text{C}_4$  clusters. They reported MAE values for  $\text{Co}_4\text{C}_2$  and  $\text{Co}_{12}\text{C}_4$  as 25 K (0.54 meV/Co atom) and 61 K (0.44 meV/Co atom) respectively. The MAE value for  $\text{Co}_4\text{C}_2$  was found almost nine times larger than the bulk hcp Co (65  $\mu\text{eV}/\text{atom}$ ). They mentioned the reduction of MAE/atom as the size of the cluster was increased is consistent with the fact that for very large clusters, the anisotropy should approach its value in the bulk system. They mentioned several factors as probable causes for enhancement in MAE. These are: (i) larger orbital moment compared to bulk, (ii) increase in the spin moment on the Co atoms, (iii) mixing between Co d and the p states of the A atoms. But no further analysis was done.

Given this state of affairs, to understand the effects of various factors controlling the MAE values of these those Co systems we have studied the properties  $\text{Co}_4\text{A}_2$  systems with (A=C, Si, Ge, N, P and As) using DFT. The details are given in chapter 4.

## 1.4 Polar oxide

The interest and the richness of the field of oxide surfaces lies in its interdisciplinary nature and in the diversity of questions it raises, on both fundamental and various novel applications. Research on oxide surfaces started more recently

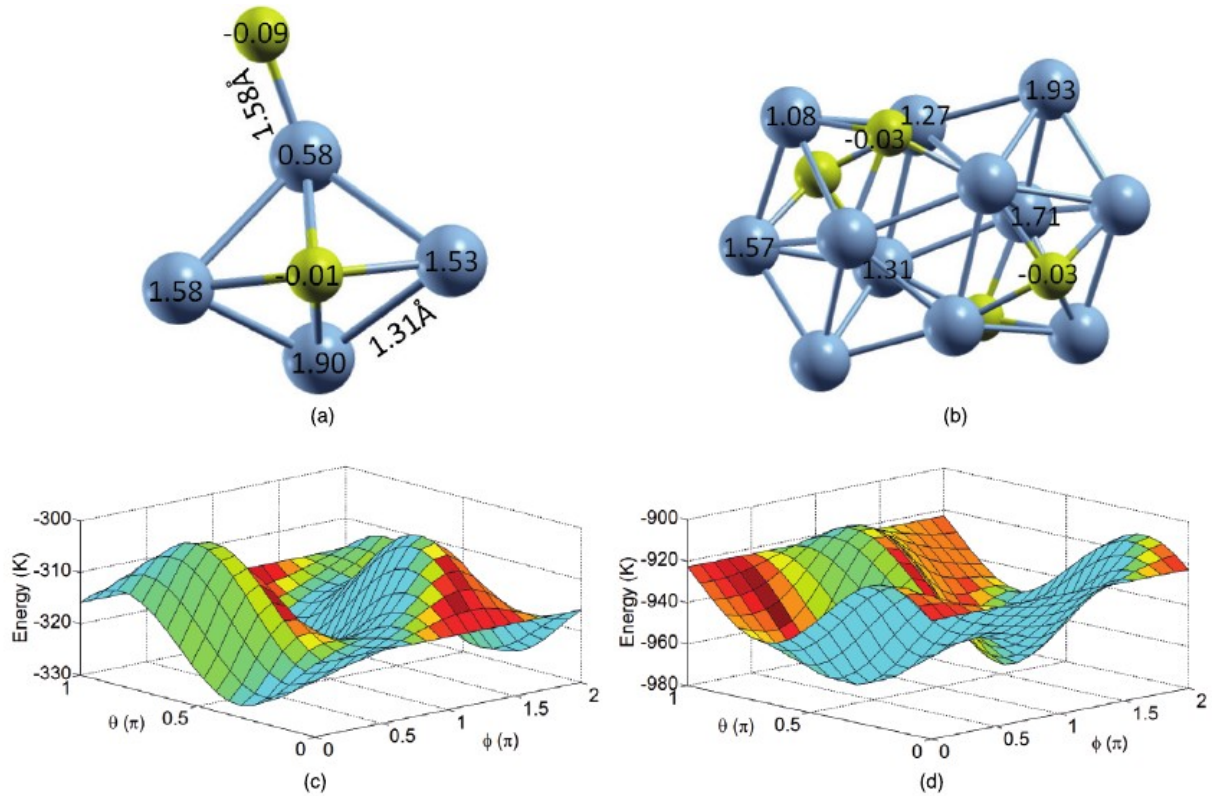


Figure 1.16: Relaxed clusters (a)  $\text{Co}_4\text{C}_2$  and (b)  $\text{Co}_{12}\text{C}_4$  with the z-axis perpendicular to the plane. The number near each atom represents the local moment of that atom in  $\mu_B$ . (c) and (d) are the anisotropy landscapes of  $\text{Co}_4\text{C}_2$  and  $\text{Co}_{12}\text{C}_4$  clusters respectively, with  $\theta$  and  $\phi$  as the polar and azimuthal angles respectively. Figure is adapted from [6].

compared with metal or semiconductor surfaces, because of difficulties in preparing well-controlled single crystal surfaces and implementing spectroscopic techniques which probe the local atomic and electronic structures. Oxides have variety of crystallographic structures e.g rocksalt, corundum, spinel, inverse spinel, wurtzite, perovskite - for the simplest ones that reflect the subtle mixing of ionicity and covalency in the metal-oxygen bonding and the specificities for the d electrons in transition metal oxides [146]. In case of forming mixed valence compounds like magnetite ( $\text{Fe}_3\text{O}_4$ ), metal atoms with several oxidation states are involved. Stabilization of oxide layers of different stoichiometries can be done by

tuning the experimental conditions like temperature, partial oxygen pressure, etc. Despite nearly two decennial of efforts, the exploration of such a rich behaviour is still fragmentary.

Polar oxide surfaces are one of the most important type of oxide surfaces. There are three major trends have been found in case of polar oxides. The first trend concerns the scaling of the structure size (particles size, device feature sizes, etc.) into the sub 100-nm regime. There has been a trend in recent years to strengthen the utilization of these effects and to synthesize oxide ceramics where the properties are dominated by size effects. A second trend is regarding the fact that advanced functional components are made of material systems rather than of discrete materials. Material integration issues play an important role which is driven by the interest in integrating functions of polar oxides in to conventional semiconductor chips as well as for the evolution of multifunctional components and systems. The third trend concerns the role of theory and modeling. The materials and device design is more and more accompanied and guided by modeling, like thermodynamics, finite-element methods, and ab-initio calculations.

There exists a macroscopic polarization along the surface normal in a polar oxide surface and the instability of surface has an electrostatic origin. The combined effect of orientation and termination is responsible for these polarization and surface instability. Like ferroelectric materials, a depolarization field is required to stabilize these surfaces. This can be achieved in various ways like by a deep modification of the surface electronic structure by total or partial filling of surface states. This leads to surface metallization sometimes. Another way is strong changes in the surface stoichiometry- spontaneous desorption of atoms, faceting, large cell reconstructions for the ordering of surface vacancies, adsorption of impurities, etc [147]. These processes can lead to original surface

configurations, where the local environment of the surface atoms is different from the bulk or from non-polar terminations. Here some electronic surface states may appear in the gap of the oxide. As a result, the cations and surface oxygens may present an enhanced acid or basic character respectively with important implications on reactivity [148]. The reconstructed surfaces which are formed due to the polar instability, can be used as nano-structured substrates for growing artificial structures with some specific conformations. They may drive specific growth modes like the formation of size-controlled clusters [149], when they involve large unit cells.

### 1.4.1 ZnO and BeO

ZnO and BeO are found in wurtzite and zinc blende phases. ZnO is a very popular polar oxide semiconductor with a direct band gap  $E_g=3.44$  eV [150]. It is not only used in window layers in photo voltaic devices, varistors for voltage-surge protection, UV absorbers, gas sensors, catalytic devices etc but it has various novel applications like transparent field effect transistors, UV laser diodes, memristors, in high-temperature high-field electronics also. From experimental works of Zu et al. [151] and Bagnall et al. [152] it was found clearly that ZnO thin films can be reached to the level of active semiconductor grade.

#### 2DEG at ZnO surface

Wurtzite ZnO surface has been extensively used in studies investigating 2 dimensional electron gas (2DEG) while interfaced with some other oxides. There are several important studies with ZnO/Zn(Mg)O hetero structure where 2DEGs have been investigated [153–162]. Two dimensional electron gas(2DEGs) has extensive applications to fabricate high electron mobility transistor (HEMT) type

field effect devices [163]. Two-dimensional electron systems (2DESs) in Transition Metal Oxides Interfaces (TMOs) have been studied extensively over the last decade. There are several experimental and theoretical works specially on SrTiO<sub>3</sub>/LaAlO<sub>3</sub> interfaces [164–172]. The hetero structures are usually grown using molecular beam epitaxy (MBE) [164, 165]. On the other hand a 2DEG was also demonstrated in samples grown with metal-organic vapor deposition which is suitable for mass production [159, 161, 162]. Study of Hall effect and capacitance measurements confirmed the presence of the 2DEG at these hetero structures [153, 156, 157]. Tsukazaki et al. observed Shubnikov de Haas oscillation and the quantum Hall effect in a high-mobility 2DEG in polar ZnO/Mg<sub>x</sub>Zn<sub>1-x</sub>O grown by laser MBE [154]. There the electron density could be controlled in a range of  $0.7 \times 10^{12}$  to  $3.7 \times 10^{12}$  per square centimeter by tuning the Mg content in the barriers. 2DEG has been conventionally created at semiconductor interfaces or surfaces utilizing various methods. Typical examples are electrostatic gating using a field effect transistor structure as in SiO<sub>2</sub>/Si [173] or modulation doping as in AlGaAs/GaAs [174]. But the formation mechanism of 2DEG in Mg<sub>x</sub>Zn<sub>1-x</sub>O/ZnO is not similar to these hetero structures, without external field or impurity doping 2DEG is naturally present when the interface is formed. Uncompensated charges also remain at the interface due to the difference in polarization between Mg<sub>x</sub>Zn<sub>1-x</sub>O and ZnO, leading to a large internal electric field. By introducing additional charge carriers at the interface, such disorder can be suppressed for improving growth technique [175]. Ye et al.[161] and Han et al. [160] reported spin-polarized 2DEG at ZnO/Zn(Mg)O interfaces. Betancourt et al.studied the formation and properties of the 2DEG at ZnO/Zn(Mg)O interfaces using first-principles calculations based on hybrid density functional theory [176]. The 2DEG arises from the polarization discontinuity at the interface between the

two materials. An electric field generated in bulk wurtzite ZnO due to uncompensated bound charges which are at the interfaces. This electric field confines free carriers close to the interface. The type of the confined carriers is determined by the interface termination. And the charge density can be tuned by the amount of Mg doping.

Ding et al. reported high-density 2DEG at Zn-polar BeMgZnO/ZnO hetero structures interface using MBE [177]. High 2DEG concentration in MgZnO/ZnO hetero structures requires growth of the MgZnO barrier at relatively low temperatures. But it affects the ternary quality that in turn decreases potential field effect transistor performance. When it alloyed with BeO the sign of strain in the BeMgZnO barrier on ZnO switches from compressive to tensile. Piezoelectric and spontaneous polarization becomes additive in the BeMgZnO/ZnO hetero structures. As a result, a 2DEG concentration of  $1.2 \times 10^{13}$  per centimeter square is achieved in the  $\text{Be}_{0.03}\text{Mg}_{0.41}\text{Zn}_{0.56}\text{O}/\text{ZnO}$  hetero structure. Rodel et al. studied the 2DEG in ZnO by depositing pure aluminum on its surface in ultrahigh vacuum and characterize its electronic structure by using angle-resolved photo emission spectroscopy [178]. As Al oxidizes into alumina, oxygen vacancies created which dope the bulk conduction band of ZnO and confine the electrons near its surface. They reported electron density of the 2DEG is up to two orders of magnitude higher than those obtained in ZnO hetero structures.

### **2DEG at BeO surface**

Wurtzite BeO has the same crystal structure like ZnO. In the most recent experiment Wang et al. investigated the BeO layer with macroscopic polarization on top of the AlGa<sub>N</sub> barrier layer increases the 2DEG density in the triangular quantum well (QW) at the interface of the AlGa<sub>N</sub>/Ga<sub>N</sub> hetero structure [179]. From

electronic band bending of BeO and a deeper triangular QW, which was observed from the simulated conduction band profile, one can understand BeO layer can modify the polarization field at the AlGa<sub>N</sub>/Ga<sub>N</sub> interface. Good quality HEMT can be found by increasing sheet carrier concentration 14% with respect to the conventional HEMT.

The origin of such 2DEG lies in the polar discontinuity between the polar and non polar interface. Here we have explored whether 2DEG can be found naturally at the surface of wurtzite BeO and ZnO. The details are given in chapter 5. In wurtzite materials there are two kinds of bonds between two elements, one is parallel to C axis, other one is slanted. These studies of polar surface has been performed on shuffle surface, ie, parallel bond to C axis has been cut. In case of wurtzite BeO there are some studies with shuffle surface using DFT. The shuffle surface becomes a 2-d layered structure of Be-O like honey comb lattice. Chen et al. studied electrical and optical properties of Ge/BeO 2d hetero structure using Density Functional Theory with Dispersion (DFT-D) [180]. Wu et al. studied electronic and magnetic properties of BeO nanoribbons (BeO NRs) and their stability in through extensive density functional theory calculations [181].

## 1.5 Structure of the thesis

In summary my thesis consists of two separate system. One is atomic cluster system and the another one is polar oxide surface. In both cases I have studied the electronic and magnetic properties within the frame work of DFT. Motivated by the interesting ideas and enormous applications of atomic clusters and the polar oxide surfaces, I have performed these works which are mentioned in details in several chapters in following manner. **Chapter 2** is devoted to the methods

and techniques used to perform the calculations in this thesis. Techniques for solving the Kohn-Sham DFT using plane-wave basis sets, and construction of PAW potentials are discussed. The next sections contain an overview of *ab-initio* molecular dynamics simulations and climbing image nudged elastic band methods. The methods that incorporate the dispersion interactions within the DFT framework are also discussed. The evolutionary algorithm, Bader charges have also been discussed. I have briefly discussed the theory of magneto crystalline anisotropy energy in the framework of DFT and density functional perturbation theory (DFPT) in this chapter.

**Chapter 3** presents our studies of globally optimized TaSi<sub>16</sub> clusters over HOPG using the vdW-DF2 method. A summary of the experimental results is presented as motivation. We find that the cage structure remains stable on deposition on HOPG. The cluster is physisorbed and was almost not reactive with exposure to oxygen. Ab-initio molecular dynamics simulations at 400 K and 700 K show that at these temperatures, the structure is distorted but the cage is maintained.

**Chapter 4** discusses the factors controlling the MAE of small Co clusters doped with group 14 and group 15 elements (C, Si, Ge, N, P, As). The MAE (defined as the energy difference between the easy and hard direction of spin in presence of spin orbit coupling) has been calculated for Co<sub>4</sub>A<sub>2</sub> clusters. No trend of MAE with dopant atom was found. MAE values of the clusters was visualized as a function of four quantities (i) HOMO-LUMO gap, (ii) spin moment, (iii) mixing parameter (mixing of Co d and dopant p orbital) and (iv) difference of orbital angular momentum values between easy and hard direction. In summary we have found low HOMO-LUMO gap and high spin moment are mainly

responsible for higher values of MAE irrespective of the doping elements. Large difference of orbital angular momentum values played some role in determining higher MAE values, whereas the mixing parameter does not have any significant contribution in MAE.

**Chapter 5** discusses the electronic structures of wurtzite BeO and ZnO glide surfaces. In both cases the bulk insulator to surface metal transition has been studied by electronic structure calculations by gradually increasing the vacuum level above the top atomic layer. As we increase the distance between the slab and its periodic image along the  $c$  axis keeping the atomic arrangements bulk-like, the band gap decreases gradually with the lowest energy conduction band coming towards the Fermi level, and at some critical vacuum level it becomes metallic. We have found emergence of 2DEG at the glide surfaces in both oxides. Apart from this surface metallicity we have found magnetization there, where the bulk materials are non-magnetic. The peaks near the Fermi level in the electronic densities of states lead to stoner instability. The metallic character in the glide surfaces have been found due to polar catastrophe. It was clearly found from the planar average potential plot, that the potential energy of electron in the vacuum was not constant. The electrons felt a force along  $c$  axis and as a result they come from the slab into the vacuum, and a 2DEG formed.

**Chapter 6** discusses about the study regarding the stability of the glide surfaces of BeO and ZnO. Using DFPT we have performed the phonon dispersion calculation. The dynamical instability were confirmed from imaginary frequencies in both cases. Displacing the atoms along the soft phonon modes leads to reconstruction of the surface with lower energy. However, the metallicity is maintained demonstrating that it is a robust feature of these surfaces.

# CHAPTER 2

## Theoretical Methods

### 2.1 Introduction

Materials consist of atoms and molecules, which basically include positively charged nuclei and negatively charged electrons. Electrons are very light weight particles so they have to be treated by quantum mechanics, where for nuclei classical mechanics can be applied as they are comparatively massive than electrons. The electronic, magnetic and chemical properties of materials can be explained by the behavior of electrons. In the early 19<sup>th</sup> century, Drude (1900) and Lorentz (1909) tried to understand the conduction of electrons in metals assuming that metals contain free electrons that move in a uniform positive background generated by the ions. They explained the electrical conductivity in metals but unfortunately, other properties of the metallic systems could not be explained by their theory. In 1920, after the development of quantum mechanics, significant progress has been found in understanding the properties of materials. Materials have been classified into metals, semiconductors and insulators after formation of band theory of independent electrons in 1930. To describe electron-electron interaction a numbers of

theoretical methods have been proposed such as Hartree-Fock method [182–184], Møller-Plesset perturbation theory, [185], coupled cluster theory [186] later.

In 1960s, after density functional theory (DFT) was formulated, significant rapid progress in electronic structure calculations were made. DFT is a quantum mechanical method which is used in physics and chemistry to investigate the electronic structure of many-body systems, particularly atoms, molecules and solids. An analytical solution of the many-electron Schrödinger equation is not available. In practice the numerical solution is effectively impossible for large number of electrons due to the finite speed and memory of computers. DFT is used as a mean of circumventing solution of the many-electron Schrödinger equation. In DFT the properties of a many-electron system can be determined by using as functionals of the electronic density. Usually it is known as first principle method as without any adjustable parameter, it allows to determine many properties of a condensed matter system . For real materials and to design new materials it has become a very useful tool for understanding the characteristic properties of materials. It is also very useful for making specific predictions of various experimentally observable phenomena.

## 2.2 The many body problem and Born-Oppenheimer Approximation

The ultimate goal of most approaches in solid state physics and quantum Chemistry is the solution of the time-independent, non-relativistic Schrödinger equation.

$$\hat{H}\Psi_i(\mathbf{r}_1, \mathbf{r}_2, \dots, \mathbf{r}_N, \mathbf{R}_1, \mathbf{R}_2, \dots, \mathbf{R}_M) = E_i\Psi_i(\mathbf{r}_1, \mathbf{r}_2, \dots, \mathbf{r}_N, \mathbf{R}_1, \mathbf{R}_2, \dots, \mathbf{R}_M) \quad (2.1)$$

The description of a system with a set of atomic nuclei and electrons interacting via Coulombic electrostatic forces can be given in terms of  $N$ -body interacting Hamiltonian<sup>1</sup> as:

$$\begin{aligned} \hat{H} = & - \sum_{A=1}^M \frac{1}{2M_A} \nabla_A^2 - \sum_{i=1}^N \frac{1}{2} \nabla_i^2 + \frac{1}{2} \sum_{A=1}^M \sum_{B \neq A}^M \frac{Z_A Z_B}{|\mathbf{R}_A - \mathbf{R}_B|} \\ & + \frac{1}{2} \sum_{i=1}^N \sum_{j \neq i}^N \frac{1}{|\mathbf{r}_i - \mathbf{r}_j|} - \sum_{A=1}^M \sum_{i=1}^N \frac{Z_A}{|\mathbf{R}_A - \mathbf{r}_i|} \end{aligned} \quad (2.1)$$

Here  $\mathbf{R} = \{\mathbf{R}_A, I = 1, \dots, M\}$  is a set of  $M$  nuclear coordinates, and  $\mathbf{r} = \{\mathbf{r}_i, i = 1, \dots, N\}$  is a set of  $N$  electronic coordinates.  $Z_A$  and  $M_A$  are the nuclear charges and masses, respectively. The first and second terms represent the kinetic energy contributions ( $T_n$  and  $T_e$ ) of the nuclei and electrons respectively. The third and fourth terms represent the repulsive interactions ( $V_{nn}$  and  $V_{ee}$ ) of the nuclei and electrons respectively. The attractive potential ( $V_{ne}$ ) between the nuclei and electrons is presented by the last term.

As the exact solution of 2.1 is not found, due to the presence of nucleus-nucleus and electron-electron interactions, we have to make approximations to progress. The first important approximation is the so-called Born-Oppenheimer approximation [187]. The main assumption is in many-body systems, electronic and the nuclear motion can be separated. This idea arises from the fact that nuclei are around  $10^3$  times heavier than the electrons and move much slower than the electrons. So we can consider the electrons are moving in the field of fixed nuclei. Hence we can assume the nuclear kinetic energy is zero and their potential energy is almost a constant. In this approximation, electrons can be considered in their ground state with respect to the momentary positions of the

---

<sup>1</sup>In atomic units:  $\hbar = m_e = e = 1/4\pi\epsilon_0 = 1$

nuclei at all the times. Thus the full Hamiltonian ( $\hat{H}$ ) in Eq. (2.1) can be split into two parts: a nuclear subsystem ( $\hat{H}_n$ ) and an electronic subsystem ( $\hat{H}_e$ ). These are explicitly shown as

$$\hat{H}_n = \hat{T}_n + \hat{V}_{nn} \quad (2.2)$$

$$\hat{H}_e = \hat{T}_e + \hat{V}_{ne} + \hat{V}_{ee}. \quad (2.3)$$

The many body wave function  $\Psi(\mathbf{r}, \mathbf{R})$  can be written as

$$\Psi(\mathbf{r}, \mathbf{R}) = \sum_n \Theta_n(\mathbf{R}) \Phi_n(\{\mathbf{R}\}, \mathbf{r}), \quad (2.4)$$

where  $\Theta_n(\mathbf{R})$  are the nuclear wave functions and  $\Phi_n(\{\mathbf{R}\}, \mathbf{r})$  are the electronic wave functions which is parametrically dependent on the positions of the nuclei. So the total energy of the system is equal to the sum of the nuclear energy ( $E_N$ ) and electronic energy ( $E$ ),  $E_{tot} = E_N + E$ . For a fixed nuclear configuration, the electronic energy can be determined by solving the electronic Schrödinger equation,

$$\hat{H}_e \Phi(\mathbf{R}, \mathbf{r}) = E \Phi(\{\mathbf{R}\}, \mathbf{r}). \quad (2.5)$$

It is still impossible to get exact solution of Eq. (2.5) for the electron-electron interactions, and further approximations are required. Hartree-Fock approximation is one of the fundamental approaches for solving the electronic Schrödinger equation (Eq. (2.5)). In Hartree-Fock approximation, the many-electron problem is reduced into an effective one electron problem. It is a mean-field theory where an electron moves in an average field which is generated by the other electrons. The  $N$ -electron wave function  $\Phi(\{\mathbf{R}\}, \mathbf{r})$  is approximated by a single Slater-

determinant of single particle wave functions here. This ensures the antisymmetry of the many-body wave function upon particle exchange, and hence the exchange effect in an exact manner is included. But Coulomb correlations is not included here.

In order to improve upon the Hartree-Fock approximation, other methods have been proposed that include correlation effects. These incorporate the second or fourth order perturbation theory by Møller and Plesset (MP2 or MP4) [185], configuration interaction (CI), multiconfiguration self-consistent field (MCSCF), and coupled cluster approaches (CC) [187, 188]. These are quite accurate methods, but are very expensive computationally. DFT is a good alternative to these wave function based methods. It replaces the complicated  $N$ -electron wave function and the associated Schrödinger equation by a formulation which is entirely based on the electron density  $\rho(\mathbf{r})$  only.

## 2.3 The Density functional theory

### 2.3.1 The Hohenberg-Kohn (HK) theorems

Hohenberg and Kohn [189] formulated an exact formal variational principle to determine the ground state energy of a many-electron system in 1964. The electron density is chosen to be the basic variable in their theory. They gave two theorems to build the foundation of DFT.

**Theorem I:** *The external potential  $v(\mathbf{r})$  is uniquely determined by the ground state electron density  $\rho(\mathbf{r})$  within a trivial additive constant.* Thus the full Hamiltonian of the form 2.1 is determined by the ground state density, except for a constant shift of the energy. So all properties of the many-electron system such as its total energy, kinetic energy, and potential energy are also functionals of the

ground state electron density  $\rho(\mathbf{r})$ .

**Theorem II:** For a trial density  $\tilde{\rho}(\mathbf{r})$ , such that  $\tilde{\rho}(\mathbf{r}) \geq 0$  and  $\int \tilde{\rho}(\mathbf{r}) d\mathbf{r} = N$ , the total energy functional  $E[\tilde{\rho}]$  has a lower bound equal to the ground state energy  $E[\rho(\mathbf{r})]$  of the system:

$$E[\rho(\mathbf{r})] \leq E[\tilde{\rho}(\mathbf{r})], \quad (2.6)$$

where  $\rho(\mathbf{r})$  is the ground state electron density of the system.

From the first theorem, at a certain external potential  $v(\mathbf{r})$  the total energy functional for an electronic system can be written as,

$$E_v[\rho] = T_e[\rho] + V_{ne}[\rho] + V_{ee}[\rho] = F_{HK}[\rho] + \int \rho(\mathbf{r})v(\mathbf{r})d\mathbf{r}, \quad (2.7)$$

where

$$F_{HK}[\rho] = T_e[\rho] + V_{ee}[\rho], \quad (2.8)$$

$F_{HK}$  is known as the Hohenberg-Kohn functional which is a universal functional of  $\rho(\mathbf{r})$  because of its independence on the external potential. this includes kinetic energy of the electrons  $T_e[\rho]$  and the interaction energy between the electrons  $V_{ee}[\rho]$ .

A variational principle for  $E_v[\rho(\mathbf{r})]$  with  $\rho(\mathbf{r})$  as the basic variable is provided by the second KS theorem. The ground state density  $\rho(\mathbf{r})$  is given by the minimization of the total energy functional  $E_v[\tilde{\rho}(\mathbf{r})]$  with respect to trial density  $\tilde{\rho}(\mathbf{r})$ . From  $\rho(\mathbf{r})$  the ground state energy  $E[\rho(\mathbf{r})]$  of the system is determined. Thus ground state density  $\rho(\mathbf{r})$  which minimizes  $E[\rho(\mathbf{r})]$  can be found via the

stationary principle

$$\delta\{E_v[\rho] - \mu[\int \rho(\mathbf{r})d\mathbf{r} - N]\} = 0, \quad (2.9)$$

where  $\mu$  is the Lagrange multiplier for the constraint  $\int \rho(\mathbf{r})d\mathbf{r} = N$ . Eq. (2.9) gives the Euler-Lagrange equation,

$$\mu = \frac{\delta E_v[\rho]}{\delta \rho(\mathbf{r})} = v(\mathbf{r}) + \frac{\delta F_{HK}[\rho]}{\delta \rho(\mathbf{r})}, \quad (2.10)$$

where  $\mu$  represents the chemical potential of the  $N$ -electron system.

### 2.3.2 The Kohn-Sham (KS) equations

In principle, if the exact functional  $F_{HK}$  is known, an exact solution for the ground-state energy would be given by Eq. (2.10). Unfortunately, the exact form of  $F_{HK}$  is unknown. This leaves the Hohenberg-Kohn theorems without much of practical relevance. An ansatz was given by Kohn and Sham [190] In 1965. This states that the exact ground state density of an interacting system can be identified with the ground state density of a reference system of noninteracting electrons. Thus the problem of the system of interacting electrons is mapped onto a reference system of non-interacting electrons with introducing a set of single particle equations, popularly known as Kohn-Sham equations. The ground state density  $\rho(\mathbf{r})$  of a non-interacting system can be written as

$$\rho(\mathbf{r}) = \sum_{i=1}^N |\psi_i(\mathbf{r})|^2, \quad (2.11)$$

where  $\psi_i(\mathbf{r})$  present one-electron orbitals known as Kohn-Sham orbitals. The Hamiltonian for non-interacting reference system with the same ground state

density  $\rho(\mathbf{r})$  can be written as

$$\hat{H}_R = \sum_{i=1}^N \left[ -\frac{1}{2} \nabla_i^2 + v_{eff}(\mathbf{r}_i) \right]. \quad (2.12)$$

Here the effective potential  $v_{eff}(\mathbf{r})$  is such that the ground state density of  $\hat{H}_R$  is same as  $\rho(\mathbf{r})$ . As  $\hat{H}_R$  is non-interacting, the ground state wave function  $\Psi_s(\mathbf{r})$  is a Slater determinant of the  $N$  lowest-energy eigenfunctions.

The kinetic energy  $T_s[\rho]$  of the reference system can be written as

$$T_s[\rho] = \langle \Psi_s | -\frac{1}{2} \sum_{i=1}^N \nabla_i^2 | \Psi_s \rangle = -\frac{1}{2} \sum_{i=1}^N \langle \psi_i | \nabla^2 | \psi_i \rangle. \quad (2.13)$$

By solving the one-electron Schrödinger equation, one can obtain the one-electron orbitals  $\psi_i(\mathbf{r})$

$$\left[ -\frac{1}{2} \nabla^2 + v_{eff}(\mathbf{r}) \right] \psi_i(\mathbf{r}) = \hat{H}_{KS} \psi_i(\mathbf{r}) = \epsilon_i \psi_i(\mathbf{r}), \quad (2.14)$$

where  $\hat{H}_{KS}$  represents the one-electron Hamiltonian and the Kohn-Sham orbital energies are represented by  $\epsilon_i$ . Thus there is a transformation of interacting system to a noninteracting system, in which electrons move in an effective potential  $v_{eff}(\mathbf{r})$ . The universal functional  $F_{HK}$  can be written using Eq. (2.13) and Eq. (2.8) as,

$$F_{HK}[\rho] = T_s[\rho] + J[\rho] + E_{xc}[\rho], \quad (2.15)$$

where  $J[\rho]$  is classical Coulomb energy term and it is defined as,

$$J[\rho] = \frac{1}{2} \iint \frac{\rho(\mathbf{r})\rho(\mathbf{r}')}{|\mathbf{r} - \mathbf{r}'|} d\mathbf{r} d\mathbf{r}'. \quad (2.16)$$

$E_{xc}[\rho]$  is exchange-correlation energy with the definition given as,

$$E_{xc}[\rho] = (T_e[\rho] - T_s[\rho]) + (V_{ee}[\rho] - J[\rho]). \quad (2.17)$$

The kinetic correlations which are ignored in  $T_s[\rho]$ , are included in the exchange-correlation energy. The exchange-correlation energy also contains the non-classical part of the electron-electron interaction energy. By substituting Eq. (2.15) in the total energy functional (Eq. (2.7)), the Kohn-Sham energy functional is obtained as

$$E_{KS}[\rho] = \int \rho(\mathbf{r})v(\mathbf{r})d\mathbf{r} + T_s[\rho] + J[\rho] + E_{xc}[\rho]. \quad (2.18)$$

Now minimizing the Kohn-Sham energy functional  $E_{KS}[\rho]$  with respect to density  $\rho(\mathbf{r})$ , under the constraint  $\int \rho(\mathbf{r})d\mathbf{r} = N$ , we get the Euler-Lagrange equation as

$$\mu = v(\mathbf{r}) + \frac{\delta T_s[\rho]}{\delta \rho(\mathbf{r})} + \frac{\delta J[\rho]}{\delta \rho(\mathbf{r})} + \frac{\delta E_{xc}[\rho]}{\delta \rho(\mathbf{r})}. \quad (2.19)$$

$\mu$  is the chemical potential of the reference system. This should coincide with the chemical potential of the interacting system. Using equations (2.10) and (2.19), one can define the KS effective potential as

$$\begin{aligned} v_{eff}(\mathbf{r}) &= v(\mathbf{r}) + \frac{\delta J[\rho]}{\delta \rho(\mathbf{r})} + \frac{\delta E_{xc}[\rho]}{\delta \rho(\mathbf{r})}, \\ &= v(\mathbf{r}) + \int \frac{\rho(\mathbf{r}')}{|\mathbf{r} - \mathbf{r}'|} d\mathbf{r}' + v_{xc}(\mathbf{r}), \end{aligned} \quad (2.20)$$

where the exchange-correlation potential  $v_{xc}(\mathbf{r})$  is defined as

$$v_{xc}(\mathbf{r}) = \frac{\delta E_{xc}[\rho]}{\delta \rho(\mathbf{r})}. \quad (2.21)$$

Electrons move in an effective potential  $v_{eff}(\mathbf{r})$ , which depends on the classical Coulomb potential, exchange-correlation potential, and the external potential  $V_{ext}(\mathbf{r})$  in the Kohn-Sham formalism. The total energy of the system can be written as

$$E[\rho] = \sum_{i=1}^N \epsilon_i - \frac{1}{2} \int \frac{\rho(\mathbf{r})\rho(\mathbf{r}')}{|\mathbf{r} - \mathbf{r}'|} d\mathbf{r}d\mathbf{r}' + E_{xc}[\rho] - \int \rho(\mathbf{r})v_{xc}(\mathbf{r})d\mathbf{r} \quad (2.22)$$

As  $v_{eff}(\mathbf{r})$  depends on the density  $\rho(\mathbf{r})$  through the classical Coulomb potential and exchange-correlation potential  $v_{xc}(\mathbf{r})$ , which in turn depend on the  $\psi_i(\mathbf{r})$ , only self-consistently the solution of Eq. (2.14) and Eq. (2.11) can be obtained. For a given nuclear configuration, we start with some trial charge density and calculate  $v_{eff}(\mathbf{r})$  in order to solve these equations. The Kohn-Sham equations are solved then to get  $\psi_i$ 's, and the new charge density  $\rho(\mathbf{r})$  is obtained. until the old and new charge densities become same or the change in energies obtained in two consecutive iterations is below a predefined tolerance the same process is repeated iteratively. Thus the

The Kohn-Sham solutions would lead to the exact ground state energy, if the exact forms of  $E_{xc}[\rho]$  were known. Thus in principle, the Kohn-Sham approach is exact. When we have to decide on an explicit form for the functional which is unknown for the exchange-correlation energy ( $E_{xc}$ ), the approximation only enters then. Therefore to find better and better approximations to the exchange-correlation energy is the central goal of modern density-functional theory.

### 2.3.3 The exchange-correlation functional

The local density approximation (LDA) [190], the simplest approximation for  $E_{xc}$  was introduced by Kohn and Sham. The main idea of this approximation is to construct the exchange-correlation energy for an electronic system having an inhomogeneous density to be composed of locally homogeneous regions. The expression of the exchange-correlation energy given as

$$E_{xc}^{LDA}[\rho] = \int \rho(\mathbf{r})\varepsilon_{xc}(\rho(\mathbf{r}))d\mathbf{r}, \quad (2.23)$$

where  $\varepsilon_{xc}(\rho(\mathbf{r}))$  is the exchange-correlation energy per particle of a homogeneous electron gas with density  $\rho(\mathbf{r})$ . The corresponding exchange-correlation potential is,

$$v_{xc}^{LDA}(\rho(\mathbf{r})) = \frac{\delta E_{xc}^{LDA}[\rho]}{\delta \rho(\mathbf{r})} = \varepsilon_{xc}[\rho(\mathbf{r})] + \rho(\mathbf{r})\frac{\partial \varepsilon_{xc}^{LDA}[\rho]}{\partial \rho}. \quad (2.24)$$

Again,  $\varepsilon_{xc}(\rho(\mathbf{r}))$  can be separated into exchange and correlation contributions

$$\varepsilon_{xc}(\rho) = \varepsilon_x(\rho) + \varepsilon_c(\rho). \quad (2.25)$$

By the Hartree-Fock approximation for a homogeneous electron gas, the exchange part can be calculated as given in Ashcroft and Mermin [191].

$$\varepsilon_x(\rho) = -\frac{3}{4}\left(\frac{3}{\pi}\right)^{1/3}\rho(\mathbf{r})^{1/3}. \quad (2.26)$$

There is no such an explicit functional form to express the correlation part  $\varepsilon_c(\rho)$ . From the highly accurate quantum Monte Carlo calculations of Ceperly and Alder [192], numerical values are known only. This has been fitted to analyt-

ical forms by Vosko, Wilk and Nusair [193] and Perdew and Zunger [194]. In most of the current electronic structure calculations these are used

One can write the extension of LDA for spin-polarized systems with charge densities  $\rho_{\uparrow}(\mathbf{r})$  and  $\rho_{\downarrow}(\mathbf{r})$ , (for up and down spin electrons respectively)

$$E_{xc}^{LSDA} = -\frac{3}{2} \left( \frac{3}{4\pi} \right)^{1/3} \int [\rho_{\uparrow}(\mathbf{r})^{4/3} + \rho_{\downarrow}(\mathbf{r})^{4/3}] d\mathbf{r} + \int \rho(\mathbf{r}) \varepsilon_c(\rho_{\uparrow}(\mathbf{r}), \rho_{\downarrow}(\mathbf{r})) d\mathbf{r}. \quad (2.27)$$

This is mentioned as local spin density approximation (LSDA). Here  $\varepsilon_c(\rho_{\uparrow}(\mathbf{r}), \rho_{\downarrow}(\mathbf{r}))$  is the correlation energy per electron in a homogeneous electron gas.

It seems from the above discussion, that LDA should be a good approximation for the slowly varying electron density  $\rho(\mathbf{r})$ . It produces good geometries for covalent, ionic, or metallic systems. But the band gaps in semiconductors and insulators are underestimated by LDA. In case of strongly correlated systems, specially for Mott insulators it can't reproduce the properties also. For improvement of LDA intense efforts have been devoted. One of the straightforward correction to the LDA is, construction of an exchange-correlation functional based on electron density as well as its gradient. This approximation is well-known as generalized gradient approximation (GGA) [195, 196].

$$E_{xc}^{GGA}[\rho_{\uparrow}, \rho_{\downarrow}] = \int d\mathbf{r} \rho(\mathbf{r}) \varepsilon_{xc}(\rho(\mathbf{r})) F_{xc}(\rho_{\uparrow}, \rho_{\downarrow}, |\nabla \rho_{\uparrow}|, |\nabla \rho_{\downarrow}|, \dots), \quad (2.28)$$

where  $F_{xc}$  is dimensionless and is chosen by a predefined set of criteria. Depending on the form of the function  $F_{xc}$  a large number of distinct GGA functionals are found. The Perdew-Burke-Ernzerhof functional (PBE) [197] and the Perdew-Wang functional (PW91) [198] are two most widely used functionals in

the literature.

## 2.4 The Plane wave basis set

In practice, the KS orbitals are expanded in terms of some basis functions. For periodic systems, the most common approach to solve the KS equations is to expand in plane wave basis sets. The plane wave expansion of the KS orbitals can be written as follows [199].

$$\psi_i(\mathbf{r}) = \frac{1}{\sqrt{\Omega}} \sum_{\mathbf{q}} c_{i,\mathbf{q}} e^{i(\mathbf{q}\cdot\mathbf{r})}, \quad (2.29)$$

where  $\Omega$  is the volume of the crystal composed of  $N_{cell}$  primitive cells each of volume  $\Omega_{cell}$ . The  $c_{i,\mathbf{q}}$  are the expansion coefficients of the wave function in the basis of orthonormal plane wave, denoted by  $\phi_{\mathbf{q}}(\mathbf{r})$ , where  $\phi_{\mathbf{q}}(\mathbf{r}) = \langle \mathbf{r} | \mathbf{q} \rangle$  satisfy  $\langle \mathbf{q}' | \mathbf{q} \rangle = \delta_{\mathbf{q},\mathbf{q}'}$ . As plane waves are orthonormal, on expansion of the KS equations upon this basis set transformed into a simple matrix eigenvalue problem. Another advantage of plane waves is as they are not biased to a particular atom, all region in the space are treated on an equal footing and the calculations do not involve errors coming from a basis set superposition issue. The Hellman-Feynman theorem can be applied directly to calculate atomic forces as plane wave basis is independent of atomic position.

Now inserting the plane wave expansion of  $\psi_i(\mathbf{r})$  in Eq. (2.14), and taking inner product with  $|\mathbf{q}'\rangle$ ,

$$\sum_{\mathbf{q}} \langle \mathbf{q}' | \hat{H}_{eff} | \mathbf{q} \rangle c_{i,\mathbf{q}} = \epsilon_i \sum_{\mathbf{q}} \langle \mathbf{q}' | \mathbf{q} \rangle c_{i,\mathbf{q}} = \epsilon_i c_{i,\mathbf{q}'}. \quad (2.30)$$

The matrix element of the kinetic energy operator can be written as

$$\langle \mathbf{q}' | -\frac{1}{2}\nabla^2 | \mathbf{q} \rangle = \frac{1}{2}|\mathbf{q}|^2\delta_{\mathbf{q},\mathbf{q}'}. \quad (2.31)$$

As the effective potential  $v_{eff}$  has the periodicity of the lattice, so it can be expressed as a sum of the Fourier components.

$$v_{eff}(\mathbf{r}) = \sum_m v_{eff}(\mathbf{G}_m)exp(i\mathbf{G}_m \cdot \mathbf{r}), \quad (2.32)$$

where  $\mathbf{G}_m$  are the reciprocal lattice vectors and  $V_{eff}(\mathbf{G}_m)$  represent the Fourier components of  $v_{eff}(\mathbf{r})$ .

$$v_{eff}(\mathbf{G}) = \frac{1}{\Omega_{cell}} \int_{\Omega_{cell}} V_{eff}(\mathbf{r})exp(-i\mathbf{G} \cdot \mathbf{r})d\mathbf{r}. \quad (2.33)$$

Thus the matrix element of  $v_{eff}$  can be written as

$$\langle \mathbf{q}' | v_{eff} | \mathbf{q} \rangle = \sum_m v_{eff}(\mathbf{G}_m)\delta_{\mathbf{q}'-\mathbf{q},\mathbf{G}_m}. \quad (2.34)$$

The nonzero matrix elements of the  $v_{eff}$  are only found when  $\mathbf{q}$  and  $\mathbf{q}'$  differ by a reciprocal lattice vector  $\mathbf{G}_m$ . Assuming  $\mathbf{q} = \mathbf{k} + \mathbf{G}_m$  and  $\mathbf{q}' = \mathbf{k} + \mathbf{G}_{m'}$  for any given  $\mathbf{k}$ , the Schrödinger-like equation is given by

$$\sum_m \langle \mathbf{k} + \mathbf{G}_{m'} | \hat{H}_{eff} | \mathbf{k} + \mathbf{G}_m \rangle c_{i,m}(\mathbf{k}) = \epsilon_i c_{i,m'}(\mathbf{k}), \quad (2.35)$$

$$\sum_m \left[ |\mathbf{k} + \mathbf{G}_m|^2 \delta_{m,m'} + v_{eff}(\mathbf{G}_m - \mathbf{G}_{m'}) \right] c_{i,m}(\mathbf{k}) = \epsilon_i(\mathbf{k}) c_{i,m'}(\mathbf{k}). \quad (2.36)$$

The equation 2.36 is the basic Schrödinger-like equation for a periodic crystal

expanded with a plane wave basis set. For a given  $\mathbf{k}$ , eigenfunctions of the Eq. (2.35) are given by Eq. (2.29), with the sum over  $\mathbf{q}$  restricted to  $\mathbf{q} = \mathbf{k} + \mathbf{G}_m$ .

Hence

$$\begin{aligned}\psi_{i,\mathbf{k}}(\mathbf{r}) &= \frac{1}{\sqrt{\Omega}} \sum_m c_{i,m} \exp(i(\mathbf{k} + \mathbf{G}_m) \cdot \mathbf{r}), \\ &= \exp(i\mathbf{k} \cdot \mathbf{r}) \frac{1}{\sqrt{N_{cell}}} u_{i,\mathbf{k}}(\mathbf{r}),\end{aligned}\tag{2.37}$$

where

$$u_{i,\mathbf{k}}(\mathbf{r}) = \frac{1}{\sqrt{\Omega_{cell}}} \sum_m c_{i,m} \exp(i\mathbf{G}_m \cdot \mathbf{r}); \quad \Omega = N_{cell}\Omega_{cell}.$$

This is the well known Bloch's theorem. The periodicity of the crystal is carried by  $u_{i,\mathbf{k}}(\mathbf{r})$  here. For each  $\mathbf{k}$ , the allowed reciprocal vectors  $\mathbf{G}$  are infinite. Hence, in principle infinite number of plane waves are required to represent the wave functions with infinite accuracy. However, for the plane waves the coefficient  $c_{i,m}(\mathbf{k})$  with small kinetic energy are typically given more importance than those with large kinetic energy. Hence the plane wave basis set can be truncated with including only plane waves with kinetic energies less than a predefined energy cutoff  $E_{cut}$ ,

$$\frac{1}{2}|\mathbf{k} + \mathbf{G}|^2 \leq E_{cut}.\tag{2.38}$$

Some inaccuracies may be introduced by employment a finite basis set. So appropriate convergence tests have to be performed in order to find out  $E_{cut}$  value which is sufficiently large for computing the property of interest with required accuracy.

## 2.5 The pseudopotential theory

The physical and chemical properties of crystals mostly depend on a very good approximation only on the distribution of the valence electrons. In chemical bonds, the core electrons do not participate and around the nuclei they are strongly localized. On the other hand, a large number of plane wave basis functions are required to describe the deeply bound core electrons. This increases the computational cost. In The pseudopotential approximation [200–202] the electronic wave functions can be expanded using a much smaller number of plane waves. The screened and weaker pseudopotential replaces the strong ionic potential here. The chemically active valence electrons are considered explicitly only in this approach. Here the inert core electron are eliminated within the “frozen-core approximation”. All the quantum-mechanical and electrostatic interactions of the valence electrons with the cores, like the nuclear Coulomb attraction screened by the core electrons, Pauli repulsion, and exchange and correction between core and valence electrons, are accounted for by the pseudopotential which depends on angular momentum.

The concept of pseudopotentials is shown in Figure. 2.1(a). Here true valence wave function  $\Psi$  is peaked far away from the nucleus (dashed curve). Near the nucleus it has strong oscillations. This ensures it is orthogonal to the core states. High energy cutoffs are demanded by the description of these nodes by plane wave. Within the core region the true valence wave function  $\Psi$  does not contribute significantly. It can be approximated by a smooth and nodeless “pseudo-wave function”  $\Psi_{ps}$ . The core region is defined by a cut-off radius  $r_c$ . This includes all the nodes of the all-electron valence wave functions. So  $\Psi_{ps}$  is constructed in such a way that outside the core radius, it matches with the true valence wave

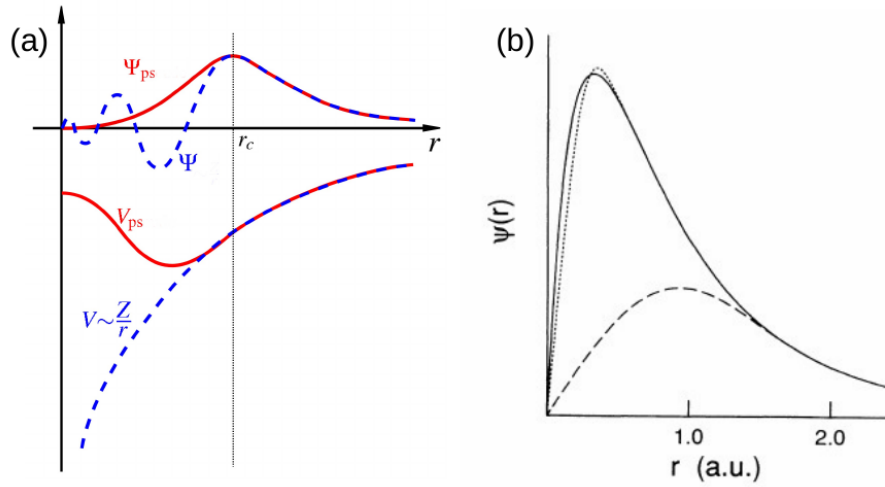


Figure 2.1: (a) Schematic diagram of all-electron (solid lines) and pseudoelectron (dashed lines) potentials and their corresponding wave functions. The radius at which pseudoelectron and all-electron values match is indicated  $r_c$  (b) Oxygen 2p radial wave function (solid line) and corresponding norm-conserving [206] (dotted line) and ultrasoft [207] (dashed line) pseudo wave functions. The figure is reproduced from Ref. [207]

function and inside the core radius, it can smoothen the strong oscillations.

The pseudopotential  $V_{ps}$  is defined as the effective potential corresponding to the pseudo wave function  $\Psi_{ps}$  within the core region. There are several schemes for construction of pseudopotentials proposed by various authors e.g. Troullier and Martins [203, 204], Kerker [205], Hamann, Schlüter, and Chiang [206], Vanderbilt [207], Goedecker-Teter-Hutter [208]. In general, pseudopotentials can be formed in the following manner.

- (i) For a chosen electronic configuration of the atom, the eigenvalues of the pseudo-wave functions and true wave functions should be identical.
- (ii) Outside a cutoff radius  $r_c$ , both wave functions should be identical.
- (iii) The pseudo-wave function should be nodeless. (iv) At  $r_c$  the logarithmic derivative of both the wave functions should agree .

“norm-conserving” pseudopotentials are a special class of pseudopotentials, where within the core region, the norm of the pseudo-wave function equals the norm of the all electron wave function. More accuracy and good transferability properties have been found in “norm-conserving” pseudopotentials. This pseudopotential formed in one environment (usually the atom) is able to give faithful description of the valence properties in different chemical environments.

Good transferability has the requirement that the core radius  $r_c$  to be just larger than the position of the outermost maximum of the true wave function. This is the main constraint with the norm-conserving pseudopotentials. This is because of the fact that, the pseudo wave function can only then reproduce the charge distribution of the true wave function. For example,  $r_c$  is smaller for the  $2p$  state compared to the  $3p$  stat. Because there is no state with the same angular momentum for  $2p$  state to which it has to be orthogonal. So the pseudo wave function for  $2p$  state is similar to the all-electron wave function (Fig. 2.1(b)) as inside the core radius, it has to match the charge corresponding to the all-electron wave function. Near the core A  $2p$  state is more strongly peaked in comparison to the  $3p$  state. As a consequence, a large number of plane waves are required for the sharp peak of  $2p$  state for its accurate representation in comparison to the  $3p$  state. The same pattern is true for  $d$  states of the second-row transition metals. Therefore, for elements having strongly localized orbitals like transition metals and rare-earth elements, the resulting norm-conserving pseudopotentials have smaller value of the cut-off radius  $r_c$  and so require large plane wave basis sets. The required computational time and efforts thus increased for this. By relaxing the norm-conservation condition, Vanderbilt [207, 209] showed that this problem can be solved. This greatly reduced the cutoff of energy as a large value of cut-off radius  $r_c$  could be used. Within the core region, the pseudo wave

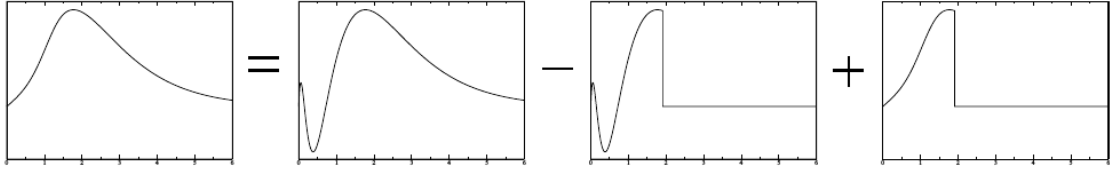


Figure 2.2: Schematic representation of the PAW transformation. The auxiliary wave function is constructed from the full wave function by subtracting the oscillatory part close to an atom and replacing it by a smooth function. Figure is adopted from reference [210]

function  $\Psi_{ps}$  can be made much softer. However this results in a charge deficit in the core region. To compensate for this charge deficit, augmentation charges are introduced in the core region. Augmentation charges are defined as the charge density difference between true and pseudo-wave functions. The core radius  $r_c$  can now be chosen quite large independently of the position of the maximum of the true wave function. To restore the charge distribution of the true wave function accurately, a small cutoff radius must be used for the augmentation charges only. These pseudopotentials are called as ultra-soft pseudopotentials.

### 2.5.1 Projector Augmented Wave method (PAW)

All information on the full wave function close to the nuclei is lost in the pseudopotential method. This is a major drawback of this method. The calculation of certain properties, such as hyperfine parameters can be influenced by this.

In 1994 the PAW method was developed by Blöchl [211]. In principle it is a frozen-core all electron method. In this method, the advantage and accuracy of all-electron methods is combined with pseudopotential methods which are computationally less expensive. Kresse and Joubert in 1999 [212] derived its close connection to the ultra-soft pseudopotential. The PAW method is based

on the division of the whole space  $\Omega_w$  into distinct regions: a collection of non-overlapping spherical regions (the augmentation spheres) around each atom  $\Omega_a$  and the remainder, the interstitial region  $\Omega_1$ .

$$\Omega_w = \Omega_1 + \bigcup_a \Omega_a. \quad (2.39)$$

The plane wave basis sets are ideal for the interstitial region  $\Omega_1$ . But these are difficult to use to describe the wave function in the augmentation spheres. In order to circumvent this problem, auxiliary smooth wave functions  $\tilde{\Psi}_i(\mathbf{r})$  can be introduced. These  $\tilde{\Psi}_i(\mathbf{r})$  can be obtained from the all-electron wave function  $\Psi_i(\mathbf{r})$  via an invertible linear transformation  $\mathcal{T}$ .

$$|\Psi_i\rangle = \mathcal{T} |\tilde{\Psi}_i\rangle, \quad (2.40)$$

where  $i$  is composite index for band,  $\mathbf{k}$ , and spin. This gives the transformed KS equations,

$$\hat{H}_{KS} |\Psi_i\rangle = \epsilon_i |\Psi_i\rangle \Rightarrow \hat{H}_{KS} \mathcal{T} |\tilde{\Psi}_i\rangle = \epsilon_i \mathcal{T} |\tilde{\Psi}_i\rangle. \quad (2.41)$$

$$\mathcal{T}^\dagger \hat{H}_{KS} \mathcal{T} |\tilde{\Psi}_i\rangle = \mathcal{T}^\dagger \mathcal{T} \epsilon_i |\tilde{\Psi}_i\rangle. \quad (2.42)$$

Auxiliary wave functions are found by solving Eq. (2.42) and then transforming them back to true wave function using Eq. (2.40). In each atomic region the operator  $\mathcal{T}$  modifies the smooth auxiliary wave function, such that the resulting all-electron wave functions can have the correct nodal structures. The operator

$\mathcal{T}$  can be written as,

$$\mathcal{T} = 1 + \sum_a \mathcal{T}^a, \quad (2.43)$$

where  $\mathcal{T}^a$  is the transformation centered on atom  $a$  and it has no effect outside a certain atom specific augmentation region that is defined by  $|\mathbf{r} - \mathbf{R}^a| < r_c^a$ .  $\mathbf{R}^a$  specifies the position of atom  $a$  here. Thus outside the augmentation spheres, the auxiliary and all-electron wave functions are identical. The cutoff region of radius  $r_c^a$  should be chosen in a manner such that between the augmentation spheres there are no overlaps. The true wave function  $\Psi_{AE}^n$  can be expanded in terms of partial waves  $\phi_l^a$  inside the augmentation spheres. One can define a corresponding auxiliary smooth partial wave  $\tilde{\phi}_l^a$  for each of these partial waves, and can be written as,

$$|\phi_l^a\rangle = (1 + \mathcal{T}^a) |\tilde{\phi}_l^a\rangle. \quad (2.44)$$

$$\mathcal{T}^a |\tilde{\phi}_l^a\rangle = |\phi_l^a\rangle - |\tilde{\phi}_l^a\rangle. \quad (2.45)$$

Hence the local operator  $\mathcal{T}^a$  adds the difference between the true and auxiliary partial wave functions for every atom. This is schematically depicted in Figure 2.2. By calculating the expectation value of the operator in terms of either the true or auxiliary wave function we can evaluate any physical quantity.

$$\langle A \rangle = \sum_n f_n \langle \Psi_i | A | \Psi_i \rangle = \sum_n f_n \langle \tilde{\Psi}_i | \mathcal{T}^\dagger A \mathcal{T} | \tilde{\Psi}_i \rangle, \quad (2.46)$$

Here  $f_n$  represents the occupation number of the valence states. Thus the PAW

method is not any traditional pseudopotential method, rather it is an all-electron method. It uses information of full potential and density. The converged results of the PAW method is independent of a reference system like an isolated atom. no transferability error is found here and the high spin atoms can be efficiently described using PAW meyhod.

## 2.5.2 van der Waals corrections

It is well known that the long-range electron correlation that are responsible for the van der Waals (vdW) interactions<sup>2</sup>. can not be described by the popular DFT functionals like LDA or GGA. The dispersion interactions can not be captured by standard exchange-correlation functionals. They are viewed as non-local electron correlations. An accurate estimation of vdW forces in conjunction with DFT functionals is not trivial and is still a matter of discussion. Grimme [213–215] proposed one of the dispersion-corrected DFT approach. It is known as DFT-D2 (or DFT-D) method. For accounting medium and long-distance dispersive forces, a semi-empirical attractive term is added with the DFT energy here. Hence total energy is now written as

$$E_{tot} = E_{\text{DFT}} + E_{\text{disp}}, \quad (2.47)$$

Here  $E_{\text{DFT}}$  presents the DFT total energy which is calculated for a given exchange-correlation functional and  $E_{\text{disp}}$  presents a pair-wise semi-empirical dispersion

---

<sup>2</sup>van der Waals forces is a general term which include the forces between (1) two permanent dipoles (Keesom force), (2) a permanent dipole and a corresponding induced dipole (Debye force) (3) two instantaneously induced dipoles (dispersion force). In this thesis van der Waals forces and dispersion forces as synonyms are used.

correction given by

$$E_{\text{disp}} = -s_6 \sum_{i=1}^{N_{\text{at}}-1} \sum_{j=i+1}^{N_{\text{at}}} \frac{C_6^{ij}}{R_{ij}^6} f_{\text{damp}}(R_{ij}, R_0^{ij}). \quad (2.48)$$

Here  $N_{\text{at}}$  represents the number of atoms in the system,  $s_6$  is a global scaling factor which depends on the exchange-correlation functional. Here  $C_6^{ij}$ 's are the dispersion coefficients for the atom-pair  $ij$  and  $R_{ij}$  is the interatomic distance. In case of a pair of different elements, the value of  $C_6^{ij}$ 's is determined by the geometric mean of the coefficients of individual elements.  $f_{\text{damp}}$  is a damping function which determines the range of the dispersion correction. It avoids divergence of the  $R_{ij}^6$  term at small distances and double-counting effects of correlation at intermediate distance.

$$f_{\text{damp}}(R_{ij}, R_0^{ij}) = \frac{1}{1 + \exp(-d(R_{ij}/s_{r,n}R_0^{ij} - 1))}, \quad (2.49)$$

Here  $R_0^{ij}$  is cutoff radius which is taken as the average of the empirical atomic vdW radii for the atom pair. The steepness of the damping function is determined by the global constant  $d$ . (the higher the value of  $d$ , the closer it is to a step function).  $s_{r,n}$  is a scaling factor which determines the range of interaction covered by the given DFT exchange-correlation. In the DFT-D2 method, in the DFT part we used the PBE exchange correlation functional and the value of  $s_6$  is taken as 0.75. We considered pair interactions up to a radius of 8 Å and used the default values of other parameters given in VASP [216–218] in all our calculation.

There is one another approach, where the dispersion forces are treated within the DFT framework, by incorporation of a non-local correlation functional. Dispersion forces originate due to interactions between multipole moments arising

out of fluctuations of charge density around the atoms. In DFT-D2 method, through a semi-empirical approach only dipole-dipole interaction is included. Here the higher order interactions are neglected. A method which calculates the dispersion energy solely based on the electron density was proposed by Dion *et al.*, [219, 220]. In this method, the exchange-correlation energy  $E_{xc}$  is calculated as

$$E_{xc} = E_x^{\text{GGA}} + E_c^{\text{LDA}} + E_c^{\text{nl}}, \quad (2.50)$$

Here  $E_x^{\text{GGA}}$  is the exchange energy in the revPBE approximation [221],  $E_c^{\text{LDA}}$  is the local correlation energy which is calculated within LDA, and  $E_c^{\text{nl}}$  represents the non-local term describing the dispersion energy. It can be calculated as

$$E_c^{\text{nl}}[\rho] = \int d\mathbf{r}_1 d\mathbf{r}_2 \rho(\mathbf{r}_1) \phi(\mathbf{r}_1, \mathbf{r}_2) \rho(\mathbf{r}_2), \quad (2.51)$$

The kernel  $\phi(\mathbf{r}_1, \mathbf{r}_2)$  is dependent on the distance  $|\mathbf{r}_1 - \mathbf{r}_2|$ , charge density  $\rho$  and its gradient [220]. This method is known as van der Waals density functional (vdW-DF) method. It adds the description of dispersion interactions within the DFT formalism and self-consistently calculates the correlation of all ranges. In this method, dispersion effects are included naturally via the charge density and are independent of the parameters. This is the biggest advantage of vdW-DF over DFT-D2. The vdW-DF method improves the bond lengths of the dispersion bonded systems significantly in comparison to the LDA or GGA results. But vdW-DF overestimates the long range dispersion interactions and gives bond lengths with large value in comparison to experimental data [222, 223] for some materials (*e.g.*, graphene, systems with hydrogen bonds). Although dispersion effects are purely correlational in nature, somehow in the dispersion regime, the

exchange part of revPBE used to produce repulsive interaction . Hence large intermolecular binding distances and inaccurate binding energies are given by the exchange part of revPBE. Lee *et al.* [224] proposed a second version of the van der Waals density functional to circumvent this problem. They incorporated a less repulsive exchange functional (rPW86 [225]) in this approach. It is known as the vdW-DF2 method. This method has been found to give more appropriate results for a large number of materials. Later several other vdW functionals have also been proposed for improving the performance of the dispersion bonded systems such as optB88-vdW, optPBE-vdW, vdW-DF2C09<sub>x</sub>, vdW-DFC09<sub>x</sub> *etc.* Detailed comparative studies of these methods for a number of materials are given in Ref. [223, 226, 227]. We have performed all calculations using VASP where these methods have been implemented by J. Klimes [222, 223] using the algorithms of Roman-Perez *et al.* [228]. More details about the methods have been given in Ref. [219, 220, 224].

## 2.6 Calculation of properties beyond electronic energies

### 2.6.1 Geometry optimization

The main agenda of geometry optimization is to find out the lowest energy structure of a system from an arbitrary starting geometry. The motion of the nuclei and the electrons can be separated within Born-Oppenheimer approximation. So a geometry optimization is performed in a two step process, (i) For a given geometry, the self consistent electronic calculation, (ii) the ionic relaxation of the nuclei according to the Hellmann-Feynman theorem [229]. The Hellmann-

Feynman force acting on the  $I^{th}$  atom can be written as

$$\mathbf{F}_I = -\frac{\partial E_{total}}{\partial \mathbf{R}_I} = -\left[\frac{\partial E_N}{\partial \mathbf{R}_I} + \frac{\partial E}{\partial \mathbf{R}_I}\right]. \quad (2.52)$$

$\mathbf{R}_I$ 's represents the position of the  $I^{th}$  atom.  $E_N$  and  $E$  are the energies for nucleus and electron respectively. The forces coming from the electrons  $\mathbf{F}^e$  on the  $I^{th}$  nuclei can be written as

$$\begin{aligned} \mathbf{F}_I^e &= -\frac{\partial}{\partial \mathbf{R}_I} \langle \Psi_s | \hat{H}_e | \Psi_s \rangle \\ &= -\left\langle \Psi_s \left| \frac{\partial \hat{H}_e}{\partial \mathbf{R}_I} \right| \Psi_s \right\rangle - \left\langle \frac{\partial \Psi_s}{\partial \mathbf{R}_I} \left| \hat{H}_e \right| \Psi_s \right\rangle - \left\langle \Psi_s \left| \hat{H}_e \right| \frac{\partial \Psi_s}{\partial \mathbf{R}_I} \right\rangle. \end{aligned} \quad (2.53)$$

As  $\Psi_s$  is an eigenfunction of  $\hat{H}_e$ ,

$$\begin{aligned} \mathbf{F}_I^e &= -\left\langle \Psi_s \left| \frac{\partial \hat{H}_e}{\partial \mathbf{R}_I} \right| \Psi_s \right\rangle - E \left\langle \frac{\partial \Psi_s}{\partial \mathbf{R}_I} \left| \Psi_s \right\rangle - E \left\langle \Psi_s \left| \frac{\partial \Psi_s}{\partial \mathbf{R}_I} \right\rangle, \\ &= -\left\langle \Psi_s \left| \frac{\partial \hat{H}_e}{\partial \mathbf{R}_I} \right| \Psi_s \right\rangle - E \frac{\partial}{\partial \mathbf{R}_I} \langle \Psi_s | \Psi_s \rangle. \end{aligned} \quad (2.54)$$

$\Psi_s$  are normalized  $\langle \Psi_s | \Psi_s \rangle = 1$  and thus last term in the above Eq. (2.54) vanishes. Then total force on the  $I^{th}$  atom thus becomes

$$\mathbf{F}_I = -\frac{\partial E_N}{\partial \mathbf{R}_I} - \left\langle \Psi_s \left| \frac{\partial \hat{H}_e}{\partial \mathbf{R}_I} \right| \Psi_s \right\rangle. \quad (2.55)$$

Hence we can calculate the forces on the nuclei using Eq. (2.55). In order to move the nuclei towards the local minimum, the optimization techniques such as the steepest descent (SD) or conjugate gradient (CD) method can be used, once the forces are known. Hence a new nuclear configuration will be generated. In the new nuclear configuration the same process (electronic self-consistent cycle) will be repeated to calculate the forces using Eq. (2.55). The nuclei are moved

again to new positions, based on the new forces. until the force on each atom becomes below a predefined threshold value, this process is continued. The nuclei reach an equilibrium configuration, which is a local minimum of their potential energy surface (PES)<sup>3</sup>. at the end of this process,

## 2.6.2 Finding the minimum energy structure of clusters

### Global minimization of gas phase clusters

The optimization technique described above describes only the nearest local minimum on PES. One has to scan the whole PES and should compare the energies of all the minima, to obtain the global minimum of the PES. As the number of local minima increases exponentially with the number of atoms in the cluster, the task becomes non-trivial. So a systematic search scheme has to be used for reducing unnecessary scan of higher energy local minima (poor sampling regions). Evolutionary algorithm or genetic algorithm is one such technique. It is implemented in USPEX [230–233]. The basic idea of the algorithm is to start with a set of initial structures and then evolve them using operators like heredity, mutation etc. For good initial guesses, usually the initial structures are formed by applying possible point group symmetries for a given size  $P$  of the cluster to randomly produced atomic coordinates. These initial structures are relaxed to their nearest local minima using a local optimization technique (steepest descent (SD) or conjugate gradient (CG)) later. The energies of all the optimized structures are then compared. A certain number of worst (with high energy) structures are rejected among the relaxed structures. The remaining structures play the role of parents in the creation of the next generation structures. By applying the

---

<sup>3</sup>A potential energy surface describe the energy of system as a function of all nuclei configuration in a  $3P - 6$  dimensional space.

heredity, atomic permutation, soft-mutation, and mutation operators [231, 232], the new generation is produced. Heredity produces new structures by matching slices (chosen in random direction and with random positions) of the parent structures. A certain fraction of the new generation is generated with mutation by changing the positions of some atoms in random manner. Atoms are moved along the eigenvectors of the softest normal mode of vibrations in soft-mutation operator. These low frequency modes are associated with the low curvature of PES. The structures obtained by these variational operations are then optimized to their nearest local minima. As a consequence, new structures are obtained those were separated by barriers on the PES. A certain number of optimized structures of this generation are considered as parents for the next generation. This cycle continues until the lowest energy structures of a given number of generations turn out to be the same. The best structure is obtained at the end of these cycles, as calculated global minimum of the cluster of size  $P$ .

### **Structure optimization of supported clusters: A random rotation technique**

The clusters can land on the substrate at all possible positions and in all possible orientations randomly as discussed in section 1.1.5, in LECBD experiments. To mimic this process we consider the special symmetry points as the bonding sites on a given surface. A number of orientations of the cluster at each site were considered. Assuming an incoming cluster as a rigid body, we place its center of mass (CM) at some height ( $h$ ) above the special symmetry points of the surface. The height  $h$  value is usually taken as the sum of the covalent radii of the two adjacent surface and cluster atoms or little higher value than the sum. By rotating the cluster around its CM using Euler angles, we generated different orientations.

In LECBD experiments clusters have small impact energies as mentioned earlier. The incoming cluster does not dissociate on its impact with the substrate as its kinetic energy is small enough. We can take the simplified view that the cluster is stationary and its structure is relaxed on the substrate. Due to small impact energy, it is assumed that cluster lands with zero kinetic energy.

It we take  $\mathbf{R}_I$  are the coordinates of the cluster atoms, the new rotated coordinates  $\mathbf{R}'_I$  can be found by,

$$\mathbf{R}'_I = \mathbf{A}\mathbf{R}_I \quad (2.56)$$

$$\mathbf{A} = \begin{bmatrix} \cos(\psi)\cos(\phi) - \cos(\theta)\sin(\phi)\sin(\psi) & \cos(\psi)\sin(\phi) + \cos(\theta)\cos(\phi)\sin(\psi) & \sin(\psi)\sin(\theta) \\ -\sin(\psi)\cos(\phi) - \cos(\theta)\sin(\phi)\cos(\psi) & -\sin(\psi)\sin(\phi) + \cos(\theta)\cos(\phi)\cos(\psi) & \cos(\psi)\sin(\theta) \\ \sin(\theta)\sin(\phi) & -\sin(\theta)\cos(\phi) & \cos(\theta) \end{bmatrix},$$

where  $\mathbf{A}$  is the matrix [234] for transforming the coordinates  $\mathbf{R}_I$  to new rotated coordinates  $\mathbf{R}'_I$ . The Euler angles  $(\phi, \theta, \psi)$  are the sequences of three elemental rotations about the axes of the coordinate system. At first a cluster is rotated about the  $z$ -axis with an angle  $\phi$ , the second rotation is done by an angle  $\theta$  about the intermediate  $x$ -axis which is changed due to first rotation. The last rotation is performed by an angle  $\psi$  about the new  $z$ -axis as changed due to last two rotations. The allowed values of  $\phi, \theta$  and  $\psi$  are  $[0, 2\pi]$ ,  $[0, \pi]$  and  $[0, 2\pi]$  respectively. These angles have been chosen from uniform random distributions among the allowed values. We get a particular orientation of the cluster from each triplet  $(\phi, \theta, \psi)$ . All these initial configurations is relaxed to the nearest local minimum. We determine the most preferred structure of the adsorbed cluster by comparing the adsorption energies (defined later) of all the optimized configurations.

### 2.6.3 Molecular dynamics simulations

All the methods, mentioned above are applicable to systems at zero temperature. But in experiments dynamics of nuclei play an important role to determine the properties of the system as these are performed at finite temperatures. By performing Molecular dynamics (MD) simulations [235–238] we can study the dynamics of the nuclei. Here we can follow the trajectories of the nuclei at finite temperatures. In this method the nuclei are assumed to be classical particles and their motions are described by the Newtonian mechanics. By integrating the classical equations of motion of the nuclei, their equilibrium and dynamic properties are studied in this method. Treating the nuclei as classical particles is a very good approximation (except for the light elements). Because at room temperature atoms have large mass and their de Broglie wavelengths ( $\lambda \sim 0.1 \text{ \AA}$ ) are much smaller than the interatomic distances (of the order of a few  $\text{\AA}$ ).

For a set of nuclei having an interaction energy  $E(\{\mathbf{R}_J\})$  the basic equations of motion are written as

$$M_I \ddot{\mathbf{R}}_I = -\frac{\partial E(\{\mathbf{R}_J\})}{\partial \mathbf{R}_I} = \mathbf{F}_I(\{\mathbf{R}_J\}). \quad (2.57)$$

These equations are integrated using discrete time steps numerically. At the end of a small time step, we can predict the new nuclei positions and velocities using approximate numerical methods. The atomic forces are recalculated at the new positions and another step in time is made. In a typical simulation, this procedure is repeated many thousands of times. We used the most widely used Verlet algorithm in our MD simulations. No explicit velocities is used in the Verlet algorithm. It only requires force at time  $t_0$  and the positions at time  $t_0$  and  $t_0 + \Delta t$  respectively to get the position of every particle at time  $t_0 + \Delta t$ . For

this reason it is very straightforward method along with a modest requirement of storage. Using the Taylor expansion the position  $\mathbf{R}_I(t_0 + \Delta t)$  can be expanded as

$$\mathbf{R}_I(t_0 + \Delta t) = \mathbf{R}_I(t_0) + \mathbf{U}_I(t_0)\Delta t + \frac{\mathbf{F}_I(t_0)}{2M}(\Delta t)^2 + \frac{\ddot{\mathbf{R}}_I(t_0)}{6}(\Delta t)^3 + \mathcal{O}(\Delta t)^4.$$

Similarly,

$$\mathbf{R}_I(t_0 - \Delta t) = \mathbf{R}_I(t_0) - \mathbf{U}_I(t_0)\Delta t + \frac{\mathbf{F}_I(t_0)}{2M}(\Delta t)^2 - \frac{\ddot{\mathbf{R}}_I(t_0)}{6}(\Delta t)^3 + \mathcal{O}(\Delta t)^4,$$

where  $\mathbf{U}_I(t_0)$  is the velocity of  $I^{th}$  particle at time  $t_0$ . Combining the above equations, we can write

$$\mathbf{R}_I(t_0 + \Delta t) = 2\mathbf{R}_I(t_0) - \mathbf{R}_I(t_0 - \Delta t) + \frac{\mathbf{F}_I(t_0)}{M}\Delta t^2. \quad (2.58)$$

In a similar manner we can calculate the velocities at time  $t_0$

$$\mathbf{U}_I(t_0) = \frac{\mathbf{R}_I(t_0 + \Delta t) - \mathbf{R}_I(t_0 - \Delta t)}{2\Delta t} + \mathcal{O}(\Delta t^4). \quad (2.59)$$

Once we know the positions at  $\mathbf{R}_I(t_0)$  and  $\mathbf{R}_I(t_0 - \Delta t)$ , we can determine the positions at subsequent time intervals. The error in the estimation of new positions is only  $\mathcal{O}(\Delta t^4)$  in Verlet algorithm. The total energy is conserved and for long runs the simulations remain stable inspite of the fact that the equations are only approximate for any finite  $\Delta t$ .

The forces on the nuclei are determined by the electron-nuclei and nuclei - nuclei interactions. The electrons stay in their instantaneous ground state as the nuclei move in Born-Oppenheimer approximation. The Hellmann-Feynman

theorem (2.55) can be used to calculate the forces on the nuclei. The total energy of the system of nuclei and electrons using the Kohn-sham formalism can be written as

$$E_{tot}^{KS}[\rho](\mathbf{R}) = \int \rho(\mathbf{r})v(\mathbf{r})d\mathbf{r} + T_s[\rho] + J[\rho] + E_{xc}[\rho] + V_{nn}(\mathbf{R}). \quad (2.60)$$

The forces can be determined as

$$\mathbf{F}_I = -\frac{\partial E_{tot}^{KS}[\rho](\mathbf{R})}{\partial \mathbf{R}_I} = -\int \rho(\mathbf{r})\frac{\partial v(\mathbf{r})}{\partial \mathbf{R}_I}d\mathbf{r} - \frac{\partial V_{nn}(\mathbf{R})}{\partial \mathbf{R}_I}. \quad (2.61)$$

Hence at each time step of the MD simulation, to determine the potential  $v(\mathbf{r})$ , we have to solve an electronic problem for a given nuclei configuration. The total force on  $I^{th}$  atom is calculated using Eq. (2.61) later. This approach is known as Born-Oppenheimer molecular dynamics (BOMD). We can generate a number of time-correlated points which are trajectory of each particle in the phase-space using Eq. (2.58). The average kinetic energy of the system can be written using the equipartition theorem as,

$$\frac{N_f}{2}k_B T = \left\langle \frac{1}{2}M_I \dot{\mathbf{R}}_I^2 \right\rangle, \quad (2.62)$$

Here  $N_f$  ( $N_f = 3P - 3$  for a system with a fixed total momentum) is the degrees of freedom. Using velocities of the atoms we can calculate the instantaneous temperature .

$$T(t) = \sum_{I=1}^P \frac{M_I \dot{\mathbf{R}}_I^2(t)}{k_B N_f}. \quad (2.63)$$

## Molecular dynamics at constant temperature

The total energy of the system is conserved as mentioned above. So there is a fluctuation of kinetic energy as well as the instantaneous temperature around their average values of the system. The MD simulations of this type generates a microcanonical (NVE) ensemble. To replicate the real experiments more faithfully, MD simulation at constant temperature would be more practical. One approach to control the temperature is the extended system dynamics where the physical system is attached to a fictitious thermostat widely known as Nosé Hoove thermostat [239–243]. An additional fictitious degree of freedom  $s$  (corresponding to the thermostat) is added to the physical system in this approach. The total energy of the physical system is now allowed to fluctuate by a thermal contact with the thermostat. But the total energy of the extended system is still conserved. It has been shown [239] that this extended system produces a canonical ensemble in the physical system, due to exchange of heat between the physical system and the fictitious degree of freedom. The fictitious mass  $Q$  associated with the degree of freedom  $s$  controls the coupling between the two systems. The time step of the physical system  $\Delta t$  is unequal to the time step of the extended system  $\Delta t''$ . It is scaled according to  $\Delta t = \Delta t''/s$ . The temperature of the system is related to the average value of the kinetic energy. By controlling the velocity, a temperature control can be achieved. The velocity of the physical system  $U_I$  can be controlled by the variable length of the physical time step as  $U_I = d\mathbf{R}_I/dt = sd\mathbf{R}_I''/dt'' = sU_I''$ . Here  $U_I''$  is velocity in the extended system.  $\mathbf{R}_I$  and  $\mathbf{R}_I''$  are the positions of the particles in physical and extended system respectively with  $\mathbf{R}_I = \mathbf{R}_I''$ . More details about this method can be obtained in Ref. [239, 240]

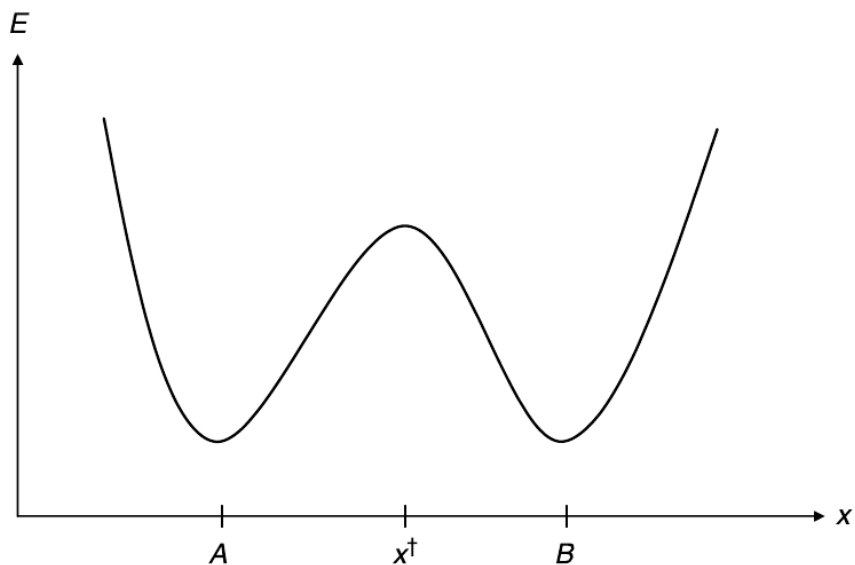


Figure 2.3: Schematic 1D energy profile showing minimum energy path (MEP) which connect two local minima A and B separated by a transition state  $X^\ddagger$  [244].

#### 2.6.4 Nudged elastic band method

An important problem in condensed matter physics and in theoretical chemistry is to find out a minimum energy path (MEP) between two local minima of the PES. This has been shown in Fig. 2.3 schematically. Here energy of the system is plotted against the reaction path. In 1 dimension, roughly a MEP can be defined as a line connecting two local minima (A and B) which pass through a transition state ( $X^\ddagger$ ) of the PES. In a multidimensional space, MEP is the line which connects local minima passing through the saddle point (SP). The energy at the SP is the potential energy maximum along the MEP. It is the minimum energy which is known as the activation energy is required for the reaction to take place. In plane-wave DFT calculations the most widely used method for finding MEP and the activation barrier is the nudged elastic band (NEB) method [245]. In this method, The MEP is obtained by generating a set

of images (different configurations) of the system between the initial and final states. All these images are connected through fictitious springs which mimic an elastic band. Optimization of this band with involving minimization of the forces on the images gives a MEP between A and B.

Let us take an elastic band has  $M+1$  images which are denoted as  $[\mathbf{X}_0, \mathbf{X}_1, \mathbf{X}_2, \dots, \mathbf{X}_M]$ . Successive images are connected through springs of force constant  $k_1, k_2, \dots, k_{M-1}$ . Different atomic configurations  $\mathbf{X}_m = \{\mathbf{R}_I^m, I = 1, \dots, P\}$  are described by different image. The two end points  $\mathbf{X}_0$  and  $\mathbf{X}_M$  are kept fixed during the optimization. These are the initial and final states (correspond to the local minima A and B respectively). The rest  $M - 1$  intermediate images are adjusted regarding the optimization of the elastic band. To calculate the force acting on the system (called as true force), DFT is used for each image.

$$\mathbf{F}_m^t = -\nabla E_{tot}(\mathbf{X}_m). \quad (2.64)$$

The spring forces are calculated as

$$\mathbf{F}_m^s = k_{m+1}(\mathbf{X}_{m+1} - \mathbf{X}_m) - k_m(\mathbf{X}_m - \mathbf{X}_{m-1}). \quad (2.65)$$

A local tangent at an image  $m$  is a unit vector  $\hat{\boldsymbol{\tau}}_m = \boldsymbol{\tau}_m/|\boldsymbol{\tau}_m|$  which points along the line defined by the two adjacent images  $\mathbf{X}_{m+1}$  and  $\mathbf{X}_{m-1}$ .  $\boldsymbol{\tau}_m$ . This can be calculated by the bisection of the two unit vector as

$$\boldsymbol{\tau}_m = \frac{\mathbf{X}_m - \mathbf{X}_{m-1}}{|\mathbf{X}_m - \mathbf{X}_{m-1}|} + \frac{\mathbf{X}_{m+1} - \mathbf{X}_m}{|\mathbf{X}_{m+1} - \mathbf{X}_m|}. \quad (2.66)$$

In NEB method, the optimization [246, 247] of the band is achieved through a force projection scheme where the spring forces do not interfere with the conver-

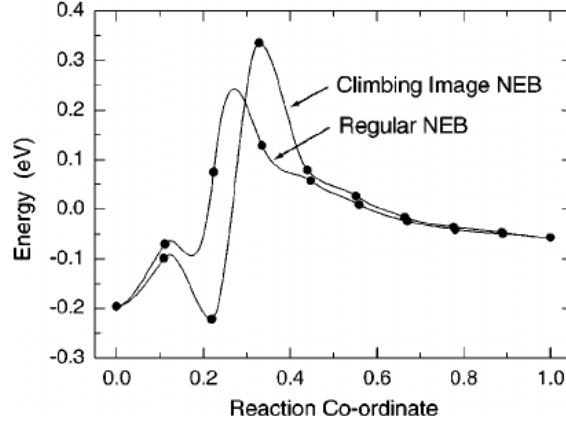


Figure 2.4: DFT calculations of the MEP for  $\text{CH}_4$  dissociative adsorption on the Ir(111) surface. A comparison between a regular NEB calculation and a CI-NEB calculation, both involving 8 movable images. The regular NEB results in a low resolution of images near the SP, and underestimates the activation energy. The CI-NEB put one of the images at saddle point giving accurate energy barriers [246].

gence of the elastic band. The total force acting on an image is the sum of the true force perpendicular to the local tangent and spring forces along the local tangent in this method. Hence the total force acting on an image  $m$  is shown as

$$\begin{aligned} \mathbf{F}_m &= \mathbf{F}_m^t|_{\perp} + \mathbf{F}_m^s|_{\parallel}, \\ &= -[\nabla E_{tot}(\mathbf{X}_m) - (\nabla E_{tot}(\mathbf{X}_m) \cdot \hat{\boldsymbol{\tau}}_m)\hat{\boldsymbol{\tau}}_m] + (\mathbf{F}_m^s \cdot \hat{\boldsymbol{\tau}}_m)\hat{\boldsymbol{\tau}}_m. \end{aligned} \quad (2.67)$$

In this projection scheme, the spacings between the images along the band is controlled by the parallel spring force components and perpendicular true force components direct the elastic band towards the MEP. The other components of the forces ( $\mathbf{F}_m^t|_{\parallel}$  and  $\mathbf{F}_m^s|_{\perp}$ ) are ignored here. Then an optimization algorithm is used to relax the  $M - 1$  images according to the forces in Eq.(2.67). All the images are optimized simultaneously. Thus we can obtain new position as well as new forces for the images. As it is an iterative scheme, so the same cycle will be

repeated till the perpendicular components of true force becomes zero (or below a pre-defined tolerance).

An elastic band is optimized to the MEP and the position of the SP is interpolated as shown in Fig. 2.4. The energy barrier can be calculated by comparing the energies of the initial local minimum (A) and SP. But in various cases, the resolution of MEP obtained by NEB method is not good near the SP. As a result, the energy barriers obtained with inaccuracy. A small modification was introduced in NEB to get rid of this problem. This is known as climbing image nudged elastic band method (CI-NEB) [246]. Here, one identifies an image with the highest energy ( $m_{max}$ ) after few iterations with the regular NEB. Then this image is made to move uphill in energy along the elastic band by removing the spring forces entirely. Then the force on this image is calculated as

$$\mathbf{F}_{m_{max}} = -\nabla E_{tot}(\mathbf{X}_{m_{max}}) + 2(\nabla E_{tot}(\mathbf{X}_{m_{max}}) \cdot \hat{\boldsymbol{\tau}}_{m_{max}})\hat{\boldsymbol{\tau}}_{m_{max}}. \quad (2.68)$$

The climbing image will have the perpendicular component of true force and negative of parallel component of true force, which will drag it uphill towards the SP. The climbing image converges to the SP when the forces are converged. The CI-NEB brings one of the images right to the SP giving the accurate energy barrier. The more details are found in Ref. [246, 247].

### 2.6.5 Bader charges

Charge transfer between atoms are often used to understand the properties of molecules and materials. However the DFT methods give the electronic charge distribution and we need some special techniques to determine the charge transfer between atoms. The Bader scheme [104] is purely based on the topology of the

electronic charge density  $\rho(\mathbf{r})$ , with a definite value at each point in space inside a molecule or a material. All the information about the atoms, bonds and structure of the system are carried by the topology of the charge density. The critical points  $\rho(\mathbf{r}_c)$  (CP) of the charge density correspond to the maximum, minimum or the saddle point of the charge density distribution and satisfy the following equation

$$\nabla\rho(\mathbf{r}_c) = 0. \quad (2.69)$$

In the neighborhood of a CP, the behavior of the density  $\rho$  is obtained by a Taylor series expansion about  $\mathbf{r}_c$ . One can obtain a real and symmetric Hessian matrix of  $\rho$  by neglecting the higher order terms. Then it is diagonalized to obtain a set of eigenvectors and corresponding eigenvalues. The eigenvalues correlate with the principal curvature of  $\rho(\mathbf{r})$  at the CP while the eigenvectors correspond to the related axes. Each CP can be labeled by  $(\omega, \sigma)$ , where  $\omega$  (rank) is the number of non-zero curvatures and  $\sigma$  (signature) is the sum of signs of the curvatures. For a stable CP in 3 dimension,  $\omega = 3$ . There are four possible CP's of rank 3.

- $(3, -3)$ , when all curvatures of  $\rho(\mathbf{r})$  are  $< 0$ , and  $\rho(\mathbf{r})$  is found with a local maximum at  $\mathbf{r}_c$ .
- $(3, -1)$ , when 2 curvatures are negative and  $\rho(\mathbf{r})$  is a maximum at  $\mathbf{r}_c$  in the plane defined by these two axes. The third axis has positive curvature and  $\rho(\mathbf{r})$  is minimum at  $\mathbf{r}_c$  along the axis perpendicular to the plane defined by other axes with positive curvature.
- $(3, +3)$ , when all curvatures are positive and  $\rho(\mathbf{r})$  has a local minimum at  $\mathbf{r}_c$ .

One can calculate the trajectories of  $\nabla\rho$  known as the gradient paths. It can

be obtained by following way. One can calculate the gradient vector of  $\rho$  at some arbitrary point  $\mathbf{r}_0$  and move a distance  $\Delta\mathbf{r}$  in the direction of vector  $\nabla\rho(\mathbf{r}_0)$ . This is repeated until the path generated here, ends. In this process one can obtain all the trajectories of the  $\nabla\rho$ , that represent the gradient vector field of the charge density for a fixed configuration of the nucleus. All trajectories originate or found to be terminated at a CP where  $\nabla\rho = 0$ , which also applies to any point at infinity. A schematic phase diagram of trajectories in the neighborhood of a CP is illustrated in figure. 2.5. In 1 dimension,  $\rho$  has a maximum at the (1,-1) CP and two gradient vectors terminate here. At a (1,+1) CP,  $\rho$  has a minimum and two gradient vectors originate here. Similarly in 2dimension, at a (2,-2) CP, all trajectories of  $\nabla\rho$  terminate. At a (2,+2) CP these trajectories originate. (2,0) CP is quite interesting, with eigenvalues of opposite sign ( $\sigma = 0$ ) and  $\rho$  has the saddle point at the CP. In this case, the two trajectories associated with the axis of negative curvature terminate at the CP, where two trajectories associated with the positive curvature will originate at the CP. All other trajectories formed by the linear combination of the the associated eigenvectors ignore the CP. In 3 dimension, a (3,-1) CP has two negative eigenvalues and one positive eigenvalue. Trajectories associated with the pair of negative eigenvalues as well as trajectories obtained from the linear combination of associated eigenvectors terminate at the CP defining a surface. Two trajectories associated with the positive curvature originate at the CP. The charge density has a maximum in the surface at the CP and along the perpendicular axis it has a minimum at the same point. In similar manner, all trajectories terminate at the (3,-3) CP corresponding to one of the nuclei of the system. The region of space traveled by all the trajectories which end at a particular nucleus is known as the basin of attraction for the nucleus (also known as Bader volumes). As all (3,-3) CP's correspond to the position of

the nuclei, space of any molecular charge distribution can be separated to disjoint regions (basins). These basins are partitioned by the interatomic surfaces which terminate at the (3,-1) CP's. The boundary of basins of the nuclei is defined by the interatomic surface  $S(\mathbf{r})$ . This interatomic surface satisfies the following constraint

$$\nabla\rho(\mathbf{r}) \cdot \hat{n}(\mathbf{r}) = 0 \quad \text{for all the points on the surface } S(\mathbf{r}), \quad (2.70)$$

Here  $\hat{n}(\mathbf{r})$  represents the unit vector which is perpendicular to the surface at each point  $\mathbf{r}$ . Hence the interatomic surface is also called as the zero-flux surface.

We can summarize, the main idea as the division of the space of the molecular charge distribution in terms of Bader volumes. Each Bader volume contain a single charge density maximum mostly at a nucleus. These volumes are partitioned by a surface on which charge density is minimum normal to the surface. The charge which is enclosed within a Bader volume is approximated as the electronic charge of the enclosed atom. So the electronic charge of an atom within the molecule or a material can be calculated by integrating the charge density within the Bader volume. One can calculate the charge transfer to/from that atom in the system by subtracting this electronic charge of an atom within the molecule from the charge of the isolated atom, . More details about the method are found in Ref. [248–251].

## 2.6.6 Calculation of phonons

In condensed matter, such as solids and some liquids, a phonon is known as collective excitation in a periodic elastic arrangement of atoms or molecules. It is a quantum mechanical description of an elementary vibrational motion where

uniform oscillation at a single frequency of a lattice of atoms or molecules is found. Quantization of energy and specific heat of solid was introduced by Einstein AND Debye. Theory of phonons give accurate information on the force constants, piezoelectric constants, static dielectric constants, electron-phonon interactions etc. In Born-Oppenheimer approximation, the total energy can be viewed as a function of the positions of the nuclei  $E(\mathbf{R}_i)$ . There are two approaches in the calculation of phonons using first-principles theory.

- (1) Direct calculation of total energy as a function of the positions of the atoms (frozen phonon method)
- (2) Perturbative approach involving calculations of the derivative of energy (response function method)

### **Frozen phonon method**

In frozen phonon method, a small, but finite perturbation is frozen in the system, and the total energy and forces are calculated for the nuclei “frozen” at positions  $R_I$ .

- In this method the forces between every atom in the crystal is found and the force constant matrix of the crystal has been constructed. This force constant matrix then allows us to calculate the normal modes of at any particular wavevector,  $q$ .
- To calculate the forces caused by an atom  $i$ , we displace atom  $i$ , and then use DFT to calculate the forces on every atom using the Hellman-Feynman theorem.

The force constant is defined as

$$C_{I,\alpha;J,\beta} \approx -\frac{\Delta F_{I,\alpha}}{\Delta R_{J,\beta}} \quad (2.71)$$

and dynamical matrix  $D_{I,\alpha;J,\beta}$  is computed from the force constant matrix as

$$D_{I,\alpha;J,\beta} = C_{I,\alpha;J,\beta} \frac{1}{\sqrt{M_I M_J}} \quad (2.72)$$

- By diagonalization of the dynamical matrix, phonon frequencies and eigenvectors are obtained .

### **Advantage and disadvantages of frozen phonon method**

It is generally quicker and computationally cheaper than the Linear Response method.

In frozen-Phonon Method large super cells are required for accurate calculation of the force constant matrix. The periodic boundary conditions involved in DFT calculations cause problems for the frozen phonon method. During the displacement of one atom in a small unit cell forces are generated on all the atoms in the same unit cell. For periodic boundary condition, the forces are also created but also on the periodic images of these atoms.

### **Density functional perturbation theory**

In perturbation theory the hamiltonian  $\hat{H}^0 + \lambda\Delta\hat{H}$  is systematically expanded as in powers of the perturbation. The first order term depends on unperturbed wavefunctions and  $\Delta\hat{H}$  to the first-order are given as the generalized force on an

atom. The second derivatives of ground state energy with respect to the perturbation are required to obtain the interatomic force constants (IFCs). This is nuclear displacements, which can be calculated using electronic structure methods efficiently. This is given by

$$\frac{\partial^2 E(\mathbf{R})}{\partial \mathbf{R}_I \partial \mathbf{R}_J} = \int \frac{\partial n(\mathbf{r})}{\partial \mathbf{R}_J} \frac{\partial V_{[R]}(\mathbf{r})}{\partial \mathbf{R}_I} d\mathbf{r} + \delta_{IJ} \int n(\mathbf{r}) \frac{\partial^2 V_{[R]}(\mathbf{r})}{\partial \mathbf{R}_I \partial \mathbf{R}_J} d\mathbf{r} + \frac{\partial^2 E_N}{\partial \mathbf{R}_I \partial \mathbf{R}_J} \quad (2.73)$$

The linear response of the charge density with respect to atomic positions can be calculated as:

$$\frac{\partial n(\mathbf{r})}{\partial \mathbf{R}_I} = 4Re \sum_{n=1}^{N/2} \psi_n^*(\mathbf{r}) \frac{\partial \psi_n(\mathbf{r})}{\partial \mathbf{R}_I} \quad (2.74)$$

The derivatives of KS orbitals,  $\frac{\partial \psi_n(\mathbf{r})}{\partial \mathbf{R}_I}$  are calculated as:

$$(H_{SCF} - \epsilon_n) \frac{\partial \psi_n(\mathbf{r})}{\partial \mathbf{R}_I} = \left( \frac{\partial V_{SCF}(\mathbf{r})}{\partial \mathbf{R}_I} - \frac{\partial \epsilon_n}{\partial \mathbf{R}_I} \right) \psi_n(\mathbf{r}) \quad (2.75)$$

with first-order derivative of self-consistent potential given as:

$$\frac{\partial V_{SCF}(\mathbf{r})}{\partial \mathbf{R}_I} = \frac{\partial V_{[R]}(\mathbf{r})}{\partial \mathbf{R}_I} + e^2 \int \frac{1}{|\mathbf{r} - \mathbf{r}'|} \frac{\partial n(\mathbf{r}')}{\partial \mathbf{R}_I} d\mathbf{r}' + \int \frac{\delta v_{xc}}{\delta n(\mathbf{r}')} \frac{\partial n(\mathbf{r}')}{\partial \mathbf{R}_I} d\mathbf{r}' \quad (2.76)$$

$$\frac{\partial \epsilon_n}{\partial \mathbf{R}_I} = \langle \psi_n | \frac{\partial V_{SCF}}{\partial \mathbf{R}_I} | \psi_n \rangle \quad (2.77)$$

The above equations form a set of self-consistent set of equations to calculate response to an external perturbation,  $V_{ext}$ . By employing efficient iterative techniques like conjugate gradients or the steepest descents, the linear system can be

solved. These calculations can be carried out to get phonon dispersion curves for any material, and it agrees nearly with experiments. Other information obtained from the phonon calculations are phonon density of states and electron-phonon coupling.

### 2.6.7 Magneto crystalline anisotropy (MCA)

Spin orbit coupling (SOC) is the origin of the MCA. it is a quantum effect with relativistic origin which destroys the rotational invariance of the spin quantization axis. So the energy of the system becomes dependent on the direction of the spin with respect to the crystallographic axes, when the SOC is included in it.

The fully relativistic Hamiltonian can be written as the sum

$$H = H^{NR} + \delta H^{(1)} + \delta H^{(2)} + \dots \quad (2.78)$$

on the non-relativistic Hamiltonian

$$H^{NR} = \frac{1}{2m} \left( \mathbf{p} - \frac{e}{c} \mathbf{A} \right)^2 + e\phi \quad (2.79)$$

and relativistic corrections with different orders of magnitude with respect to  $1/c$ . The popularly known Zeeman term is found here as the first-order correction term. It is used to describe the interaction of particle spin moment with external magnetic field  $\mathbf{B} = \nabla \times \mathbf{A}$  :

$$\delta H^{(1)} = H^{Zeeman} = \mu_B \boldsymbol{\sigma} \cdot \mathbf{B}. \quad (2.80)$$

Here  $\mu_B = e\hbar/2mc$  is the Bohr magneton. The electron is found here with intrinsic magnetic (spin) moment  $\mu_B \boldsymbol{\sigma}$  which has no relation with its orbital motion,

which is interacting with the magnetic field. The second-order terms represent the mass-velocity correction, the Darwin shift and the spin-orbit coupling (SOC) term.

$$\begin{aligned}\delta H^{(2)} &= H^{Mass-velocity} + H^{Darwin} + H^{SOC} \\ &= -\frac{p^4}{8m^3c^2} + \frac{e\hbar^2}{8m^2c^2}\Delta\phi + \frac{e\hbar}{4m^2c^2}(\nabla\phi \times \mathbf{p}) \cdot \boldsymbol{\sigma}\end{aligned}\quad (2.80)$$

In spin index, the first two terms become diagonal and hence they are mentioned as scalar-relativistic corrections. whereas the non-diagonal characteristics are present in SOC term. It couples the orbital degrees of freedom and electron spin and plays the main role as the origin of magneto-crystalline anisotropy (MCA).

### Spin-orbit coupling for a spherically-symmetric field

The spin-orbit coupling (SOC), can be viewed as an interaction of the spin moment with the magnetic field, which is felt by the moving electron. Usually SOC lifts degeneracy by splitting the energy states (typically of the order of few to few hundred meV). These states are degenerate in case of a non-relativistic description. The SOC term can be written in an atom with a spherically-symmetric potential  $\phi(\mathbf{r})$ , as

$$H^{SOC} = \frac{e\hbar}{4m^2c^2}(\nabla\phi \times \mathbf{p}) \cdot \boldsymbol{\sigma} = \frac{\hbar}{4m^2c^2} \frac{1}{r} \frac{dV}{dr} (\mathbf{r} \times \mathbf{p}) \cdot \boldsymbol{\sigma} = \xi(r)\mathbf{L} \cdot \mathbf{S}\quad (2.81)$$

Here  $V = e\phi$  represents electron potential energy,  $\mathbf{L} = (\mathbf{r} \times \mathbf{p})/\hbar$  and  $\mathbf{S} = \boldsymbol{\sigma}/2$  denote the orbital and spin momentum operators respectively. And

$$\xi(r) = \frac{\hbar^2}{2m^2c^2} \frac{1}{r} \frac{dV}{dr} \quad (2.82)$$

is the so-called SOC strength constant which increases with atomic number  $Z$  of the element. It has the following expression for non zero angular momentum states in hydrogen like atoms

$$\xi(r) = \frac{\hbar^2}{2m^2c^2} \frac{1}{r} \frac{dV}{dr} = \frac{mc^2(Z\alpha)^4}{4n^3l(l+1/2)(l+1)} \quad (2.83)$$

$\alpha$  is the fine structure constant. The SOC instigates physical phenomena, like magneto-crystalline anisotropy, the Rashba effect, and it plays crucial role in topological insulators, which have drawn a lot of attraction for their fascinating physics and potential applications in spintronics [252]. The total energy of the system is dependent on the orientation of spin moment with respect to the crystallographic axis, if SOC is included. Physically, this difference arises for the crystal field that supports the orbital motion of the electron along the preferred direction.

Using  $\langle \mathbf{r} | i\lambda \rangle = R_{i\lambda}(r) Y_i(\lambda\theta, \phi)$  where  $R_{i\lambda}(r)$  and  $Y_{i\lambda}(\theta, \phi)$  are the radial and spherical harmonic functions, respectively. The matrix elements of SOC potential can be written as

$$V_{i\lambda\sigma, j\mu\sigma'}^{SOC} = \xi_{i\lambda\mu} \langle \bar{\lambda}\sigma | \mathbf{L} \cdot \mathbf{S} | \bar{\mu}\sigma' \rangle \delta_{ij} = \xi_{i\lambda\mu} \langle \bar{\lambda} | \mathbf{L} | \bar{\mu} \rangle \langle \sigma | \mathbf{S} | \sigma' \rangle \delta_{ij} \quad (2.84)$$

where  $\bar{\lambda}$  and  $\bar{\mu}$  are the angular parts of the atomic orbital.

## Methods for calculating MCA

Several different methods are found in the literature to calculate the MCA : i) self-consistent method [253], ii) force theorem scheme [254], iii) perturbation treatment [255, 256], iv) Bruno formula [257] and v) other methods like, for large-scale systems empirical Neel-like model [258] and torque method [259] for systems having uniaxial symmetry.

### Self-consistent method

Self-consistent scheme is based on a direct calculation of the total energy difference of the two different orientations of spin magnetization in presence of spin-orbit coupling. This is included in the K-S equations in the presence of the self-consistent full-relativistic potential. It has the form

$$MCA = E_{tot}[\hat{\mathbf{m}}_1] - E_{tot}[\hat{\mathbf{m}}_2] \quad (2.85)$$

Here  $\hat{\mathbf{m}}_1$  and  $\hat{\mathbf{m}}_2$  are the two different orientations of magnetization. This method is exact and straightforward in principle. But usually it requires a long self-consistent field (SCF) loop which implies the diagonalization of large matrices including SOC. So it is very much computationally demanding and called as “brute force method”. The SCF with SOC is hard to converge as a well-converged charge density or potential is required here. Hence it is a challenging method of calculation MCA for large systems.

### Force theorem

MCA is defined as the fully relativistic total energy difference between two different magnetization directions. Like the case of 3d systems, if the modifica-

tion of the potential induced SOC is small, the so-called force theorem (FT) [254, 260, 261] is applied. The MCA is considered as the band energy difference (not the total energy difference) obtained after a one-step diagonalization of the full SOC included Hamiltonian, starting from a pre converged self-consistent scalar relativistic (without SOC) density/potential. The difference in band energy between two spin directions  $\hat{\mathbf{m}}_1$  and  $\hat{\mathbf{m}}_2$  can be written as,

$$MCA_{FT} = E_{band}[\hat{\mathbf{m}}_1] - E_{band}[\hat{\mathbf{m}}_2] = \int^{E_F^1} E n_1(E) dE - \int^{E_F^2} E n_1(E) dE \quad (2.86)$$

Here  $n_1(E)$  and  $n_2(E)$  represent the density of states and  $E_F^1$  and  $E_F^2$  are the Fermi level of the configurations  $\hat{\mathbf{m}}_1$  and  $\hat{\mathbf{m}}_2$  respectively. The Fermi levels are obtained by the condition on the total numbers of electrons  $N$  in the system :

$$N = \int^{E_F^1} n_1(E) dE = \int^{E_F^2} n_1(E) dE \quad (2.87)$$

It should be mentioned that, using FT method not only computational cost can be saved significantly, but it is numerically very stable also. Because the self-consistent effect including SOC is ignored here. So only one iteration is required for the perturbed systems.

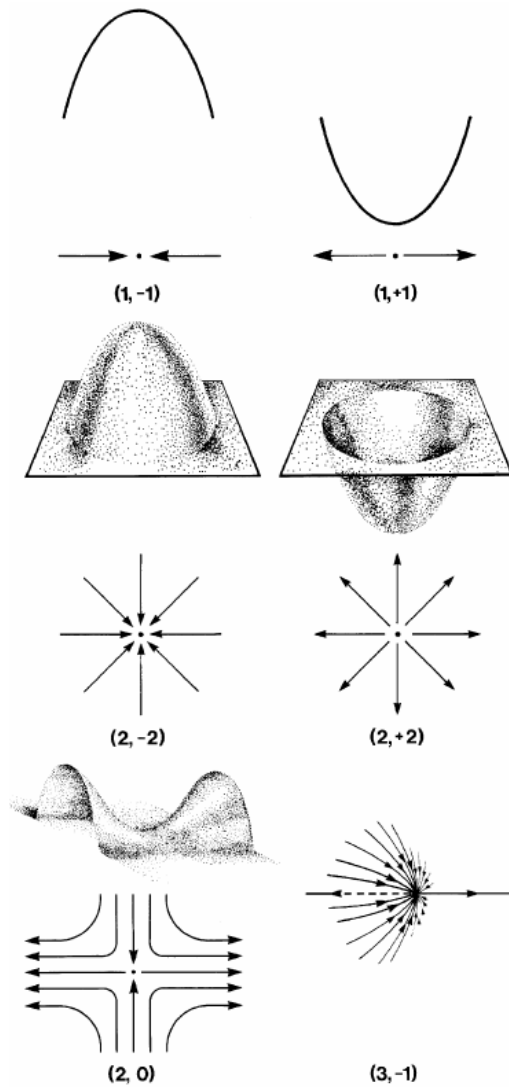


Figure 2.5: Phase portraits. A pair of gradient paths terminates or originates respectively, at the CP for a 1D maximum or minimum. In 2D, all of the gradient paths in a plane terminates or originates, at the maximum or minimum (CP) respectively. At  $(2,0)$  CP, a pair of paths originates at the CP, (positive curvature), and another pair terminates at the CP (negative curvature). All other gradient paths avoid the CP. A 3D display of a  $(3, 1)$  CP shows the set of trajectories that terminate at the CP and define a surface and the unique pair that originates there and defines a line [104].

## Adsorption of TaSi<sub>16</sub> cluster on HOPG

### 3.1 Motivation

The initial motivation of the studies on transition metal doped silicon cluster came from the discovery of carbon fullerenes. Questions were asked whether fullerenes made by Si would also be stable, and could be used as building blocks to synthesize novel materials. Unlike C, as  $sp^2$  hybridization in Si is not favorable, hollow Si cages were found to be unstable. But very interestingly when a Si cage encapsulates a transition Metal (TM) atom, it becomes stable. Over the last couple of decades TM encapsulating silicon cage clusters have been studied extensively [3, 51, 52, 61, 78, 95, 262].

Hiura et al.[61] showed experimentally, that for a particular TM atom, TMSi<sub>n</sub> cluster of a fixed size is more stable compared to its neighbors. As an example, WSi<sub>12</sub> was found to be the most stable cluster in the WSi<sub>n</sub> series. According to their suggestion the relative stability of these clusters is determined by the so-called 18-electron rule of the organometallic chemistry. The assumption was that each Si atom donates one electron to the central TM atom and clusters

with 18 valence electrons on the TM atom were more stable. The  $\text{WSi}_{12}$  cluster follows this rule. Khanna and co-workers claimed  $\text{CrSi}_{12}$ [79] and  $\text{FeSi}_{10}$ [85] to be the most stable clusters in the respective  $\text{TMSi}_n$  series over limited ranges of size. Notably, both these clusters nominally satisfy the 18-electron rule. In mass abundance experiments of Koyasu et al.,  $\text{ScSi}_{16}$ ,  $\text{TiSi}_{16}$ , and  $\text{VSi}_{16}^+$  were found to be most abundant among the anion, neutral, and cation clusters respectively[63]. This opened a new line of argument which claimed that  $\text{TMSi}_n$  clusters follow electron-counting rules much like the shell models in simple metal clusters. Sen and Mitas and Guo et al. pointed out that simple electron-counting rules are not generally valid[75, 78].

Though the origin of enhanced stability of certain  $\text{TMSi}_n$  clusters remains a matter of debate, what is definitely established is that there are some clusters with enhanced stability. For example, experiments from Nakajimas group established that  $\text{TaSi}_{16}^+$  is more stable than neighboring sizes, and this was rationalized by the electron-counting rule (20- electron filled shell)[98].

As is clear, numerous studies, both theoretical and experimental, have addressed fundamental properties of  $\text{TMSi}_n$  clusters in the gas phase. There were no studies trying to use them in applications, or studying their properties after deposition on a substrate, often a precondition for application. The first such attempt has come from Nakajimas group. In a recent experiment, they have deposited stable  $\text{TaSi}_{16}^+$  clusters on a highly oriented pyrolytic graphite (HOPG) substrate[4].

The main motivation in this set of experiments was to explore formation of assemblies of  $\text{TaSi}_{16}$  on the HOPG substrate. Structure and electronic properties of the deposited clusters were studied using scanning tunneling microscopy (STM), X-ray photo emission spectroscopy (XPS), and ultra-violet photo emission spec-

trospectroscopy (UPS) probes. While STM gives information about atomic structure, XPS and UPS probe energies of the core and valence electron levels, respectively. STM and XPS measurements were performed both on the as-deposited samples and after heating them at 400 and 720 K. In order to check the so-called superatomic character of TaSi<sub>16</sub>, they also studied reaction of the deposited clusters with oxygen.

After deposition, the clusters retained their metal-enclosing cage structures and formed small islands. The height of the islands was found to be about 1 nm in STM experiments, which indicates a one-layer thickness. Based on the XPS results, in the as-deposited clusters, the Si cage was inferred to be highly symmetric. Individual clusters were discernible at 400 K also. There were some shifts in the XPS peaks found after heating at 720 K. This was presumed to be because of partial coalescence of the clusters or coalescence between the clusters and the HOPG substrate. Any definite peaks in the valence electron levels were not found in UPS spectra. This was supposed to be due to rapid transition of the cluster between close-lying isomers with quite different electronic structures. The clusters showed considerable resistance to oxidation establishing their chemical stability. In the reaction with oxygen, the Si cage reacted more readily than the encapsulated Ta atoms, indicating that the cage structures were still maintained.

While these experiments provided a lot of information on the behavior of TaSi<sub>16</sub> clusters deposited on HOPG, it is important to recall that none of these provides microscopic insights. In order to have a microscopic picture of the system one needs atomistic calculations. Therefore, in order to better understand this important cluster-substrate system, and to further qualify the reported experimental results, we have performed first-principles calculations on free and HOPG-deposited TaSi<sub>16</sub> clusters using density functional theory (DFT) [263].

One difference with the experiments, however, is that we study deposition of neutral clusters, while in experiments cation clusters were deposited. We avoid study of cation clusters due to technical reasons. First, we cannot strictly ensure that the electron is removed from the cluster. Second, plane wave DFT codes cannot deal with charged systems. A compensating uniform background charge is introduced. Energy convergence with respect to cell size is slow in such cases. In any case, HOPG being a good electrical conductor, the charge on the cluster before deposition is perhaps not important, and hence, studying an overall neutral system is appropriate. We confirm many of the conclusions derived from the experiments, but there are some differences too. Therefore, these calculations complement the experimental studies.

## 3.2 Computational methods

All calculations were performed within the framework of plane wave DFT as implemented in the VASP code[216, 217, 264–266]. An energy cutoff of 600 eV was used for the plane wave basis set. Interaction between the valence electrons and the ion cores was represented by the projector augmented wave (PAW) potentials[211]. Brillouin zone integrations were performed with the  $\Gamma$ -point only both for isolated clusters and HOPG supported clusters.

A global search were performed to find out minimum energy structure of isolated Tasi<sub>16</sub> cluster using evolutionary algorithm. We used USPEX[230–233] code for this global search. The initial population was generated in a completely random manner, without any constraint on point group symmetry. Population in each subsequent generation was produced through the application of variational operations of heredity, mutation, and soft mutation[232]. A population size of

34 was maintained in each generation. The fitness criterion for choosing the best structures was the energy of the clusters. Calculation was continued up to a maximum of 25 generations subject to the condition that, if the energy of the best structure did not change over 17 successive generations, it would be stopped. Energies were calculated using the plane wave PAW method within the DFT using the VASP code. The clusters were placed inside a box whose size was generated automatically by USPEX. For each structure, energy calculations in VASP were performed at five increasing levels of accuracy in terms of both the force convergence criterion and energy cutoff. For the first two levels, the energy cutoff was determined by the ENMAX of the POTCAR files (245 eV). For the next three levels it was 320 eV. For the first level the force convergence criterion was 0.2 eV/Å, for the next two levels it was 0.01 eV/Å, and in the final level it was 0.001 eV/Å. The global search was performed using the spin-unpolarized PBE-GGA exchange-correlation functional. At the end of the global search we collected the best structure from each generation. These structures were further optimized using the vdW-DF2 functional in a spin-polarized calculation. The vdW-DF2 functional was used because this functional is used for study of TaSi<sub>16</sub> on graphite. Use of vdW-DF2 is necessitated by the fact that graphite is not described well by the local density (LDA) or semilocal (GGA) approximations in DFT. We discuss this in next section. For the reoptimization calculation, the energy cutoff was set at 600 eV and the force convergence criterion was 0.001 eV/Å. We reoptimized each of the structures selected from USPEX in the doublet, quartet, and sextet spin states. Sometimes, different initial structures converged to the same final structure after relaxation. For every structure the doublet state was found to have the lowest energy.

The HOPG surface was represented by a repeated slab geometry. The graphite

slab in the simulation cell contained three carbon layers with a vacuum layer of 25 Å separating two successive slabs. Each layer was in the shape of a rhombus with sides of 14.88 Å. Such a large surface supercell ensures that the distance between the cluster in the simulation cell and its periodic images is at least 12 Å so that there are no interactions between them. Carbon atoms in the two top layers were fully relaxed while the bottom layer of atoms was kept fixed to simulate a bulk-like termination.

For the study of reaction with oxygen molecules, we used both the PBE and vdW-DF2 functionals. We got qualitatively same results in the two methods. All other parameters were the same as stated above. For the finite-temperature molecular dynamics (MD) calculations, the temperature was fixed by a Nose - Hoover thermostat[239–243]. Two carbon layers were used in order to reduce computational costs. The Verlet algorithm was used to integrate the equations of motion of the ions. Other parameters were the same as in zero-temperature calculations. As mentioned earlier, MD calculations were performed at 400 and 700 K as the deposited clusters were heated to these two temperatures. At 400 K, a time step of 2 fs was used, and at 700 K the time step was set at 1.5 fs due to faster motion of the ions.

## 3.3 Results and discussions

### 3.3.1 Bulk graphite

As LDA and GGA functionals do not incorporate dispersion interactions, which is necessary for studying graphite system we used methods that incorporate these by incorporating van der Waals correction. In particular, DFT-D2, vdW-DF, and vdW-DF2 were used. All are discussed earlier in previous chapter. For DFT-D2

we used the PBE exchange-correlation. The cutoff distance was kept at 10 Å for pairwise interactions. We used the default  $C_6$  parameter values given in VASP.

We have calculated in plane lattice constant ( $a$ ), interplanar spacing ( $c$ ) cohesive energy ( $E_c$ ), and interlayer binding energy ( $E_B$ ) using different methods. The values of these quantities along with the experimental results are given in table 3.1 The  $E_c$  and  $E_B$  are defined as

$$E_c = N_C E_C - E_T(\text{graphite}) \quad (3.1)$$

Here  $N_C$  is the total number of C atom in bulk graphite.  $E_C$  is the energy of an isolated C atom.  $E_T(\text{graphite})$  represents total energy of bulk graphite.

$$E_B = 2E_T(\text{graphene}) - E_T(\text{graphite}) \quad (3.2)$$

Here  $E_T(\text{graphene})$  is the total energy of a single graphene sheet.

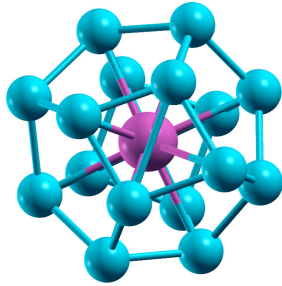
Functionals	$a(\text{Å})$	$c(\text{Å})$	$E_c$ (eV/atom)	$E_B$ (meV/atom)
Experimental	2.46[267]	3.35[267]	7.37[268]	$52 \pm 5$ [269]
LDA	2.45	3.32	9.00	23.40
PBE-GGA	2.47	4.34	7.99	1.08
DFT-D2	2.46	3.26	8.09	49.98
vdW-DF	2.48	3.63	7.52	53.641
vdW-DF2	2.48	3.55	7.50	51.739

Table 3.1: Properties of bulk graphite for different exchange correlation functionals

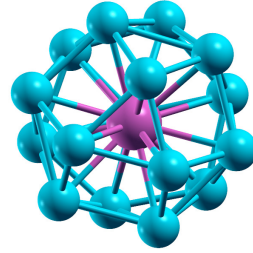
LDA gives good results for  $a$  and  $c$  values in comparison with experiments. But the LDA values for  $E_c$  and  $E_B$  do not agree with experiments. Though the local and semi-local approximations in DFT do not describe dispersion forces binding successive layers in graphite, for LDA it is a lucky coincidence of getting the  $c$  value closed to the experiment. The PBE-GGA[197] functional works well

for  $a$  but performs very poorly for  $c$  and  $E_B$ . DFT-D2 gives good results for  $a$ , but  $c$  is underestimated. DFT-D2 does better than LDA and PBE for  $E_B$ . The nonlocal correlation functional vdW-DF performs well for  $a$  but overestimates  $c$  by nearly 9%.  $E_c$  and  $E_B$  are reproduced well. The vdW-DF2 method corrects the overestimation in  $c$  and produces all quantities in reasonable agreement with experiment.

### 3.4 Structure of Isolated TaSi<sub>16</sub> Clusters



(a) Lowest energy doublet structure for TaSi<sub>16</sub> cluster with vdW-DF2



(b) Lowest energy doublet structure for TaSi<sub>16</sub> cluster without vdW-DF2

Figure 3.1: Ground state optimized structures for TaSi<sub>16</sub> from same initial structure with different exchange correlation

The lowest energy structure we obtained using the vdW-DF2 method is shown in Fig. 3.1(a). The Ta atom is enclosed within an almost symmetric Si cage. The average nearest neighbour Si-Si distance in this structure is 2.4 Å. This is very close to the bulk Si-Si distance of 2.35 Å. The Ta-Si distances vary between 2.84 Å and 2.93 Å. These are slightly larger than the sum of their covalent radii, 2.49 Å. This structure is similar to the slightly distorted  $D_{4d}$  structure reported by Lopez et al. [270]. However, in their PBE-GGA calculations, this was 40

meV higher than the ground state which had a  $C_{3v}$  symmetry. In fact starting from the same initial structure obtained after global search, after reoptimization with PBE-GGA without vdW-DF2, we got the lowest energy structure not at all with  $D_{4d}$  symmetry. It looks rather the ground state  $C_{3v}$  structure reported by Lopez et al. The  $C_{3v}$  structure is 1.14 eV higher in vdW-DF2. This structure is shown in Fig. 3.1(b). Our calculated ground state structure shown in Fig3.1 (a) also looks similar as the converged structure reported by Guo et al.[271] . Guo et al. started relaxing with initial structure of TaSi<sub>16</sub> cluster with  $C_{4v}$  point group symmetry. In their structure optimization they have included the relativistic effects.

All the higher energy isomers within 1 eV of the ground state are shown in Fig3.2. It is interesting to note that in all of these the Ta atom is encapsulated within a Si cage. In fact, we did not find any isomer with an exohedral Ta up to 2 eV from the ground state. These are shown in Appendix.

### 3.4.1 Magnetic moment and charge transfer of ground state TaSi<sub>16</sub>

We have extended our works to study the superatomic behaviour of TaSi<sub>16</sub> cluster supported on HOPG, so we took the re-optimized structure with vdW-DF2. As vdW-DF2 gives reasonable results for graphite for its in-plane lattice constant inter planer spacing etc. discussed earlier, We have confined the calculation of magnetic moment, charge transfer between atoms in the cluster and cluster with the substrate for the lowest energy isomer with vdW-DF2 only.

The magnetic moment for lowest energy structure of TaSi<sub>16</sub> cluster was found as  $0.99\mu_B$ . The isolated Ta atom has three unpaired electrons. But in the TaSi<sub>16</sub> cluster the moment of the central Ta atom is delocalized. Thus, the moment is quenched partially due to bond formation with the Si cage. Si being more electronegative than Ta. This may involve some charge transfer between the central Ta atom to the Si cage. To get a quantitative estimate we calculated Bader[104] charges on all atoms. We find a charge transfer of  $1.1e$  ( $e$  is the electronic charge) from central Ta atom to the Si cage. Hence the Ta atom has a slightly positive charge in the cluster. This result agrees with the fact mentioned by Shibuta et al.[4]. In their XPS measurements, the Si  $2p_{3/2}$  core level was found to be nearly at the same energy (99.08 eV) as in bulk Si (99.2 eV). The Ta  $4f_{7/2}$  level is at 0.6 eV higher binding energy (BE) compared to the bulk. Since the core-level BE is expected to shift by 1 eV for a charge transfer of  $e$  neglecting screening effects, this indicated transfer of  $0.6e$  from Ta to the Si cage. Our calculations are in rough agreement with this. This small amount of charge, distributed over 16 Si atoms, does not cause any appreciable shift of the Si  $2p$  core level BE. They found a single energy location for the Si  $2p_{3/2}$  peak from all

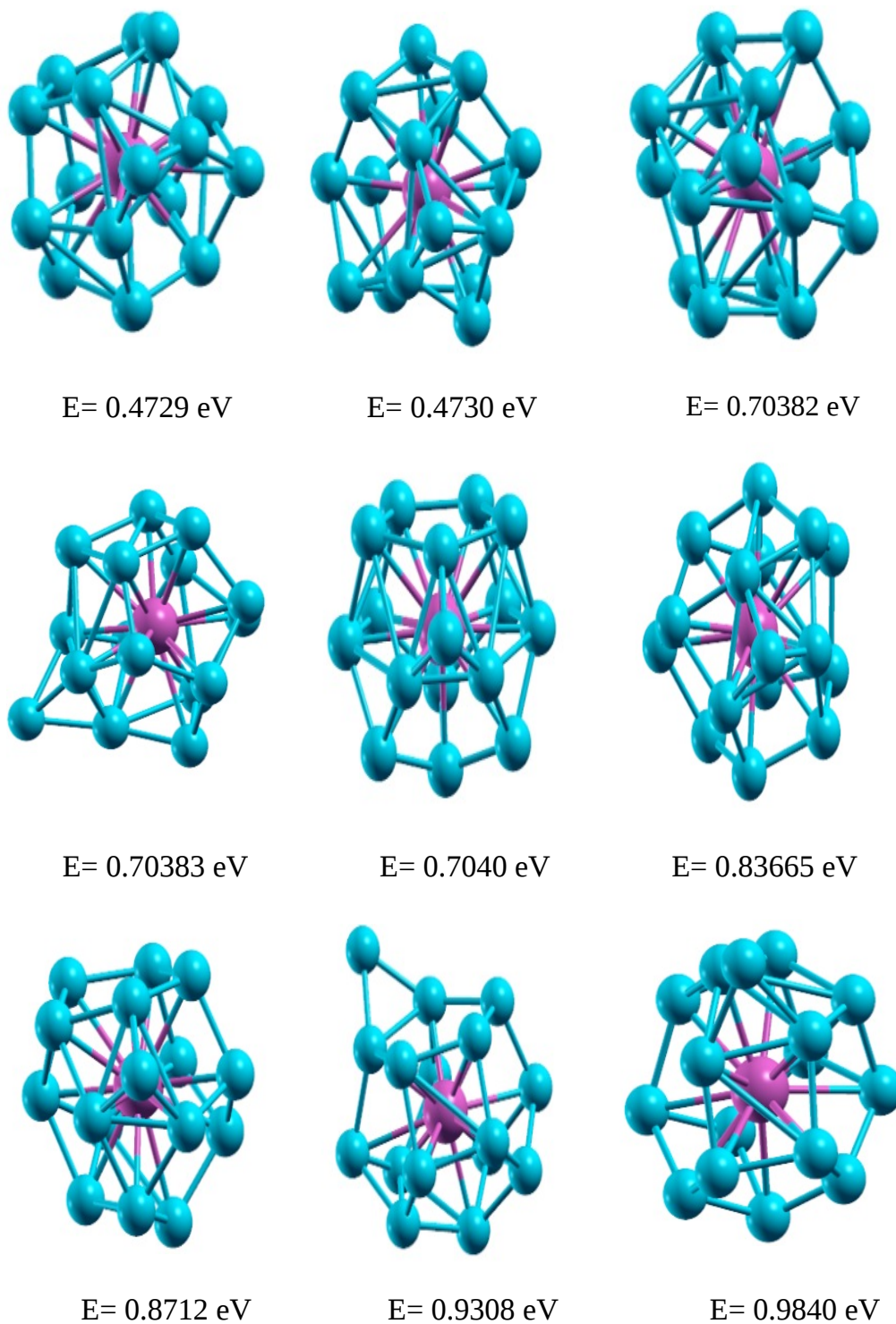


Figure 3.2: Structures of isolated globally optimized  $\text{Tasi}_{16}$  cluster with energy level upto 1 eV higher from ground state, calculated including vDW-DF2.

the atoms suggesting that all the Si atoms are in similar chemical environments. In other words, the Si cage around the central Ta atom is highly symmetric. This is consistent with our calculated ground-state structure.

## 3.5 Adsorption of TaSi<sub>16</sub> on HOPG

### 3.5.1 Structure of deposited TaSi<sub>16</sub> clusters

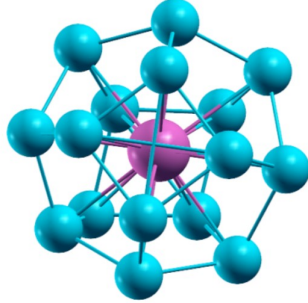


Figure 3.3: Relaxed structure of deposited TaSi<sub>16</sub> cluster on HOPG

We deposit only the ground state structure of the gas phase TaSi<sub>16</sub> cluster on HOPG. We restrict our studies only to the lowest energy isomer mainly due to computational costs. Since the cluster-substrate interaction is weak, as we establish in the following discussion, we believe the gas phase structure and properties of the all isomers would be preserved after deposition.

Energetic stability of a cluster at different points on a substrate can be evaluated in various ways. Which one of these is relevant will depend on the way one explores the system experimentally. The cohesive energy  $E_{coh}$  of the deposited cluster along with the substrate is defined as

$$E_{coh} = n_{Si}E_{Si} + E_{Ta} + N_C E_C - E_T(cl/graphite) \quad (3.3)$$

Here  $n_{Si}$  is the number of Si atoms in the cluster which is 16 in our case.  $N_C$  is the total number of C atoms in the graphite layers.  $E_{Si}$ ,  $E_{Ta}$  and  $E_C$  are the energies of isolated Si, Ta and C atoms respectively.  $E_T(cl/graphite)$  is the total energy of TaSi<sub>16</sub> adsorbed graphite slab. The adsorption energy  $E_a$  is defined as the energy gained due to adsorption of a gas phase cluster on the substrate and is given by

$$E_a = E_T(cl) + E_T(graphite) - E_T(cl/graphite) \quad (3.4)$$

Here  $E_T(cl)$  is the total energy of the gas phase TaSi<sub>16</sub> cluster at its local minimum of structure.  $E_T(graphite)$  is the total energy of the graphite slab. The desorption energy of a cluster  $E_d$ , defined as the minimum energy required to desorb it after adsorption on the substrate is defined as

$$E_d = E_T^{dist}(cl) + E_T(graphite) - E_T(cl/graphite) \quad (3.5)$$

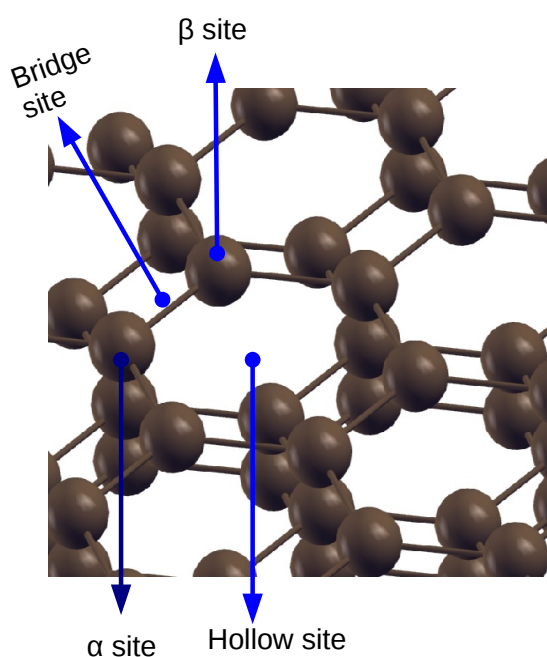
Here  $E_T^{dist}(cl)$  is the total energy of the isolated TaSi<sub>16</sub> cluster in the shape it takes after deposition on the substrate. Since we are depositing a single isomer, we will use only  $E_a$  to understand its relative stability at different adsorption sites and in different orientations.  $E_{coh}$  and  $E_d$  will necessarily follow the same trend.

The relaxed structure of the deposited TaSi<sub>16</sub> cluster on HOPG is almost same as that of the free cluster before deposition on substrate. It is shown in Fig3.3 The distortion is negligible.

Comparing Figure 3.1 and Figure 3.3, it is clear that the Ta encapsulated 16 atoms caged Si cluster maintains its gas phase structure even after deposition on HOPG and even the shape of the cage remains same as before deposition like

Figure 3.1. The distortion from the  $D_{4d}$  cage structure too negligible to detect by eye estimation. We have calculated the energy of the deposited cluster in the shape it takes after adsorbed on HOPG. It is 4.5 meV higher than the isolated cluster before deposition. In the distorted cluster the average Si-Si bond length is 2.35 Å and the Ta-Si bond length ranges from 2.85 Å to 2.97 Å, which is almost same as in the gas phase Figure 3.1.

### 3.5.2 Comparative study of $TaSi_{16}$ cluster at different site on HOPG



$\alpha$  site: A Carbon atom that has another C atom below it in the 2nd layer

$\beta$  site: A Carbon atom with no C atom directly below it in 2nd layer

Hollow site: No Carbon atom (Centre of the hexagon )

Bridge site: The mid point of the connecting line of  $\alpha$  and  $\beta$  site

Figure 3.4: Special symmetry points on HOPG

In LECBD experiments, clusters land on the substrate randomly so that they can approach the substrate at any point and in any random orientation. To mimic this process we have used the random rotation method in case of surface supported clusters. TaSi<sub>16</sub> clusters are placed above the special symmetry sites  $\alpha$ ,  $\beta$ , hollow and bridge on HOPG. These are shown in Figure 3.4.

At each site a number of random orientations of the clusters are considered. The shortest C-Si distance in the initial structures is kept greater than the sum of their covalent radii. The random orientations of the cluster are generated by treating it as a rigid body, and choosing the Euler angles of rotation randomly. We have taken four different random orientations at each point. This gives us sixteen initial configurations of the cluster on the substrate. Given the large size of the cluster, and the consequent large lateral size of the substrate, we could not explore more initial structures due to computational limitations. All the initial structures are relaxed to their nearest local minima using VASP as discussed earlier. We present the adsorption energies of TaSi<sub>16</sub> in all sixteen structures obtained from the random initial structures in Table 3.2. Some important points to be noted are, i)  $E_a$ 's of all the structures are rather small, all less than an eV; ii)  $E_a$ 's are all quite close, the difference being from a few meV's to a hundred meV; iii) the second structure at the  $\beta$  site has the highest  $E_a$  among these. We would like to mention that orientation of the TaSi<sub>16</sub> cluster in structure 2 at the  $\beta$  site is not the same as that in structure 2 at the other sites, as these orientations are generated completely randomly. This is true for all orientations. Now we discuss properties of the deposited cluster in its highest  $E_a$  structure. The relaxed structure of TaSi<sub>16</sub> adsorbed on HOPG with highest  $E_a$  is shown in Figure 3.5.

Table 3.2: Adsorption energies of a TaSi<sub>16</sub> cluster on HOPG in different structures.

Site	Orientation	$E_a(eV)$	$E_d(eV)$
$\alpha$	1	0.852	0.862
	2	0.824	0.831
	3	0.729	0.745
	4	0.721	0.733
$\beta$	1	0.854	0.865
	2	0.872	0.877
	3	0.741	0.760
	4	0.743	0.754
Hollow	1	0.866	0.868
	2	0.785	0.795
	3	0.743	0.757
	4	0.714	0.723
Bridge	1	0.861	0.862
	2	0.758	0.767
	3	0.736	0.752
	4	0.740	0.746

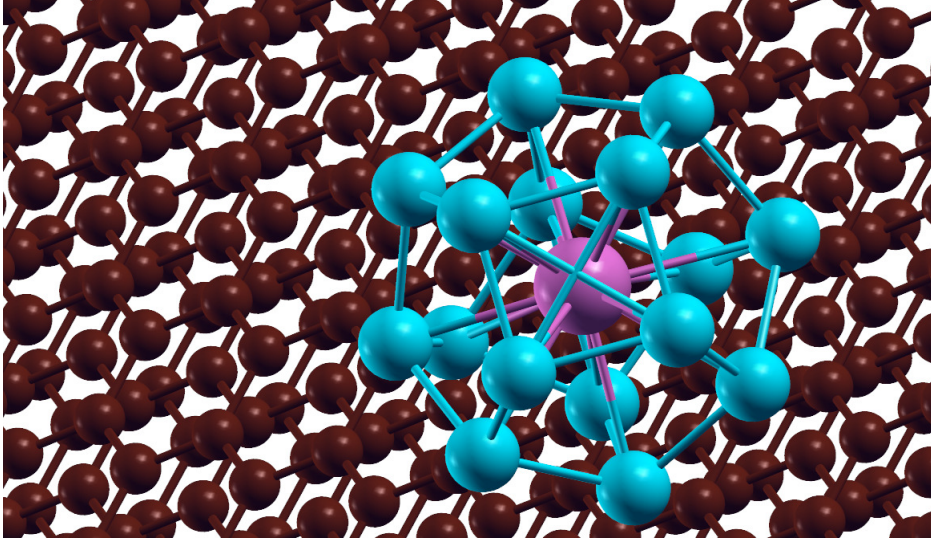


Figure 3.5: Adsorbed TaSi<sub>16</sub> on HOPG at  $\beta$  site with highest  $E_a$ .

### 3.5.3 Properties of adsorbed TaSi<sub>16</sub> cluster on HOPG with highest $E_a$

We found the minimum Si-C distance to be 3.43 Å which is larger than the sum of the covalent radii of the carbon and silicon atom which is around 1.84 Å. A small adsorption energy and a large Si-C distance confirms that there is no chemical bond formation between the cluster and the graphite surface. The cluster is thus physisorbed. This is interesting because one would generally expect C and Si atoms to form strong covalent bonds. But the  $\pi$  electrons on a graphite surface do not do so.

The magnetic moment on the deposited cluster system turned out to be  $0.99\mu_B$ , same as the free cluster. Since graphite is non-magnetic, this suggests that the spin moment of the free cluster remains undisturbed, and the moment should be localized on the cluster. This also indicates that there is no charge transfer between the cluster and the HOPG substrate. In order to confirm the last point we calculated Bader charges on all the atoms. There is negligible charge transfer ( $0.02 e$ ,  $e$  is electronic charge ) from the cluster to the substrate. We also plot an iso-surface of the spin density in the system as shown in Figure 3.6

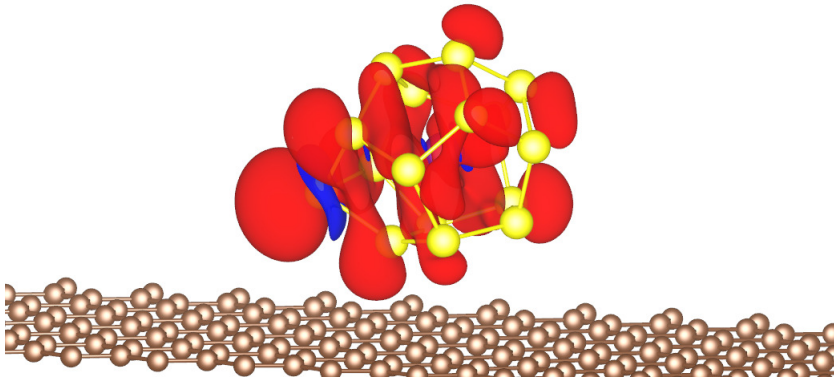


Figure 3.6: Spin density isosurface in TaSi<sub>16</sub> cluster deposited on HOPG.

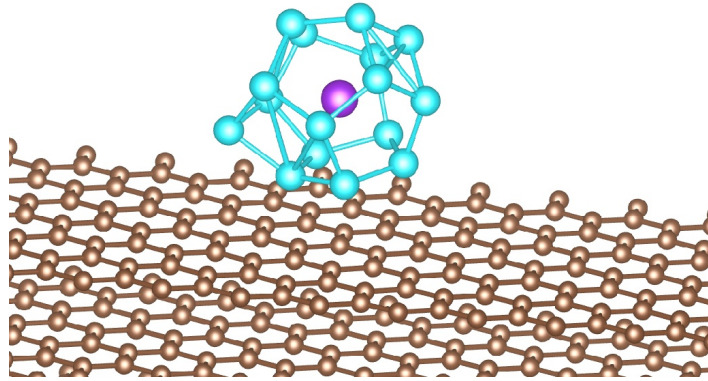
Clearly, the spin is localized on the cluster. These findings are consistent with a physisorption scenario. More importantly, these are consistent with the experimental observations as Shibuta et al. as they found the binding energy of the Si  $2p_{3/2}$  core level in the HOPG deposited TaSi<sub>16</sub> cluster to be very close to that in the bulk Si indicating a very small charge transfer from the cluster to the substrate. One difference should be indicated here. Our calculations are for a single cluster on the substrate, while the measurements are for an island of clusters. Yet, one can assume that the qualitative picture remains the same in the two cases.

In order to ascertain this point further, we analyze the charge density difference ( $\Delta\rho$ ) of the cluster- HOPG system. ( $\Delta\rho$ ) is defined as follows.

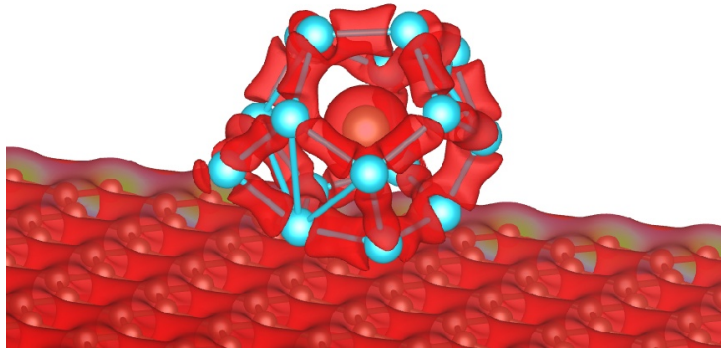
$$\Delta\rho(\vec{r}) = \rho_{cl/graphite}(\vec{r}) - (\rho_{cl}(\vec{r}) + \rho_{graphite}(\vec{r})) \quad (3.6)$$

“ $\rho$ ” s are the charge density of the respective systems. Any chemical bond between the cluster and the substrate atoms would show up as additional charge density in their intervening region. We plot a  $\Delta\rho$  isosurface in Figure 3.7(a) for an isovalue  $0.06 e/bohr^3$ . For comparison, a total charge density isosurface for the cluster-graphite system at the same value is shown in Figure 3.7(b).

Clearly, no isosurface is seen in Figure 3.7 (a). A  $\Delta\rho$  isosurface shows up between the cluster and the substrate only for values as small as  $10^{-5} e/bohr^3$ . This confirms that there are no cluster substrate chemical bonds. This is interesting because one would generally expect C and Si atoms to form strong covalent bonds. But the  $\pi$  electrons on a graphite surface do not do so. The height of the cluster, measured as the distance between the top layer carbon atom and the



(a)



(b)

Figure 3.7: Isosurface plots for (a)  $\Delta\rho$  and (b) total charge density with isovalue  $0.06 e/\text{bohr}^3$ .

highest Si atom, was found to be 1.12 nm, the same as in the experiments[4]. Thus, our calculations confirm the experimental claim that the islands are one cluster layer in thickness.

### 3.5.4 Structural and chemical stability: Reaction with oxygen

Shibuta et al.[4] studied the reaction of  $\text{TaSi}_{16}^+$  with oxygen, for establishing its stable superatomic character. Reaction of the cluster with oxygen, and any oxide formation, interpreted through core-level XPS spectra.  $\text{TaSi}_{16}$  showed substantial resistance toward reaction with oxygen. No changes in the core-level BE were observed below an oxygen exposure of  $10^4$  L (1 L (Langmuir) = exposure at  $10^{-6}$  Torr for 1 second). At  $5 \times 10^{10}$  L, the Si 2p and Ta 4f peaks stay at their original energies, but additional peaks appear at higher BE for both components indicating oxide formation. The Si 2p peak evolves more rapidly than the Ta 4f peak indicating that Si atoms react with oxygen more easily.

We have repeated this in our calculations. Since the deposited clusters essentially have the same structure and electronic properties as the free ones, we performed these calculations on free, isolated  $\text{TaSi}_{16}$  clusters to reduce the computational costs. Oxygen molecules were brought close to different faces of the Si cage. Several such initial structures were generated, keeping the Si-O larger than the sum of their covalent radii in each case. We have performed the spin polarized calculation in doublet quartet and sextet spin states. All these structures were then relaxed to their nearest local minima.

In all relaxed structures some of the  $\text{O}_2$  molecules dissociate, and the oxygen atoms get bonded to the nearby Si atoms forming their oxide, but did not find an oxygen atom getting inside the cage and forming an oxide of Ta. The above feature was found true for all spin states. In fact, we have checked the reaction of  $\text{O}_2$  with the cluster both in PBE-GGA and with vdW-DF2. In both case the dissociated oxygen atoms get attached to the Si atoms and not with the central

Ta atom.

We could not perform any calculation by inserting even a single  $O_2$  molecule inside the cage. As there were no suitable position for the  $O_2$  molecule such that the O-Ta and O-Si bond lengths are a little bit greater than sum of their respective covalent radii.

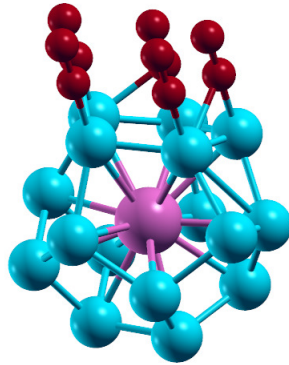


Figure 3.8: Initial structure for reaction with Oxygen

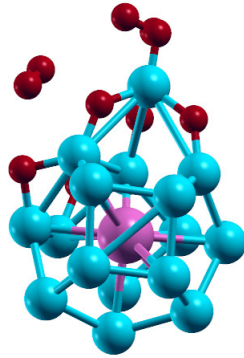


Figure 3.9: Relaxed structure after oxygen atoms get attached with the cluster

We performed one calculation with the TaSi<sub>16</sub> cluster deposited on HOPG with  $O_2$  molecules in one face of the cluster. We choose the surface such that Oxygen molecules could not come close to the C atoms as we wanted to observe how the cluster reacts with the Oxygen molecules after deposited on the substrate.

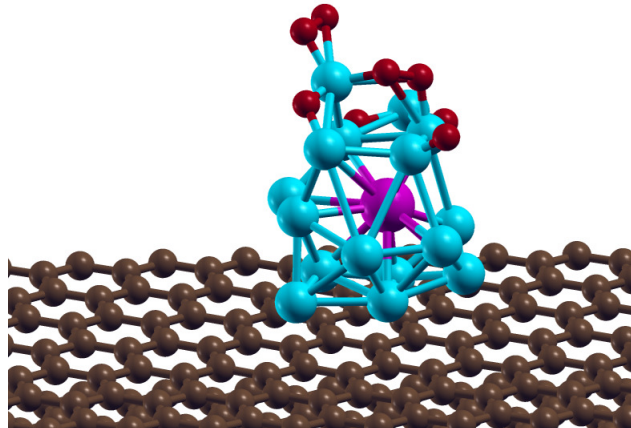


Figure 3.10: Relaxed structure of deposited cluster on HOPG including reaction with Oxygen

From Fig 3.9 and Fig 3.10 it is found that some of the Oxygen molecules dissociated and made bonds with the Si atoms and the central Ta atom did not get oxidized. The cluster also maintains its basic cage structure but it gets distorted markedly as mentioned in the experiment by Shibuta et al.

### 3.5.5 Finite temperature behavior: Molecular dynamics simulation

After heating the deposited cluster system at 700 K for 16 hours, Shibuta et al[4] observed a shift of the Si 2p core level to a slightly higher binding energy, while the Ta 4f binding energy remained almost unchanged. This was interpreted as a change in the silicon cage structure, perhaps due coalescence of the clusters, or partial coalescence of the cluster with the HOPG substrate. After heating at 400 K, individual clusters were still discernible. In order to have a microscopic insight into how the deposited clusters behave at finite temperatures, we performed a molecular dynamics of the system at 400 K and 700 K. Since we have a single cluster in our simulation cell, it is obviously not possible to study coalescence of

clusters. But any coalescence of the cluster with the HOPG substrate will be observable. Whether the Ta atom is enclosed inside the Si cage, even if there is any cluster-substrate coalescence, will also be clear. In addition, how or whether the clusters diffuse on the substrate will be visible.

We started the MD calculations from the lowest energy structure for the adsorbed cluster. For 400 K temperature we continued the ab initio molecular dynamics calculation up to 10 ps. During this simulation we found that the Ta encapsulated 16 atom Si cluster is vibrating on the HOPG. But it never diffused on the substrate. The structure becomes distorted at different time steps but it always maintained its cage structure with keeping Ta atom in the almost center of the cage formed by 16 Si atoms. The shape of the deposited cluster changes very rapidly and it never turned to a different isomer atleast upto 10 ps.

For MD simulation at 700 K we found the same behaviour of the deposited cluster as that at 400 K. We have continued our calculation upto 9 ps. The cluster maintains its cage structure here also with some distortion. The Si-Si bond lengths as well as the Ta-Si bond lengths were fluctuating more rapidly than 400 K.

From the ab initio molecular dynamics calculation at both the temperatures it is found that the TaSi<sub>16</sub> cluster maintains its metal encapsulating framework even at high temperature. According to Shibuta et al. after heating at temperature around 400 K the individuality of the TaSi<sub>16</sub> remained discernible in the STM images for the aggregated islands on HOPG. For both the temperatures the deposited cluster on HOPG maintained its basic cage structure with distortion. This behaviour agrees with the fact reported by Nakajima et al. that after heating at a temperature near 700 K the Si 2p level slightly shifted toward the higher binding energy (99.5 eV) and asymmetrically broadened on the higher BE side.

But the shape of Ta 4f level was almost unchanged.

### **Energy barrier between two lowest energy configurations: CI-NEB method**

There was little diffusion of the cluster at either temperature over this time scale. This is surprising because a physisorbed cluster having weak binding to the substrate may diffuse easily. It was difficult for us to continue ab initio MD calculations beyond picosecond time scales for such a large system. Instead, we try to estimate the diffusion time scale by assuming an activated behavior so that the rate of diffusion is given by the Arrhenius equation  $Aexp(-\Delta/K_B T)$ . Here,  $\Delta$  is the energy barrier and  $A$  is the attempt frequency. We estimate the energy barrier between the two lowest energy configurations of the cluster on the substrate using the climbing image nudged elastic band (CI-NEB) method as mentioned in chapter 2.

In our CI-NEB calculation we have taken the initial configuration as with highest  $E_a$  and final configuration as second highest  $E_a$  as mentioned in table 3.2. We have taken 4 images between initial and final structures. Due to high computational costs we could not perform the CI-NEB calculation with HOPG supported TaSi<sub>16</sub> cluster with large number of images. Our estimate of the barrier  $\Delta = 1.42$  eV as shown in Fig3.11. Assuming a typical value of  $10^{14}$  for  $A$ , the crossover rate is found to be  $5 \times 10^3$  s<sup>-1</sup> at 700 K. This suggests a diffusion time scale of a few tenths of a millisecond. Though out of the reach of ab initio MD calculations, this is clearly within experimental time scales, and so aggregation of clusters was observed. More importantly, there was no coalescence between the cluster and the substrate. Therefore, changes seen in the XPS spectra are either due to intercluster coalescence or distortions in the shape of the individual

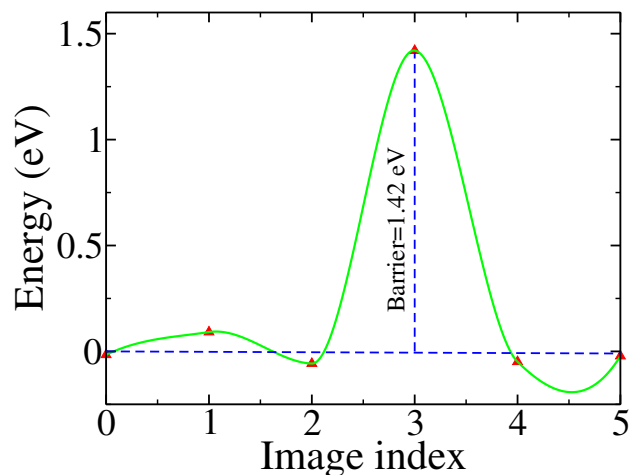


Figure 3.11: Energy barrier from CI-NEB calculation

clusters.

Absence of transition to other isomers, at least over a time scale of picoseconds, has some bearing on a speculation in Shibuta et al.s paper. Absence of a definite peak in UPS spectra was surmised to be due to rapid transition between different isomers, in analogy with  $\text{VSi}_{16}^+$  [70]. While we rule out transition between isomers, we offer an explanation for the lack of UPS peaks based on our MD results. The central idea is that the distortions in the cluster structure at finite temperature cause enough change in the energies of the valence electron levels for any UPS peaks to get washed out. By following the energy of the highest occupied molecular orbital (HOMO) level of the TaSi 16 cluster during the MD simulations we find that it can change by as much as 1 eV. Variations of the HOMO energy with time at both temperatures are shown in Fig3.12. Perhaps this large variation in the HOMO (and other valence levels) is responsible for absence of any distinct peaks in UPS.

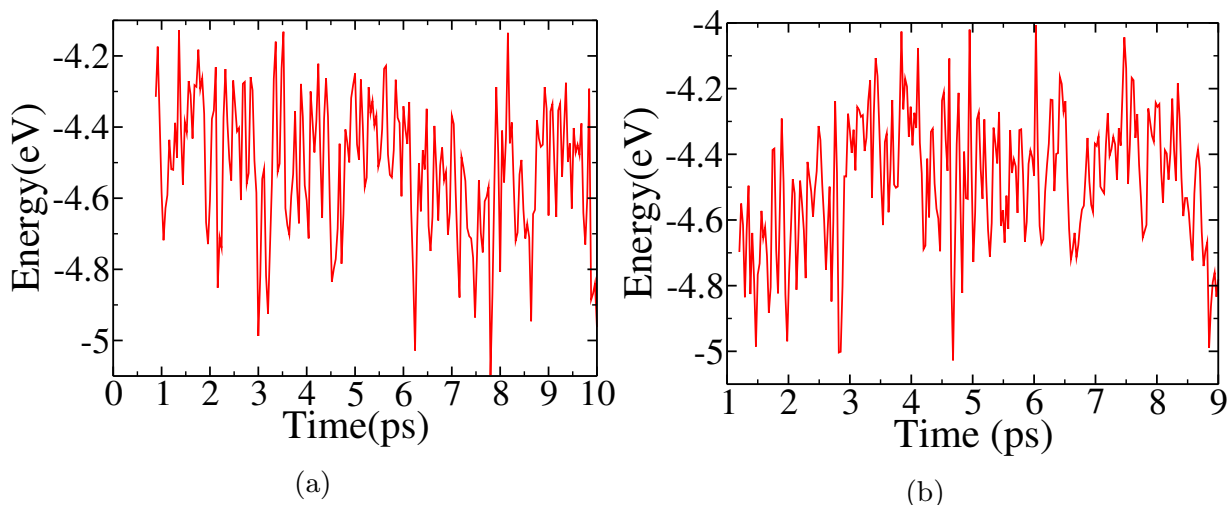


Figure 3.12: Variation of HOMO energy of deposited TaSi 16 cluster at (a) 400 K and (b) 700 K.

### 3.6 Conclusions

We have studied free and HOPG-supported TaSi<sub>16</sub> cluster using DFT methods deriving fresh physical insights into this system in light of the recent experiments by Shibuta et al. For the first time, a global search for the ground-state structure of the neutral TaSi<sub>16</sub> cluster is performed. A symmetric structure of the Si<sub>16</sub> cage encapsulating the Ta atom explains why only a single core-level peak is observed for all the Si atoms, while a small charge transfer from Ta to the Si atoms explains why there is little shift in the Si core-level energies. Energetics of TaSi<sub>16</sub> on HOPG and charge density isosurface plots suggest that the cluster is physisorbed. There is little change in either the geometric or the electronic structure of the cluster after deposition. This is an ideal situation for forming self-assemblies of the deposited clusters. Reaction of the cluster with O<sub>2</sub> molecules is also studied in a limited way. Ab initio MD simulations at finite temperatures show that the deposited cluster does not transform to other isomers up to 700 K

and there is no coalescence between the cluster and the substrate. Rather, the vibrations of the cluster around its lowest energy structure is sufficient to cause changes in the energy position of HOMO and other valence levels so that no peaks are observed in UPS. While our calculations validate some of the conclusions in ref [4], they suggest different atomistic details for some others. Therefore, these two studies complement each other and together provide valuable information on this important system.

# Designing of rare earth free permanent magnet: Insights from small Co cluster

## 4.1 Motivation

For modern society, high performance permanent magnets are very important key technology . These form essential parts in various devices in a wide range of applications. These include hybrid and electric cars, wind turbines, motors in many household appliances, satellite communications systems[272] and magnetic data storage systems. Because of supply risk and increasing demand of rare earth (RE) elements Dy, Tb, Nd, Eu, Yb; which used in formation of permanent magnets, there is an urgent drive to design permanent magnets without RE elements.

The most widely used permanent magnets (PM) in present day applications are  $\text{Nd}_2\text{Fe}_{14}\text{B}$  and SmCo type alloys,  $\text{SmCo}_5$  in particular. NdFeB magnets are used in modern acoustic transducers which are used in speakers, consumer electronic devices, cell phones, cars etc. NdFeB magnets are necessary for eco-friendly

transport and sustainable energy production. NdFeB magnets have also been used in hard disk drives. SmCo magnets are well known for their use in musical instruments like electric guitars and headphones. These are widely used in high-end electric motors used in the more competitive classes in slotcar racing, turbomachinery etc.

These are distinguished by (i) the high magnetic field they can create and (ii) their high resistance to opposing magnetic fields. A high spontaneous magnetization and high magneto-crystalline anisotropy or magnetic anisotropy energy (MAE) are the main required criteria for an efficient PM. Generally they are required to have large Curie temperature ( $T_c$ ), large saturation magnetization ( $M_s$ ), and large coercivity ( $H_c$ ). The last two properties are conveniently expressed together in what is called the energy product or  $(BH)_{max}$ . Large coercivity is a result of large anisotropy energy[272].

Nd<sub>2</sub>Fe<sub>14</sub>B has an energy product of 512 kJ/m<sup>3</sup>. SmCo-type magnets have energy product of 294 kJ/m<sup>3</sup>, and a large  $T_c$  in excess of 800° C. But as they are more expensive so there is a search for alternative ways to form permanent magnets without RE.

Among the RE-free hard magnets currently in use are FePt, CoPt and HfCo alloys[113]. However, Pt and Hf are also very expensive metals, and so there is a search for less expensive alternatives. Some theoretical modeling has played an important role in such searches. The works by Burkert et al.[119], and Delczeg-Czirjak et al.[123] are mentioned in chapter 1. Reichel et al.[126] have shown in their experiments that doping of C in FeCo alloy allows for thick films for obtaining large MAE.

El-Gendy et al.[5] synthesized cobalt-carbide nano-particles by wet chemical means that had MAE values close to 100 eV/Co (0.75 MJ/m<sup>3</sup>), significantly

larger than that of bulk hcp Co. These had a blocking temperature of 571 K, and  $T_c$  equal to 650 K, both much higher than room temperature. An even larger MAE of 4.6 MJ/m<sup>3</sup> was found in CoFe<sub>2</sub>C nano-particles, a value comparable to that of the Nd-based 2-14-1 alloy[145]. Such large increases in MAE in nanoscale systems is interesting, and opens a practical way of designing permanent magnets without RE elements.

After the encouraging experimental findings, one requires fundamental understanding of the factors that control MAE in these systems in order to design new materials. Islam and Khanna addressed this issue in their work on Co<sub>4</sub>A<sub>2</sub> (A=C, Si) clusters[6]. They found large enhancement of MAE compared to bulk Co in Co<sub>4</sub>C<sub>2</sub> and Co<sub>4</sub>Si<sub>2</sub> clusters, and their assemblies. They mentioned several factors as probable causes for increase in MAE. These are: (i) larger orbital moment compared to bulk, (ii) increase in the spin moment on the Co atoms, (iii) mixing between Co d and the p states of the A atoms. But, no further analysis for this was presented.

Given this state of affairs, we addressed the following questions. Are C and Si the best dopants, or there are other dopants that lead to larger MAE in Co clusters? Do heavier dopant atoms (Ge, for example), due to their larger spin-orbit coupling compared to C and Si, produce higher MAE? Which factors, among the three mentioned above, affect MAE most significantly? Once an understanding of these basic issues are put on a firm basis, this can then be used in design of new systems, whether at the nano scale or in the bulk.

For this purpose we study structural and magnetic properties of Co<sub>4</sub>A<sub>2</sub> clusters, where A is one of the following elements from group 14 and 15: C, Si, Ge, N, P and As. We present the details of our work and our major conclusions in the following sections.

## 4.2 Computational methods

All calculations were performed within the framework of plane wave DFT as implemented in the VASP code[216, 217, 264–266]. Projector augmented wave (PAW) potentials [211] represented the interaction between the valence electrons and the ion cores. To identify the low energy structures for  $\text{Co}_4$ ,  $\text{Co}_6$  and  $\text{Co}_4\text{A}_2$  clusters at first a global search was performed employing an evolutionary algorithm. The USPEX[230–232] code was used for this. The initial population for each cluster species was generated without any constraint on point group (PG) symmetry, i.e., coordinates of the cluster atoms were generated in a completely random manner. Population in each subsequent generation was produced through the application of variational operations of heredity, mutation, and soft mutation[232]. A population size of 12 (10 for  $\text{Co}_4$ ) was maintained in each generation. The fitness criterion for choosing the best structures was the energy of the clusters. Calculation was continued up to a maximum of 25 generations (15 for  $\text{Co}_4$ ) subject to the condition that, if the energy of the best structure was unchanged over a predecided number of successive generations, it would be stopped. This number was initially set equal to the number of atoms in the clusters, i.e., 6. However, this gave a relatively small number of distinct structures in case of Si, Ge, N and As, and was, therefore, was increased to 10.

The energies of these clusters were calculated using DFT. Clusters were placed inside a box whose size was generated by USPEX automatically. A minimum vacuum length of 15 Å was enforced on all sides of the cluster to nullify the interaction of a cluster with its periodic image. Using the  $\Gamma$ -point only, the Brillouin zone integrations were performed. For each structure, energy calculations in VASP were performed at five increasing levels of accuracy in terms of both the kinetic energy

cutoff and force convergence criterion. For the first two levels, the kinetic energy cutoff was determined by the ENMAX of the POTCAR files of Co (268 eV). For the next three levels it was 320 eV. For the first level the force convergence criterion was 0.2 eV/Å. For the next three levels it was 0.1 eV/Å, and in the final level it was 0.01 eV/Å. This global search was performed using the spin-polarized PBE-GGA exchange-correlation functional[197]. After finishing the global search with, the best structure from each generation were collected. These structures were again optimized using PBE-GGA in a spin-polarized calculation. For this re-optimization calculation, the kinetic energy cutoff was set at 600 eV and the force convergence criterion was 0.001 eV/Å. The re-optimization of the structures which were selected from USPEX, were performed in all possible spin states from  $S_z = 0$  to 6, or even higher in some cases, where  $S_z$  is the z-component of spin, and is equal to half the difference between the number of up and down spin electrons, the usual convention in DFT. Also,  $S_z$  corresponds to a spin moment of  $M_S = 2S_z$ , where the factor 2 is the gyromagnetic ratio,  $g$ .

For calculating MAEs, the energies of the clusters with various orientations of the spin moment were calculated with adding the spin-orbit coupling term in the Hamiltonian. The details are mentioned in chapter 2. A spherical polar coordinate system was considered in which the  $x$  and  $z$  axes coincide with those of our cubic supercell. The polar angle  $\theta$  and azimuthal angle  $\phi$  for the spin direction were varied in the intervals  $[0,\pi]$  and  $[0,2\pi]$  respectively. 11 values each for  $\theta$  and  $\phi$  giving a total of 121 directions were taken. Energies of a cluster was calculated with the spins pointing along each of these directions. The magnetic easy axis is designated as the direction for which the energy is lowest. The direction giving the highest energy is designated as the hard axis. Difference in energy between these two spin directions is the measure of MAE.

Energy of a cluster in presence of spin-orbit coupling was calculated using two different methods. In the first method, charge density and wave functions were read in from a previously converged calculation without spin-orbit coupling. The charge density was kept unchanged during the calculation of total energy in presence of the spin-orbit term. In the second method, total energy was calculated by performing a fully self-consistent calculation, i.e., the charge density was varied, and energy was optimized in presence of the spin-orbit coupling term. More details about treatment of spin-orbit coupling within PAW formalism can be found in reference[273]. For a few clusters, the self-consistent method failed in presence of the spin-orbit term. In cases that both the methods worked, they gave the same result.

## 4.3 Results and discussions

### 4.3.1 Pure Co<sub>4</sub> and Co<sub>6</sub> clusters

In case of pure Co<sub>4</sub> and Co<sub>6</sub> ground state structure, our results agrees well with previously reported results. Two lowest energy structures and spin states for both Co<sub>4</sub> and Co<sub>6</sub> are shown in Figure 4.1.

Co<sub>4</sub> turns out to have a little distorted tetrahedral structure having D<sub>2d</sub> PG symmetry with M<sub>S</sub> = 10 μ<sub>B</sub>. PG symmetry of the clusters are determined by the VMD software[274]. This result agrees with the reported results of Datta et al.[275] who also found a magnetic moment of 10 μ<sub>B</sub> in the ground state of Co<sub>4</sub>. But they did not report any distortions from the tetrahedral symmetry. The next higher energy cluster is a planar rhombus with D<sub>2h</sub> PG symmetry also with M<sub>S</sub> = 10 μ<sub>B</sub>. This is 0.075 eV higher than the ground state.

The ground state of Co<sub>6</sub> cluster was found with octahedron(O<sub>h</sub>) PG symmetry.

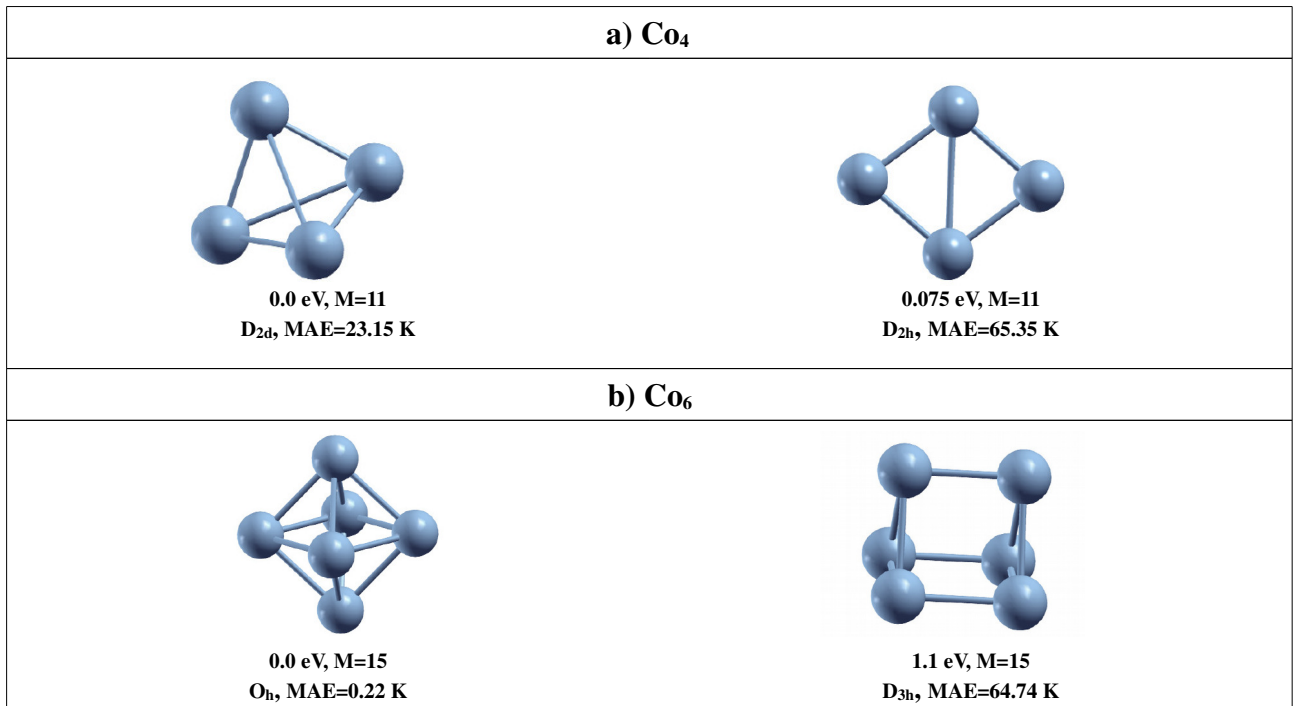


Figure 4.1: Two lowest energy Co<sub>4</sub> and Co<sub>6</sub> clusters obtained from global search.

Its magnetic moment was found as  $14 \mu_B$ . This is in agreement with the results of Datta et al.[275]. However, like them, no cluster with  $M_S = 12 \mu_B$  was found close to the ground state. The next isomer is 1.1 eV higher which has D<sub>3h</sub> PG symmetry and magnetic moment  $14 \mu_B$  as shown in Figure 4.1(b).

## 4.4 Doped Co clusters

As mentioned earlier, the doped clusters are also obtained by global search. The group 14 elements doped clusters are discussed first followed by group 15. All doped clusters within  $\sim 0.5$  eV of the ground state for each species are discussed here.

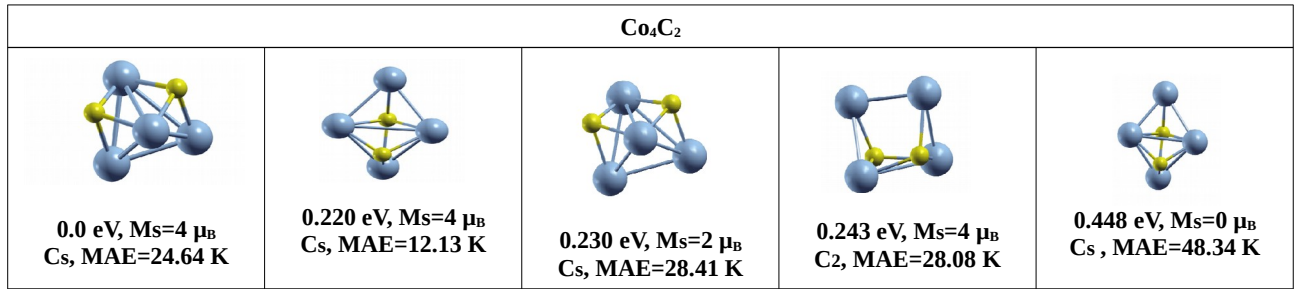


Figure 4.2: Globally optimized  $\text{Co}_4\text{C}_2$  clusters: upto  $\sim 0.5$  eV

#### 4.4.1 $\text{Co}_4$ doped with group 14 elements

The ground state structure of  $\text{Co}_4\text{C}_2$  has been found to have  $C_s$  PG symmetry, and  $M_S = 4 \mu_B$ . The next higher energy cluster has magnetic moment  $M_S = 4 \mu_B$  in  $C_s$  symmetry but with very different arrangement of the atoms from the ground state. This is 0.22 eV higher than the ground state. The second higher energy cluster is nearly degenerate with the previous one, 0.23 eV higher than the ground state, has the same  $C_s$  symmetry as the ground state and arrangement of atoms almost same as the ground state, but has magnetic moment  $2 \mu_B$ . The next cluster is at 0.243 eV from the ground state, has  $M_S = 4 \mu_B$  and  $C_2$  symmetry. The next one is 0.448 eV higher than the ground state, and is a singlet in  $C_s$  symmetry. Four more clusters within  $\sim 0.6$  eV of the ground state have been obtained.  $\text{Co}_4\text{Si}_2$  has  $D_{2h}$  PG symmetry in the ground state, as shown in Figure 4.3 and with  $M_S = 6 \mu_B$ . The next higher energy cluster is also with magnetic moment  $6 \mu_B$  and is 0.106 eV above the ground state, but with PG symmetry  $D_{4h}$ . The next isomer is also a  $D_{4h}$  structure, 0.439 eV higher than ground state, and with  $M_S = 4 \mu_B$ . Rest of the clusters we obtained are more than 0.5 eV higher than the ground state. With doping group 14 Ge element,  $\text{Co}_4\text{Ge}_2$  also has a  $D_{4h}$  structure in its ground state as was obtained from global search, and

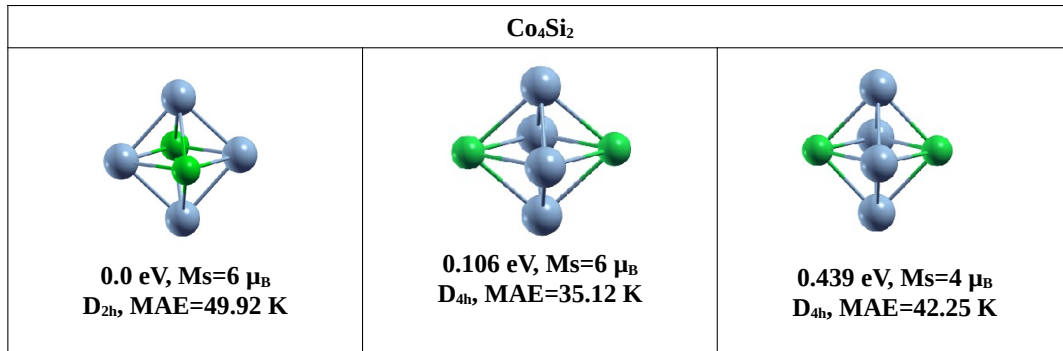


Figure 4.3: Globally optimized Co<sub>4</sub>Si<sub>2</sub> clusters: upto ~ 0.5 eV

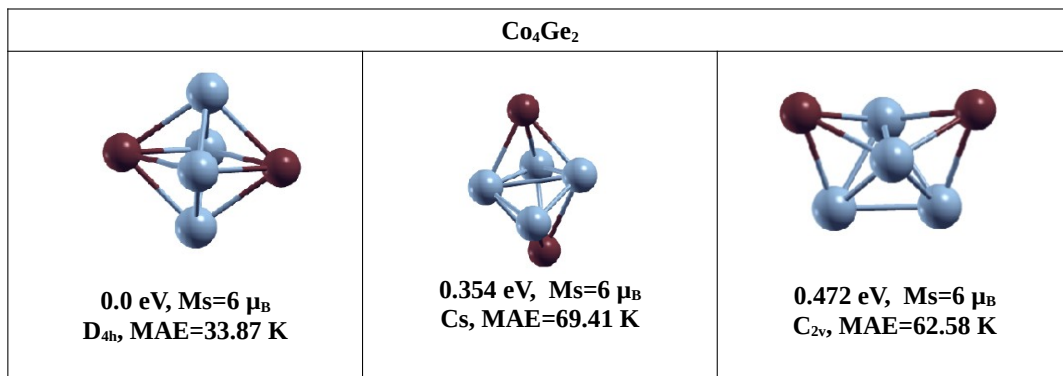


Figure 4.4: Globally optimized Co<sub>4</sub>Ge<sub>2</sub> clusters: upto ~ 0.5 eV

with  $M_S = 6 \mu_B$ . The next higher energy cluster with energy 0.354 eV higher than ground state also has magnetic moment  $6 \mu_B$  but has  $C_s$  symmetry. The next is also in  $M_S = 6 \mu_B$  state, 0.472 eV higher and with  $C_{2v}$  PG symmetry.

#### 4.4.2 Doped with group 15 elements

The globally optimized ground state Co<sub>4</sub>N<sub>2</sub> cluster has  $C_s$  PG symmetry and  $M_S = 8 \mu_B$  as shown in Figure 4.5. The interesting fact here is the two N atoms attach as a dimer to the Co<sub>4</sub> cluster, which is in a tetrahedral structure, in the ground state. In fact, except for the next higher energy cluster, with the  $C_{2v}$  PG

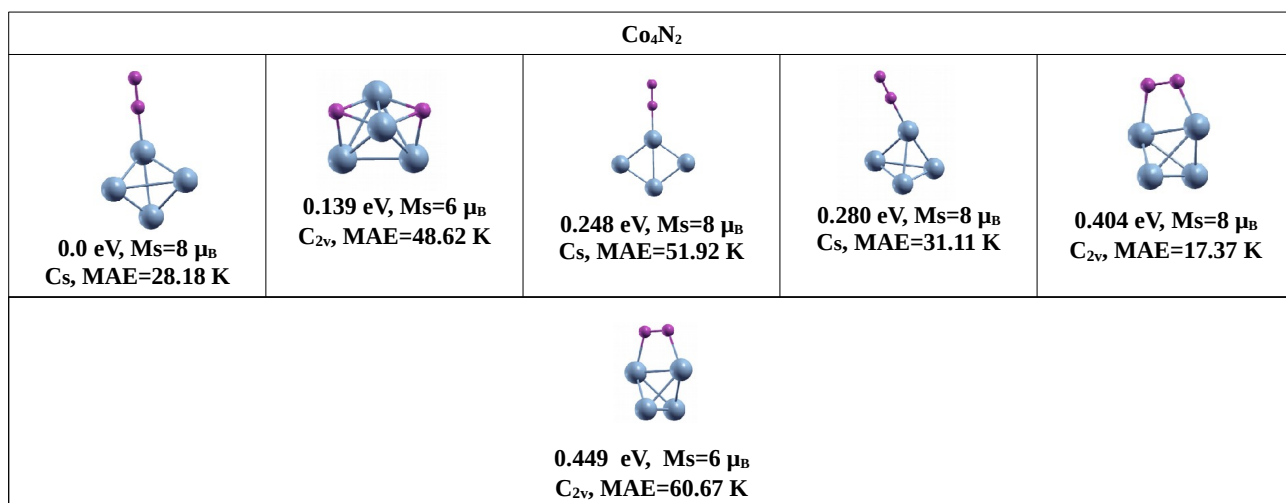


Figure 4.5: Globally optimized Co<sub>4</sub>N<sub>2</sub> clusters: upto  $\sim 0.5$  eV

symmetry and  $M_S = 6 \mu_B$ , all other structures shown in Figure 4.5 maintain this structural pattern. This could be due strong N-N triple bond in an N<sub>2</sub> dimer. It is energetically favorable for it to attach to Co<sub>4</sub> as a single unit rather than bonding dissociatively. In the third high energy cluster, the N<sub>2</sub> dimer attaches to a planar Co<sub>4</sub> cluster in rhombus structure. It has C<sub>s</sub> PG symmetry and magnetic moment  $8 \mu_B$ . The next one again has C<sub>s</sub> PG symmetry and  $M_S = 8 \mu_B$ , but the N<sub>2</sub> dimer now attaches to a tetrahedral Co<sub>4</sub> motif. In case of the two next higher energy isomers, N<sub>2</sub> dimer attaches to distorted Co<sub>4</sub> tetrahedra, and both the N atoms are bonded to Co atoms. Both structures have C<sub>2v</sub> symmetry. They are 0.404 and 0.449 eV above the ground state, and have  $M_S = 8 \mu_B$  and  $M_S = 6 \mu_B$  respectively.

The ground state for Co<sub>4</sub>P<sub>2</sub> was found a C<sub>2v</sub> structure with magnetic moment  $6 \mu_B$  as shown in Figure 4.6. The next isomer is 0.041 eV above the ground state and has  $M_S = 8 \mu_B$  was found with C<sub>2v</sub> PG symmetry but with different atomic

<b>Co<sub>4</sub>P<sub>2</sub></b>				
 <b>0.0 eV, M<sub>S</sub>=6 μ<sub>B</sub></b> <b>C<sub>2v</sub>, MAE=35.12 K</b>	 <b>0.041 eV, M<sub>S</sub>=8 μ<sub>B</sub></b> <b>C<sub>2v</sub>, MAE=5.57 K</b>	 <b>0.082 eV, M<sub>S</sub>=6 μ<sub>B</sub></b> <b>C<sub>1</sub>, MAE=26.13 K</b>	 <b>0.110 eV, M<sub>S</sub>=6 μ<sub>B</sub></b> <b>D<sub>4h</sub>, MAE=19.41 K</b>	 <b>0.198 eV, M<sub>S</sub>=8 μ<sub>B</sub></b> <b>C<sub>s</sub>, MAE=44.47 K</b>
 <b>0.450 eV, M<sub>S</sub>=0 μ<sub>B</sub></b> <b>C<sub>2v</sub>, MAE=17.5 K</b>		 <b>0.459 eV, M<sub>S</sub>=4 μ<sub>B</sub></b> <b>C<sub>s</sub>, MAE=29.14 K</b>		

Figure 4.6: Globally optimized Co<sub>4</sub>P<sub>2</sub> clusters: upto ~ 0.5 eV

arrangement from the lowest energy structure. The next one is a C<sub>1</sub> and with magnetic moment 6 μ<sub>B</sub>. It is 0.082 eV higher in energy. The fourth and the fifth ones are M<sub>S</sub> = 6 μ<sub>B</sub> and M<sub>S</sub> = 8 μ<sub>B</sub> having D<sub>4h</sub> and C<sub>s</sub> symmetry respectively. They are 0.11 and 0.198 eV above the ground state respectively. The last two clusters are 0.45 eV above the ground state, are with 0 magnetic moment and M<sub>S</sub> = 4 μ<sub>B</sub> with C<sub>2v</sub> and C<sub>s</sub> PG symmetry respectively.

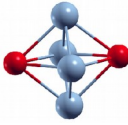
<b>Co<sub>4</sub>As<sub>2</sub></b>				
 <b>0.0 eV, M<sub>S</sub>=8 μ<sub>B</sub></b> <b>D<sub>4h</sub>, MAE=50.14 K</b>	 <b>0.034 eV, M<sub>S</sub>= 8μ<sub>B</sub></b> <b>C<sub>2v</sub>, MAE=16.28 K</b>	 <b>0.142 eV, M<sub>S</sub>=6 μ<sub>B</sub></b> <b>C<sub>2v</sub>, MAE=39.32 K</b>	 <b>0.244 eV, M<sub>S</sub>=8 μ<sub>B</sub></b> <b>C<sub>s</sub>, MAE=70.36 K</b>	 <b>0.485 eV, M<sub>S</sub>=2 μ<sub>B</sub></b> <b>C<sub>s</sub>, MAE=38.59 K</b>

Figure 4.7: Globally optimized Co<sub>4</sub>As<sub>2</sub> clusters: upto ~ 0.5 eV

The next group 15 elements As when doped with Co, the globally optimized lowest energy isomer of Co<sub>4</sub>As<sub>2</sub> was found with magnetic moment 8 μ<sub>B</sub> and it is

with PG  $D_{4h}$ . The next one is also one with  $M_S = 8 \mu_B$ , and is 0.034 eV higher than the ground state. It has PG symmetry  $C_{2V}$ . The third one is a  $C_{2v}$ ,  $M_S = 6 \mu_B$  and 0.142 eV from the ground state. The fourth one has again magnetic moment  $8 \mu_B$  and has a  $C_s$  PG symmetry. It is 0.244 eV from the ground state. The last cluster is a  $C_s$  with magnetic moment  $2 \mu_B$  and is 0.485 eV above the ground state as shown in Figure 4.7.

It is observed that all the doped clusters have lower spin moments in their respective ground states compared to the  $Co_4$  cluster mentioned in earlier section 4.3.1. Bonding with non-magnetic dopants is responsible for reduction in moments. C leads to the largest decrease in magnetic moment, for N and As it was obtained as smallest. In comparison with the  $Co_6$  cluster,  $Co_4A_2$  clusters can be treated as two Co atoms being replaced by non magnetic atoms. It was found the magnetic moments in these  $Co_4A_2$  clusters are much lower than that in the pure  $Co_6$  cluster as shown in Figure 4.1(b).

### 4.4.3 Discussions on MAE:search for trends

After obtaining the ground states for each of the species, the MAEs were calculated for all of them. The main goal is to find any patterns in MAE based on the non magnetic dopant A atom. The ground state  $Co_4C_2$  cluster has a MAE of 24.64 K as shown in Figure 4.2. This matches with the results of Islam and Khanna [6]. Their reported MAE is for a completely different structure and spin state. For dopants from group 14,  $Co_4Si_2$  and  $Co_4Ge_2$  have MAEs of 49.92 K and 33.87 K in their respective ground states respectively. Islam and Khanna [6] has reported an anisotropy of 40.34 K for  $Co_4Si_2$ , but their structure is very different.

For the group 15 elements, the  $Co_4N_2$  cluster has been found the ground state

with MAE of 28.18 K.  $\text{Co}_4\text{P}_2$  with 35.12 K and for  $\text{Co}_4\text{As}_2$  the MAE is 50.14 K respectively as shown in Figure 4.6 and 4.7 respectively.

The calculated MAE values for the ground state  $\text{Co}_4$  and  $\text{Co}_6$  clusters are 23.2 K and 0.22 K respectively as depicted in Figure 4.1. Hence it is clear that all the doped clusters have larger MAE compared to  $\text{Co}_4$ .

However, the broad picture is that there are no trends in the MAE of these clusters depending on the group or period to which the dopant atoms belong. As a summary it is found that Group 15 elements N and P lead to similar MAE values as group 14 elements C and Ge respectively and Si has MAE value comparable to As. The  $\text{Co}_4\text{C}_2$  has the lowest MAE among all the clusters in their ground states.

As no pattern has been found in the MAE of the ground state clusters, MAE of few higher energy isomers for each dopant were calculated. MAE values for clusters having energy upto 0.5 eV from the ground state isomer of each species have been mentioned in previous sections. The higher energy clusters for  $\text{Co}_4\text{C}_2$  have MAEs 12.13, 28.41, 28.08 and 48.34 K respectively. Thus, while one of the clusters has very low MAE, one has MAE as large as that of  $\text{Co}_4\text{Si}_2$ . In case of  $\text{Co}_4\text{Si}_2$ , both the higher energy clusters have lower MAEs compared to the ground state.  $\text{Co}_4\text{Ge}_2$  is showing different feature, the two higher energy clusters have higher MAEs: 69.41 K and 62.58 K. Those are enough higher values than the MAE of the ground state cluster. Higher energy  $\text{Co}_4\text{N}_2$  clusters show an interesting MAE values. Some of them have much larger MAE than the ground state: 48.62, 51.92 and 60.67 K; there is one that has a much lower MAE: 17.37 K. In case of  $\text{Co}_4\text{P}_2$ , most of the higher energy clusters have lower MAE than the ground state. One of these is as low as 5.57 K. Only one cluster, with  $C_s$  PG symmetry, at 0.198 eV, has a higher MAE of 44.47 K. For  $\text{Co}_4\text{As}_2$  one of the higher

energy clusters has a higher MAE as 70.36 K compared to the ground state. The other three have lower MAEs. Hence no correlations was found between MAEs and the dopant type even in the higher energy clusters.

#### **4.4.4 Central question: Which is(are) responsible factor(s) for controlling the MAE value?**

As no straight forward pattern for MAE values of  $\text{Co}_4\text{A}_2$  clusters has been found, the central question arises as which one(s) among spin and orbital moments, HOMO-LUMO gap and d-p mixing is/are the most significant determinant(s) of MAE. For addressing the question, MAE of large number of clusters (total 60 clusters, including the isomers with energy upto 0.5 eV as mentioned in the previous sections) from each species were calculated.

#### **Role of predicted entities for controlling calculated MAE values in $\text{Co}_4\text{A}_2$ clusters**

For defining the degree of mixing between the Co d and dopant p states, at first it has to be noted that all the frontier orbitals are dominated by the Co d states. There are small contributions from the dopant p states. The mixing parameter is defined here as

$$M_{dp} = \frac{c_d - c_p}{c_d + c_p} \quad (4.1)$$

Here  $c_d$  is noted as the sum of weights of the Co d orbitals to the highest occupied and lowest unoccupied molecular orbitals (HOMO and LUMO).  $c_p$  is the sum of weights of the dopant p states to the same orbitals. In the calculations with

plane wave basis, contribution of a particular atomic orbital (AO) to a molecular orbital (MO) is obtained by projecting the MO onto a spherical harmonic  $Y_m^l$ , which is finite within a sphere of a certain predefined radius centered on the corresponding atom, and has the same (l, m) as the AO. The way it is defined,  $M_{dp}$  is a real number in the range [0, 1]: 0 indicates equal d and p contributions, while 1 would mean no contributions from the p states. So Larger d-p mixing would lead to smaller values of  $M_{dp}$  according to the relation 5.1.

To determine the role of spin magnetic moments, the sum of the absolute values of the spin moments on all the atoms ( $\sum_i |m_i|$ , where  $m_i$  is the spin moment on the i-th atom in the cluster). Spin moment on a particular atom is defined as the difference between the total up and down spin electron densities with a sphere around that atom. As spheres cannot fill space, these atomic spheres should either leave voids or overlap with neighboring ones. Thus the sum of atomic spins either leads to an underestimation or overestimation of the total moment. In this case, there is an underestimation. But fortunately that does not change the qualitative picture at the end of these analyses. It is important to take  $\sum_i |m_i|$  rather than the total spin of the cluster. As MAE originates from spin-orbit coupling, is essentially an atomic property, and depends on the spin on each individual atom rather than their mutual orientation.

To determine the role of orbital moment the quantity

$$\Delta L = \sum_i |L_{easy,i} - L_{hard,i}|$$

in which  $L_{easy,i}$  and  $L_{hard,i}$  are the orbital moments on the i-th atom when spins are aligned along the easy and the hard axes respectively, is considered. This consideration is important because Bruno has suggested that in 3d transition

metal systems, MAE can be expressed as  $\frac{\lambda}{4}|L_{easy} - L_{hard}|$  [257],  $\lambda$  being the spin-orbit coupling constant of the atom as discussed in the method chapter.

### Scatter plots: Visualization of MAE as functions of different parameters

To address this central question which is/are the controlling factor/factors of MAE of a cluster, scatter plots on different planes defined by two of the four factors (HOMO-LUMO gap,  $M_{dp}$ ,  $\sum_i |m_i|$ ,  $\Delta L$ ) have been shown.

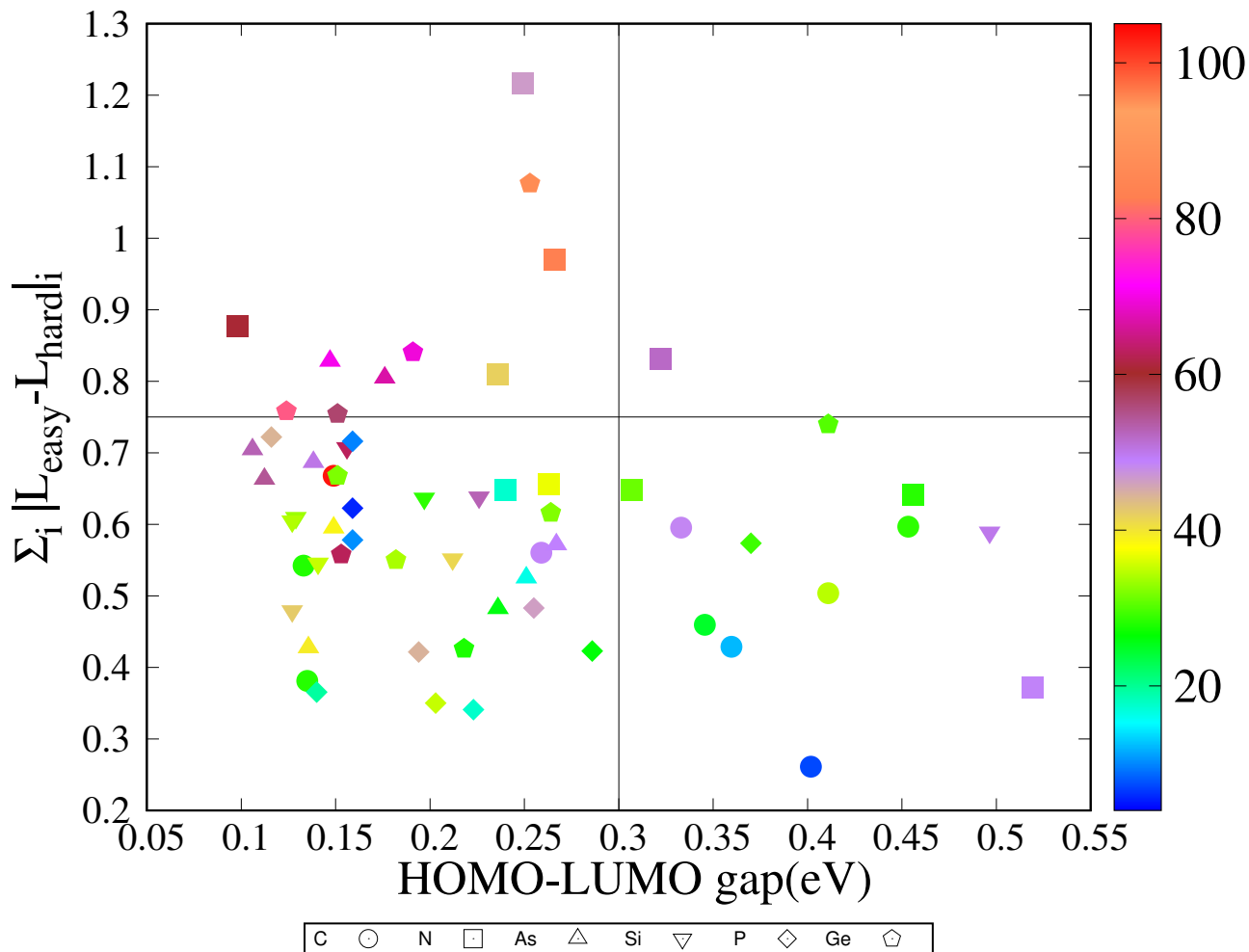


Figure 4.8: MAE in HOMO-LUMO gap -  $\Delta L$  plane

Figure 4.8 shows the all  $\text{Co}_4\text{A}_2$  clusters and their MAEs in the HOMO-LUMO

gap- $\Delta L$  plane. The color bar in the right is the MAE values in K. Different symbols have been used for different doping elements. On this plane, clusters with larger MAE are clearly separated to the low gap region. Low MAE clusters appear mostly in the lower half-plane, whereas high MAE clusters also appear towards the high  $\Delta L$  region.

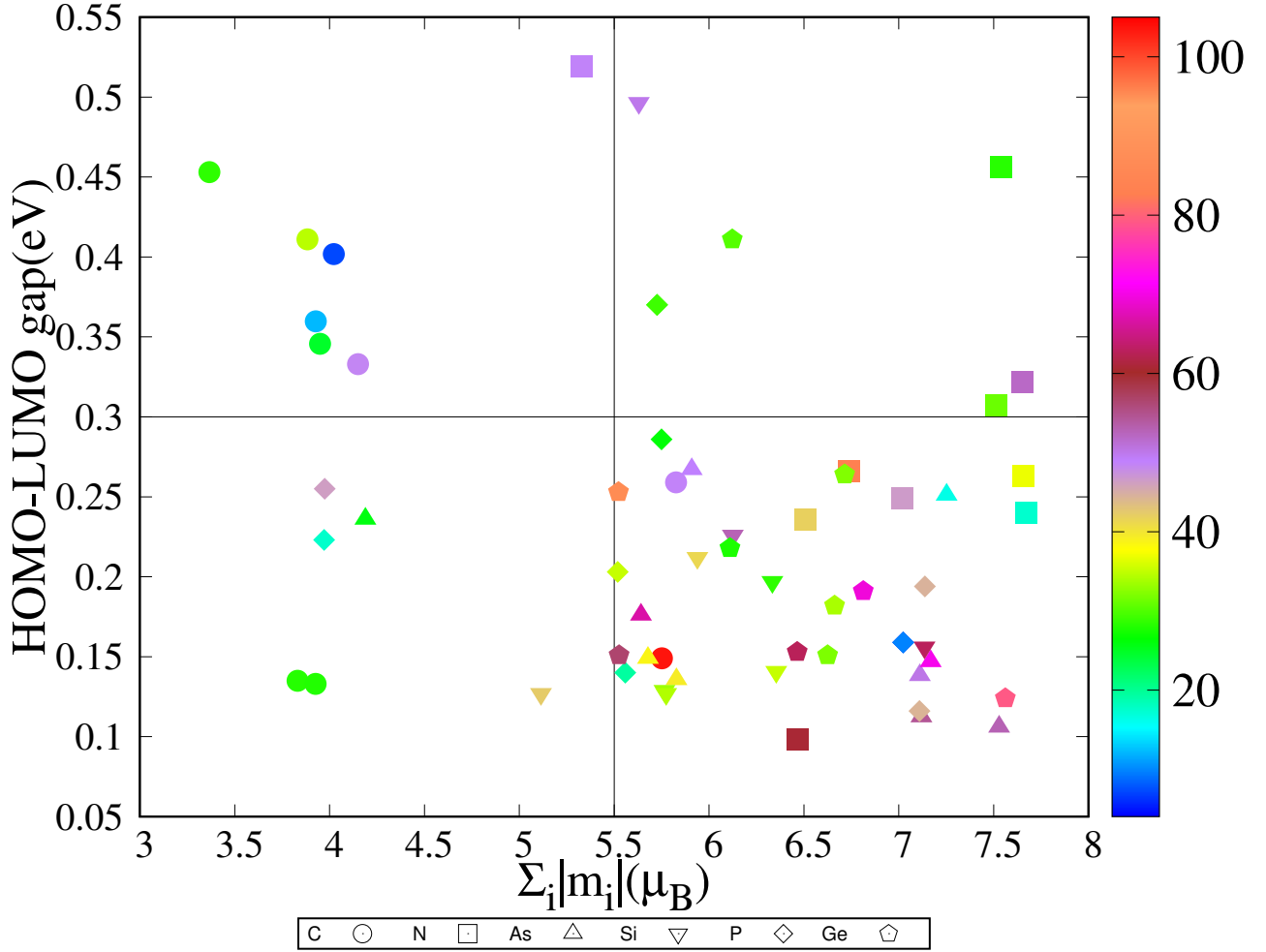


Figure 4.9: MAE in  $\sum_i |m_i|$  - HOMO-LUMO gap plane

In the  $\sum_i |m_i|$  - gap plane as shown in Figure 4.9 most of the the high valued MAE clusters are found in the lower right i.e., high  $\sum_i |m_i|$  - low gap quadrant. While some clusters with lower MAE also appear in this quadrant, most low MAE

clusters are located in the left half-plane and upper half-plane corresponding to either low  $\sum_i |m_i|$  or large HOMO-LUMO gap. Hence a positive correlation between MAE and  $\sum_i |m_i|$  has been found. Also, smaller HOMO-LUMO gaps lead to larger MAE values here.

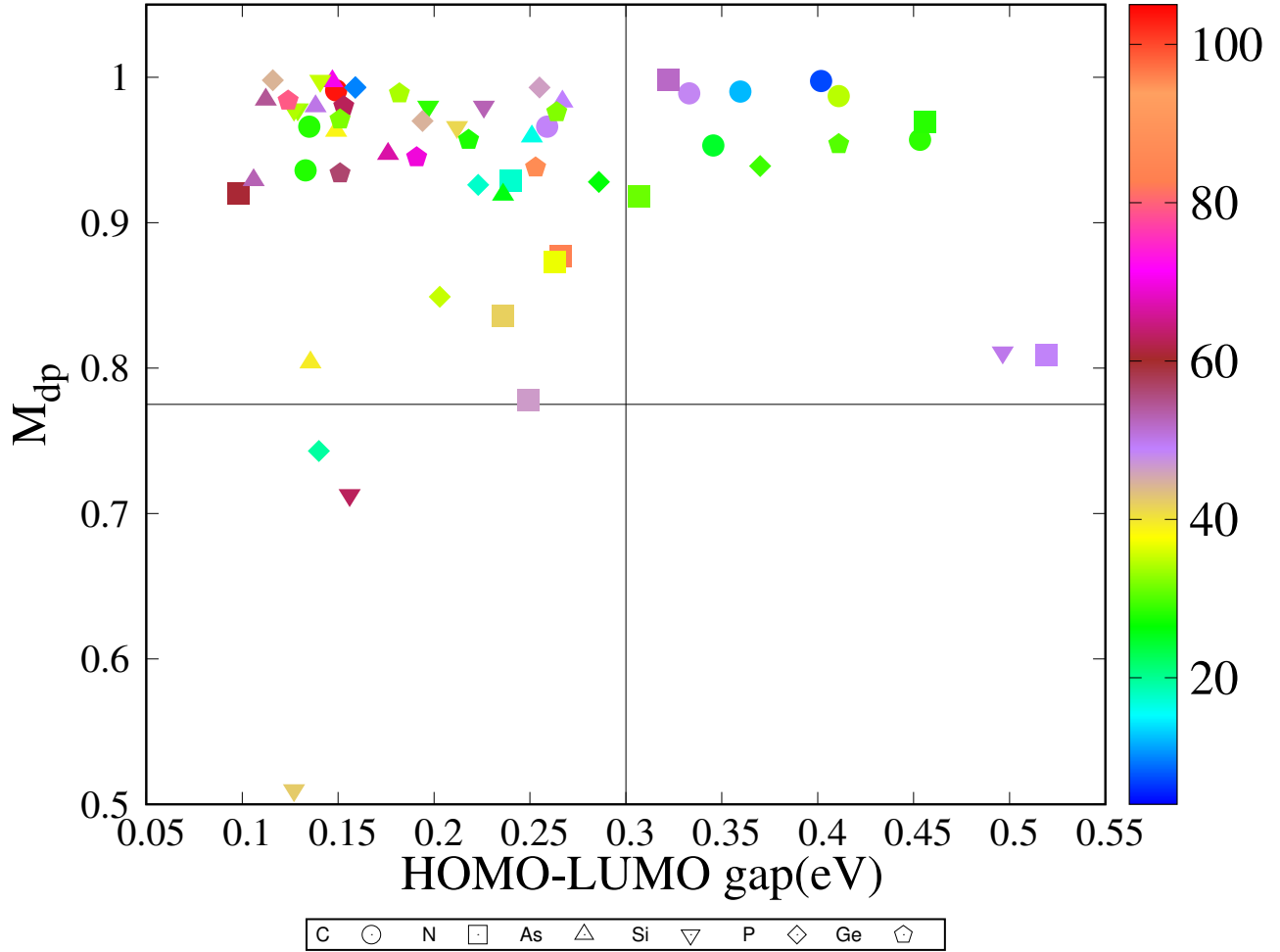


Figure 4.10: MAE in HOMO-LUMO gap -  $M_{dp}$  plane

Figure 4.10 shows the distribution of clusters and their MAEs in the gap- $M_{dp}$  plane. However, all large MAE valued clusters appear in the left half-plane. Thus smaller HOMO-LUMO gaps lead to larger MAE as same as earlier pictures.

Figure 4.11 shows that most of the high MAE clusters are found in the high-

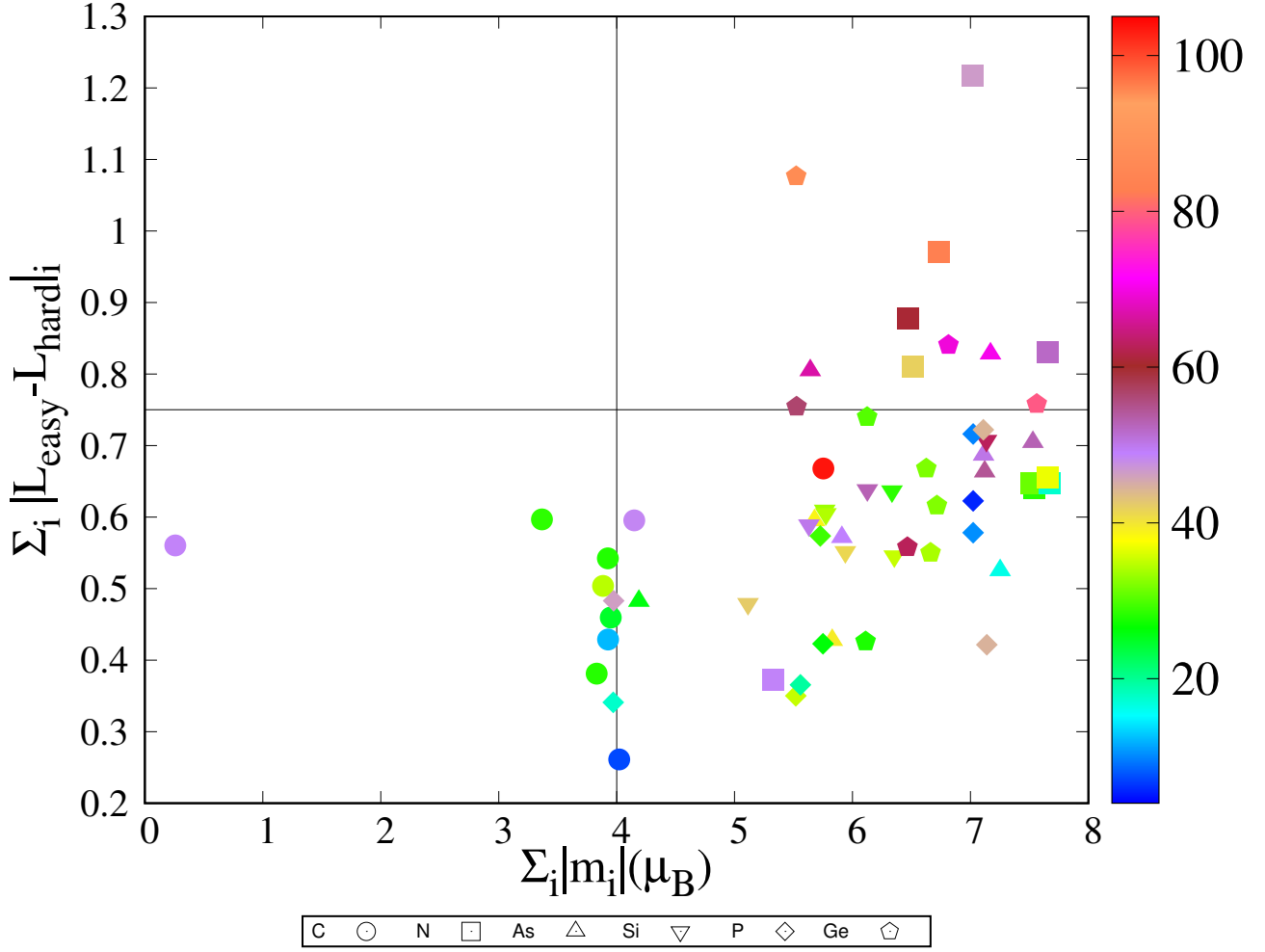


Figure 4.11: MAE in  $\sum_i |m_i| - \Delta L$  plane

spin value the plane. Thus, again a positive correlation between  $M_S$  and MAE has been observed. Here most of the high MAE valued clusters also have larger  $\Delta L$ .

In Figure 4.12, which represents MAE in  $\sum_i |m_i| - M_{dp}$  plane, most of the clusters are located in the upper half of the  $\sum_i |m_i| - M_{dp}$ , irrespective of their MAE values. There are only three clusters in the lower halves. Of the clusters in the upper half planes, most of them appear close to  $M_{dp} = 1$ . This indicates that mixing between d and p sates are small in all clusters.

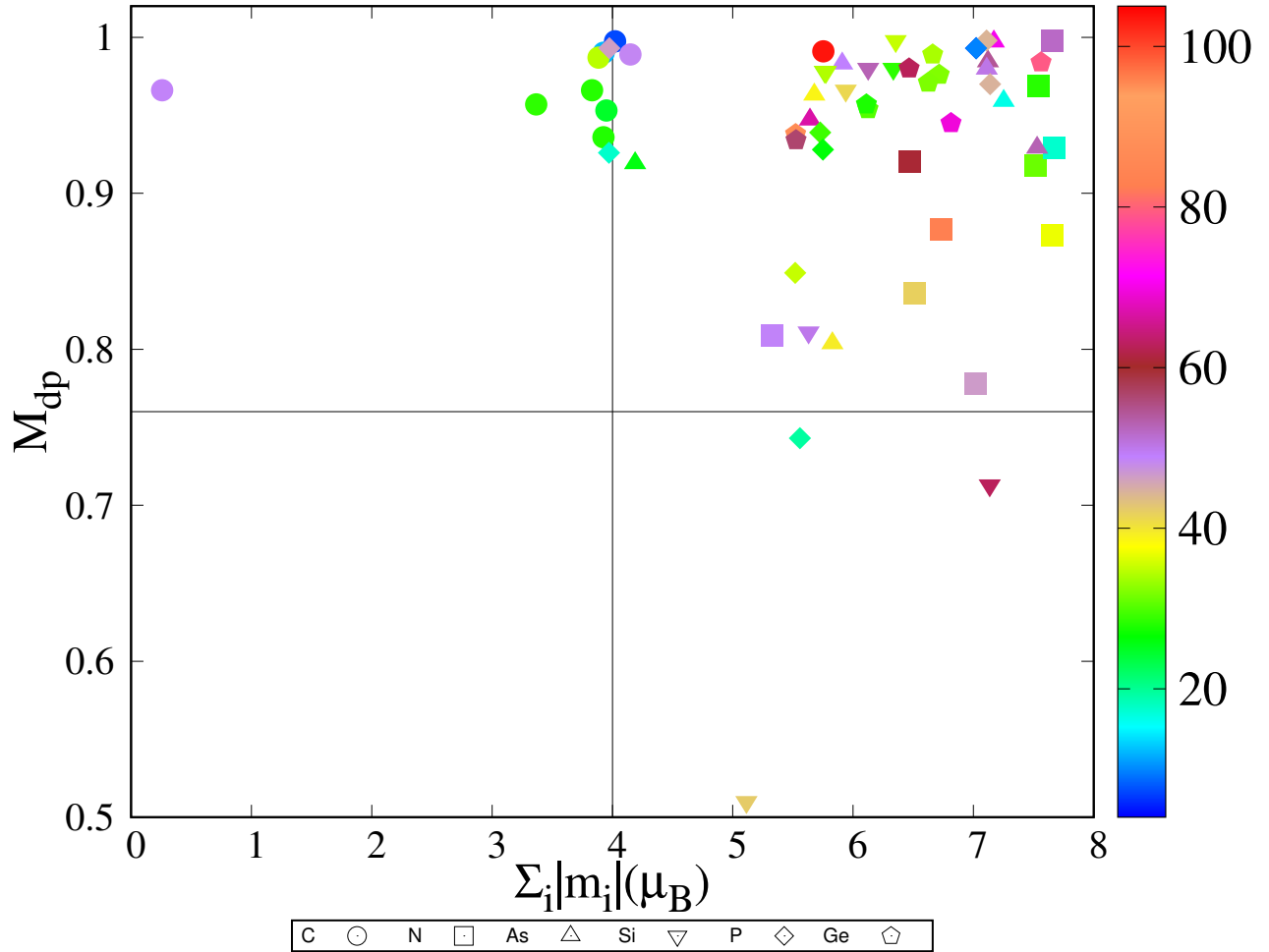


Figure 4.12: MAE in  $\sum_i |m_i| - M_{dp}$  plane

Here, in Figure 4.13, the locations of the clusters are same as Figure 4.12. As most of the clusters, irrespective of their MAE values, are closed to  $M_{dp} = 1$ , so it indicates that the degree of mixing is not a direct determinant of MAE in these clusters.

In summary, it is found that, HOMO-LUMO gap plays a determining role, smaller values leading to larger MAE. Also a larger value of  $\Delta L$  helps to have a higher MAE. There is a strong positive correlation between  $\sum_i |m_i|$  and MAE. The higher  $\sum_i |m_i|$  regions are more crowded with  $\text{Co}_4\text{A}_2$  clusters as depicted in

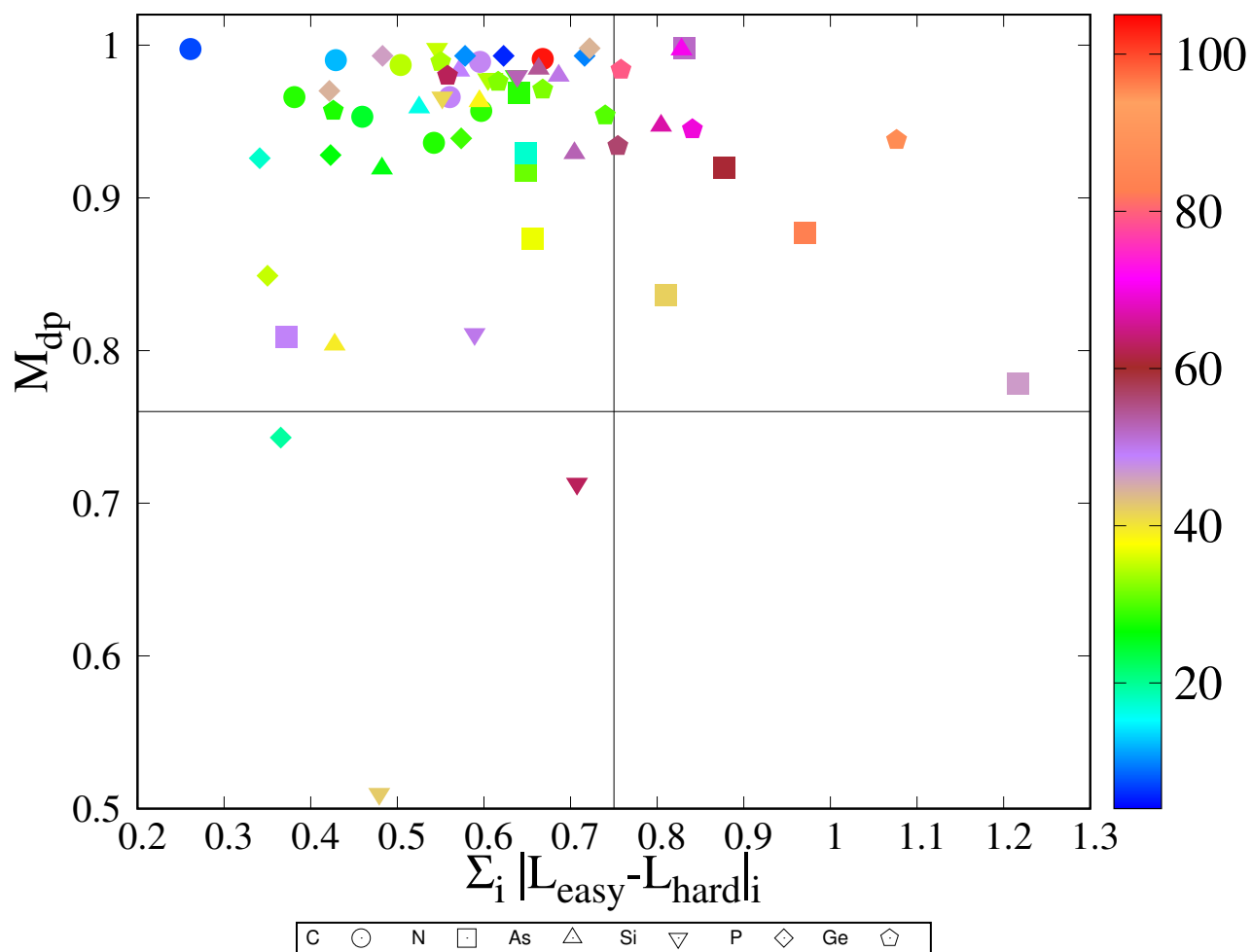


Figure 4.13: MAE in  $\Delta L - M_{dp}$  plane

the scatter plots. The role of  $M_{dp}$  in MAE values is not very clear and probably it is not an important entity for controlling MAE of  $\text{Co}_4\text{A}_2$  clusters.

## A few more analysis with HOMO-LUMO gap and $\sum_i |m_i|$ :The most important determinant of MAE

The fact that MAE is mostly determined by  $\sum_i |m_i|$  and HOMO-LUMO gap can be justified from a perturbative approach. Since the spin-orbit coupling constant is small for 3d elements (in comparison with RE elements), compared to other energy scales, one can take it as a perturbation in the full Hamiltonian. First non-vanishing contributions come from the second order terms[255, 276, 277]. Change in ground state energy is given by the expression[276]

$$\Delta_2 = -\lambda^2 \sum_{o,u} \frac{|\langle o | \vec{\sigma} \cdot \vec{L} | u \rangle|^2}{\varepsilon^u - \varepsilon^o} \quad (4.2)$$

Here o and u represent the occupied and unoccupied states respectively, and  $\varepsilon^o$  and  $\varepsilon^u$  are their energies. MAE is dependent both on  $\lambda$ , and the matrix element of the operator  $\vec{\sigma} \cdot \vec{L}$  between occupied and unoccupied states, and hence depends on the nature of these states as well. It is perhaps due to this reason that Co<sub>6</sub> has such a small MAE in its ground state. However, it is interesting that there is a positive correlation between MAE and  $\sum_i |m_i|$ . MAE and inverse of the gap in a large number of cases in a fully self-consistent treatment of the spinorbit coupling term.

## 4.5 Conclusions

From self-consistent DFT calculations we find the ground state, and a large number of low energy structures and spin states for pure Co<sub>4</sub>, Co<sub>6</sub> and Co<sub>4</sub>A<sub>2</sub> clusters have been found. To our knowledge, ours is the first work reporting such re-

sults. We then calculate MAE of these clusters, and show that there is no simple relation between the MAE of  $\text{Co}_4\text{A}_2$  clusters, and the dopant atom A. Rather, irrespective of the dopant, or even in pure Co clusters, MAE is determined by the sum of the absolute values of the magnetic moments on all the atoms, and the HOMO-LUMO gap of the cluster, MAE bearing an approximately linear correlation with  $\frac{(\sum_i |m_i|)^2}{\text{gap}}$ . This is shown in our paper [278] A larger  $\Delta L$  also supports a larger MAE.

As already indicated before, the analysis we attempted here is of a statistical nature, but the sample size is relatively small. Still, the trends we find in the scatter plots convincingly point towards the above conclusion. On general physical grounds, particularly in view of Burkert et al.s work, who based their analysis on perturbative arguments, we can expect this to hold true for larger systems as well, whether at the nanometer or bulk scale. A further test and use of the these ideas will be in case of designing novel nano-scale permanent magnets.

# Electronic and magnetic properties of polar oxide surface: Emergence of 2DEG

## 5.1 Motivation

In recent years polar oxides as well as its surface have received increasing attention, due to their novel applications in various devices as well as from a fundamental perspective properties[279]. The polar oxide surfaces are interesting for fundamental issues regarding their stability, their surface atomic configurations (relaxations, reconstructions, non-stoichiometry, etc)[147]. The specificity comes from the combined effect of orientation and termination which is responsible for the existence of a macroscopic polarization along the surface normal and a surface instability of electrostatic origin.

Beryllium oxide (BeO) is the only alkaline-earth oxide which crystalizes in the hexagonal wurtzite structure[280] at room temperature, whereas the other oxides in this family have the rock salt structure. For the BeO system, it has a hexagonal phase of wurtzite (WZ), cubic phase of zinc blende (ZB), and cubic phase

with the rock salt structure. Among them, WZ BeO is the most stable[280] one. BeO has drawn much attention due to its outstanding properties, such as high hardness[281], high melting point and outstanding radiation resistance[282]. It is widely used in many high-performance semiconductor parts due to its good thermal conductivity[283] and good electrical resistivity[284]. It is also used as a structural ceramic for high-performance microwave devices, vacuum tubes, magnetrons, and gas lasers. The large band gap of BeO, which is almost 10.6 eV[285], makes it very useful for application in optoelectronic devices[286].

ZnO is an important and widely used polar oxide semiconductor with a direct band gap  $E_g=3.44$  eV [150]. It is used in window layers in photo voltaic devices, varistors for voltage-surge protection, UV absorbers, gas sensors, catalytic devices etc but it has various novel applications like transparent field effect transistors, UV laser diodes, memristors, in high-temperature high-field electronics. It has large electronic applications as passive components for studying the topics related to transparent conducting oxide films to be used for photovoltaics and displays. From experimental works it has been found that ZnO thin films can be reached to the level of active semiconductor grade [151, 152] as mentioned earlier.

Two dimensional electron gas (2DEG) has useful applications in high electron mobility transistor (HEMT) type field effect devices[163] as mentioned in chapter 1. Two-dimensional electron systems (2DESs) at the interfaces of polar superlattices of TMOs have been studied extensively over the last decade with several experimental and theoretical works particularly on SrTiO<sub>3</sub>/LaAlO<sub>3</sub> interfaces [164–172]. In recent experiments 2DEGs have been investigated at ZnO/Zn(Mg)O hetero structure [153–162].

All these studies are mostly done on shuffle surface of wurtzite BeO and ZnO interfaced with some other materials. Here the glide surfaces of BeO and ZnO

have been studied using DFT.

## 5.2 Computational methods

All calculations were performed within the framework of plane wave DFT as implemented in the VASP code[216, 217, 264–266]. The projector augmented wave (PAW) potentials[211] represented the interaction between the ion cores and the valence electrons.

To determine optimized lattice constants of bulk BeO and its surface structure, kinetic energy cut off were taken as 563 eV. Brillouin zone integrations were performed with  $7 \times 7 \times 4$  K points by using gamma-centered grid, and for surface it was  $7 \times 7 \times 1$ . Energy convergence criterion was  $10^{-5}$  eV. The force convergence criterion during structural relaxation was kept as  $0.001 \text{ eV}/\text{\AA}$  on every atom.

In case of wurtzite ZnO bulk calculation the kinetic energy cutoff has been kept as 600 eV with K-mesh as  $8 \times 8 \times 6$  Monkhorst-Pack formalism. As Zn contains 3d electrons, so only DFT with LDA or GGA underestimates the experimental value of band gap largely. In our calculation we have checked for it with LDA calculation without U parameter and it is found as 0.809 eV where the experimental value is 3.44 eV [287]. To improve the band gap we invoked the U correction on Zn atoms. We took GGA+U calculation with U value as 5 eV.

## 5.3 Results and discussions

### 5.3.1 Bulk BeO and ZnO

We have found the optimized lattice constants  $a$  and  $c$  for wurtzite bulk BeO using different exchange-correlation functional. The table is attached below.

Table 5.1: Optimized lattice parameters of wurtzite BeO estimated using different exchange correlation energy functionals

Method	$a$ Å	$c$ Å
Experimental	2.698 [288]	4.377 [288]
LDA	2.674	4.344
GGA-PBE	2.711	4.400
GGA-PW91	2.660	4.425

From the above results it is found that LDA underestimates both the lattice constants and PBE-GGA[197] overestimates them in small amount. We have chosen the lattice constants according to PBE-GGA in further calculations. As PW91 underestimates  $a$  and overestimates  $c$ , so to keep  $c/a$  ratio closed to the experimental value we have chosen PBE-GGA. The bond lengths are shown in figure 5.1 For this bulk BeO the electronic structure calculation gives a band gap of 7.41 eV. The experimental value of band gap is 10.5 eV. [289]

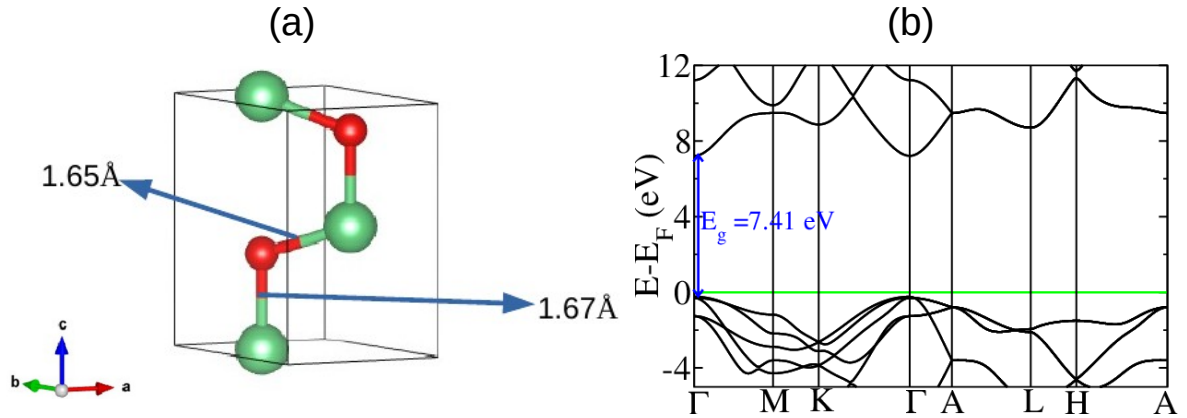


Figure 5.1: (a) Atomic and (b) electronic structure of wurtzite BeO. Green sphere represents Be atom and red sphere represents O atom.

For wurtzite ZnO from GGA+U calculation, with U value as 5 eV for Zn d-orbitals we got the in plane lattice parameter  $a=3.243 \text{ \AA}$  and out plane lattice constant  $c=5.198 \text{ \AA}$  and the band gap is 1.43 eV. The experimental values of  $a$

and  $c$  are 3.249 Å and 5.201 Å [290]. The atomic and electronic structures are shown below.

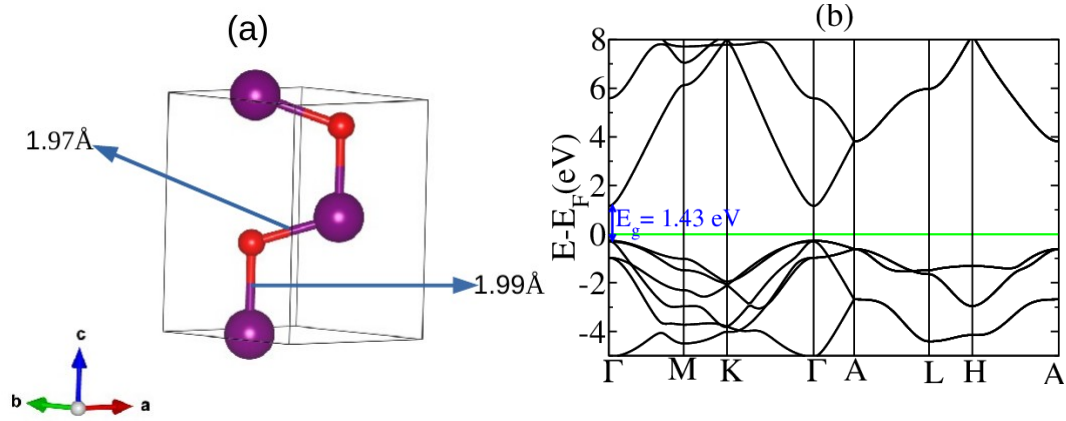


Figure 5.2: (a) Atomic and (b) electronic structure of wurtzite ZnO. Purple sphere represents Be atom and red sphere represents O atom.

### 5.3.2 Electronic structure of glide surface of BeO and ZnO

As shown in the wurtzite bulk unit cell atomic structure, there are two kinds of bonds. One perpendicular to the  $xy$  plane and other one is slanted. The shuffle and glide surface atomic structures are shown in case of BeO along 0001 direction. Here we have shown  $1 \times 1 \times 3$  supercell of wurtzite BeO glide surface.

We have performed the electronic structure calculations for BeO glide surface with  $1 \times 1 \times 3$  super cell. As the unit cell contains 2 Be and 2 O atoms, so in this super cell there are 6 Be and 6 O atoms. We have relaxed the structure by keeping a vacuum of 10.84 Å on top O atom. Relaxed structure of glide surface remains almost same as that of initial structure shown in figure 5.4.

The electronic structure calculation of the relaxed structure of glide BeO surface in figure 5.4 (b) is found metallic as shown in figure 5.5. For spin polarized calculation, the relaxed glide surface, was found with energy 0.374 eV lower than

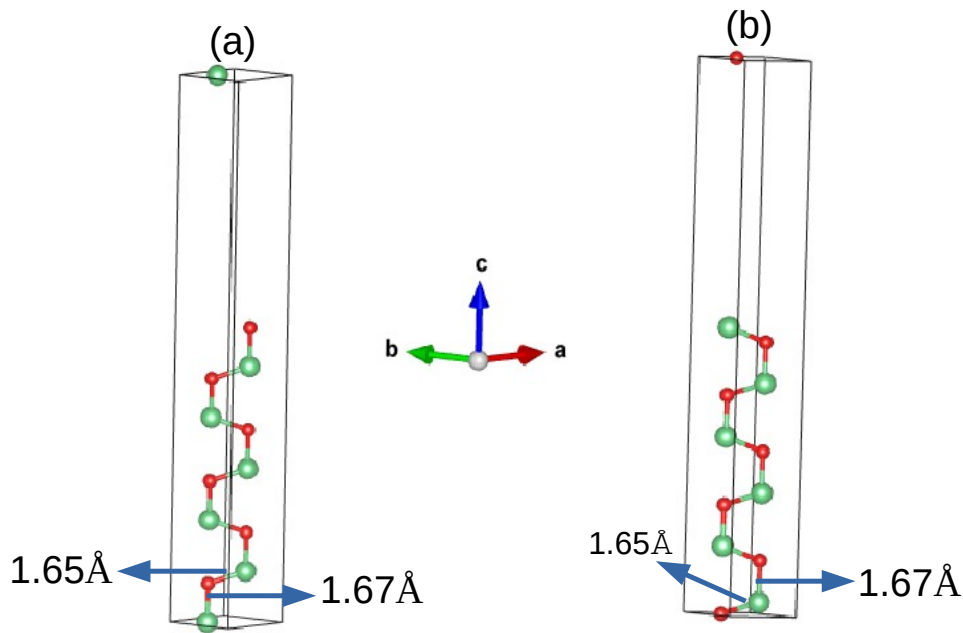


Figure 5.3: Bulk like Atomic structure of (a) glide and (b) shuffle surface of  $1 \times 1 \times 3$  wurtzite BeO.

the spin unpolarized one. We have found the relaxed glide surface has a finite magnetization  $1.51 \mu_B$ .

For ZnO also the relaxed atomic structure of glide surface remains almost same as initial bulk like one as shown below. The glide surface of ZnO is also metallic like BeO in both the spin unpolarized and spin polarized calculation. In case of ZnO the spin polarized relaxed structure is lower in energy by 0.641 eV than the spin unpolarized relaxed structure. We have found a magnetic moment  $1.4508 \mu_B$  in spin polarized ZnO glide surface.

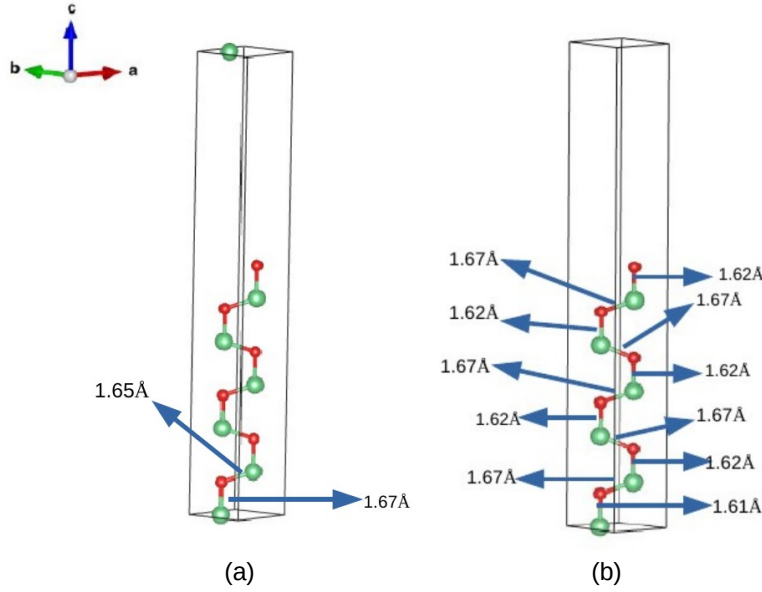


Figure 5.4: (a) Bulk like structure, (b) relaxed structure of (0001) glide surface of BeO.

### 5.3.3 Bulk insulator to surface metal transition:cleaving of crystal

#### Electronic and magnetic properties of cleaved BeO glide plane

We analyze this bulk insulator to surface metal transition as a function of distance of separation at the plane that cleaves the bulk crystal into surfaces, and calculate the electronic structure with gradually increasing distance of separation. We have kept the atomic positions in  $1 \times 1 \times 3$  super cell of BeO glide surface as bulk like and increased the vacuum level (denoted as  $d_{vac}$  on top O atom ( $O_6$ ) in figure 5.8).  $c_0$  is noted as 3 times the bulk unit cell  $c$  value. For this  $1 \times 1 \times 3$  super cell, ie  $13.2 \text{ \AA}$ . Hence the distance between the slab and it's periodic image has been increased gradually with increasing of vacuum thickness above the slab. The vacuum thickness is defined as  $d_{vac}$ ,  $d_{vac} = c - c_0$ . The slabs with various  $d_{vac}$  are shown in figure 5.9 In each case we have found the band gap ( $E_g$ ) decreases

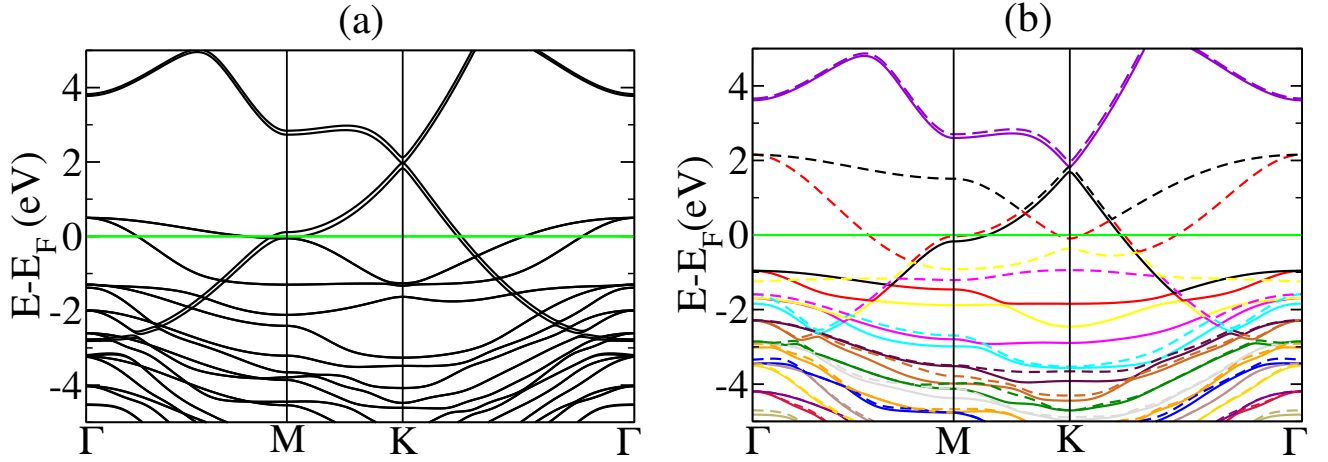


Figure 5.5: Electronic structure of BeO glide surface obtained using (a) spin unpolarized and (b) spin polarized calculation respectively. The same colour has been used for a band of states spin up (solid lines) and spin down (dashed lines) channels for (b). Green solid line parallel to X axis represents Fermi level.

from the bulk value gradually and at a certain vacuum level it becomes metallic. Evolution of electronic structure with various  $d_{vac}$  is shown in figure 5.10. From figure 5.10 panel (e) it is found, that the system becomes just metallic when  $d_{vac}$  value equals  $1\text{\AA}$ , and with  $d_{vac}$  value  $1.2\text{\AA}$ , magnetization appears in the surface as shown in panel(f) of figure S7. With increasing vacuum thickness, magnetization value was increased after the critical value of  $d_{vac}$   $1\text{\AA}$  and becomes saturated at  $2\text{\AA}$ , shown in figure 5.11.

### Emergence of 2DEG at glide surface of BeO

As mentioned earlier, that at some critical distance between the bottom Be atom ( $\text{Be}_1$  in figure 5.8(a)) and its periodic image, the insulating system turns out to be metallic, and the first lowest energy conduction band crossed Fermi level by decreasing the band gap gradually, we have plotted the 2d contour of the charge density for this particular band in figure 5.12. We have plotted the charge density

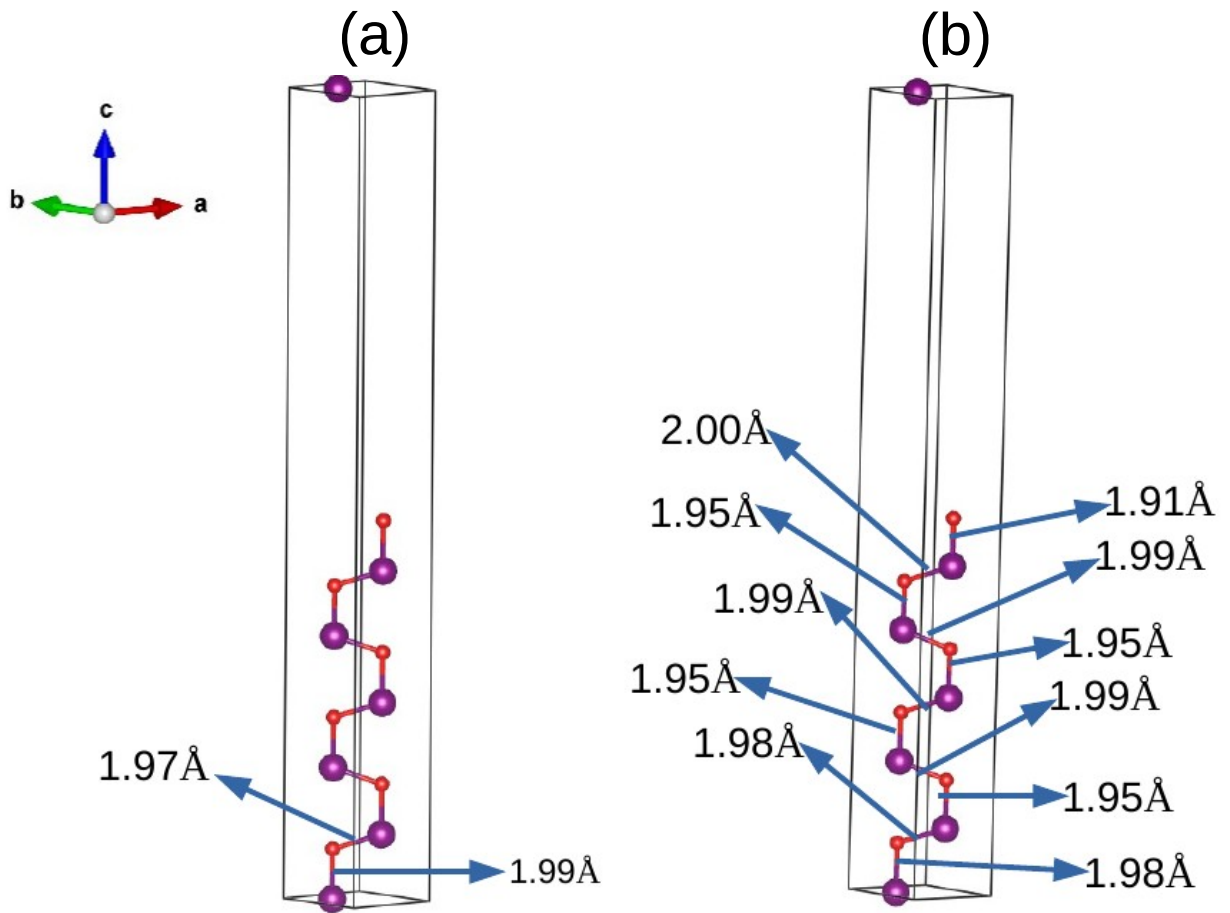


Figure 5.6: (a) Bulk like structure, (b) relaxed structure of (0001) glide surface of ZnO.

in two dimension for the planes in the region between the top O atom and the periodic image of the bottom Be atom. We have taken the top O atom ( $O_6$ ) at the center of the plane containing it assuming this plane has z-coordinate zero. Now we move toward the periodic image of  $Be_1$  atom, along z axis, perpendicular to the plane containing  $O_6$ , . We have found the distribution of charge density at different parallel planes, all are perpendicular to z axis. When the distance between  $Be_1$  and its periodic image is just  $c_0$ , ie  $d_{vac}=0.0\text{\AA}$ , all electrons are gathered in the central O atom ( $O_6$ ) for the plane, as we move towards the image

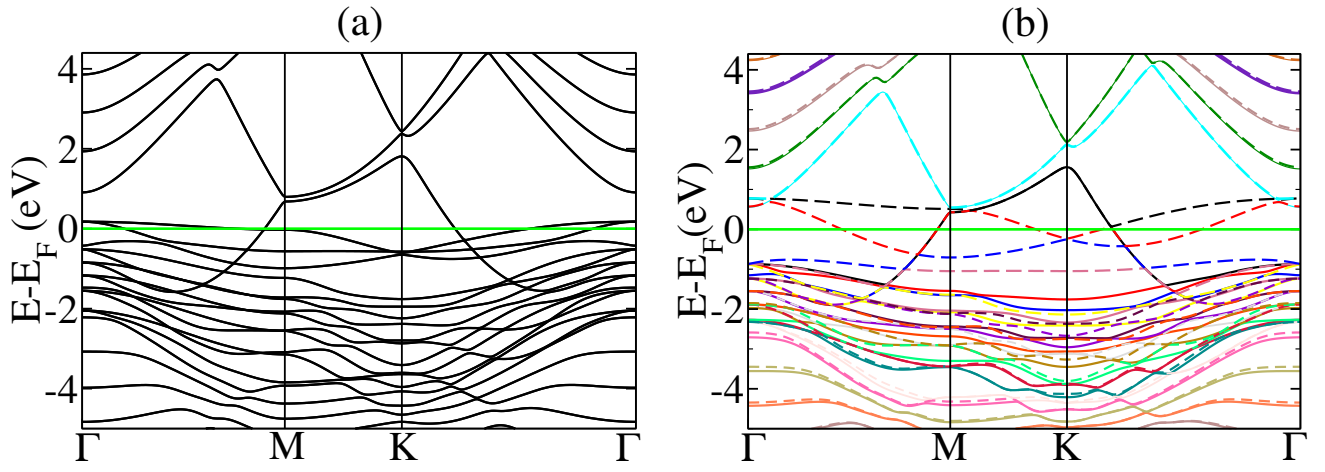


Figure 5.7: Electronic structure of ZnO glide surface obtained using (a) spin unpolarized and (b) spin polarized calculation respectively. The same colour has been used for a band of states spin up (solid lines) and spin down (dashed lines) channels for (b). Green solid line parallel to X axis represents Fermi level.

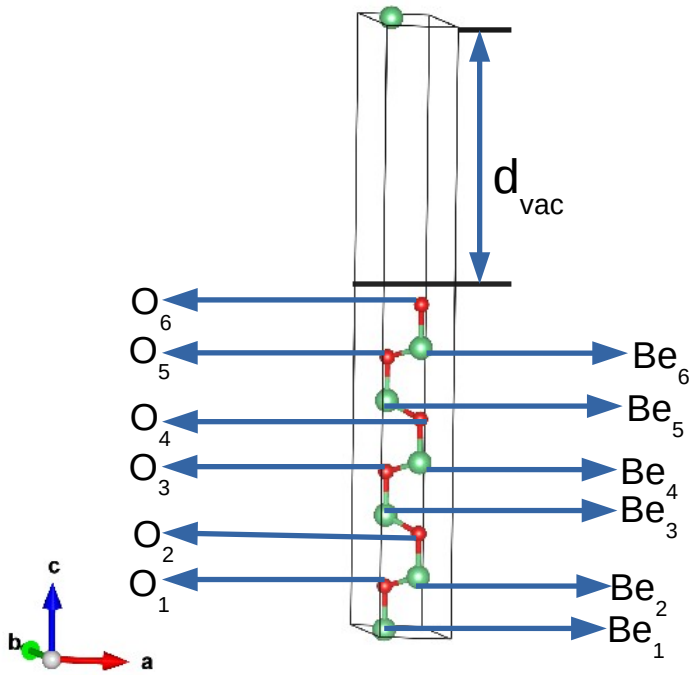


Figure 5.8: Labeling of atoms and  $d_{vac}$  for BeO  $1 \times 1 \times 3$  glide BeO surface

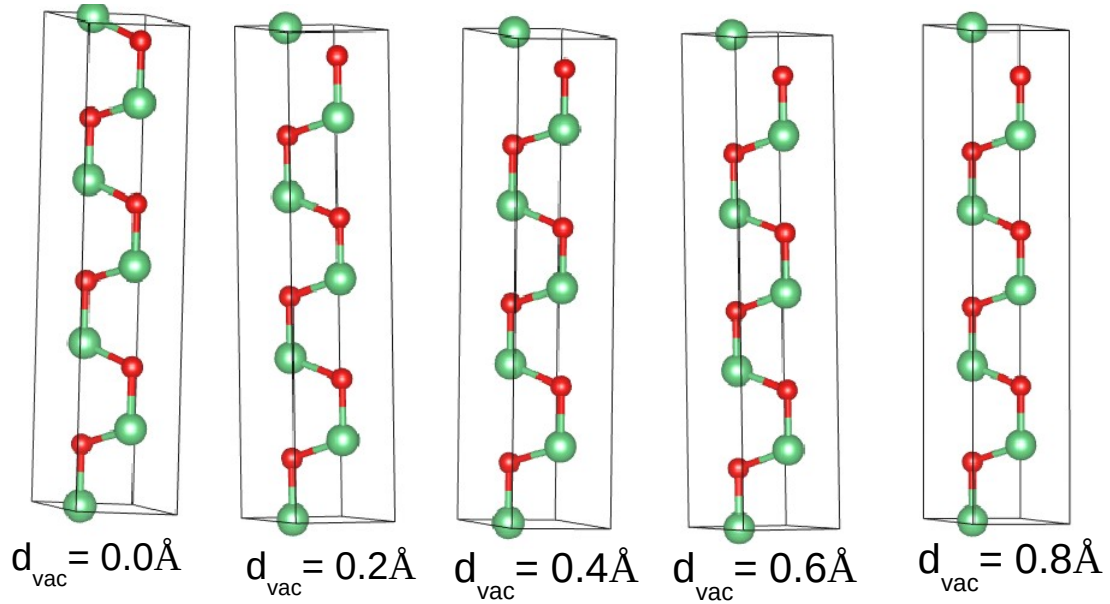


Figure 5.9: Cleaving across (0001) plane achieved with gradual increment in distance between the slab and its periodic image(vacuum thickness) maintaining the bulk structure.

Be atom, there is no existence of electron gas in an intermediate parallel plane. It has been spread with very little amount only in the plane containing image Be atom, as shown in figure S12. Now as we gradually increased the  $d_{vac}$  value from 0 to  $0.2\text{\AA}$  and so on shown in figure S6, we have found the electron density has been spread not only in the  $\text{Be}_1$  containing plane, but some intermediate planes between the  $\text{O}_6$  and image of  $\text{Be}_1$  atom containing plane. The two dimensional distribution of electron density for the lowest energy conduction band has been depicted in figure 5.12 with  $d_{vac}=0.6\text{\AA}$ .

### **$\text{O}_6$ is responsible for metallicity and magnetism in glide BeO surface**

Metallicity and magnetism is mainly coming from terminal O atom ( $\text{O}_6$ ). It is clear from the projected density of state plot for down spin channel in figure 5.13. Metallic contribution is mainly coming from terminal O atom, clear from

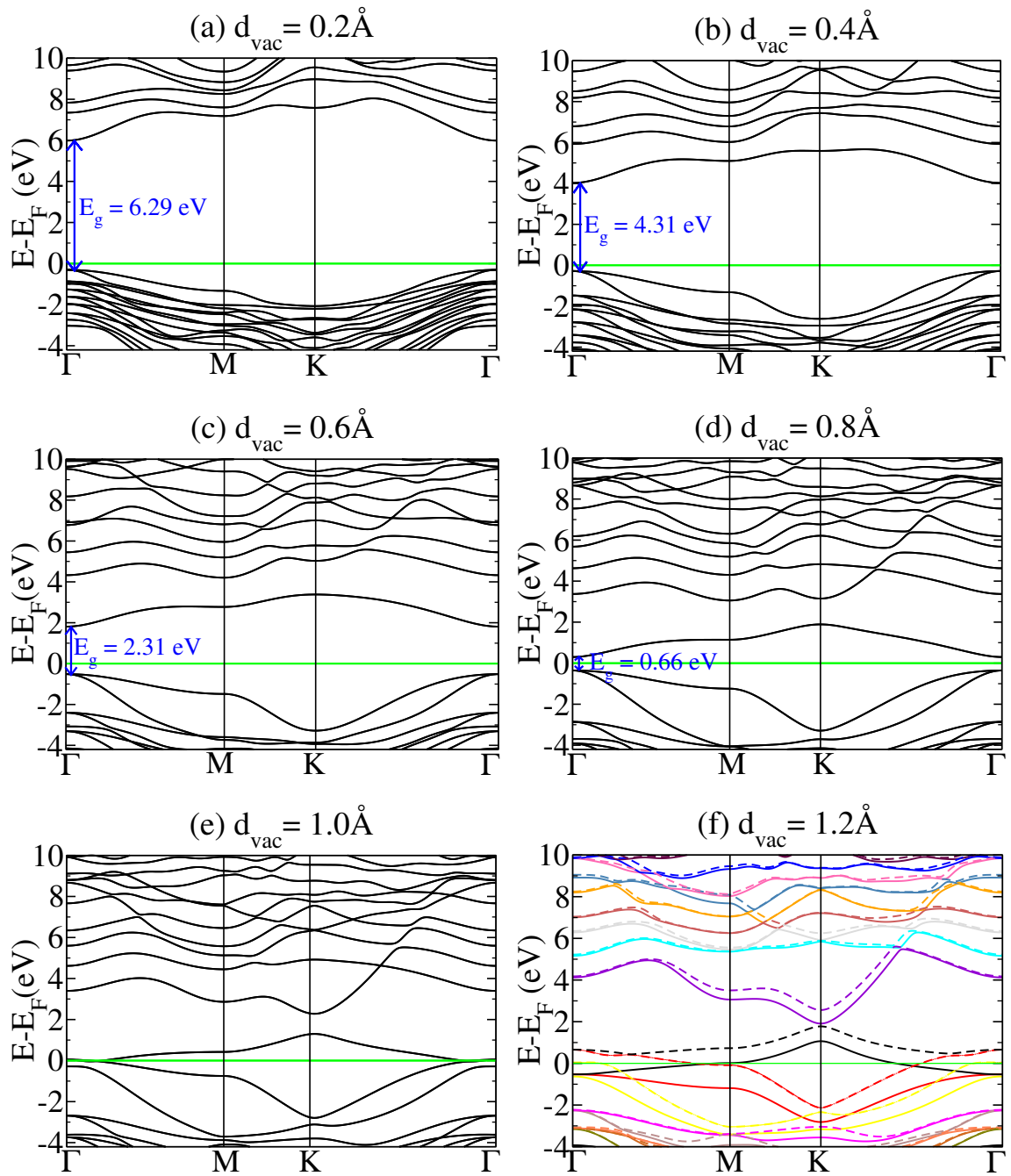


Figure 5.10: Evolution of electronic structure during cleavage of BeO at basal glide plane: Origin of 2DEG

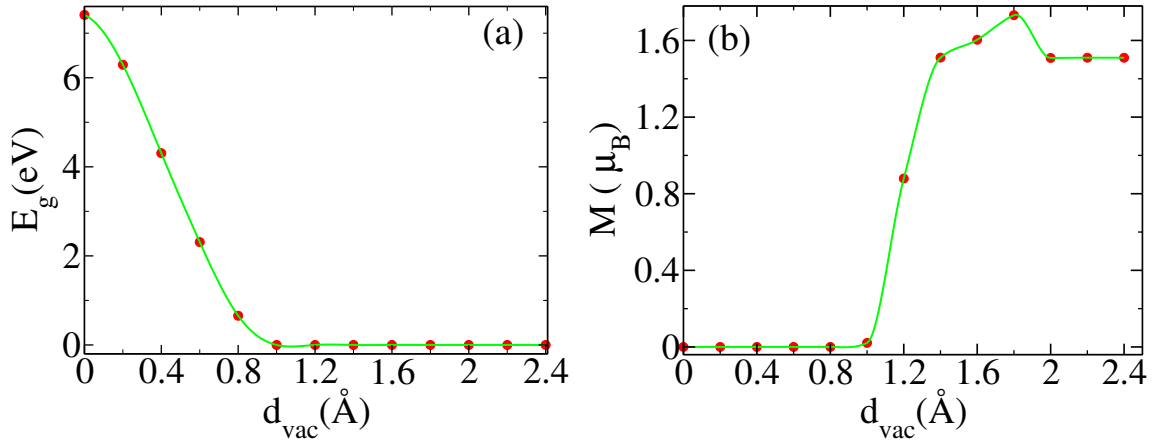


Figure 5.11: Emergence of metallicity and magnetization upon cleavage as seen in (a) band gap ( $E_g$ ) and (b) magnetization ( $M$ ) with interplanar separation at cleavage  $d_{vac}$  as defined in figure 5.8 (a)

down spin channel and for up spin very small contribution from terminal Be atom ( $Be_1$ ), as shown in panel (a) in figure 5.14. So the surface atoms are responsible for metallic character of BeO glide plane. From the isosurface of spin density plot it is more clear that the terminal  $O_6$  atom is responsible for the magnetism in the glide surface as shown in figure 5.15. To check whether this magnetization occurs due to Stoner instability we performed spin unpolarized calculation for relaxing the oxygen terminated BeO glide surface. We found peak near Fermi level in total density of states profile as shown in figure 5.13(b). From figure 5.13 it is clear that the peak near Fermi level occurs due to terminal O atom ( $O_6$ ). The Be atoms did not contribute for this Stoner instability shown clearly from figure 5.16

## Internal electric field from planar averaged potential:origin of metallicity

From the figure 5.17 we have seen the electrons associated with O<sub>6</sub> atom has the highest planar average potential energy and for the Be<sub>1</sub> atom these are with lowest planar average potential energy. This leads to polar catastrophe in the BeO glide surface, the valance bands in bulk crosses the Fermi level in the glide surface, and the system becomes metallic. There is no constant value of vacuum potential energy for the electrons. It will feel a change in potential energy in vacuum region and towards right the potential energy is lower than left, as a result electrons moving towards positive  $z$  direction and 2DEG is formed.

## Magnetoelectric effect in glide BeO surface

To check the effect of electric field on the magnetization at BeO glide surface we add a saw-tooth potential as a function of  $z$ , and simulated effects of an electric field as implemented in QUANTUM ESPRESSO [291] package. Field strength varying from 0.0 V/Å to 1 V/Å in the intervals of 0.01 V/Å. Electric field was applied at the middle of the vacuum with dipole correction to eliminate the effects of periodic boundary condition of the BeO slab. From the slope of figure 5.18 we have calculated the magneto electric coupling coefficient( $\alpha$ ). It is defined as

$$\alpha = \mu_0 \frac{\Delta M}{\Delta E} \quad (5.1)$$

$\mu_0$  is the vacuum permeability:  $4\pi \times 10^{-7} \text{Newton/Amp}^2$   $M$  magnetization (magnetic moment per unit volume)  $E$  Applied electric field. We have found  $\alpha$  as 2.97 ps/meter which is comparable to the magneto electric coupling coefficient of a famous magneto electric compound Cr<sub>2</sub>O<sub>3</sub>, which has the value 4.31 ps/meter[292]

in bulk.

### **Electronic and magnetic properties of cleaved ZnO glide plane**

Like wurtzite BeO, the electronic structure of cleaved ZnO glide surfaces have been studied with increasing the  $d_{vac}$  gradually and keeping the atomic position as bulk. The band gap was decreased gradually like BeO as the lowest energy conduction band comes towards the Fermi level. For a critical value of  $d_{vac}$  the ZnO glide surface becomes metallic and magnetization appears. It is clearly shown in figure 5.19 The variation of band gap and magnetization with  $d_{vac}$  is shown in figure 5.20

### **Emergence of 2DEG at glide surface of ZnO**

Like BeO glide surface, emergence of 2DEG is also in case of ZnO. It is depicted in figure 5.21 with  $d_{vac}=0.6\text{\AA}$ .

### **Regarding magnetization in glide ZnO surface**

Like BeO glide plane in case of ZnO  $O_6$  is responsible for metallicity and magnetism. It is clear in the figure 5.22 (a) and (c). Like BeO stoner instability is also found here.

### **Planar averaged potential for ZnO glide surface**

We have found the same pattern of planar averaged potential of glide ZnO surface. The electrons in the vacuum feel a force along c axis and emergence of 2DEG have been found.

### Magnetoelectric effect in ZnO glide surface

On applying perpendicular electric field in the vacuum region as saw tooth potential, the absolute magnetization value was varying with amplitude of electric field in case of glide ZnO also.

## 5.4 Conclusions

We have thoroughly studied the glide surface of wurtzite BeO and ZnO within the framework of DFT. In both cases these are found metallic with emergence of 2DEG. The magnetization was also appeared here, where in bulk both are insulating and non magnetic. Moreover the linear relationship of appreciable linear magneto electric properties made these systems more interesting. The calculated value of magnetoelectric coupling coefficient is near about the bulk  $\text{Cr}_2\text{O}_3$ . These 2DEG, magnetization and magneto electric coupling effect are useful in various devices. For this the stability of this glide system should be studied, which are done later.

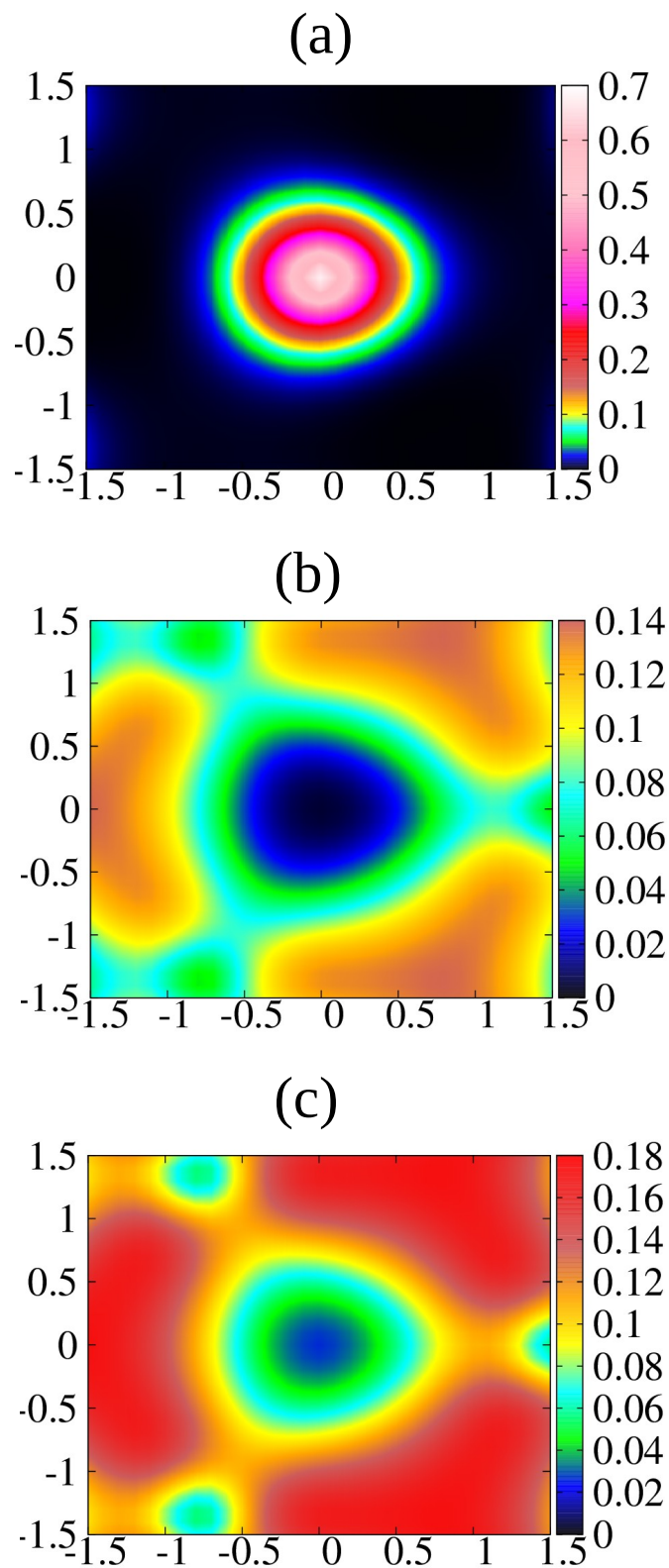


Figure 5.12: Contour plots of charge density of the lowest energy conduction band with  $d_{vac}=0.6\text{\AA}$ , in (a) plane containing  $O_6$ .(b) intermediate plane between  $O_6$  and periodic image of  $Be_1$  (c) plane containing periodic image of  $Be_1$ .

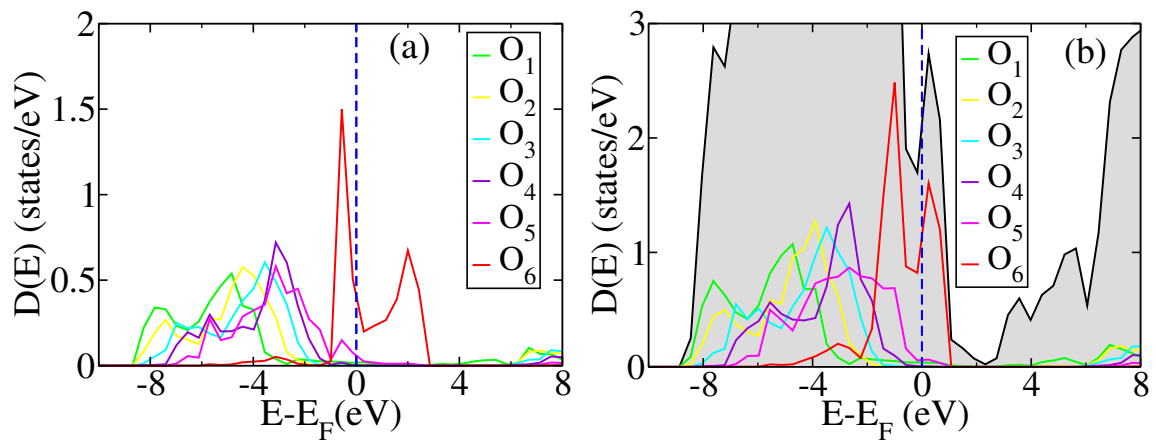


Figure 5.13: Projected density of states of the relaxed structure of (0001) glide surface of BeO showing contribution of O atoms (a) spin polarized with down spin channel (b) spin unpolarized. The vertical dashed line indicates the Fermi level.

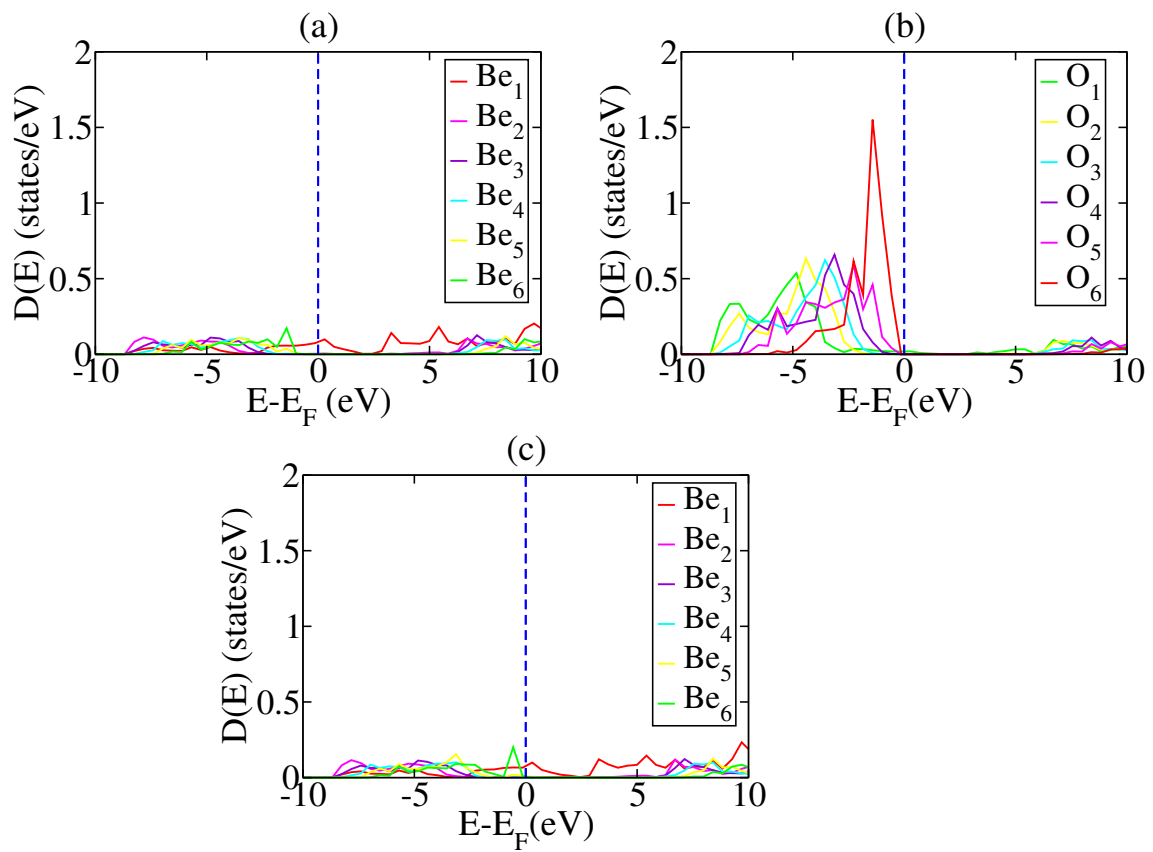


Figure 5.14: Projected density of states. Upper panels (a) and (b) are for up spin channel with contributions from all Be and all O atoms respectively. Lower panel (c) for down spin channel with Be contributions. The dashed blue line indicates the Fermi level.

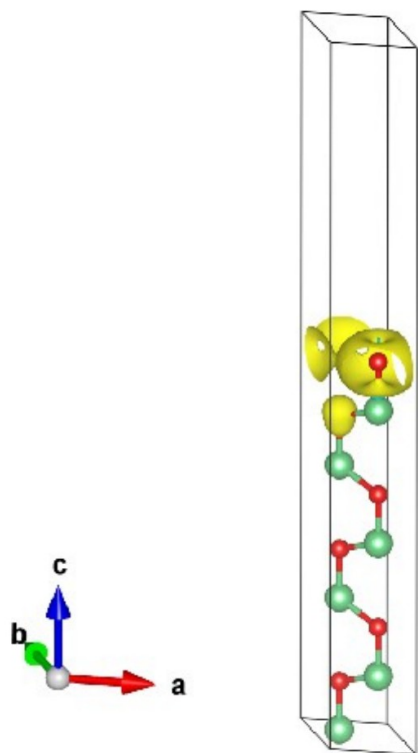


Figure 5.15: Isosurface of spin density of BeO slab terminated with glide surfaces.

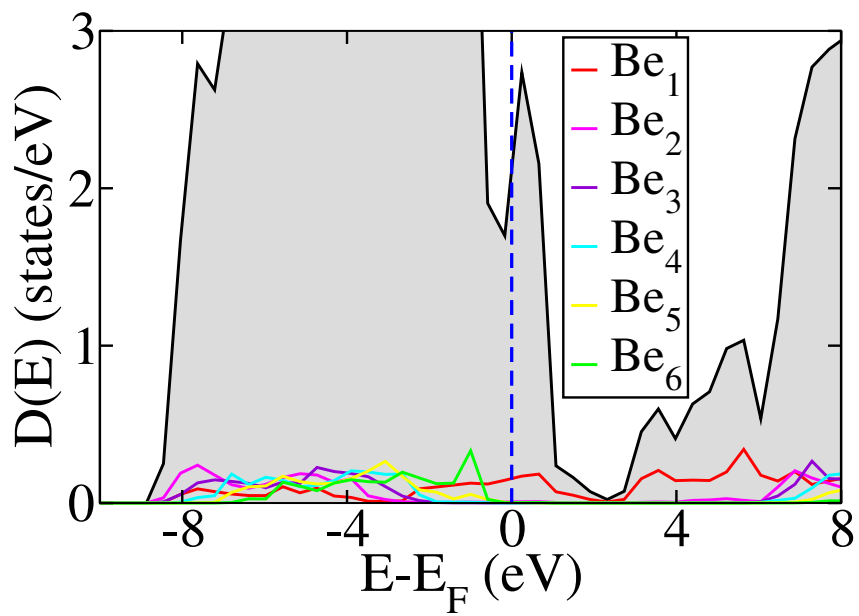


Figure 5.16: Density of states projected on the orbitals of Be atoms.

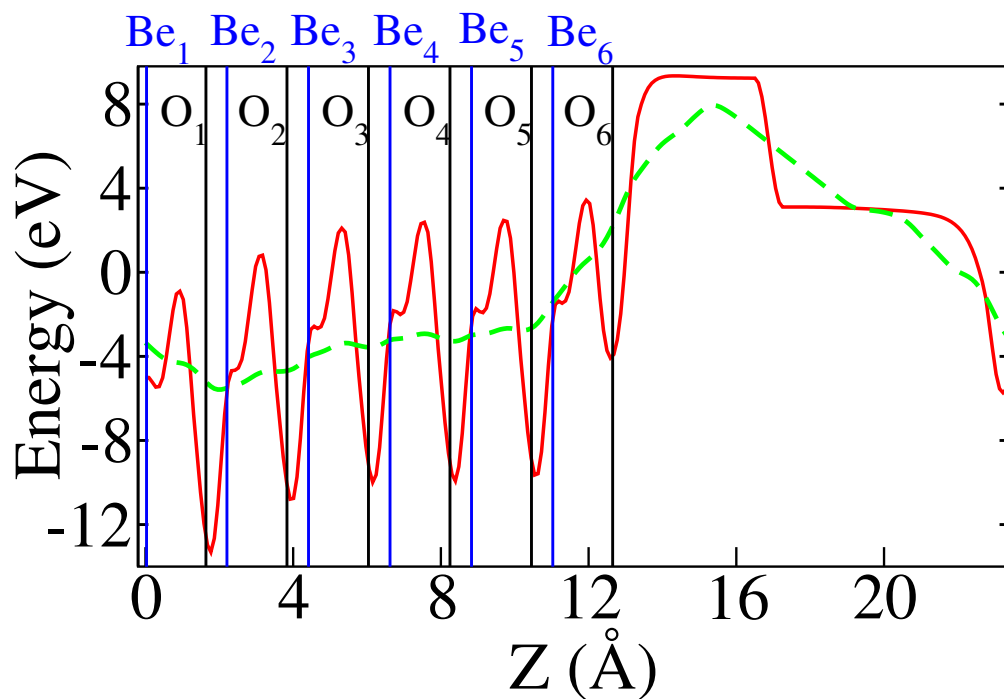


Figure 5.17: Planar (red solid line) and macroscopic (green dashed line) average of the electrostatic potential along  $z$  axis (direction perpendicular to the glide surface of BeO), obtained employing dipole correction, demonstrating its spontaneous dipole and an internal electric field causing polar catastrophe.

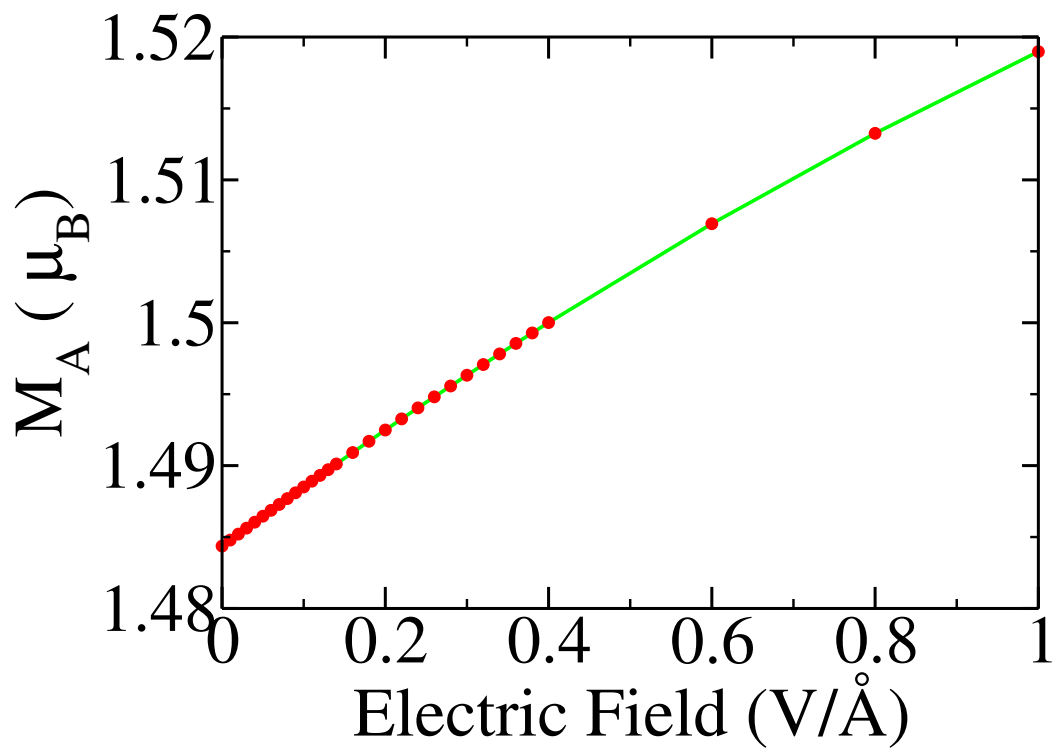


Figure 5.18: Magnetoelectric effect evident in linear variation in magnetization at (0001) glide surface of BeO in response to electric field perpendicular to the surface.

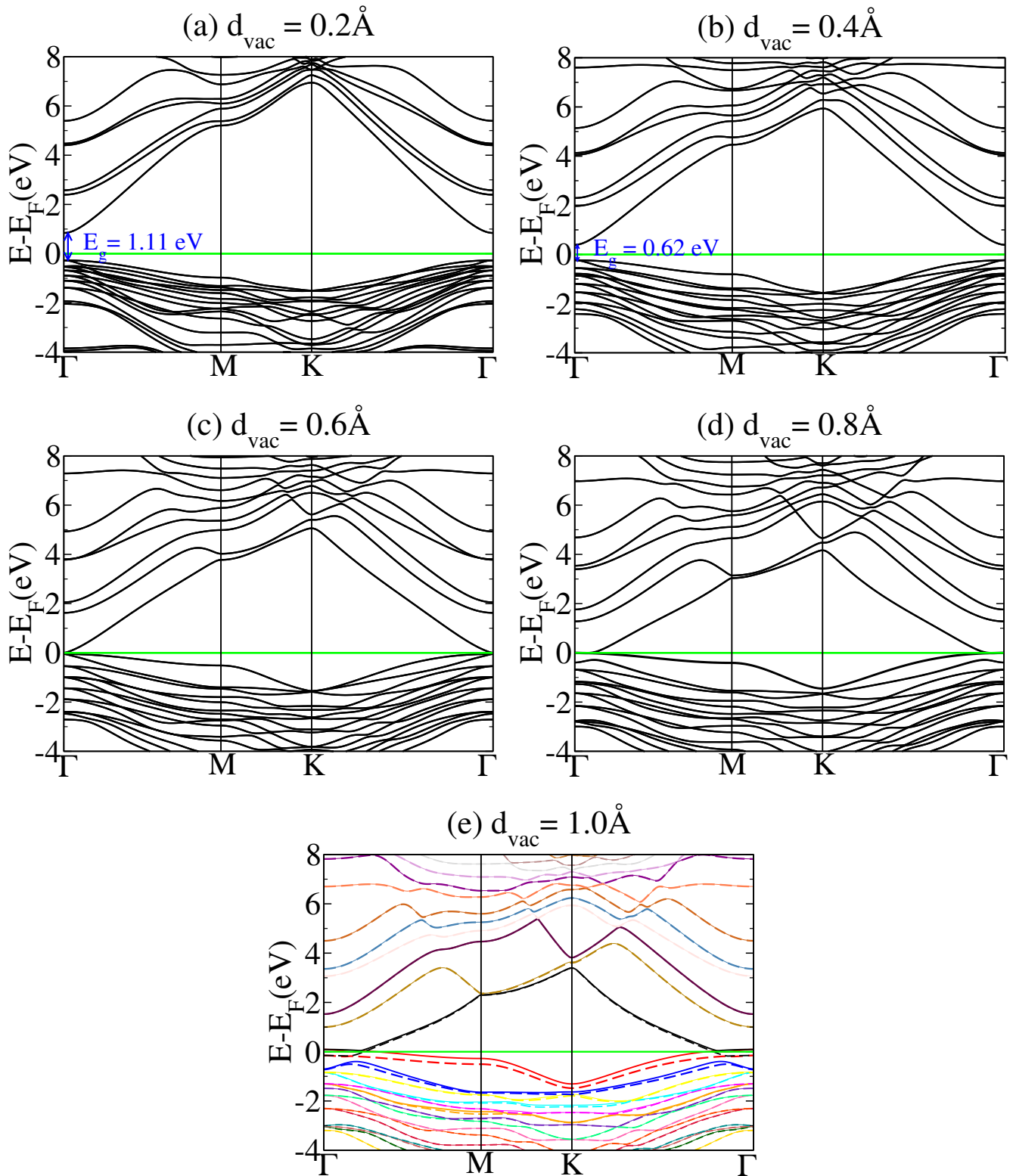


Figure 5.19: Evolution of electronic structure during cleavage of ZnO at basal glide plane: Origin of 2DEG

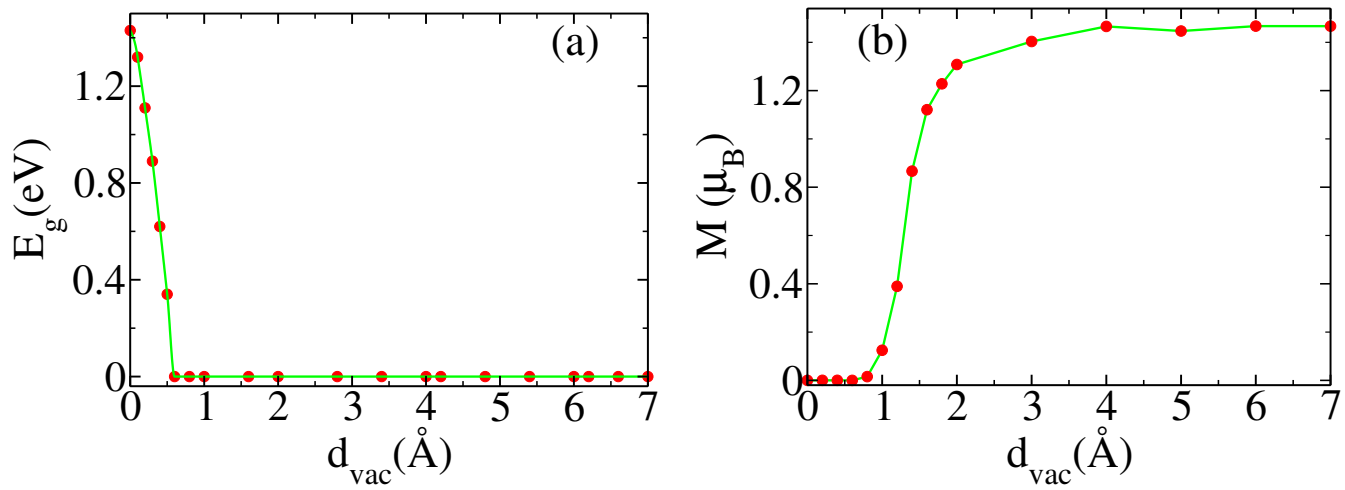


Figure 5.20: Emergence of metallicity and magnetization upon cleavage as seen in (a) band gap ( $E_g$ ) and (b) magnetization ( $M$ ) with interplanar separation at cleavage  $d_{vac}$ .

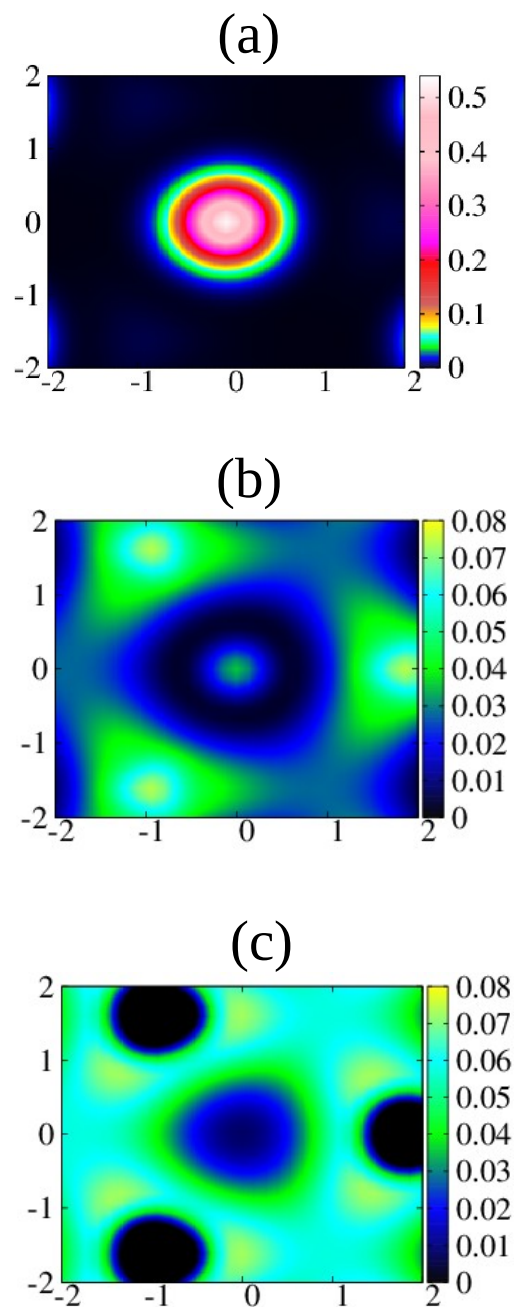


Figure 5.21: Contour plots of charge density of the lowest energy conduction band with  $d_{vac}=0.6\text{\AA}$ , in (a) plane containing  $O_6$ .(b) intermediate plane between  $O_6$  and periodic image of  $Zn_1$  (c) plane containing periodic image of  $Zn_1$ .

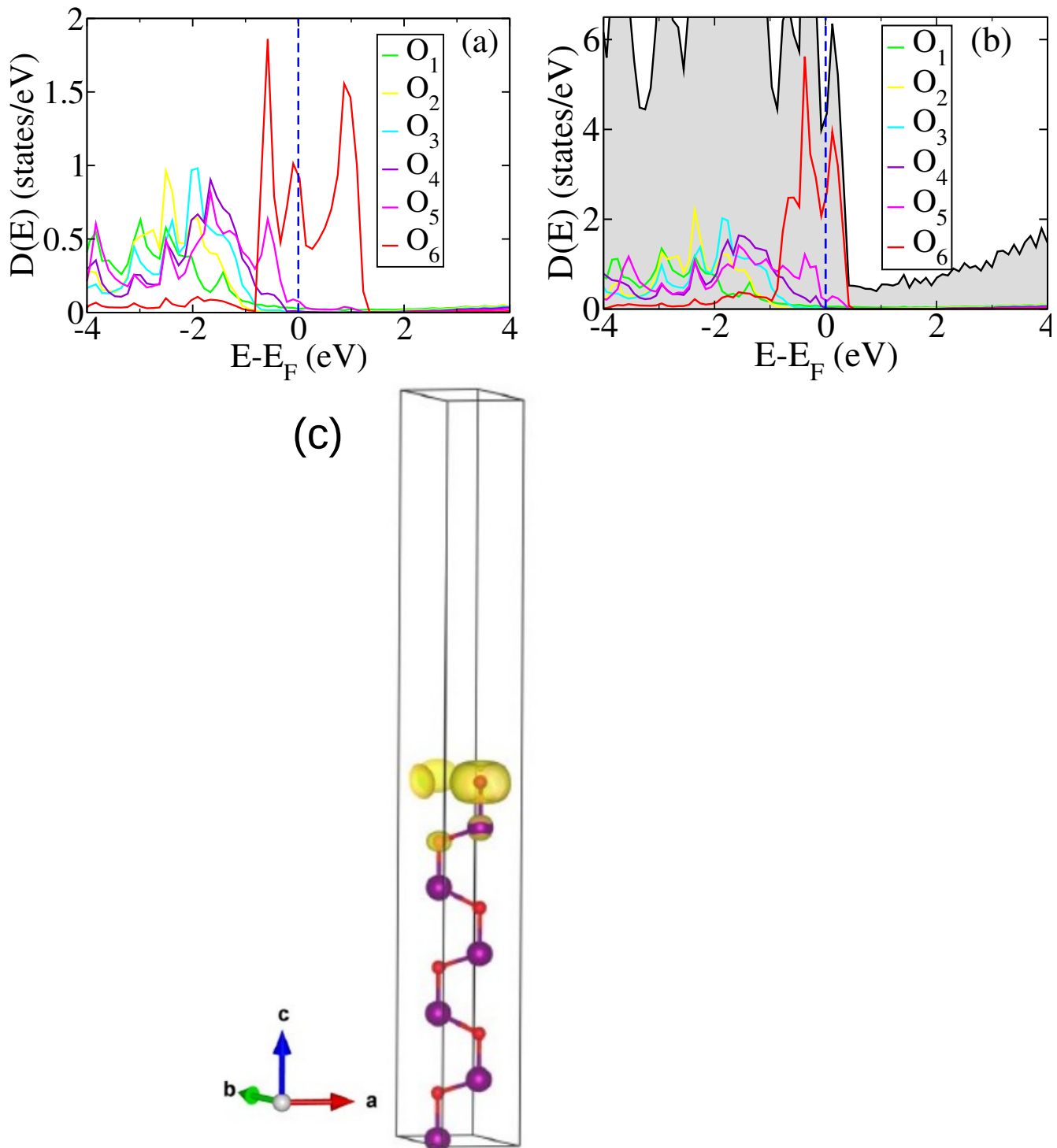


Figure 5.22: Projected density of states of the relaxed structure of (0001) glide surface of ZnO showing contribution of O atoms (a) spin polarized with down spin channel (b) spin unpolarized. The vertical dashed line indicates the Fermi level. (c) Spin density iso surface for ZnO glide surface.

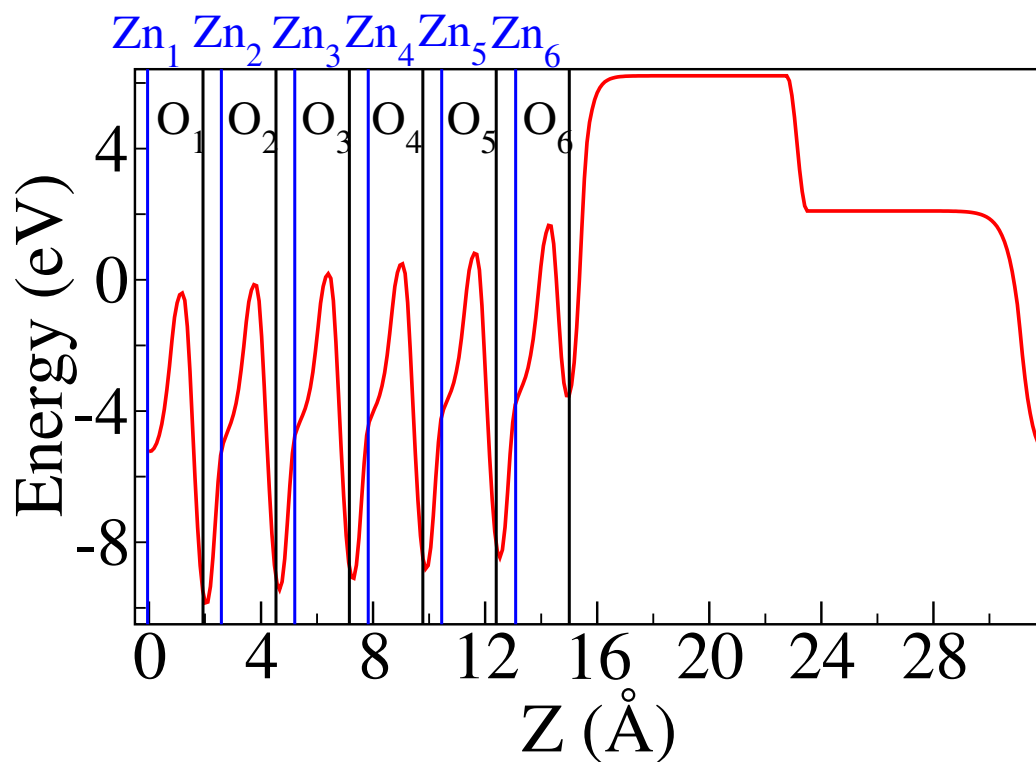


Figure 5.23: Planar averaged potential of ZnO along c axis with dipole correction

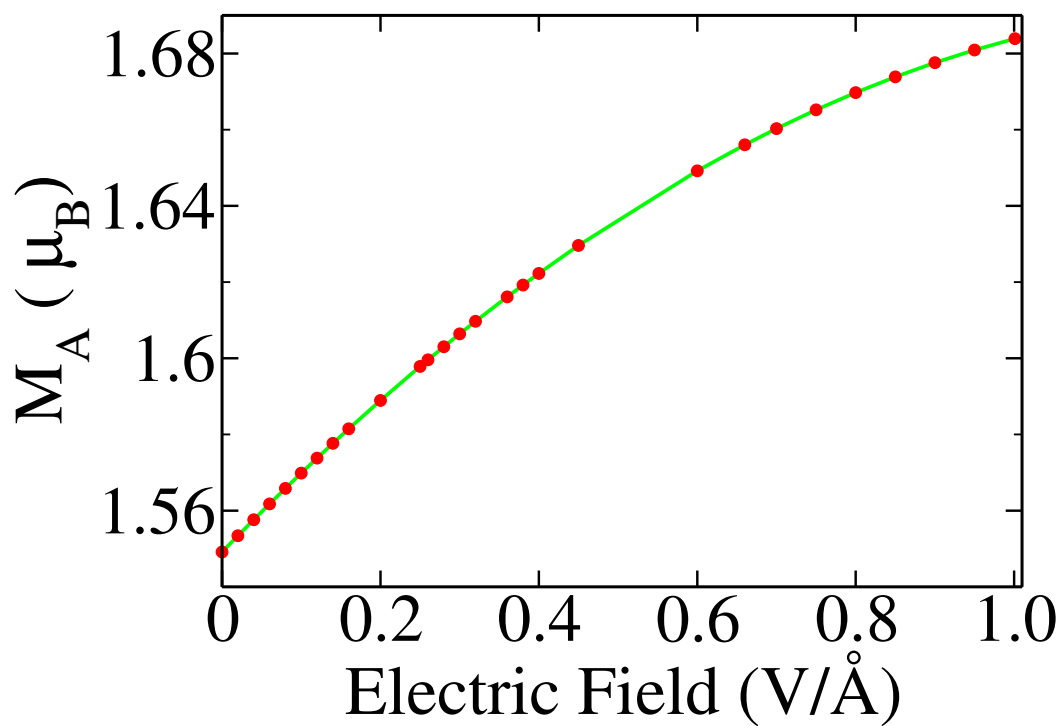


Figure 5.24: Magnetolectric behaviour ZnO glide plane.

# Studies on dynamical stability of glide BeO and ZnO surfaces

## 6.1 Motivation

In the study of glide surfaces of wurtzite BeO and ZnO in chapter 5, we have found metallization with emergence of 2DEG. Now to check the dynamical stability of the glide BeO and ZnO surfaces we have further performed phonon calculations with this surfaces within the framework of DFPT as described in chapter 2.

## 6.2 Dynamical stability BeO glide surface

We found  $1 \times 1 \times 3$  BeO glide surface is higher in energy by 7.75 eV with respect to bulk. We analyzed the structural stability of the glide surface through determination of their phonon spectra. We determine dynamical matrices and phonons at wave-vectors on a  $2 \times 2 \times 1$  mesh in the BZ using DFT linear response (QUANTUM ESPRESSO [291] implementation based on Greens function). From these, dynamical matrices and phonons at arbitrary wave vectors are obtained using

Fourier interpolation.

### 6.2.1 Phonon dispersion of BeO glide surface

We have found BeO  $1 \times 1 \times 3$  glide surface is structurally unstable. It is clear from the phonon dispersion as shown in figure 6.1. There are 3 unstable modes depicted in the phonon dispersion plot. Among them at M point the imaginary frequency has maximum with value  $346i \text{ cm}^{-1}$ . The other two unstable modes have significant imaginary values at M and K points. To get rid of the M-point instability, we

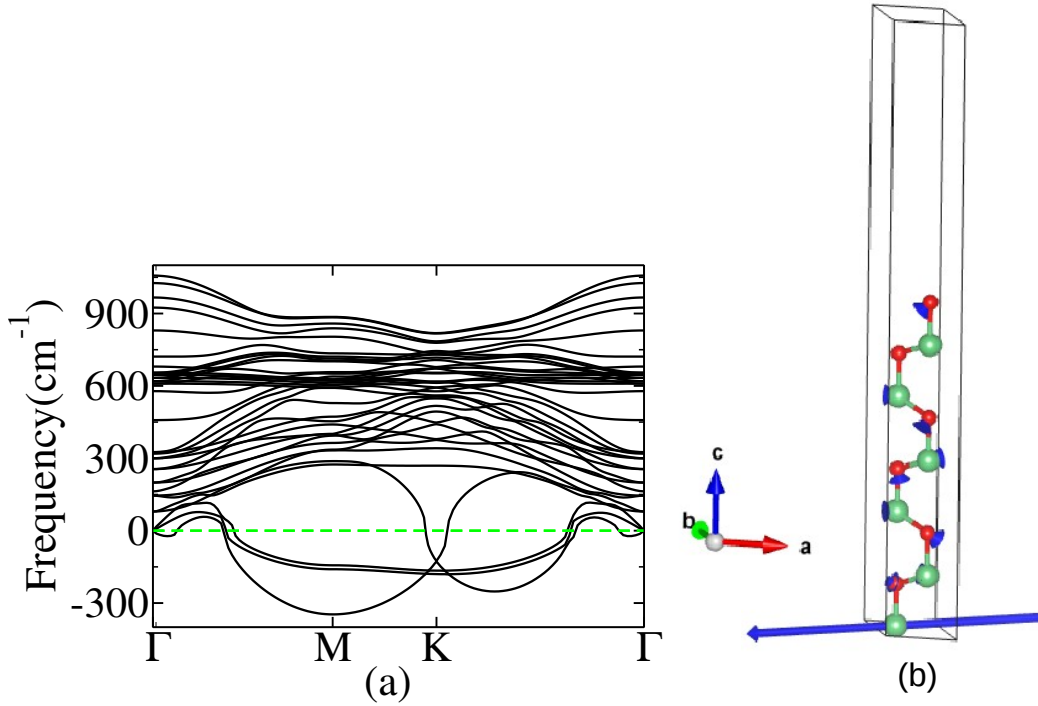


Figure 6.1: (a) Phonon dispersion of (0001) glide surface of BeO shown in Figure 5.4(a). (b) visualization of highest imaginary modes at M point, showing lattice instabilities at M point that would cause its reconstruction.

relaxed a  $2 \times 1 \times 1$  super cell of initial  $1 \times 1 \times 3$  glide surface. On freezing the eigen-displacements of the highest unstable mode at M-point of the  $1 \times 1 \times 3$  glide surface we obtained a distorted structure with Be-O bonds lengths changed associated

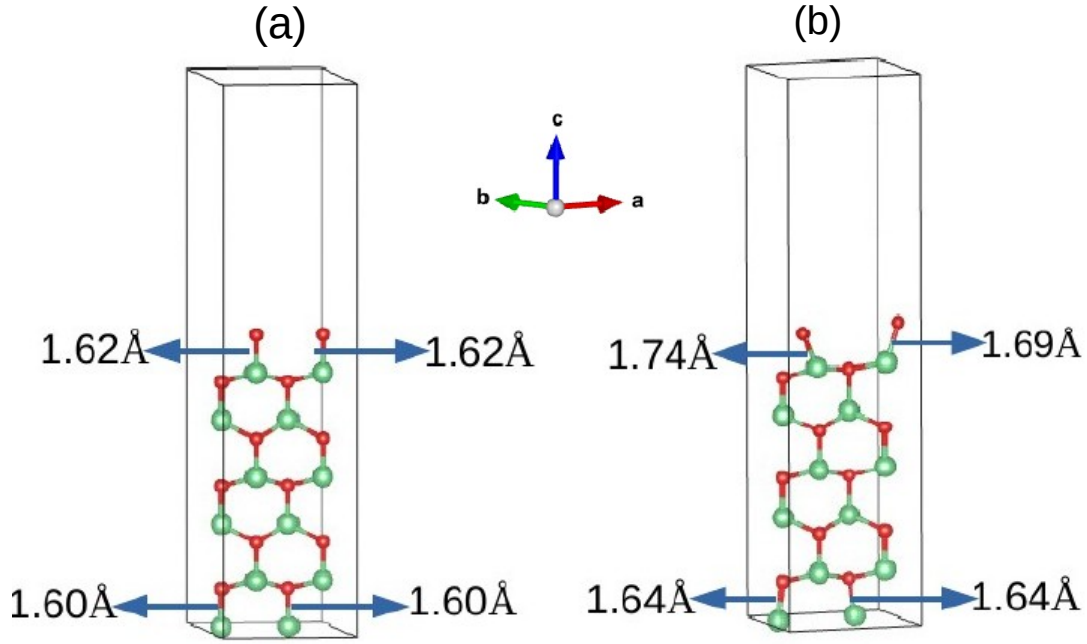


Figure 6.2: Reconstructed structure of  $2 \times 1 \times 1$  supercell of BeO (0001) glide surface of figure 5.4 (a) with eigen displacements for unstable mode at M point, initial (a) and relaxed (b).

with surface atoms as shown in figure 6.2. The distorted relaxed structure, as shown in figure 6.2(b) is lower in energy by 1.373 eV with respect to the twice undistorted  $1 \times 1 \times 3$  structure (5.4 (a)). The distorted system is metallic as shown in figure 6.3 but non magnetic. With this reconstructed structure of BeO glide surface we have further studied phonon dispersion to check it's dynamical stability. There is one unstable mode for this reconstructed structure as shown in figure 6.4 Maximum value of imaginary frequency is found here at S point. Its value is  $259i \text{ cm}^{-1}$ . We relaxed again the  $2 \times 2 \times 1$  super cell of earlier reconstructed structure. Eventually we have performed  $4 \times 2 \times 1$  super cell of initial  $1 \times 1 \times 3$  structure , no of atoms here 8 times the initial one. After freezing the eigen-displacements of the unstable mode at S-point of the earlier reconstructed glide surface we obtained a distorted structure as depicted in figure

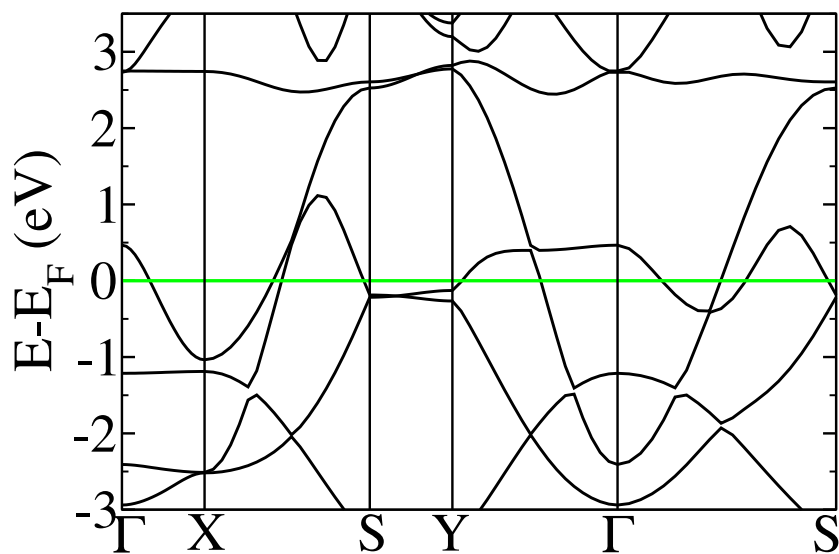


Figure 6.3: Electronic structure of reconstructed  $2 \times 1 \times 1$  supercell BeO glide surface (as shown in figure 6.2 (b))

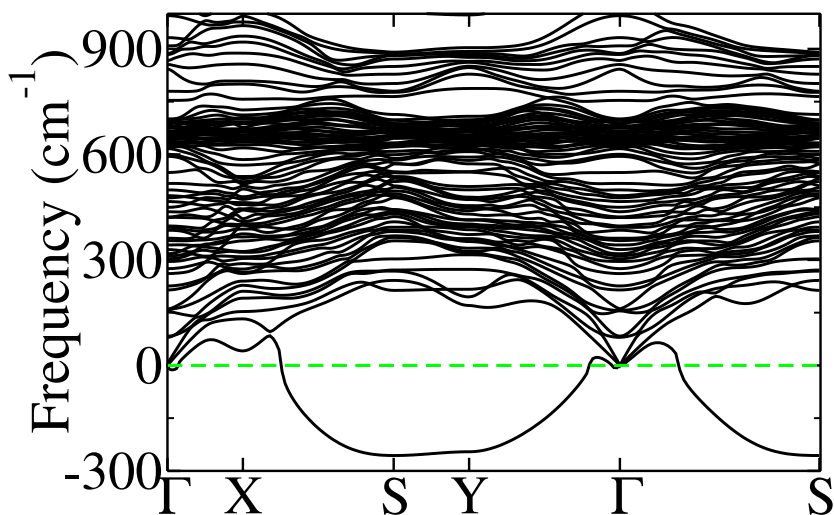


Figure 6.4: Phonon dispersion of reconstructed  $2 \times 1 \times 1$  supercell BeO glide surface (as shown in figure 6.2(b))

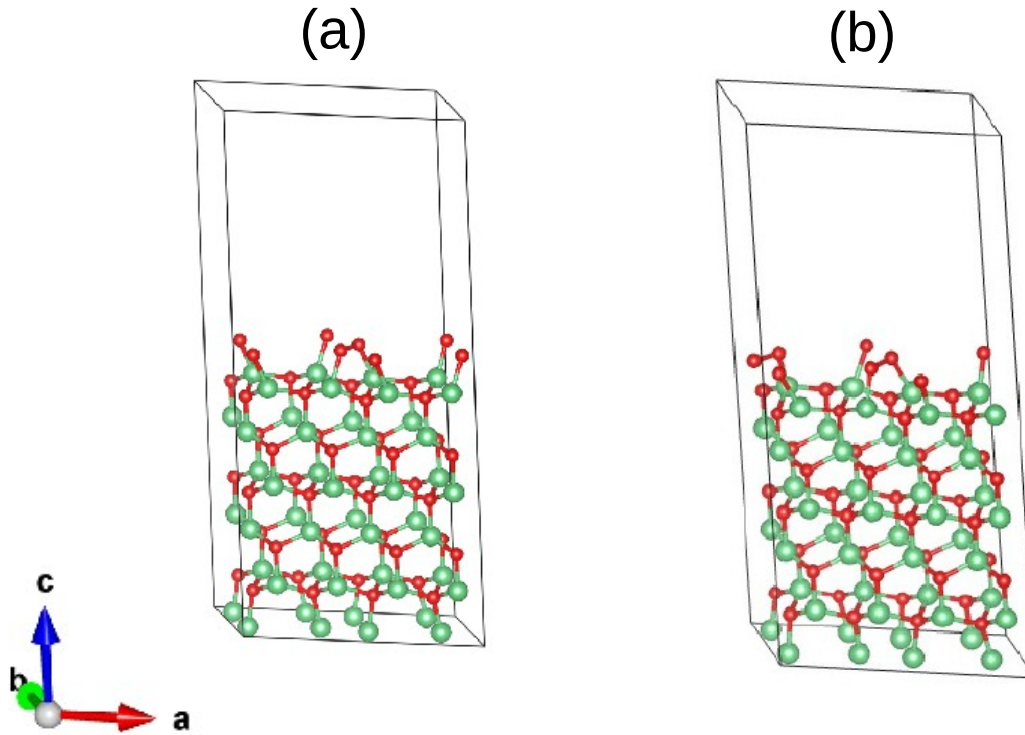


Figure 6.5: Reconstructed structure of  $2 \times 2 \times 1$  supercell BeO glide surface (as shown in figure 6.2 (b) with eigen displacements for imaginary mode at S point). Panel (a) and (b) for initial and relaxed structure respectively.

6.5 This reconstructed structure is also metallic and it is lower in energy by 9.515 eV lower than 8 times of unreconstructed  $1 \times 1 \times 3$  BeO glide surface. In this case we have found spin polarized and spin unpolarized reconstructed structure with almost same energy and both are metallic, shown in figure

### 6.3 Dynamical stability of ZnO glide surface

Like BeO we have performed some calculation to understand the dynamical stability of ZnO glide surface. Like BeO glide surface, ZnO glide surface was also found with dynamically unstable. We have seen there are 4 imaginary modes with two of almost same value. Here also the highest imaginary frequency found

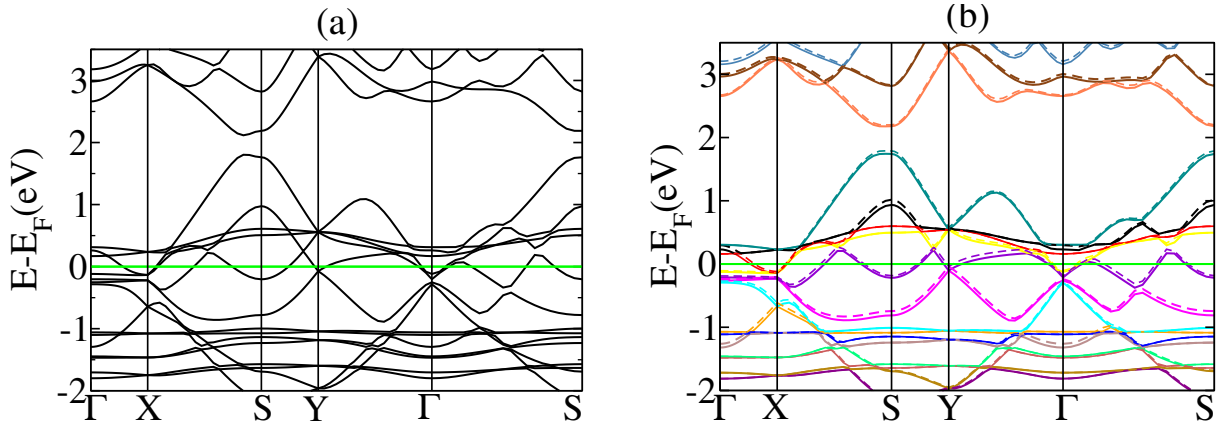


Figure 6.6: Electronic structure of  $2 \times 2 \times 1$  reconstructed glide surface of BeO (shown in figure 6.5(b)), calculated with (a) spin-independent and (b) spin-dependent DFT respectively.

at M high symmetry point and it has the value  $161.30i \text{ cm}^{-1}$ . To get rid of this

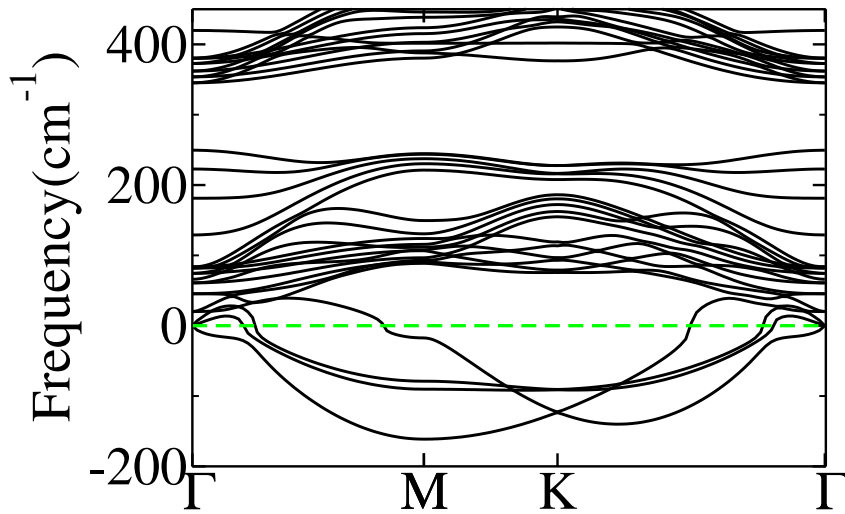


Figure 6.7: Phonon dispersion of ZnO  $1 \times 1 \times 3$  glide surface(as shown in figure 5.6(b))

M point instability we followed the same treatment done with BeO. The bond lengths of the surface atoms changed. This reconstructed relaxed surface is also metallic as found in the electronic structure shown in figure 6.9 The reconstructed relaxed  $2 \times 1 \times 1$  structure is almost 2 eV lower than the unreconstructed one.

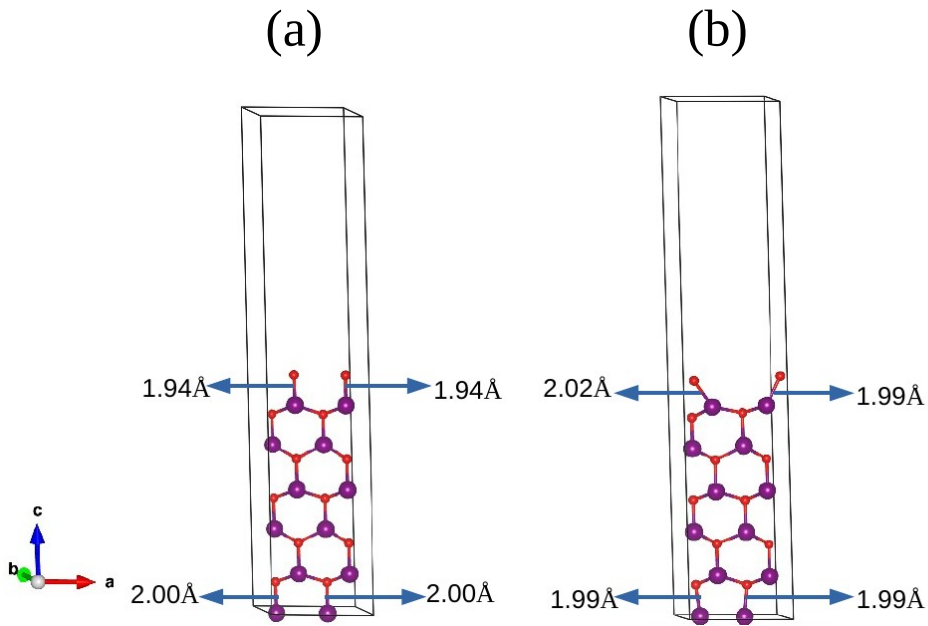


Figure 6.8:  $2 \times 1 \times 1$  reconstruction of (0001) glide surface of ZnO (shown in figure 5.6(b)), structure before (a) and after (b) relaxation.

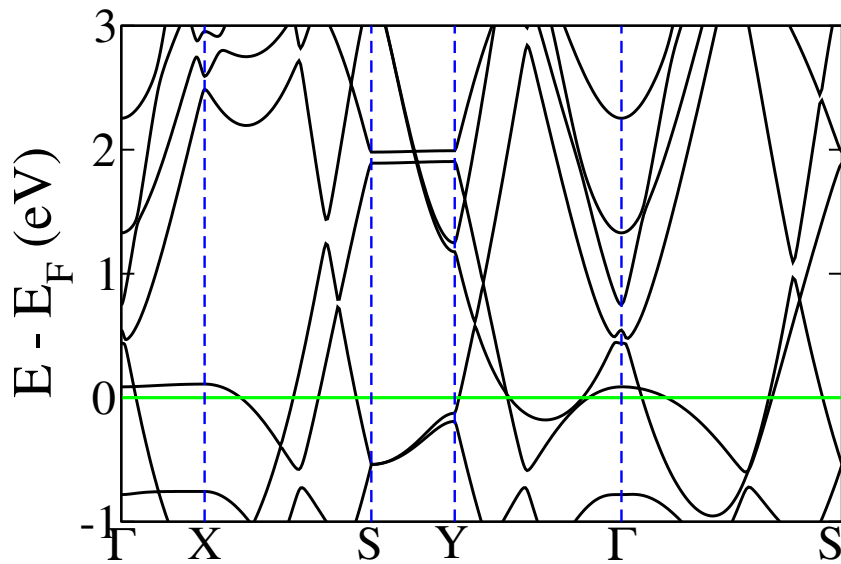


Figure 6.9: Electronic structure of ZnO  $2 \times 1 \times 1$  reconstructed glide surface (shown in figure 6.8(b)).

## 6.4 Conclusion

The study of dynamical stability using the phonon dispersion of the glide surface of wurtzite BeO and ZnO was showing a competition between structural instability and instability to form 2DEG. The reconstructed surface with lower energy remains metallic, and there was presence and absence of magnetism alternatively in the ground state at least for two consecutive reconstruction. The reconstructed glide surface becomes more and more stable as we increase its dimension in the x-y plane. We found the  $4 \times 2$  reconstructed surface is more than 9 e lower than the unreconstructed in case of BeO and also metallic with some magnetism. Usually polar surface with non vanishing dipole moments is unstable, but here stability is found in a polar surface by increasing it in x-y dimension. We checked this metallicity as well as presence of 2DEG is not dependent on the thickness of the slab along z direction. We have checked all our studies in case of ZnO glide surface also, and found the same characteristic as BeO glide surface. In this detailed study we have found the glide surface is metallic with magnetism, where the bulk material is polar insulator.

## Summary and future outlook

This thesis composed of three projects. The first two are on atomic cluster systems and the third one involves studies on polar oxide surfaces. All of them are studied incorporating first principles density functional theory (DFT) calculation.

### 7.1 TaSi<sub>16</sub> on HOPG: A DFT study

In this project extensive studies of electronic structure of HOPG supported TaSi<sub>16</sub> cluster has been performed. For computational cost a single structure has been deposited. After checking the chemical stability and molecular dynamics simulation, it was found that it is physisorbed and the cage structure distorted but it never broke. It can be predicted that these properties will remain same when more number of clusters will be deposited. So this can be taken as ideal system for self assembly of deposited cluster system which is used in cluster assembled material. Here due to weak interaction of cluster and substrate the properties of isolated clusters remains almost same after adsorbed on HOPG. Hence the next work can be performed by changing the central Ta atom with V with DFT calculatuon, as they are in same group in periodic table. For deposited TaSi<sub>16</sub>,

the experimental studies are already there. If the DFT results from V doped systems are similar as Ta doped systems, without experimental evidence of deposited V doped Si cluster, it can be predicted that if the central atom is from same group the supported cluster will behave in similar manner. If the V doped system behaves differently, then it will also very interesting to study further.

## **7.2 Designing of RE free PM: Insights from small Co clusters**

In this section of the thesis, the importance of various quantities like HOMO-LUMO gap, mixing, magnetic moment etc. has been demonstrated predicting them as possible responsible parameters for determining the MAE in doped Co cluster systems. We have studied with total 60 doped Co clusters by taking 10 of each doping elements. Incidentally mixing was not found as an important parameter for controlling the MAE of doped Co cluster systems. We checked with non magnetic doping elements from group 14 and group 15 and “which element is doped with the Co cluster”, this fact did not play any role in controlling the MAE values. The amount of mixing was found also insignificant in determination of MAE. The next work can be a checking whether mixing plays any important role while doping with non magnetic elements from other group. From these results a machine learning study can be done taking the parameters as descriptors and study further for other cluster systems with different sizes and changing the Co atom to another magnetic elements.

### 7.3 Emergence of 2DEG in polar oxide surfaces

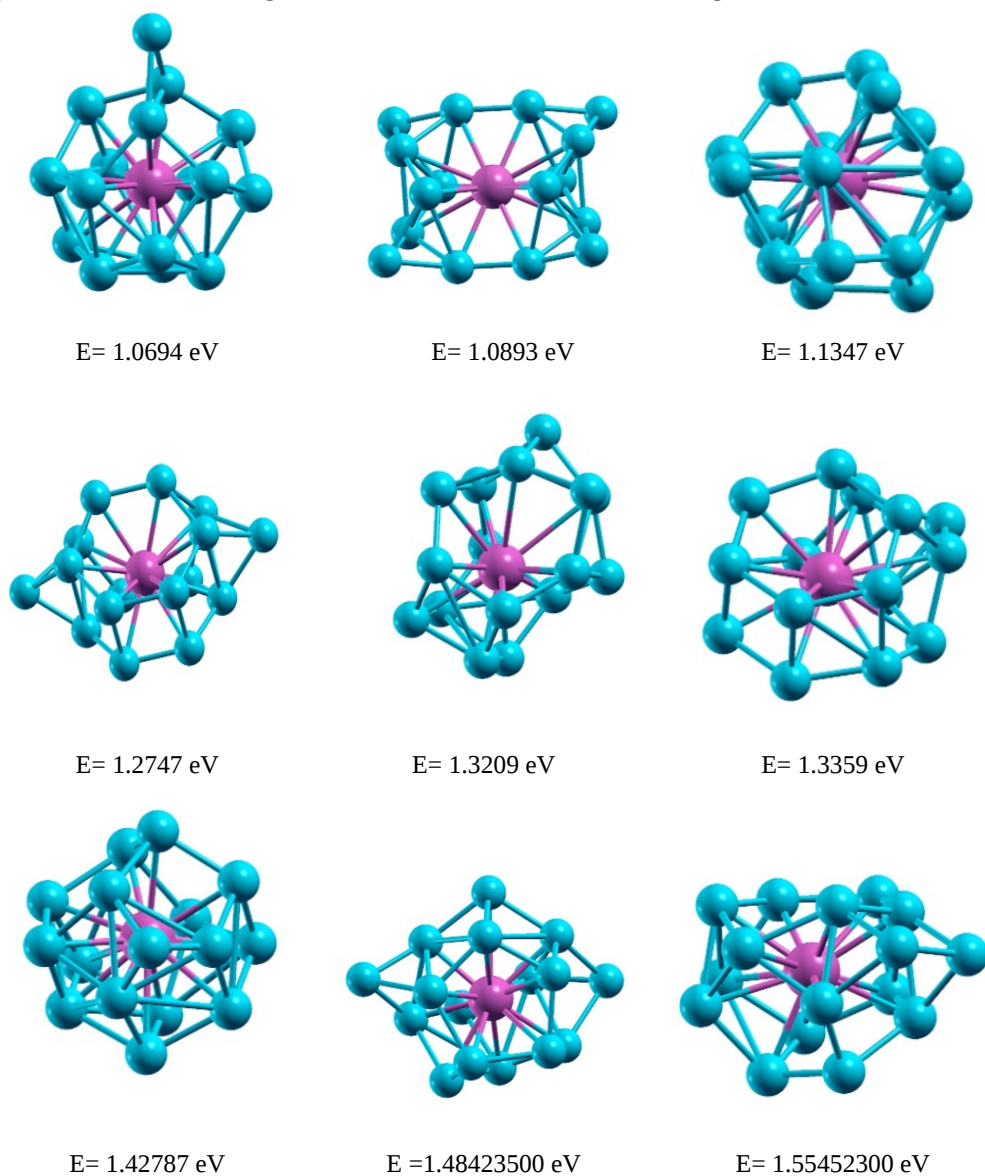
Glide surfaces of wurtzite BeO and ZnO have been studied extensively. Insulator to metal transition has been found with emergence of 2DEG in both cases. Strong magneto electric coupling found interestingly. These systems can be used further in spintronics. Most importantly the metallicity in the glide surfaces is found with surface reconstruction. The reconstructed surfaces are dynamically stable than the un reconstructed one, but metallic.

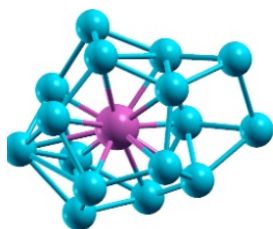
BeO is a rather large band gap insulator. It will be interesting to consider its solid solution with ZnO and its surface, substitution at the surface to control and achieve these unusual properties of 2DEG and magneto electric effect in a robust way so that they could be useful in a number of applications from catalysis to sensors.

APPENDIX **A**

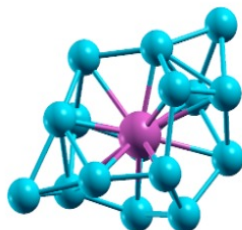
Adsorption of TaSi<sub>16</sub> cluster on HOPG

Figure A.1: Structures of isolated globally optimized  $\text{Tasi}_{16}$  cluster with energy larger than 1 eV from ground state, calculated including vDW-DF2.

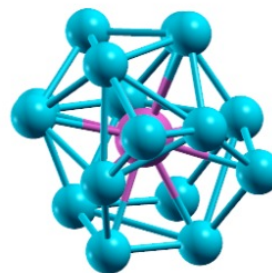




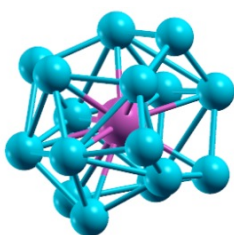
E= 1.55457100 eV



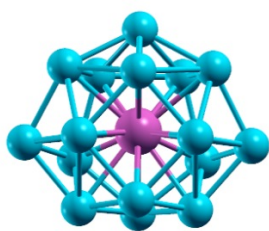
E= 1.58073900 eV



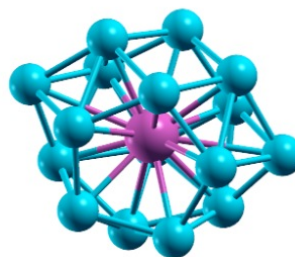
E= 1.65113600 eV



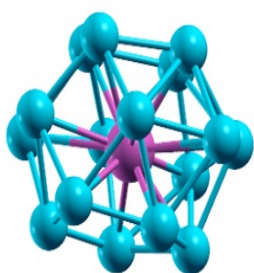
E= 1.65131500 eV



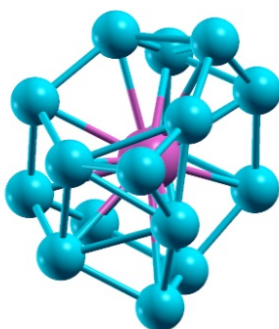
E= 1.65207500 eV



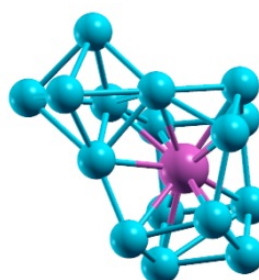
E= 1.65211300 eV



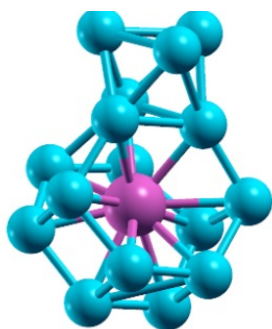
E= 1.65215200 eV



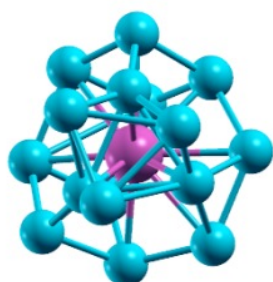
E= 1.67262300 eV



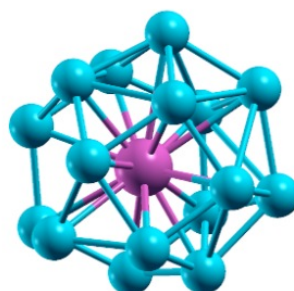
E= 1.68651800 eV



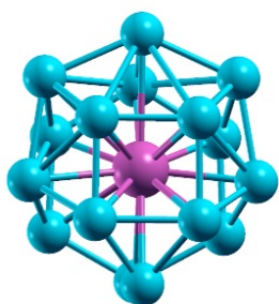
E= 1.68655600 eV



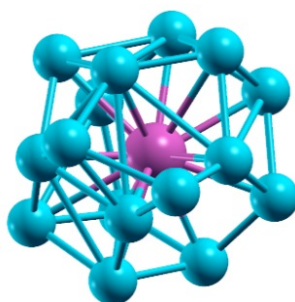
E= 1.68905800 eV



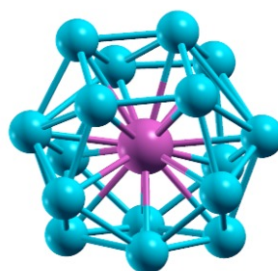
E= 1.80118700 eV



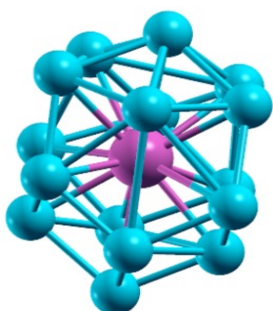
E= 1.80124300 eV



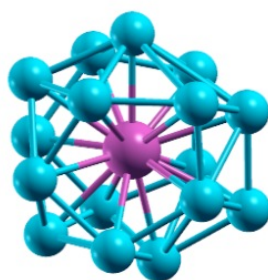
E= 1.84719000 eV



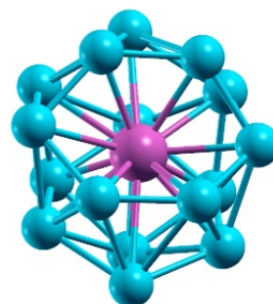
E= 1.87419000 eV



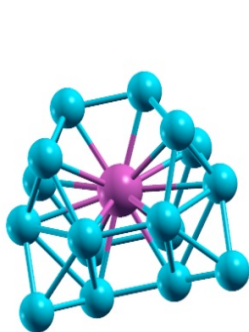
E= 1.87433900 eV



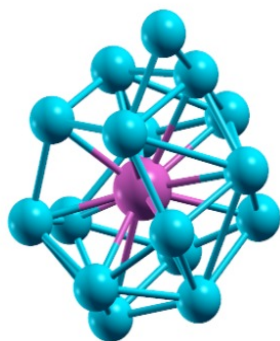
E= 1.87438400 eV



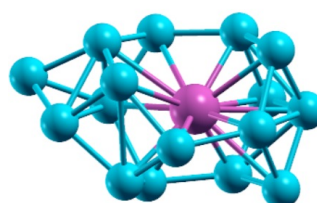
E= 1.89120600 eV



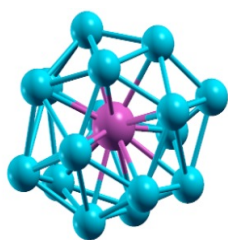
E= 1.91601300 eV



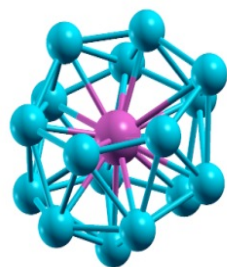
E= 1.92080800 eV



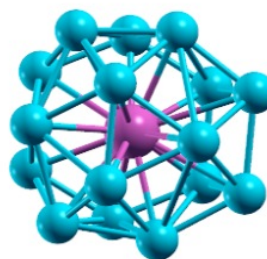
E= 1.96898700 eV



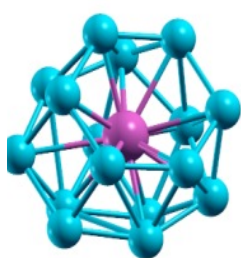
E= 1.98202600 eV



E= 1.99389400 eV



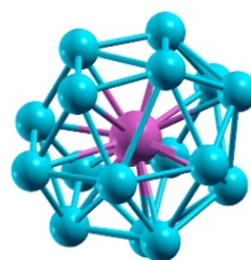
E= 2.02296600 eV



E= 2.02318900 eV



E= 2.02326300 eV



E= 2.02328200 eV

## Thesis Highlight

Name of the Student: ARPITA SEN

Enrolment No.: PHYS08201404001

Name of the CI/OCC: Harish-Chandra Research Institute

Thesis Title: FIRST PRINCIPLES STUDIES OF ELECTRONIC AND MAGNETIC PROPERTIES OF ATOMIC CLUSTERS AND SURFACES OF POLAR OXIDES

Discipline: Physical Sciences

Sub-Area of Discipline: Materials Theory

Date of viva voce: 05/04/2021

The thesis is comprised of mainly two topics (1) electronic and magnetic properties of atomic clusters both isolated and surface supported, and (2) stability and electronic structures of polar oxide surfaces. The three separated systems have been studied here including transition-metal-doped Silicon cluster deposited on graphite substrate, doped Co clusters as a building block of permanent magnetic materials, polar oxide surfaces with quite different electronic and magnetic properties from its bulk. These thesis has included the characterization of clusters and surfaces of fundamentals and technological interests by means of first principles density functional theory(DFT).

- In case of transition-metal-doped Silicon clusters, the properties can be tuned by changing the doping element as studied extensively over last 2-3 decades both theoretically and experimentally. We have studied here Ta doped  $Si_{16}$  cage clusters starting from a systematic global search of ground state structure. With the isolated ground state structure further studies have been done by checking its stability after reaction with Oxygen. Adsorption of TaSi<sub>16</sub> cluster on graphite was studied using DFT. These calculations resolve some of the issues raised by the experiments of Shubita et al. (*J. Am. Chem. Soc.* 2015, 137, 14015-14018) and provide additional insights into the system. For the first time, the ground-state structure of TaSi<sub>16</sub> is obtained through a global search employing an evolutionary algorithm and for studying the finite temperature behavior, ab initio molecular dynamics simulations have been performed which was found phsorption of cluster on substrate with small charge transfer between cluster and substrate. No diffusion has been found up to pico second time scale.
- The urgent drive from rare earth (RE) free permanent magnet (PM) is necessitated by supply side constraints with RE elements like Dy, Tb, Nd etc. PM s form essential parts in various devices in a wide range of applications including hybrid and electric cars, wind turbines, motors in many household appliances, satellite communications systems and magnetic data storage systems etc. As an alternative building block of RE free PM doped Co clusters were studied using DFT. For the first time, low energy isomers and magnetic moments of pure Co<sub>4</sub> and Co<sub>6</sub> clusters, and the doped clusters are identified through a global search employing an evolutionary algorithm. The magnetic anisotropy energy (MAE) of these clusters is then calculated. Through further analyses we establish that MAE is largely determined by the sum of absolute values of the spin moments on the individual atoms, and the HOMO-LUMO gap of the system.
- The formation of 2-dimensional electron gas at surface of polar BeO and ZnO was found from DFT calculations, which has fundamental interest as well as technical application. The surfaces of polar oxides were found as magnetic, where in bulk these are non magnetic. The metallicity was found as an effect of polar catastrophe. Applying external electric field, magnetization was changed with a significant value of magneto electric coupling make the system more useful in devices.